Flow-Pattern-Based Heat Transfer and Pressure Drop Correlations for Condensing Refrigerants in Smooth Tubes

Marcel Christians

Department of Mechanical and Aeronautical Engineering

University of Pretoria

Supervisor: Prof. L. Liebenberg
Co-supervisor: Prof. J.P. Meyer

A dissertation submitted in partial fulfillment for the degree of

Master of Engineering in Mechanical Engineering

March, 2007

Abstract

The phase-out of ozone-depleting refrigerants, such as R-12 and R-22, according to the Montreal Protocol of 1987, has provided the incentive to increase the thermal efficiency of current heating and refrigeration systems. The purpose of this study was to increase the accuracy of the predictions of both the heat transfer and pressure drop correlations for condensing refrigerants in the Intermittent flow regime. This was done utilizing a novel method involving the temporal and spectral analysis of the light intensity of the local flow regime, as seen through a sight glass. An experimental setup was designed, built and commissioned specifically for this purpose using refrigerant R-22 and a smooth tube. It was found that the accuracy of the mean heat transfer coefficient predictions increased substantially compared to other leading correlations, particularly at low mass fluxes. In terms of the pressure drop, the predictions also increased in accuracy, and it was found that the time fraction method allows for continuous predictions over flow regime transitions when using local flow-pattern-based pressure drop models. This was previously not possible.

It is the mark of an educated mind to be able
to entertain a thought without accepting it.

Aristotle

Acknowledgements

Professor Liebenberg For his advice, support, guidance and encouragement;

Professor Meyer For his counsel and guidance, as well as his financial support of my graduate studies;

Eugene van Rooyen (graduate research student) My teammate, who helped me out on more occasions than I can count. Thanks;

Jonathan Olivier & Dewald Pieterse (graduate research students) For their assistance before, during and after the experimental phase;

Danie Gouws For his help during the final months of experimentation;

M-Tech Specifically Philip de Vos, Martin van Eldik and Robbie Arrow, for their expertise, and guidance.

Contents

List of Figures

List of Tables

Nomenclature

Roman Symbols

A_c	Cross-sectional area (m^2)
A_L	Heat transfer area (m^2)
A_l	Heat transfer area (πdL)
B_i	Bias of i^{th} measurement
C_o	Distribution parameter ($C_o = \frac{<\epsilon U>}{<\epsilon><U>}$)
c_p	Isobaric specific heat (J/kgK)
D	Diameter (m)
d	Diameter (m)
E	Energy (J)
f_i	Interfacial roughness factor
F_m	Non-equilibrium mixture factor
Fr	Froude number ($Fr = \frac{G^2}{\rho_l^2 g d_i}$)
f	Friction factor
G	Mass flux (kg/m^2s)
Ga	Galileo number ($Ga = \frac{\rho_l(\rho_l - \rho_v)gd^3}{\mu_l^2}$)

g	Gravitational acceleration (m/s^2)
h	Enthalpy (J/kgK)
h	Height of the liquid pool (El Hajal *et al.* (2003) model)
h_{lg}	Isobaric latent heat of condensation (J/kg)
i	Internal energy in a control element (J/kg)
J_v	Dimensionless gas velocity ($J_v = \frac{xG}{gD\rho_v}$)
KE	Kinetic energy (J)
k	Thermal conductivity (W/mK)
L	Length of tube (m)
$\dot{m}$	Mass flow rate (kg/s)
n	Number of fins
Nu	Nusselt number ($Nu = \frac{hD}{k_l}$)
p	Pressure (Pa)
dp	Static pressure (Pa)
P	Contact perimeter (m)
Ph/Ja	Phase change number / Jakob number ($Ph = \frac{c_{p,l}(T_s - T_w)}{h_{lg}}$)
p_r	Reduced pressure, p/p_{crit}
P_i	Precision of i^{th} measurement
$\dot{Q}$	Heat transfer (W)
S	Velocity slip ratio
x	Vapor quality
$\dot{Q}$	Volumetric mass flow rate (m^3/s)

R^2	Coefficient of determination
R_c	Bell and Ghaly Resistance (W/mK)
Re	Reynolds number (GD/μ_l)
R_f	Film Resistance (W/mK)
r	Internal radius of the tube (m)
R_w	Tube wall thermal resistance (mK/W)
$\bar{v}$	Specific volume (m^3/kg)
t	Time (s)
T	Temperature (K)
T	Temperature (K)
tf	Time fraction
UA	Overall heat transfer coefficient (W/K)
U_{GL}	Gas Drift flux velocity (m/s)
u	Velocity (m/s)
dF	Wall shear force (N)
We	Weber number ($We = \frac{g(\rho_l - \rho_v)d^2}{\sigma}$)
X_{ii}	Martinelli parameter, where i can be turbulent or laminar
$x^\star$	Laminar flow dimensional number
z	Height of channel (m)

Greek Symbols

β	Volumetric quality
∂	Differential operator

Δ	Difference
δ	Liquid film thickness
ΔT_{glide}	Temperature difference due to zeotropic glide
δ	Uncertainty
ϵ	Time-averaged void fraction
ξ	Correction factor for the Thome flow pattern map
Γ	Mass generation per unit rate
μ	Kinematic viscosity (Pa/s)
ϕ	Two-phase frictional multiplier
ρ	Density (kg/m^3)
σ	Surface tension (mN/m)
τ	Wall shear stress (Pa)
τ_{knz}	z-component of the shear stress
θ	Inclination angle of channel (^{o})
θ	Falling film angle

Superscripts

$\bar{}$	Time-average
$\dot{}$	Time rate
T	Transition

Subscripts

kn	Interface between phases k and n
a	Acceleration/momentum

avg	Average
b	Bulk
bubbly	Transition between Intermittent/Bubbly flow
c	Cross sectional
c	Convective (used with h, the heat transfer coefficient)
corr	Correlations
exp	Experimental
f	Frictional
f	Film
g	Gas phase
gl	Liquid (drift flux)
grav	Gravity dominant
gu	Weighted mean (drift velocity)
h	Hydraulic
h	Homogeneous
IA	Transition between the Intermittent and Annular flow regimes
id	Inner, non-dimensionalized with the tube diameter
i	Inner
i	Pertaining to the liquid-vapor interface
k	Phase '*k*'
ld	Liquid, non-dimensionalized with the tube diameter
l	Liquid phase

LMTD Logarithmic mean temperature difference

lo Liquid only

mist Transition from Annular to Mist

mom Momentum

knz Phase k, normal to z-component

o Outer

pc in Precondenser inlet

ra Rouhani-Axelsson

ref Refrigerant

satliq Saturated liquid

satvap Saturated vapor

shear Shear-stress dominant

s Shell-side

strat Stratification angle

testin Inlet of test section

tp Two-phase

tt Turbulent liquid to turbulent vapor (for use in the Martinelli parameter)

v Vapor phase

vd Vapor, non-dimensionalized with the tube diameter

vo Vapor only

w Wall

wavy Transition from Stratified to Stratified-wavy flow

w, i Wall, inner

wl Wall per unit length

w, o Wall, outer

z Gravity height

Other Symbols

$\sum$ Sum operator

Acronyms

CFC Chlorofluorocarbons

EB Energy Balance

EEV Electronic expansion valve

EF Enhancement factor (h_m/h_s)

HCFC Hydro-chlorofluorocarbons

NI National Instruments

R-22 Chlorodifluoromethane, $CHClF_2$

ROI Region of interest

RTD Resistance temperature detector

SCXI Signal Conditioning Extensions for Instrumentation

VI Virtual Instrument

vol-ppm Parts per million, volume basis

Chapter 1

Introduction

1.1 Background

Rowland and Molina (1974) first raised the concern of the depletion of the stratospheric ozone in 1974. The authors described a chemical reaction that could result in man-made chlorofluorocarbons depleting the ozone layer for decades. The concerns raised by the data in this article led to the ratification of the Montreal Protocol in 1987. The end result of this Protocol was the proposal of a 50% reduction in CFC use by 1998, but no phase-out of hydro-chlorofluorocarbons.

The 1990 London Convention shortened the phase-out timetable internationally, while in the United States, it was shortened by the 1990 Clean Air Act. Rather than a 50% reduction in the use of CFCs, the Convention, and the US Act called for a 100% reduction in the use of CFCs in industrialized nations by 1996, and 100% elimination of HCFC use by 2015 (Liebenberg, 2002).

The phase-out also provided the opportunity to review the potentials of current commercially significant systems (ammonia, absorption, air) and other new not-in-kind technologies[1]. Besides ammonia, proposed replacement refrigerants include propane (R-290), isobutane (R-600a), and carbon dioxide (R-744). These refrigerants, commonly called "natural refrigerants", have lately been the topic of considerable research interest with the goal to establish their viability as HFC substitutes.

[1]Systems that do not use conventional refrigerants or are not vapor-compression machines

In new commercial equipment, R-134a is currently being used as low-pressure fluid replacement (mainly replacing R-12), whilst R-407C (R-32, R-125, R134a - 23/25/52% blend) is used as a high-pressure replacement fluid (mainly replacing R-22). The two zeotropic mixtures that are currently being used in large quantities as replacement fluids are R-410A (R-32/R-125 in a 50/50% blend), and R-407C. The hydro-fluorocarbon R-410A, with its azeotrope-like behaviour, is attractive for its traditional field handling practices, but also for its potential for smaller sized equipment and the possibility of improved coefficient of performance. However, the higher pressures that it works with can somewhat negate the improved coefficient of performance, especially if the existing equipment needs to be replaced to handle R-410A's operating conditions.

Furthermore, apart from environmental concerns raised by the depletion of the ozone layer, energy efficiency also came to the forefront. In the United States, the National Applicance Energy Conservation Act of 1987 promulgated a wide range of increases in minimum energy efficiency standards for refrigerators, freezers, air conditioners, and heat pumps. Typically, energy efficiency increases of 25% for domestic appliances were stipulated (Dobson, 1994).

Another consequence of both the Montreal Protocol and the subsequent stringent regulations was the development of passive heat transfer enhancement methods, such as helical and microfin tubes.

1.2 Motivation of the study

As a direct result of the combination of the above, design methodologies which were based more on experience and 'rule of thumb', rather than a solid scientific base, were proved to be inadequate to satisfactorily predict the heat transfer and pressure drop performance of heat exchangers.

Consequently, studies of flow condensation are widely available in technical literature. These studies contain not only analytical efforts to model the physics of the condensation process, but also experimental efforts to measure the heat transfer behavior of their topical fluids. In this second area, most, if not all, investigators collect data for a limited number of fluids under specific operating conditions, and then attempt to match their acquired data with existing correlations, or to

develop their own. Many correlations are available, but come without explicit range of parameters over which they can be expected to give results. This results in difficulties for the design engineer to select a correlation, due to contradictory reports as to which one is 'best'.

While it has been shown, and is now widely accepted, that the heat transfer and pressure drop are inexorably linked to the prevailing flow regime, one single unifying theory for in-tube condensation does not presently exist. Currently, a basic consensus of what the main flow regimes encountered during condensation has been reached, as well as the type of prevailing flow (film flow, or annular flow) encountered within each regime. From this, the regimes' heat transfer and pressure drop correlations are treated completely independently from each other, and in most cases, during transitions between regimes, a discontinuity in predicted values is observed. This is in direct contradiction to experimental data, where a continuous transition occurs.

Modern heat transfer correlations, especially those of Thome *et al.* (2003) and Cavallini *et al.* (2006), have shown tremendous progress in terms of modeling the physics of the condensing flow, rather than trying to forcefit data to equations not meant for those specific regimes. Case in point, the use of two-phase multipliers in heat transfer correlations, which were known to be non-descriptive of the processes in occurance most of the time, led to highly constrained correlations that were only accurate in very specific conditions.

Frictional pressure drop correlations, on the other hand, still rely on two-phase multipliers to predict the effect of the vapor and liquid phases. The main problem is that two-phase multipliers artificially segregate the flow into two separate streams. Distinct mathematical models for the pressure drop during film and annular flow that would be analogous to the models for heat transfer in said flows have not been developed. All correlations that have been developed up to now rely on the same form of the two-phase multipliers, with differing constant coefficients and exponents.

The void fraction, which is a measure of the geometric vapor quality (*i.e.* the ratio of tube cross-sectional area taken up by the vapor and the total cross-sectional area), is one of the most fundamental properties of the flow, both with

respect to heat transfer and pressure drop. However, it is quite difficult to measure the void fraction accurately, and cost-effectively.

1.3 Objectives of the study

The experimental setup utilized in this study was specifically designed and built to conduct both refrigerant evaporation and condensation experiments as part of this present study, and that of Van Rooyen (2007). As such, the first objective of this, as well as Van Rooyen's study was to validate the operation and results obtained from the setup.

As part of the validation procedure, several major components had to be discussed. The first, which to the author's knowledge is the first time it is done, was to attempt and validate the use of the laminar-turbulent Wilson plot method. The reason why this was necessary is described in Chapter 3. The Wilson plot method was to be compared against direct wall temperature measurements, and the better method selected from the two.

In terms of the heat transfer correlations, the intermittent flow regime (slug and plug flow) still presents a challenge. Due to the fact that this flow regime, from a heat transfer point of view, has a temporal mixture of shear-stress dominated and gravity dominated heat transfer modes, it is not possible to model this flow as just annular, or stratified-wavy flow. The objective in this respect was to use data obtained by Van Rooyen (2007) regarding the intermittent flow regime time fraction in which he created an intermittent flow regime time fraction indicator map. Then, with his time fraction map generated, the objective was to update the heat transfer correlation of the intermittent flow regime. Rather than utilize a single model, such as has been done in the past, the time fraction map (developed as a function of vapor quality and mass flux) would be combined with the local gravity-based and shear-stress-based flow heat transfer coefficients to give a more accurate prediction of the local intermittent heat transfer coefficient.

The primary objective in terms of the pressure drop was to present the pressure drop results, and to compare these against leading correlations. Furthermore, a study would be undertaken to attempt to link the time fraction map to the pressure drop study.

The last objective of this study was to attempt a comprehensive uncertainty analysis of the system; this includes the heat transfer coefficient, testing vapor quality, mass flux and the total, momentum and friction pressure drop as the main components to be investigated.

1.4 Layout of the dissertation

In Chapter 2, the existing literature relating to condensation heat transfer, pressure drop, two-phase flow regimes and void fraction prediction and models is discussed. The concept of time-fraction effect on the dominating heat transfer mode is introduced.

Chapter 3 describes the design, operation and instrumentation of the experimental setup. Apart from the physical layout, the control system utilized, as well as the control program written in a mixture of LabView and Matlab is discussed. The test section's more important instrumentation is discussed in further detail, as well as the test section design, and the methods of construction.

Chapter 4 is a continuation of the work begun in Chapter 2, in the sense that it only deals with existing heat transfer and pressure drop correlations. Both heat transfer and frictional pressure drop correlations for smooth and several types of enhanced tubes are discussed herein.

Chapter 5 discusses the specifics of the objectives laid out in the previous section, as well as reports the general findings from this study. Chapter 5 also critically investigates the findings presented and formulates results in line with the objectives laid out.

In Chapter 6, the major findings of this study are repeated and summarized. More importantly, perceived shortcomings in this study are addressed and areas recommended for future research.

Appendix A presents a short history of the Wilson plot method, and detailed results obtained from the study.

Appendix B also presents a short history of the Uncertainty Analysis method, the detailed calculations and the results found using several cases in the test matrix.

Appendix C offers a DVD with the raw data that was saved by the automatic data acquisition system, as shown in Chapter 3.

Chapter 2

Literature Survey

2.1 Introduction

The most important factors influencing the performance of refrigerant-based refrigeration systems are the heat transfer, pressure drop, compressor performance and the refrigerant charge. As such, the relevant theories pertaining to the heat transfer and pressure drop during flow condensation are discussed herein. The properties of the refrigerants to be used in this study are discussed, followed by a summary of the process of condensation. The state-of-the-art Thome flow map for condensing refrigerants is described, and its construction detailed. A brief discussion of void fraction models and experimental measurements is also presented. Next, flow regimes and their importance are detailed. A small discussion regarding the dominant heat transfer modes in the Intermittent flow regime follows. Finally, the major models for two-phase flow inside tubes are also discussed.

2.2 Refrigerants

The experimental refrigerant utilized in this study is R-22. Due to its wide spread use, and large availability of data, R-22 is commonly used as the baseline refrigerant in experimental investigations. Since one of the objectives of this study is to experimentally validate the system, R-22 seemed to be a good initial choice.

2.2.1 R-22: Chlorodifluoromethane

The chemical name for R-22 is chlorodifluoromethane, and its chemical formula is $CHClF_2$. Utilizing NIST's REFPROP database (National Institute of Standards and Technology, 2002), some salient properties of R-22 are given in Table 2.1.

Table 2.1: Physical properties of R-22 (National Institute of Standards and Technology, 2002)

Molar Mass	86.47 g/mol
Triple point temperature	-157.42^{o}C
Normal boiling point temperature	-40.81^{o}C
Critical temperature	96.15^{o}C
Critical pressure	4.990 MPa
Critical density	523.8 kg/m^3

R-22 is, at the moment, the most widely used refrigerant worldwide (Olivier, 2003). It is utilized in a very large spectrum of applications, such as frozen food display cases (in supermarkets), upright and chest freezers, air-conditioners, cold rooms, refrigerated storage for scientific purposes, in-transport refrigeration, industrial refrigeration, heat pumps, and commercial refrigeration. This is due to its very broad evaporation range, which goes from -40^{o}C, up to 5^{o}C.

R-22 is classified as a non-flammable and non-toxic refrigerant, with a European Community standard limit value of 1000 vol.-ppm. The Ozone Depletion Potential (ODP) value is 94.5% less than that of R-12. However, due to the remaining ODP value of 5.5%, R-22 is still labeled as a refrigerant 'dangerous for the stratopheric ozone layer'. Due to this, and due to the phase-out of hydrochlorofluorocarbons (HCFCs) mandated by the Montreal Protocol (Olivier, 2003), R-407C is being phased in as a long-term replacement to R-22 in certain applications.

2.3 Flow condensation

Flow condensation is a process which occurs when there is a phase change between gas and liquid. This can occur when vapor is put into contact with a surface that has a temperature less than the saturation temperature of the vapor. Vapor

molecules strike the cooled surface, stick to it, and condense into liquid, due to the heat transferred from the vapor into the surface. Liquid which has been condensed from a vapor is referred to as condensate.

When the liquid does not cover the entire surface, it will tend to form numerous discrete droplets, referred to as dropwise condensation. The drops usually form in non-uniformities in the surface, such as pits, cracks and cavities. It is possible that the drops may grow, and even coalesce. If this occurs, they may become large enough that the adhesive forces, due to surface tension, are overcome by gravity and vapor shear. The drop then departs the surface, leaving the surface open for new condensate drops to form and coalesce.

Otherwise, filmwise condensation occurs when a thin liquid film covers the entire condensing surface. As such, a continuous film of condensate occurs.

In terms of heat transfer, the resistance to heat transfer increases with film thickness during filmwise condensation. That is, the thicker the film layer becomes, the less efficient will the heat transfer become. In dropwise condensation the majority of the heat transfer occurs through drops of less than 100 μm in diameter (Lienhard and Lienhard, 2005). As such it is common practice to use methods that decrease the surface tension, using, for example, surface coatings, to inhibit film formation, and stimulate dropwise condensation. However, most coatings used, over time, gradually lose effectiveness due to fouling, leading, eventually to film condensation. The difference is heat transfer between modes, according to Mills (1999), is one order of magnitude.

2.4 Flow regimes in condensing horizontal two-phase flow

In-tube condensation processes are complex due to the simultaneous motion of both vapor and condensate, in a more complex manner than for external condensation. During film condensation inside tubes, various flow regimes will occur, depending on the vapor quality, mass flux, heat flux along the tube, tube orientation, and fluid properties. The heat and momentum transfer characteristics of the tube are highly dependent on the flow regimes, which can change along

the length of the tube, such that local calculations should be made to accurately predict these characteristics (Dobson and Chato, 1998a). Thus, it is evident that the prediction of the prevailing flow regime is of prime importance for the heat transfer coefficient calculation in eventual experiments on in-tube condensation.

There are two main mechanisms of condensation in smooth horizontal tubes; the first is laminar film condensation, and the second is forced convective condensation (Liebenberg, 2002). At high mass fluxes, the inertial forces are greater than the gravitational forces, such that the condensate redistributes into an annular film around the perimeter of the tube. As the condensation process continues, the refrigerant goes through a certain transition quality (which is both dependent on the fluid and the tube (Olivier, 2003), and into the Intermittent regime, which is composed of intermittent Slug flow and Plug flow, and finally, all the vapor is converted into liquid. At very high mass fluxes and high vapor quality, Mist flow is encountered; at lower vapor qualities, Bubbly flow occurs. Bubbly flow, as well as Slug and Plug flow only account for between 10–20% of the vapor quality range. In these regimes, including Annular, the major mechanism of heat transfer is forced convective condensation (Thome *et al.*, 2003). In this regime, shear stresses largely dominate the heat transfer, such that increased mass fluxes will tend to increase the heat transfer.

At low mass fluxes and vapor velocities, a condensate film forms on the tube wall; this flows down to the bottom of the tube and accumulates *i.e.* Stratified-wavy flow; this falling film comes into contact with the axially flowing vapor core and creates waves. The method of heat transfer found in the falling film can be calculated analytically with the Nusselt falling film method (Lienhard and Lienhard, 2005). Normally, due to the thickness of the condensate accumulated at the bottom of the tube, the heat transfer through this section can be neglected, such that only the heat transferred due to the thin falling film will be taken into account. The flow continues as Stratified-wavy flow until, at low vapor qualities, purely Stratified flow is found. At very low mass fluxes, Stratified flow can be found over the entire range of quality. Since the Nusselt film is very thin, the upper liquid film does not bridge the cross-section of the tube and some vapor may leave the opposite end without condensing (Thome, 2002).

As was stated previously, the local flow patterns can alter heat and momentum transfer by a large amount, such that it should be evident that that it is important for designers to predict the expected flow-pattern based on flow rate, quality, fluid properties and tube diameter. Over the years, several flow pattern maps have been proposed to predict two-phase flow transition in horizontal tubes, both for adiabatic flow and for condensation. However, out of the multitude of available flow maps for condensing flow, the map developed by El Hajal *et al.* (2003), based on the map developed for evaporation by Kattan *et al.* (1998a) has been shown to be both accurate and easy to use.

2.4.1 Thome (2002) flow pattern map

Kattan *et al.* (1998a,b) proposed the first truly comprehensive map for flow boiling in horizontal tubes; furthermore, they were also the first to generate a heat transfer correlation that was dependent on the local flow pattern.

This new approach resulted in improved accuracy regarding the heat transfer models compared to previous methods. El Hajal *et al.* (2003) adapted the flow boiling two-phase flow pattern map developed by Kattan *et al.* (1998a) for condensation inside horizontal tubes.

Furthermore, due to the very high reduced pressures found in condensation and the sensitivity of regime transitions, heat transfer and pressure drop to void fraction, they defined a new log-mean void fraction model, capable of prediciting the void fraction accurately for low (atmospheric) to very high reduced pressures (near critical pressure). In Thome (2005), a comparison between experimentally gathered void fraction data and a new logarithmic-mean void fraction model showed exceptional correlation; however, the coefficient of determination (R^2) for their curve fit was not given. This has further implications towards the uncertainty of both the pressure drop and the heat transfer data, which will be discussed in Chapter 4 and Appendix B.

Figure 2.1 shows the El Hajal *et al.* (2003) flow map, for R-134a condensing in an 8.1 mm inside diameter tube at 40^{o}C. For condensation, saturated vapor enters the tube; according to the flow map, depending on the mass flux, this vapor can either form a thin liquid film around the perimeter as Annular flow, or a liquid

layer at the bottom of the tube, and a condensate film flowing downwards due to the gravitational force, as happens in Stratified and Stratified-wavy flow.

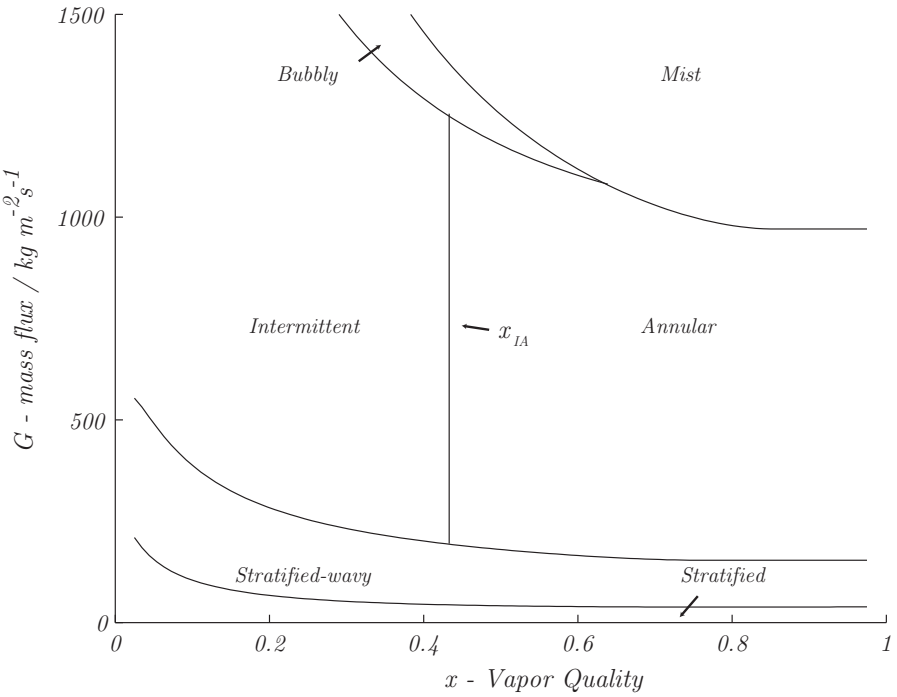

Figure 2.1: El Hajal *et al.* (2003) flow map for R-134a condensing in an 8.1 mm-diameter horizontal tube

It is also possible that, at very large mass fluxes, the flow goes into Mist flow, in which liquid droplets are entrained in a largely gaseous flow. This, however, rarely happens, and has not been studied much, due to the low amount of processes which encounter condensation at such high mass fluxes (Thome, 2005). This is all dependent on the mass flux, as can be seen on the flow map.

The transition vapor quality x_{IA} is taken as the quality at which there is a change from the Annular to the Intermittent regime. As is evident, this transition line is valid from G_{wavy} up to the Bubbly transition mass flux, G_{bubbly}. It should be understood that although the transitions between flow patterns have been demarcated by singularly defined lines (and correlating equations), these are only guidelines, as it has been shown that transition actually occurs over a range of mass flux (Thome, 2005) which can be over 50 kg/m^2s wide. It is thought that in

this transition region the flow alternates between the two end flow regimes, until the flow stabilizes into the new prevailing regime.

El Hajal *et al.* (2003) defined several models for the different flow patterns experienced in a tube. Figure 2.2 shows the models utilized for Annular flow, and for Stratified/Stratified-wavy flow. Annular flow is modeled using a thin liquid film equally distributed around the circumference of the tube with a completely uniform gaseous inner core. Stratified and Stratified-wavy flow are modeled using a model as shown in Figure 2.3. The heat transfer through the condensate pool is usually very small, compared to the heat transfered by the falling film. The heat transfer correlations will be discussed in Chapter 4.

The Thome condensation flow map is constructed from several defined equations, based on those utilized for the Kattan–Thome–Favrat evaporation flow map.

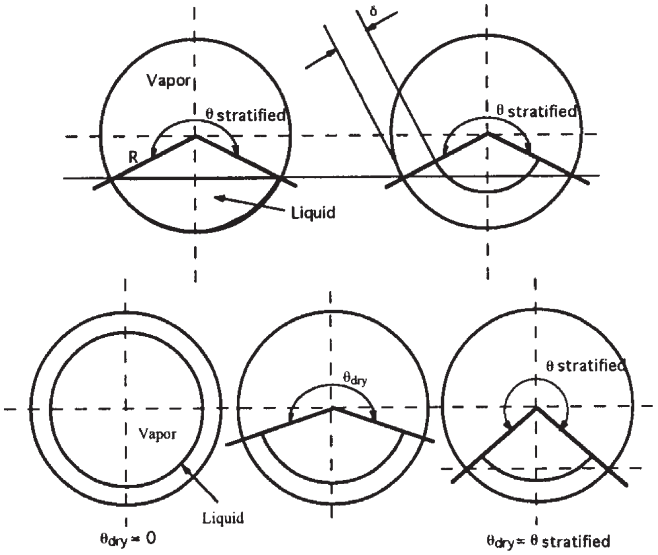

Figure 2.2: El Hajal *et al.* (2003) model for Annular and Stratified/Stratified-wavy flow

Intermittent flow, which in essence is stratified flow with large amplitude waves washing the top, is not yet modeled using a separate model; rather, the Annular flow model is presently used. The main advantage of this method is that, rather than modeling tubular flow, film flow is modeled, completely nullifying the use of two-phase multipliers.

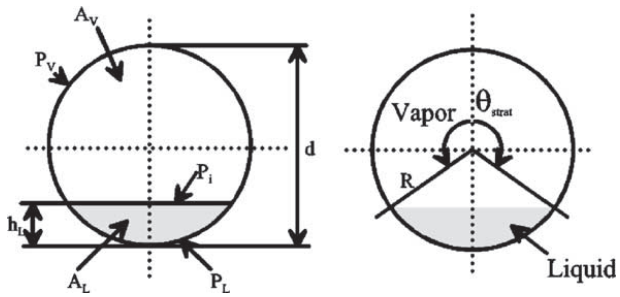

Figure 2.3: El Hajal *et al.* (2003) model for the Stratified/Stratified-wavy flow regimes

In Figure 2.3, which defines the geometrical dimensions of Stratified flow, P_L is the stratified perimeter around the bottom of the tube, P_v is the non-stratified perimeter around the top of the tube, h_l is the height of the stratified liquid, P_i is the length of the vapor-liquid interface, while A_l and A_v are the cross-sectional areas occupied by the liquid and vapor respectively.

Further, several of the above are normalized by the diameter of the tube, and are then given as shown below.

$$h_{ld} = \frac{h_l}{d} \tag{2.1}$$

$$P_{id} = \frac{P_i}{d} \tag{2.2}$$

$$A_{ld} = \frac{A_l}{d^2} \tag{2.3}$$

$$A_{vd} = \frac{A_v}{d^2} \tag{2.4}$$

In the above, to calculate the cross-sectional area of the liquid and vapor phases, it is necessary to use the void fraction ϵ. However, rather than utilize the Rouhani-Axelsson void fraction model exclusively, Thome *et al.* (2003) and El Hajal *et al.* (2003) formulated a new void fraction equation, as stated previously.

It combines the homogeneous void fraction model, which works well at high reduced pressures[1] with the Steiner (1993) version of the Rouhani and Axelsson (1970) drift-flux model. Drift-flux models are particularly attractive because they account for the velocity distributions in the vapor and liquid phases and hence include the effect of mass velocity on void fraction, which the other methods do not (El Hajal *et al.*, 2003). The homogeneous model is given as

$$\epsilon_h = \left[1 + \left(\frac{1-x}{x}\right)\left(\frac{\rho_v}{\rho_l}\right)\right]^{-1} \tag{2.5}$$

The Steiner (1993) horizontal tube expression of the vertical tube Rouhani-Axelsson method was originally chosen due to its effectiveness at low to medium pressures, but, does not go to the homogoneous model's limits at higher pressures. The Steiner (1993) model is

$$\epsilon_{ra} = \frac{x}{\rho_v}\left([1 + 0.12(1-x)]\left[\frac{x}{\rho_v} + \frac{1-x}{\rho_l}\right] + \frac{1.18(1-x)[g\sigma(\rho_l - \rho_v)]^{0.25}}{G\rho_l^{0.5}}\right)^{-1} \tag{2.6}$$

Knowing the two above void fraction models, El Hajal *et al.* (2003) investigated several methods of combining them, (without using the normal mean). The logarithmic mean void fraction (LMϵ) between the values of ϵ_{ra} and ϵ_h was found to give the best results (slightly better than a simple arithmetic mean), where the logarithmic mean void fraction ϵ is defined as

[1] This is due to the fact that the density of the vapor tends towards the density of the liquid, at which point the homogeneous void fraction model is applicable, since it assumes the vapor and liquid phases travel at the same velocity in the channel.

$$\epsilon = \frac{\epsilon_h - \epsilon_{ra}}{\ln\left(\frac{\epsilon_h}{\epsilon_{ra}}\right)} \tag{2.7}$$

Once the log-mean void fraction has been calculated, the dependent geometric parameters can also be calculated. Thus,

$$A_l = A(1-\epsilon) \tag{2.8}$$
$$A_v = A\epsilon \tag{2.9}$$

And both A_{ld} and A_{vd} can be calculated as above. Finally, the single remaining parameter that remains to be solved for is θ_{strat}, the angle that correspond to the stratification of liquid. In the original method of El Hajal *et al.* (2003), this angle had to be solved for iteratively with

$$A_{ld} = \frac{1}{8}\left((2\pi - \theta_{strat}) - \sin\left(2\pi - \theta_{strat}\right)\right) \tag{2.10}$$

However, in Thome *et al.* (2003), a non-iterative method, capable of calculating this angle to an accuracy of 0.00005 rad was utilized,

$$\theta_{strat} = 2\pi - 2\left\{\begin{array}{l} \pi(1-\epsilon) + \left(\frac{3\pi}{2}\right)^{\frac{1}{3}}\left[1 - 2(1-\epsilon) + (1-\epsilon)^{\frac{1}{3}} - \epsilon^{\frac{1}{3}}\right] \\ -\frac{1}{200}(1-\epsilon)\epsilon[1-2(1-\epsilon)][1+4((1-\epsilon)^2+\epsilon^2)] \end{array}\right\} \tag{2.11}$$

The dimensionless liquid height can be determined using

$$h_{ld} = \frac{1}{2}\left(1 - \cos\left(\frac{2\pi - \theta_{strat}}{2}\right)\right) \tag{2.12}$$

Then, the geometric expression for the interface perimeter, P_{id} in terms of θ_{strat} is

$$P_{id} = \sin\left(\frac{2\pi - \theta_{strat}}{2}\right) \tag{2.13}$$

Now, knowing the geometric parameters, the transition curve from Stratified-wavy flow to Intermittent and Annular flow can be calculated using a modified method of Zürcher *et al.* (1999), which was developed for evaporation flows. In the modified method, the transition curve is (where G is in kg/m^{2}s),

$$G_{wavy} = \left\{ \frac{16 A_{vd}^3 g d \rho_l \rho_v}{x^2 \pi^2 (1-(2h_{ld}-1)^2)^{\frac{1}{2}}} \left[\frac{\pi^2}{25 h_{ld}^2} \left(\frac{We}{Fr} \right)_l^{-1.023} + 1 \right] \right\}^{\frac{1}{2}} + 50 - 75 e^{-\frac{(x^2-0.97)^2}{x(1-x)}} \tag{2.14}$$

where,

$$\left(\frac{We}{Fr} \right)_l = \frac{g d^2 \rho_l}{\sigma} \tag{2.15}$$

Similarly, the transition curve form Stratified-wavy to fully Stratified flow can be determined by using the updated expression of Zürcher *et al.* (1999) for G_{strat} as

$$G_{strat} = \left\{ \frac{(226.3)^2 A_{ld} A_{vd}^2 \rho_v (\rho_l - \rho_v) \mu_l g}{x^2 (1-x) \pi^3} \right\}^{\frac{1}{3}} + 20x \tag{2.16}$$

The transition between Intermittent flow and Annular flow is a straight vertical line given by x_{IA} which is determined by setting the Lockhart–Martinelli parameter X_{tt} equal to 0.34 (0.32, (Olivier, 2003)) for smooth tubes, 0.688 and 0.7528 for helical and herringbone microfin tubes respectively (Olivier *et al.*, 2004). It can be seen that the higher values of the Martinelli parameter for both types of microfin tube retard the transition from Annular into Intermittent flow.

$$x_{IA} = \left\{ \left[0.2914 \left(\frac{\rho_v}{\rho_l} \right)^{-\frac{1}{1.75}} \left(\frac{\mu_l}{\mu_v} \right)^{-\frac{1}{7}} \right] + 1 \right\}^{-1} \tag{2.17}$$

As has been stated in the previous section, x_{IA} has a lower bound where it intersects the transition curve of G_{wavy}, and an upper bound where it intersects the transition curve of G_{bubbly}, as shown in Figure 2.1. The transition curve from Annular to Mist flow gives G_{mist} as

$$G_{mist} = \left\{ \frac{7680 A_{vd}^2 g d \rho_l \rho_v}{x^2 \pi^2 \xi} \left(\frac{Fr}{We} \right)_l \right\}^{\frac{1}{2}} \tag{2.18}$$

The factor ξ is

$$\xi = \left[1.138 + 2 \log \left(\frac{\pi}{1.5 A_{ld}} \right) \right]^{-2} \tag{2.19}$$

Bubbly flow is the last transition which occurs; however, it only occurs at very large mass velocities. Also, it only occurs at small vapor qualities, but the interaction between Mist flow and Bubbly flow is not well documented. The transition into Bubbly shown in Figure 2.1 is

$$G_{bubbly} = \left\{ \frac{256 A_{vd} A_{ld}^2 d^{1.25} \rho_l (\rho_l - \rho_v) g}{0.3164 (1-x)^{1.75} \pi^2 P_{id} \mu_l^{0.25}} \right\}^{\frac{1}{1.75}} \tag{2.20}$$

2.5 Void fraction models

Numerous void fraction models exist for predicting the cross-sectional void fraction of a vapor in two-phase flow in a tube, which is defined as the cross-sectional area occupied by the vapor with respect to the total cross-sectional area of the flow channel. Void fraction prediction methods may be classified as follows:

- Homogeneous models (assumes the two phases travel at the same velocity)
- One-dimensional models (minimize some paramater, such as kinetic energy)
- Drift-flux models (account for radial velocity distribution in the two phases)

The most used void fraction predictions (such as that of Zivi (1964)) ignore the important effects of mass velocity, surface tension and buoyancy. Also, void fraction rises very rapidly at low vapor qualities and then progresses toward the final value of unity, although not all void fraction models correctly go to 1.0 in their limit (Liebenberg, 2002). Due to the important effect of mass flux on void fraction, there is a big difference in void fraction depending on the method chosen at low vapor qualities but little absolute difference at large vapor qualities. For

instance, a void fraction of 0.96 produces an annular film twice as thick as a value of 0.98. Therefore, the void fraction model selected as the basis for a two-phase heat transfer or pressure drop model has a very big influence on the film thickness.

2.5.1 Homogeneous models

The homogeneous model is applicable to flows where the vapor and liquid phases travel at, or nearly at, the same velocity. This happens in such instances such as near the critical point, or at very high mass velocities where the flow regime is either Bubbly or Mist flow. The homogeneous model is

$$\epsilon_h = \left[1 + \left(\frac{1-x}{x}\right)\left(\frac{\rho_v}{\rho_l}\right)\right]^{-1} \tag{2.21}$$

2.5.2 One-dimensional energy models

The first Zivi (1964) void fraction model was proposed for Annular flow, assuming that no liquid was entrained in the central vapor core. The model is based on the premise that the total kinetic energy of the two phases will seek to be a minimum. The kinetic energy KE_k is given by (Zivi, 1964)

$$KE_k = \frac{1}{2}\rho_k u_k^2 \dot{Q}_k \tag{2.22}$$

where $\dot{Q}_k$ is the volumetric flow rate, and u_k is the phase velocity. To begin

$$\dot{Q}_v = \frac{\dot{m}A}{\rho_g}x \tag{2.23}$$

$$\dot{Q}_l = \frac{\dot{m}A}{\rho_l}(1-x) \tag{2.24}$$

The total kinetic energy of the flow is then

$$KE = \frac{1}{2}\rho_g\left(\frac{\dot{m}x}{\epsilon\rho_g}\right)^2\frac{\dot{m}xA}{\rho_g} + \frac{1}{2}\rho_l\left(\frac{\dot{m}(1-x)}{(1-\epsilon)\rho_l}\right)^2\frac{\dot{m}(1-x)A}{\rho_l} \tag{2.25}$$

This can also be rewritten as

$$KE = \frac{A\dot{m}}{2}\left[\frac{x^3}{\epsilon^2\rho_g^2} + \frac{(1-x)^3}{(1-\epsilon)^2\rho_l^2}\right] = \frac{A\dot{m}}{2}y \tag{2.26}$$

where the parameter y is

$$y = \left[\frac{x^3}{\epsilon^2\rho_g^2} + \frac{(1-x)^3}{(1-\epsilon)^2\rho_l^2}\right] \tag{2.27}$$

We can differentiate parameter y with respect to ϵ, to find the minimum kinetic energy,

$$\frac{dy}{d\epsilon} = -\frac{2x^3}{\epsilon^3\rho_g^2} + \frac{2(1-x)^3}{(1-\epsilon)^3\rho_l^2} = 0 \tag{2.28}$$

The minimum is found

$$\frac{\epsilon}{1-\epsilon} = \frac{x}{1-x}\left(\frac{\rho_l}{\rho_v}\right)^{\frac{2}{3}} \tag{2.29}$$

As such, the velocity, slip ratio is seen as

$$S = \frac{u_v}{u_l} = \left(\frac{\rho_l}{\rho_v}\right)^{\frac{2}{3}} \tag{2.30}$$

As such, the velocity ratio for these conditions is only dependent on the density ratio. The Zivi (1964) void fraction expression is

$$\epsilon = \frac{1}{1 + \frac{1-x}{x}\left(\frac{\rho_v}{\rho_l}\right)^{\frac{2}{3}}} \tag{2.31}$$

2.5.3 Drift-flux models

The drift-flux model was principally developed by Zuber and Findlay (1965). In this section, the more important sections of theory and the models utilized are defined. Figure 2.4 shows the drift-flux model utilized by Zuber and Findlay in their original work. The significant contribution of the drift-flux model is that it is able to model radial velocity distributions, rather than treat the system with a homogeneous, mean velocity.

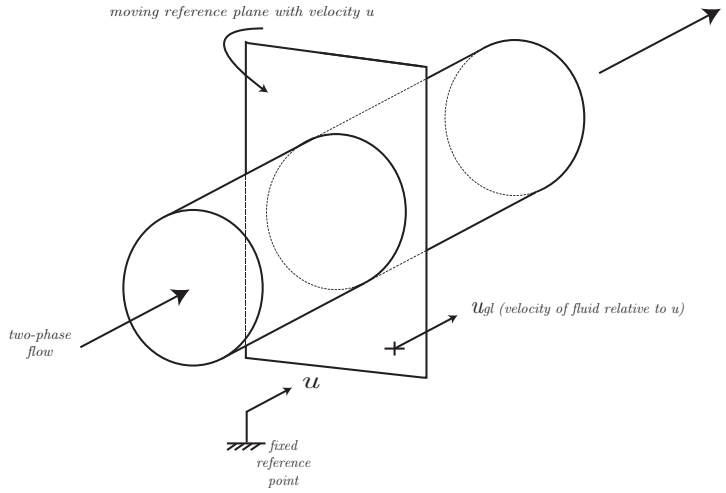

Figure 2.4: Drift-flux model

The drift flux U_{GL}, given by Zuber and Findlay (1965), represents the volumetric rate at which vapor is flowing up or down, through a unit plane normal to the channel axis that is itself travelling with the flow at a mean velocity U. To satisfy continuity, an equal and opposite drift flux of liquid U_{LG} must also pass through the same plane. These expressions are true for one-dimensional flow or at any local point in the flow. If we denote the cross-sectional average properties of the flow with <>, the mean velocity of the vapor phase U_g is (Rouhani, 1969)

$$< U_G >=< \epsilon U > + < U_{GL} > \tag{2.32}$$

and if we divide by the mean void fraction ϵ gives

$$\frac{< U_G >}{\epsilon} =< u_G >= \frac{< \epsilon U >}{< \epsilon >} + \frac{< U_{GL} >}{< \epsilon >} \tag{2.33}$$

Starting from the above, we define the distribution parameter C_o as

$$C_o = \frac{< \epsilon U >}{< \epsilon >< U >} \tag{2.34}$$

Then, a weighted mean drift velocity $< u_{GU} >$ can also be defined

$$< u_{GU} >= \frac{< U_{GL} >}{< \epsilon >} \tag{2.35}$$

Then, substituting and rearranging the above equations, and dividing by U, we find

$$\frac{< u_G >}{U} = \frac{< \beta >}{< \epsilon >} = C_o + \frac{< u_{GU} >}{< U >} \tag{2.36}$$

or

$$< \epsilon >= \frac{< \beta >}{C_o + \frac{<u_{GU}>}{<U>}} \tag{2.37}$$

where β is the volumetric quality, calculated from the volumetric flow rates of each phase, as

$$\beta = \frac{\dot{Q}_g}{\dot{Q}_G + \dot{Q}_L} \tag{2.38}$$

Now, if there is no slip between the two phases, *i.e.* there is no relative motion between the two phases ($u_{GO} = 0$), then,

$$\epsilon = \frac{\beta}{C_o} \tag{2.39}$$

Then, for homogeneous flow, $\epsilon = \beta$. It is evident then that the distribution

parameter C_o is an empirical factor that corrects one-dimensional homogeneous flow theory to separated flows to account for the fact that the void concentration and velocity profiles across the channel can vary independently of one another. The general void fraction equation can then be defined as

$$\epsilon = \frac{x}{\rho_g}\left[C_o\left(\frac{x}{\rho_g}+\frac{1-x}{\rho_l}\right)+\frac{< u_{GU} >}{G}\right]^{-1} \tag{2.40}$$

The above equation shows that the void fraction is a function of the mass flux. This model works best when used in conjunction with flow regime based distribution parameters. However it is only valuable when the drift velocity is larger than the total volumetric flux.

In a channel, the flow distribution is not uniform. As such, the distribution parameter, rather than a being a single constant, is seen to be dependent on the distribution of the local void fraction and local phase velocities in the channel. Then, the average distribution parameter is

$$C_o = \frac{\frac{1}{A}\int_A \epsilon u_{gu} dA}{\left(\frac{1}{A}\int_A \epsilon dA\right)\left(\frac{1}{A}\int_A u_{gu} dA\right)} \tag{2.41}$$

The effect of the gas voids on the velocity profile is particularly significant near the walls, giving rise to high velocity gradients, which decrease in the center of the tube. This is also seen in porous media, as described in Bear (1988).

Rouhani (1969) correlated the generalized Drift Flux Void Fraction equation using two main criteria; firstly, he designated the drift flux velocity

$$< u_{GU} >= 1.18\left[\frac{g\sigma(\rho_l-\rho_g)}{\rho_l^2}\right]^{\frac{1}{4}}(1-x) \tag{2.42}$$

The distribution parameter was taken as one of two constants, depending on the mass flux. These were

- C_o=1.1 for $G > 200$ kg/m^{2}s
- C_0=1.54 for $G < 200$ kg/m^{2}s

Rouhani and Axelsson (1970) redefined the above correlation for vertical pipes, to show

$$C_o = 1 + 0.12(1-x)\left(\frac{gd_i\rho_l^2}{G^2}\right)^{\frac{1}{4}} \tag{2.43}$$

The above is valid for void fractions larger than 0.1. Then, the Rouhani and Axelsson (1970) void fraction equation, for vertical flows, is

$$\epsilon = \frac{x}{\rho_g}\left[\left\{1 + 0.12(1-x)\left(\frac{gd_i\rho_l^2}{G^2}\right)^{\frac{1}{4}}\right\}\left[\frac{x}{\rho_g} + \frac{1-x}{\rho_l}\right] + \frac{1.18}{G}\left[\frac{g\sigma(\rho_l - \rho_g)}{\rho_l^2}\right]^{\frac{1}{4}}(1-x)\right]^{-1} \tag{2.44}$$

Steiner (1993) modified the Rouhani and Axelsson (1970) model of vertical tubes for horizontal tubes. The distribution parameter was changed to

$$C_o = 1 + 0.12(1-x) \tag{2.45}$$

This was shown to be in good agreement with experimental data. This form of expression was chosen in order to go from the limit of $C_o = 1.12$ at $x = 0$ up to $C_o = 1$ at $x = 1$.

$$\epsilon_{ra} = \frac{x}{\rho_v}\left([1 + 0.12(1-x)]\left[\frac{x}{\rho_v} + \frac{1-x}{\rho_l}\right] + \frac{1.18(1-x)[g\sigma(\rho_l - \rho_v)]^{0.25}}{G\rho_l^{0.5}}\right)^{-1} \tag{2.46}$$

2.5.4 Logarithmic-mean model

In flow condensation, due to the high reduced pressures, the Rouhani and Axelsson (1970) and Steiner (1993) models break down and are not useful when approximating the void fraction. However, El Hajal *et al.* (2003) combined the Homogeneous and the Steiner (1993) models by using a logarithmic mean, which increases the validity and accuracy of the void fraction prediction from low pressures, up to

pressures near the critical pressure. Thome *et al.* (2003) showed that the log-mean void fraction is

$$\epsilon = \frac{\epsilon_h - \epsilon_{ra}}{\ln\left(\frac{\epsilon_h}{\epsilon_{ra}}\right)} \tag{2.47}$$

In this present study, this is the void fraction method utilized. The experimental two-phase frictional pressure drop is obtainable by substracting the calculated momentum pressure drop from the measured pressure drop.

2.6 Void fraction measurement techniques

The correct prediction and measurement of the instantaneous void fraction during condensation of refrigerants inside horizontal tubes is of utmost importance, due to the void fraction's large influence on both the heat transfer and pressure drop. However, measurement of the void fractions, up to now, has been tricky, at best.

Of the more novel, non-intrusive methods that have been devised up to now, the methods of Ursenbacher *et al.* (2004); Wojtan *et al.* (2005) and De Paepe *et al.* (2006) are easy to use, and relatively cost-effective.

Wojtan *et al.* (2005) and Ursenbacher *et al.* (2004) utilize a laser sheet device to take cross-sectional pictures at an angle to the flow — they then take the oval picture and, through a proprietary image processing program, calculate the area of the vapor, the stratified angle, and the height of the liquid pool, among others. This technique works particularly well in stratified types of flow, such as Stratified, Stratified-wavy, or Annular flow with partial dry-out on the top of the tube. Intermittent flow (*i.e.* slug and plug flow) can only be successfully captured if the passing slug does not leave a liquid film, or if the liquid film is thin enough such that the image captured is not distorted. Furthermore, there should be no bubbles inside the liquid phase, as the void fraction is calculated from the vapor-liquid interface. The main positive aspect of this method is that it is able to measure the dry angle and the void fraction. The main drawback is, of course, that it is only applicable to stratified types of flow.

The capacitance void fraction measuring device, developed by De Paepe *et al.* (2006), is placed inline with the system (the tube diameter used coincides with the

tubes utilized in the rest of the system), in such a manner that the flow sees no discontinuity in its path. Three electrodes are used; two as grounding electrodes and the middle one is the sensing electrode. The different phases have different dielectric constants, and on a time-basis, due to the change in dielectric picked up (when there is change in the flow), the output of the sensor changes. This specific sensor has been calibrated to output 0-10 V when in air/water flow, while, for refrigerant flow, a change in 3 V has been shown to occur, and agrees with theory.

The main advantage of this sensor is that it is able to measure void fractions over the entire range; however, unlike Wojtan *et al.* (2005) it is not able to measure dry angle, due to the fact that it generates a mean, chordal void fraction over the tube.

This sensor has been shown to work well in air/water flows, and is still under review for application in refrigerant flow.

2.7 Time fraction

At present, two main methods of heat transfer in condensing two-phase flow in horizontal tubes have been identified, namely gravity-dominated and shear-stress dominated heat transfer (Collier and Thome, 1994; Liebenberg, 2002). However, neither one of these can adequately describe the heat transfer in the Intermittent flow regime.

Earlier sections of this Chapter and Chapter 3 both mention that the prevalent heat transfer mode in Intermittent flow is a temporal mixture of shear-stress–dominated and gravity-dominated modes; this is due to the high amplitude waves that wash the top of the tube. Modern flow-pattern-based heat transfer correlations, such as that of Thome *et al.* (2003), regard Intermittent flow as completely shear-stress dominated, while completely disregarding the time spent in secondary flow.

2.7.1 Classical heat transfer modes

The major flow regimes that have been identified as gravity-controlled are Stratified and Stratified-Wavy, in which, due to the relatively low velocity of the fluid,

condensate pools at the bottom of the tube. Although these are two distinct flow regimes, from a heat transfer model point of view, they are treated using very similar forms of the same equations.

A large number of existing heat transfer correlations, such as that of Dobson and Chato (1998b) and Shah (1979) (see Chapter 4), were not specifically developed for application when the prevailing heat transfer mode is gravity based. The correlation of Thome *et al.* (2003) is one of the few methods that correctly models the heat transfer in Stratified and Stratified-wavy flow.

In a similar manner, the shear stress model is best utilized to represent the Annular flow regime. In this model, a thin liquid film wets the perimeter of the tube, which is in contact with a fast moving vapor core.

The majority of heat transfer correlations available in the literature were specifically tailored for this type of condensation, and in fact, it is the most efficient heat transfer mode, apart from dropwise condensation; it is however very difficult to design a heat exchanger to take advantage of dropwise condensation, due to the special coating required on the inner surface of the tube, among other problems. Furthermore, about 85% of the overall heat transfer in a two-phase heat exchanger occurs in the shear-stress–dominated domain, hence the importance and wide availability of correlations for said domain.

However, not all of the flow regimes that readily occur in a horizontal tube during condensation can be described and modeled using just one of the two models above. The Intermittent flow regime, made up of both slug and plug flow defies classification of a single prevailing heat transfer mode. The next section details this particular case.

2.7.2 The Intermittent flow regime and the prevailing heat transfer mode

As was previously discussed, it is difficult to classify the Intermittent flow regime into having a single dominant heat transfer mode, as could be done with the Stratified/Stratified-wavy and Annular flow regimes. Intermittent flow can be described as a stochastic mixture of plug and slug flow (granted, plug flow occurs only at the lower vapor quality range of the flow regime). Nevertheless, due to

the randomness presented by the flow, the development of a single model that can be used for heat transfer correlations is severely hampered.

In fact, modern heat transfer correlations (such as those of Thome *et al.* (2003)) do not specifically treat the heat transfer in the Intermittent flow regime; rather, they extend the shear-stress controlled heat transfer mode into this regime, and it is stated that, experimentally, the measured heat transfer coefficients do not deviate much from the predicted results.

2.7.3 Time fraction & probability

Consider the two examples of refrigerant condensing in a horizontal tube shown in Figures 2.5 and 2.6.

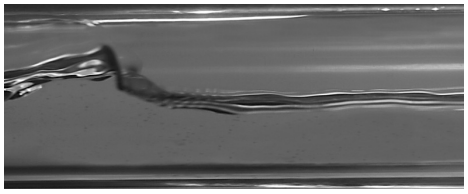

Figure 2.5: Stratified Flow?

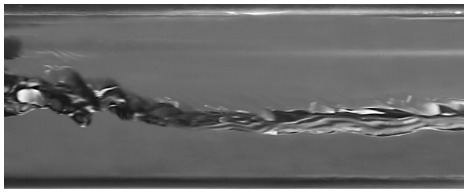

Figure 2.6: Slug Flow?

Without looking at the captions, which one describes Stratified flow, and which one shows a slug as it passes by the camera? Without additional information, it is very difficult to tell. Only taking still pictures of flow condensing in the Intermittent flow regime can lead to erroneous conclusions regarding the flow. In this case, a still image was taken as a slug went across the camera; however, over time, looking at the other stills before and after, and the objectively analyzed data, it is easy to see that a slug was traveling past the camera.

From a heat transfer perspective, this temporal variability in the flow has a large effect that has not yet been quantified. Furthermore, a simple shear-controlled model (*i.e.* Annular flow) or a gravity-controlled model will not suffice on their own.

Going back to Figure 2.6, the dominating mode of heat transfer, at that instance, can be seen to be gravity dominated, due to the thick liquid pool at the bottom of the tube, and the relatively thin layer at the top. Going to Figure 2.7,

which was also taken in the Intermittent flow regime, it can be seen that the dominating heat transfer mode should be shear-stress dominated; this we conclude from the redistributed liquid film layer around the perimeter of the tube, and a relatively clear vapor core. Notice, however, that there is still a thicker layer of liquid around the bottom; this is due to the action of gravity, and is also seen (less noticeably) in Annular flow.

Figure 2.7: Intermittent flow - between slugs

Thus, we can clearly distinguish that in a single flow regime, the two separate heat transfer modes will have an effect. So the main question now is: if analysis is carried out to find out what the probability is that at a certain vapor quality and mass flux one or the other heat transfer mode will dominate, can a more accurate method of predicting heat transfer be developed?

However we define the dominating heat transfer mode, the flow regime and its characteristics do not change; that is, although we are classifying sections of Intermittent flow as either shear-stress or gravity dominated, this does not change the fact that slugs and plugs do, in fact, occur; the analysis is only an instantaneous evaluation of the flow regime.

2.7.4 Application of temporal data in macrochannel flow

Utilizing different definitions of the term *time fraction*, this type of probabilistic temporal information has been previously implemented in both microchannel and macrochannel flow, most notably by Niño *et al.* (2002) in microchannel flow, and concurrently with this study, Jassim (2007) in macrochannel flow.

Instead of presenting a definitive map with lines depicting transitions between flow regimes, Niño *et al.* (2002) recorded the time fraction in which each flow regime was observed in the separate microchannels at each mass flux and vapor

quality. Analysis of still images taken at the given mass fluxes and vapor qualities showed that it was possible to simultaneously exhibit different flow regimes. The total time fraction of all flow regimes, as used in this study, add up to one.

Using a similar approach, Jassim (2007) characterized the flow regimes in macrochannels. In this work, three main regimes were characterized, namely Annular flow, Stratified flow, and a mixture of Liquid and Intermittent flow. Furthermore, the heat transfer, pressure drop and void fraction predictions were rewritten in terms of the total time fraction and the different flow-pattern-based predictor methods, developed by previous researchers. More importantly, his definition of the time fraction was also parametrized in term of the refrigerant thermo-physical properties.

2.8 Two-phase gas liquid flow models

In this section, the most important models of two-phase gas-liquid flow are discussed. These are the homogeneous and separated flow models, and are the primary models that have been used to determine the pressure gradient inside horizontal, inclined and vertical tubes. Several authors have used these models as the base from which they build their pressure drop correlations. However, in light of the discussion of flow patterns, and flow regime maps above, it should be noted that while flow regime-based heat transfer correlations are available that try to minimize the use of arbitrary multipliers and 'fudge-factors' (see Chapter 4), a similar method has not been developed for pressure drops.

The two models are based on the basic equations for two-phase model; the basic equations define the total static pressure gradient in terms of the frictional, acceleration and static pressure gradients.

2.8.1 Primary equations of two-phase flow

Figure 2.8 shows a simplified one-dimensional analysis of multi-phase flow in a channel. As stated in Collier and Thome (1994), the figure shows stratified multi-phase flow in an inclined channel, where there is no mass transfer between the phases. Stratified flow was chosen in this case such that the equations can be

derived in a manner that they represent the general case where each phase is in contact with each other and the wall. Mean values of velocity and density of each phase are assumed to exit across any phase normal to the flow. Furthermore, it is assumed that any pressure across any phase normal to the channel is uniform, which is not strictly true for stratified flow, and the sum of the areas of the phases are equal to the cross-sectional area of the channel.

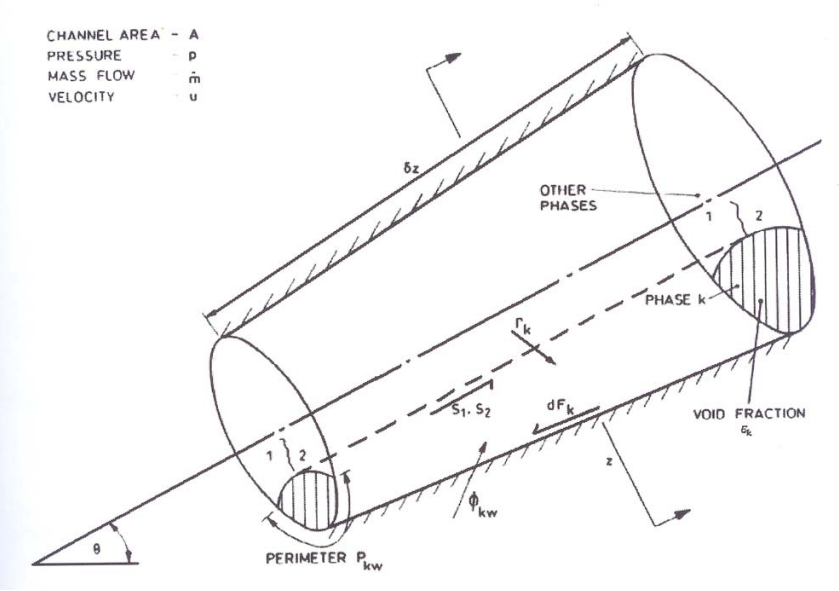

Figure 2.8: Simplified model for multi-phase flow in an element of a channel (Collier and Thome, 1994)

2.8.1.1 Conservation of mass

The equations that express conservation of mass in the channel, in the absence of any removal or addition of mass through the channel walls are, from Collier and Thome (1994)

$$\frac{\partial}{\partial t}\left(A\epsilon_k\rho_k\right) + \frac{\partial}{\partial z}\left(A\epsilon_k\rho_k u_k\right) = \Gamma_k \tag{2.48}$$

where ρ_k is the density of phase k, ϵ_k is the time-averaged void fraction inside the

channel, A is the channel cross-sectional area, and u_k is the mass-weighted mean velocity of phase k. Γ_k represents the mass transfer (mass generation rate per unit length) to phase k from the various interphase mass transfers:

$$\sum_k \Gamma_k = 0 \tag{2.49}$$

For steady state conditions, the two-phase gas-liquid flow in a constant area channel can be separated into:

$$\frac{d}{dz}\left(A_v \rho_v u_v\right) = \Gamma_v \tag{2.50}$$

$$\frac{d}{dz}\left(A_l \rho_l u_l\right) = \Gamma_l \tag{2.51}$$

where the subscripts v and l denote the vapor and liquid phases respectively. The terms in brackets are equal to the mass flow rate ($\dot{m}$), thus the above equations can be rewritten as:

$$\Gamma_v = -\Gamma_l = \frac{d\dot{m}_v}{dz} = -\frac{d\dot{m}_l}{dz} \tag{2.52}$$

Equation 2.52 shows that as the vapor mass generation rate increased over a unit length, the liquid mass generation will decrease at the same rate. As such, the total mass generation rate will always be 0 (which makes sense, if nothing is added through the channel walls). This means that even when vapor is condensed into liquid, the total mass in the system will always remain the same.

2.8.1.2 Conservation of momentum

The rate of creation of momentum of phase k within the control element plus the rate of inflow of momentum is balanced against the sum of the forces acting on that phase in the control element. The rate of creation plus the rate of inflow of phase k momentum directed along the channel axis is given by (Collier and Thome, 1994)

$$\frac{\partial}{\partial t}\left(\dot{m}_k \delta z\right) + \left(\dot{m}_k u_k + \delta z \frac{\partial}{\partial z}\left(\dot{m}_k u_k\right)\right) - \dot{m}_k u_k \tag{2.53}$$

which simplifies to

$$\frac{\partial}{\partial t}\left(\dot{m}_k \delta z\right) + \delta z \frac{\partial}{\partial z}\left(\dot{m}_k u_k\right) \tag{2.54}$$

This is balanced against the sum of the forces acting in the z-direction on phase k in the control element plus the momentum generation due to the mass transfer, given by

$$\begin{aligned}\left[A\epsilon_k p - \left(A\epsilon_k p + \delta z \frac{\partial}{\partial z}\left(A\epsilon_k p\right)\right) - \left\{p\left(-\delta z \frac{\partial}{\partial z}\left(A\epsilon_k\right)\right)\right\}\right] \\ -A\epsilon_k \rho_k \delta z \cdot g \sin\theta - \tau_{kw} P_{kw} \delta z + \sum_1^n \tau_{knz} P_{kn} \delta z + u_k \Gamma_k\end{aligned} \tag{2.55}$$

The term in the square brackets represents the pressure forces on the element and the second term the gravitational forces. The third term represents the wall shear force (dF_k) where τ_{kw} is the wall shear stress between phase k and the channel wall, while P_{kw} is the contact perimeter between the wall and phase k. The fourth term is the sum of the interfacial shear forces where τ_{knz} is the z-component of the interfacial shear stress between phase k and phase n, and P_{kn} is the contact perimeter between phase k and phase n. The final term is the rate generation of momentum of phase k due to mass transfer assuming the mass transferred across the interface is accelerated to the mean velocity of the receiving phase. If, for steady state, two-phase gas-liquid flow, the forces on phase k are summed and equated to the rate of creation of momentum for that phase, and using the fact that conservation of momentum across the interface,

$$\tau_{vl} P_{vl} dz + u_v \Gamma_v = \tau_{lv} P_{lv} dz + u_l \Gamma_l \tag{2.56}$$

Equation 2.55 simplifies to

$$Adp - \tau_{vw}P_{vw}dz - \tau_{lw}P_{vw}dz - g\sin\theta\left[A_l\rho_l + A_v\rho_v\right] = d\left(\dot{m}_l u_l + m_v u_v\right) \quad (2.57)$$

This equation represents the basic differential momentum equation for this simplified one-dimensional approach. The terms due to momentum exchange from mass transfer do not appear since they sum to 0. The net frictional force acting on each phase may be expressed in terms of the ones occupied by each phase as

$$(dF_v + S) = -\tau_{vw}P_{vw}dz - \tau_{vl}P_{vl}dz = -A_v\left(\frac{dp}{dz}\right)_{vf}dz \quad (2.58)$$

$$(dF_l - S) = -\tau_{lw}P_{lw}dz - \tau_{vl}P_{vl}dz = -A_l\left(\frac{dp}{dz}\right)_{lf}dz \quad (2.59)$$

$$(dF_v + dF_l) = -\tau_{vw}P_{vw}dz - \tau_{lw}P_{lw}dz = -A\left(\frac{dp}{dz}\right)_{f}dz \quad (2.60)$$

The term $\left(\frac{dp}{dz}\right)_f$ represents the part of the overall static pressure drop that is required to overcome friction. We can substitute Equations 2.58 – 2.60 into Equation 2.57. Rearranging, we find

$$\left(\frac{dp}{dz}\right) = \left(\frac{dp}{dz}\right)_f + \left(\frac{dp}{dz}\right)_a + \left(\frac{dp}{dz}\right)_z \quad (2.61)$$

where

$$-\left(\frac{dp}{dz}\right)_a = \frac{1}{A}\frac{d}{dz}\left(\dot{m}_v u_v + \dot{m}_l u_l\right) = G^2\frac{d}{dz}\left[\frac{x^2}{\rho_v\epsilon} + \frac{(1-x)^2}{\rho_l(1-\epsilon)}\right] \quad (2.62)$$

and

$$-\left(\frac{dp}{dz}\right)_z = g\sin\theta\left[\frac{A_v}{A}\rho_v + \frac{A_l}{A}\rho_l\right] = g\sin\theta\left[\epsilon\rho_v + (1-\epsilon)\rho_l\right] \quad (2.63)$$

Equations 2.62 and 2.58 – 2.60 represent the acceleration (deceleration) and static head components of the total pressure drop, respectively. The momentum equation relates the total static pressure gradient in terms of the separate components of friction, acceleration and static head. The frictional component has been derived in terms of the total wall shear force (Collier and Thome, 1994).

2.8.1.3 Conservation of energy

The differential energy balance is obtained by equating the rate of increase into the total energy of phase k (internal plus kinetic energy) within the control element, the rate at which total energy is convected into the control element to the rate at which heat is added to phase k, the rate at which work is done on phase k and the rate at which energy is transferred across the interface to the control element.

The rate of increase of total energy in the control volume plus the rate at which energy enters the element in the absence of the addition and substraction of mass through the channel walls is (Collier and Thome, 1994)

$$\frac{\partial}{\partial t}\left[\epsilon_k \rho_k \left(i_k + \frac{u_k^2}{2}\right) A\delta z\right] + \dot{m}\left(i_k + \frac{u_k^2}{2}\right)\delta z - \left[\dot{m}_k\left(i_k + \frac{u_k^2}{2}\right) - \delta z \frac{\partial}{\partial z}\dot{m}_k\left(i_k + \frac{u_k^2}{2}\right)\right] \tag{2.64}$$

where i_k is the internal energy, per unit mass, of phase k. The rate at which heat enters phase k within the control volume is

$$\phi_{kw} P_{kw} \delta z + \sum_{1}^{n} \phi_{kn} P_{kn} \delta z + \dot{\phi}_k A \epsilon_k \delta z \tag{2.65}$$

where and ϕ_k is the heat flux, the first term refers to the heat flow via the channel wall, over the perimeter P_{kw}, the second term refers to the heat flux via the various interfaces with the other n phases and thirdly, the internal heat generation for phase k within the control element itself. The rate at which work is done on phase k is,

$$\left[\frac{\dot{m}_k p}{\rho_k} - \left(\frac{\dot{m}_k p}{\rho_k} + \delta z \frac{\partial}{\partial z}\left(\frac{\dot{m}_k p}{\rho_k}\right)\right)\right] \quad -\dot{m}_k g \sin\theta \delta z - pA\delta z \frac{\partial \epsilon_k}{\partial t} + \Gamma_k \frac{\delta z p}{\rho_k} + u_k \sum_1^n \tau_{kn} p_{kn} \delta z \tag{2.66}$$

The term in the set of square brackets is the work done by pressure forces (excluding interfaces) while the remaining terms represent the work done by the shear and pressure forces at the interfaces with the rest of the interfaces. The rest of the terms are negligible in all but high-velocity flows, and represent the work done by shear forces at the control element surface.

Due to mass transfer across the interface between the phases is given by

$$\Gamma_k \delta z \left(i_k + \frac{u_k^2}{2}\right) \tag{2.67}$$

If we equate Equation 2.64 to the sum of Equations 2.65 to 2.67, we find

$$\begin{pmatrix} \frac{\partial}{\partial t} A \epsilon_k \rho_k \left(i_k + \frac{u_k^2}{2}\right) + \frac{\partial}{\partial z} \dot{m}_k \left(h_k + \frac{u_k^2}{2}\right) \\ -\dot{\phi}_k A \epsilon_k + pA \frac{\partial \epsilon_k}{\partial t} - \Gamma_k \left(h_k + \frac{u_k^2}{2}\right) \end{pmatrix} = \begin{pmatrix} -\dot{m}_k g \sin\theta + \phi_{wk} P_{wk} + \sum_1^n \phi_{kn} P_{kn} \\ +u_k \sum_1^n \tau_{kn} P_{kn} \end{pmatrix} \tag{2.68}$$

where h_k is the enthalpy per unit mass of phase k, and is defined as

$$h_k = u_k + \frac{p}{\rho_k} \tag{2.69}$$

For a steady two-phase gas-liquid flow in a constant area channel with no internal heat generation, Equation 2.68 becomes

$$d\left[\dot{m}_v \left(h_v + \frac{u_v^2}{2}\right)\right] + \dot{m}_v g \sin\theta \delta z = \left\{ \begin{matrix} \phi_{wv} P_{wv} \delta z + \phi_{vl} P_{vl} \delta z + u_v \tau_{vl} P_{vl} \delta z \\ +\Gamma_v \delta z \left(h_v + \frac{u_v^2}{2}\right) \end{matrix} \right\} \tag{2.70}$$

and

$$d\left[\dot{m}_l\left(h_l+\frac{u_l^2}{2}\right)\right]+\dot{m}_l g\sin\theta\delta z=\left\{\begin{array}{r}\phi_{wl}P_{wl}\delta z+\phi_{lv}P_{lv}\delta z+u_l\tau_{lv}P_{lv}\delta z\\ +\Gamma_l\delta z\left(h_l+\frac{u_l^2}{2}\right)\end{array}\right\} \quad (2.71)$$

Adding Equations 2.70 and 2.71, noting that, for conservation of mass across the gas-liquid interface requires

$$\Gamma_v\left(h_v+\frac{u_v^2}{2}\right)+\phi_{vl}p_{vl}+u_v\tau_{vl}P_{vl}=\Gamma_l\left(h_l+\frac{u_l^2}{2}\right)+\phi_{lv}p_{lv}+u_l\tau_{lv}P_{lv} \quad (2.72)$$

the following is obtained

$$\frac{d}{dz}\left[\dot{m}_v h_v+\dot{m}_l h_l\right]+\frac{d}{dz}\left[\frac{\dot{m_v}u_v^2}{2}+\frac{m_l u_l^2}{2}\right]+\left(\dot{m}_v+\dot{m}_l\right)g\sin\theta=Q_{wL} \quad (2.73)$$

where Q_{wL} is the heat transferred across the channel wall per unit length. Thus is can be rewritten as

$$-\frac{dp}{dz}\left[\frac{x}{\rho_v}+\frac{1-x}{\rho_l}\right]=\left(\begin{array}{r}\left\{\frac{dE}{dz}-\frac{Q_{wl}}{\dot{m}}\right\}+g\sin\theta\\ \left\{p\frac{d}{dz}\left[\frac{x}{\rho_v}+\frac{1-x}{\rho_l}\right]+\frac{G^2}{2}\frac{d}{dz}\left(\frac{x^3}{\rho_v^2\epsilon^2}+\frac{(1-x)^3}{\rho_l^2(1-\epsilon)^2}\right)\right\}\end{array}\right) \quad (2.74)$$

From this equation, it can be seen that the total pressure gradient is written in terms of a frictional dissipation term, an acceleration/deceleration (or momentum) head term, and a static head term. The frictional dissipation term

$$\frac{dE}{dz}-\frac{Q_{wl}}{\dot{m}} \quad (2.75)$$

includes not only the dissipation of mechanical energy due to friction at the channel wall, but also the the dissipation due to the relative motion of the phases. The internal heat generation and dissipation, as well as the kinetic and potential energy are negligible compared with the enthalpy and external heat inputs in most applications (Collier and Thome, 1994).

Furthermore, Collier and Thome (1994) state that it is possible to use either the momentum or energy equation to determine the pressure gradient. Both methods require information about the void fraction, though it has been shown that its importance differs in either case. The advantage of the energy balance approach is that it avoids the difficulty of a negative friction component (wall shear stress) which is found in Slug or Annular flow, when there is reverse flow of liquid at the channel walls.

2.8.2 Homogeneous model

The homogeneous model considers the two phases to flow as a single phase, possessing mean properties.

2.8.2.1 Assumptions and derivation of the model

The main assumptions upon which the model is based on are:

- Equal vapor and liquid velocities
- The attainment of thermodynamic equilibrium between phases
- The use of suitably defined single-phase friction factor for two-phase flow

For steady homogeneous flow, the governing equations reduce to the following:

Continuity

$$\dot{m} = A\bar{\rho}u \tag{2.76}$$

Momentum

$$-Adp - d\bar{F} - A\bar{\rho}\sin\theta dz = \dot{m}\bar{u} \tag{2.77}$$

Energy

$$\delta q - \delta w = dh + d\frac{\bar{u}^2}{2} + g\sin\theta dz \tag{2.78}$$

where, $dh = \delta q + dE + \frac{dp}{\bar{\rho}}$.

These equations use the average density and velocity of the homogeneous fluid. The homogeneous fluid density is defined as the total mass flow rate divided by the total volumetric flow rate, and can be written as

$$\bar{\rho} = \frac{\dot{m}}{Q} = \left(\frac{x}{\rho_v} + \frac{1-x}{\rho_l}\right)^{-1} = \frac{1}{\bar{v}} \tag{2.79}$$

where $\bar{v}$ is the average specific volume of the fluid. In this way,

$$\bar{u} = \frac{G}{\bar{\rho}} \tag{2.80}$$

$$\epsilon = \frac{x\bar{\rho}}{\rho_v} \tag{2.81}$$

$$(1-\epsilon) = \frac{(1-x)\,\bar{\rho}}{\rho_l} \tag{2.82}$$

The total wall shear force can be expressed in terms of the wall shear stress acting on the inside area of the channel. This is given as

$$d\bar{F} = \tau_w P dz \tag{2.83}$$

where

$$\tau_w = f_{tp}\left(\frac{\rho\bar{u}^2}{2}\right) \tag{2.84}$$

where f_{tp} is the homogeneous two-phase friction factor. Using the Fanning equation (Collier and Thome, 1994),

$$-\left(\frac{dp}{dz}\right)_f = \frac{1}{A}\frac{d\bar{F}}{dz} = \frac{\tau_w P}{A} = \frac{f_{tp}P}{A}\left(\frac{\rho\bar{u}^2}{2}\right) \tag{2.85}$$

and for the special case of a circular channel, where $\frac{P}{A} = \frac{4}{D}$

$$-\frac{dp}{dz}_f = \frac{2f_{tp}G^2}{\bar{\rho}D} \tag{2.86}$$

As such, the total static pressure gradient for the homogeneous model, as described in Collier and Thome (1994) is,

$$-\left(\frac{dp}{dz}\right) = \frac{2f_{tp}G^2}{\bar{\rho}} + G^2\frac{d}{dz}\left[\frac{x^2}{\epsilon\rho_v} + \frac{(1-x)^2}{(1-\epsilon)\,\rho_l}\right] + g\sin\theta\left\{\epsilon\rho_v + (1-\epsilon)\rho_l\right\} \tag{2.87}$$

However, in this study, only horizontal tubes are considered (no inclined tubes), thus the last term in equation 2.87 falls away

$$-\left(\frac{dp}{dz}\right) = \frac{2f_{tp}G^2}{\bar{\rho}} + G^2\frac{d}{dz}\left[\frac{x^2}{\epsilon\rho_v} + \frac{(1-x)^2}{(1-\epsilon)\,\rho_l}\right] \tag{2.88}$$

2.8.2.2 Two-phase friction factor

The terms in Equation 2.88 are definable, except f_{tp}, the two-phase friction factor. For the homogeneous model, a single phase friction factor has to be redefined in such that it may be somewhat applicable to two-phase flow. Two approaches have been followed in literature; the first, the friction factor is assumed to be equal to that which would have occurred if the total flow was assumed to be liquid. Second, a factor which uses a mean two-phase viscosity for the normal friction factor relationship is used.

In the first case, if all the fluid were liquid, the friction factor, denoted as f_{lo}, is a function of the all-liquid Reynolds number and the pipe relative roughness. As such, the frictional pressure gradient results

$$-\left(\frac{dp}{dz}\right)_f = \frac{2f_{lo}G^2}{\rho_l D}\left[1 + \frac{x\,(\rho_l - \rho_v)}{\rho_v}\right] = -\left(\frac{dp}{dz}\right)_{f,lo}\left[1 + \frac{x\,(\rho_l - \rho_v)}{\rho_v}\right] \tag{2.89}$$

where $-\left(\frac{dp}{dz}\right)_{f,lo}$ is the frictional pressure gradient calculated from the Fanning equation, when the total flow is assumed to be liquid. However, the main problem with this method, is that, as the quality goes to 1, the correct value for the friction factor cannot be found. As such, the second method, using a mean two-phase viscosity can be used. As a digression, the liquid-only Fanning friction factor for laminar flow is

$$f_{lo} = \frac{16}{Re} \tag{2.90}$$

The form of the relationship between the mean viscosity and the quality must be such as to satisfy the following conditions

$$x = 0,\ \bar{\mu} = \mu_l; \qquad x = 1, \bar{\mu} = \mu_v \tag{2.91}$$

There are several methods available; the forms suggested by McAdams et al., Cicchitti et al. and Dukler et al. (all from Collier and Thome (1994))

$$(i) \qquad \frac{1}{\bar{\mu}} = \frac{x}{\mu_v} + \frac{1-x}{\mu_l} \tag{2.92}$$

$$(ii) \quad \bar{\mu} = x\mu_v + (1-x)\,\mu_l \tag{2.93}$$

$$(iii) \quad \bar{\mu} = \bar{\rho}\left[\frac{x\mu_v}{\rho_v} + \frac{(1-x)\mu_l}{\rho_l}\right] \tag{2.94}$$

From the (turbulent) Blasius equation, the friction factor may be approximated in terms of the Reynolds number as

$$\begin{aligned} f_{tp} &= 0.079Re^{-0.25} \\ f_{tp} &= 0.079\left(\frac{GD}{\bar{\mu}}\right)^{-0.25} \end{aligned} \tag{2.95}$$

Thus, the frictional pressure gradient can be rewritten as

$$-\left(\frac{dp}{dz}\right)_f = -\left(\frac{dp}{dz}\right)_{f,lo}\left[1+\frac{x\left(\rho_l-\rho_v\right)}{\rho_v}\right]\left[1+\frac{x\left(\mu_v-\mu_l\right)}{\mu_l}\right]^{-0.25} \tag{2.96}$$

which can also be written as

$$-\left(\frac{dp}{dz}\right)_f = -\left(\frac{dp}{dz}\right)_{f,lo}\phi_{lo}^2 \tag{2.97}$$

where ϕ_{lo} is the liquid only two-phase frictional multiplier. As such, the two-phase pressure drop is expressed in terms of a single-phase pressure gradient, where the entire flow is considered as a liquid (Collier and Thome, 1994).

The major problems of this model include the fact that the assumption is that the liquid and vapor velocities are the same; however, it is known that they are mostly not equal. As such, inaccuracies and inherent errors are built-in into this correlation. The separated flow model, discussed next, treats this assumption.

2.8.3 Separated flow model

The separated flow model considers that the two phases travelling in the channel to be artificially segregated into two distinct streams (much like Stratified flow), one for liquid and the other for vapor.

Assumptions and derivation of the model

The separated flow model is based on the following premises

- Constant but not necessarily equal velocities for the vapor and liquid phases
- The attainment of thermodynamic equilibrium between phases
- The use of empirical correlations and simplified concepts to relate the two-phase friction multiplier and the void fraction to the independent variables of flow

The momentum equation may be rewritten, as was done for the homogeneous model, to give

$$-\left(\frac{dp}{dx}\right) = -\left(\frac{dp}{dz}\right)_f + G^2 \frac{d}{dz}\left[\frac{x^2}{\epsilon\rho_v} + \frac{(1-x)^2}{(1-\epsilon)\,\rho_l}\right] + g\sin\theta\left[\epsilon\rho_v + (1-\epsilon)\right] \tag{2.98}$$

The frictional pressure gradient can be expressed in terms of the single-phase pressure gradient for the total flow considered as a liquid, giving

$$-\left(\frac{dp}{dz}\right)_f = -\left(\frac{dp}{dz}\right)_{f,lo} \phi_{lo}^2 = \left(\frac{2f_{lo}G^2}{\rho_l D}\right)\phi_{lo}^2 \tag{2.99}$$

Equation 2.99 can be expressed in terms of the single-phase pressure gradient for the liquid phase, considered to flow in the channel by itself.

$$-\left(\frac{dp}{dz}\right)_f = -\left(\frac{dp}{dz}\right)_{fl} \phi^2 = \left[\frac{2f_l G^2(1-x)^2}{\rho_l D}\right]\phi_l^2 \tag{2.100}$$

Using the Blasius equation,

$$\frac{f_l}{f_{lo}} = (1-x)^{-0.25} \tag{2.101}$$

And both Equations 2.99 and 2.100 gives

$$\phi_{lo}^2 = \phi_l^2(1-x)^2\frac{f_l}{f_{lo}} = \phi_l^2(1-x)^{1.75} \tag{2.102}$$

$$-\left(\frac{dp}{dz}\right)_a = G^2\frac{d}{dz}\left[\frac{x^2}{\epsilon\rho_v} + \frac{(1-x)^2}{(1-\epsilon)\,\rho_l}\right] \tag{2.103}$$

By neglecting the compressibility of the liquid phase, we can find, expanding

$$\begin{aligned}\frac{d}{dz}\left[\frac{x^2}{\epsilon\rho_v}+\frac{(1-x)^2}{(1-\epsilon)\,\rho_l}\right] &= \frac{dx}{dz}\left\{\frac{2x}{\epsilon\rho_v}-\frac{2(1-x)}{(1-\epsilon)\rho_l}\right\} \\ &+\frac{dx}{dz}\left(\frac{\partial\epsilon}{\partial x}\right)_p\left(\frac{(1-x)^2}{(1-\epsilon)^2\rho_l}-\frac{x^2}{\epsilon^2\rho_v}\right) \\ &+\frac{dp}{dz}\left[\frac{x^2}{\epsilon}\frac{dv_v}{dp}+\left(\frac{\partial\epsilon}{\partial p}\right)_x\left\{\frac{(1-x)^2}{(1-\epsilon)^2\rho_l}-\frac{x^2}{\epsilon^2\rho_v}\right\}\right]\end{aligned} \tag{2.104}$$

As such, the total pressure gradient (static) as evaluated in this model is represented by substituting Equations 2.99 and 2.105 into Equation 2.98. This gives

$$-\left(\frac{dp}{dz}\right)=\frac{\left[\begin{array}{r}\dfrac{2f_{lo}G^2}{\rho_l D}\phi^2+g\sin\theta\left\{\rho_v\epsilon+\rho_l(1-\epsilon)\right\} \\ +G^2\dfrac{dx}{dz}\left[\dfrac{2x}{\epsilon\rho_v}-\dfrac{2(1-x)}{(1-\epsilon)\rho_l}+\left(\dfrac{\partial\epsilon}{\partial x}\right)_p\left(\dfrac{(1-x)^2}{(1-\epsilon)^2\rho_l}-\dfrac{x^2}{\epsilon^2\rho_v}\right)\right]\end{array}\right]}{\left(1+G^2\left[\frac{x^2}{\epsilon}\frac{dv_v}{dp}+\left(\frac{\partial\epsilon}{\partial p}\right)_x\left\{\frac{(1-x)^2}{(1-\epsilon)^2\rho_l}-\frac{x^2}{\epsilon^2\rho_v}\right\}\right]\right)} \tag{2.105}$$

2.9 Conclusion

Flow condensation inside horizontal tubes is a complex process. Several parameters affect the heat transfer and pressure drop characteristics of this process, including the choice of refrigerant, the type of tube utilized, the mass flux and the fluid properties (at the temperature and pressure utilized).

The void fraction, a measure of the geometrical space taken up by liquid and vapor, is the most important parameter determining two-phase flow pattern transitions, two-phase heat transfer coefficients and two-phase pressure drops.

Furthermore, to accurately predict the heat transfer using a unified method, it is necessary to predict the prevailing flow regime to a reasonable degree. For this, the Thome flow map for condensation in horizontal tubes was introduced. The method utilized to construct the flow map was elaborated on in this chapter.

The main advantages of utilizing this flow map are its ease of use, due to its non-logarithmic axes (only flow quality and mass flux are required), and the rigorous mathematical definition of the flow patterns, which present smooth transition between regimes.

Furthermore, a small discussion was developed regarding the dominating heat transfer modes in the Intermittent flow regime, and the concept of the time fraction, which can quantify the variation of this domination in a non-dimensional method, was introduced.

In Section 2.8, the basic equations for gas-liquid two-phase flow inside channels were also introduced. From these equations the basic forms of the pressure drop were introduced, namely, the momentum, gravity and friction pressure drops. However, in horizontal tubes, the pressure drop due to gravity head is negligible, so it is only fomulated from the momentum and friction pressure drops. The available history of pressure drop correlations in horizontal tubes is available in Chapter 4.

Chapter 3

Experimental Set-up

3.1 Introduction

This chapter describes the conceptualization, construction, components and commissioning of the experimental system. The experimental setup envisioned by the department was to be modular in such a way that condensation and evaporation experiments could be done on the same system. The system was to improve on the design on an existing setup used by the Rand Afrikaans University (RAU), now University of Johannesburg. The RAU system used a 12 meter long continuous condenser test section for smooth tube and a shorter length for enhanced tubes. The test section had short coaxial heat exchanger sections linked by adiabatic U bends in which the refrigerant condensed from superheated vapor to subcooled liquid. This section could not be locally controlled and measurements had to be taken at each heat exchanger section regardless of the properties at that point. The new design attempts to allow control of the properties at the inlet to the test section. Figure 3.1 shows a top view of the laboratory and the two-phase flow experimental setup.

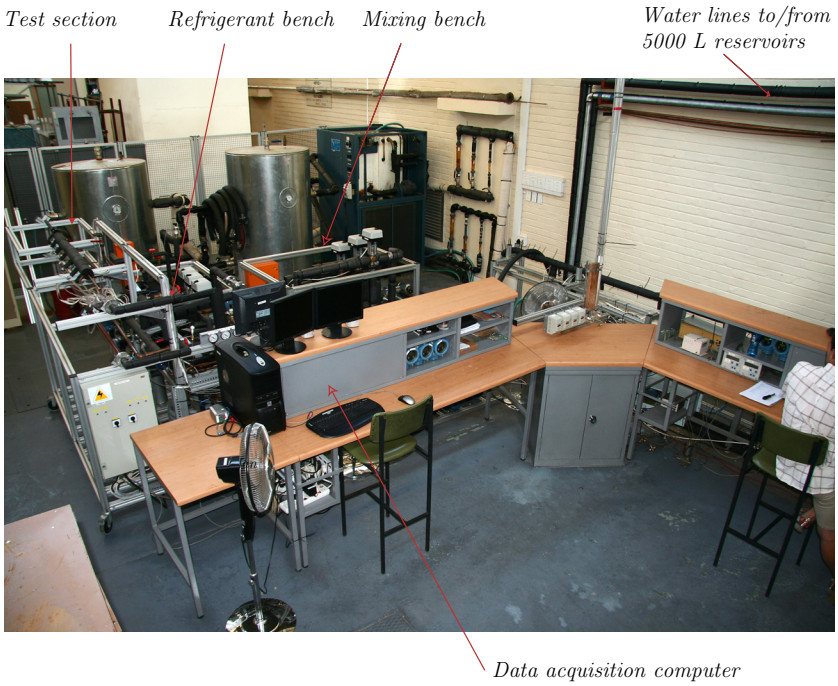

Figure 3.1: Top view of the two-phase flow experimental setup

3.2 Test facility

3.2.1 Refrigerant cycle

The modular heat pump's refrigerant cycle (see Figure 3.2), which can be used to perform both evaporation and condensation tests, allows for the test section's inlet and outlet properties of the refrigerant to be controlled. To control the mass flow, a bypass section would be used to divert the excess flow through a bypass condenser. To enable control of the refrigerant properties, the test line is made up of a sequence of heat exchangers, which is as follows: a pre-condenser to control the test section's inlet properties, the test-section condenser, a post-condenser to ensure that that the refrigerant is in the subcooled regime, and the sub-cooler, to control superheat. A simplified test schematic for condensation experimentation is shown in Figure 3.9.

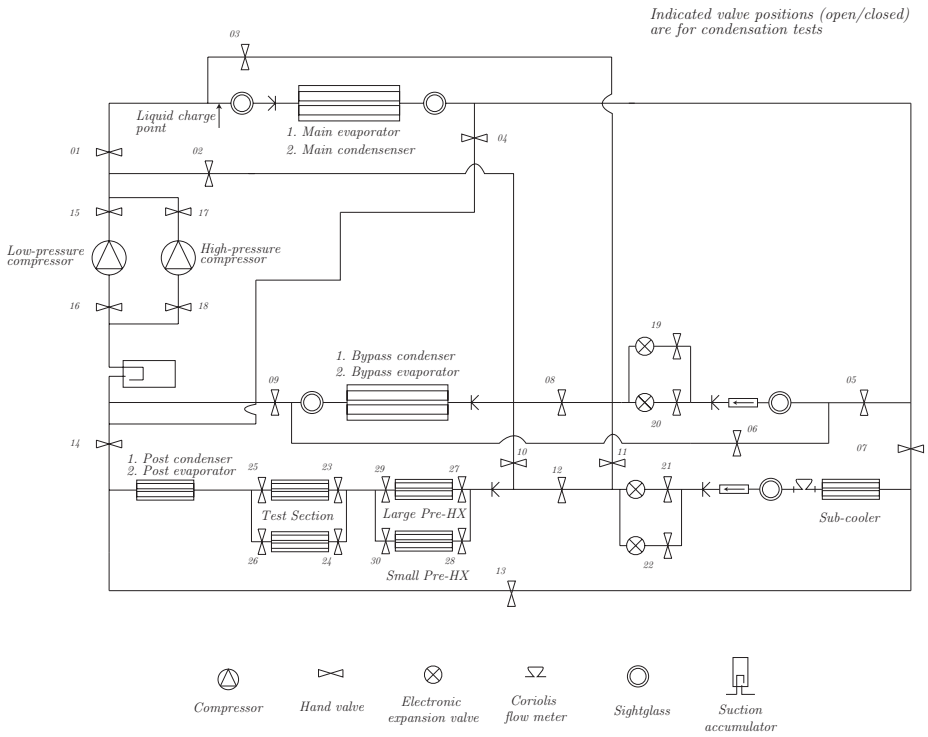

Valve Positions

1. Closed
2. Open
3. Open
4. Open
5. Closed
6. Open
7. Closed
8. Closed
9. Closed
10. Open
11. Open
12. Closed
13. Open
14. Closed
15. Open
16. Open
17. Closed
18. Closed
19. Closed/Open
20. Open/Closed
21. Closed/Open
22. Open/Closed
23. Open
24. Closed
25. Open
26. Closed
27. Open
28. Closed
29. Open
30. Closed

Figure 3.2: Physical refrigerant pipe connection schematic

This system utilizes a Copeland scroll ZR72 (10 kW nominal cooling) compressor that delivers smooth flow in the refrigerant loop. This selection was done to minimize the pressure pulses present when using reciprocating-type compressors.

In addition, the screw compressor does not require as much lubrication as its reciprocating counterpart. Figure 3.3 shows arear-view of the test bench. The compressor is protected by internal thermal overload and over current protection systems including: a low-pressure switch set to a pressure of 300 kPa at the inlet of the compressor, a high-pressure switch set to 2500 kPa at the outlet of the compressor, and a safety high-pressure switch that ensures that the inlet pressure to the compressor is below 1200 kPa and that there is a pressure difference greater than 300 kPa between the compressor ports.

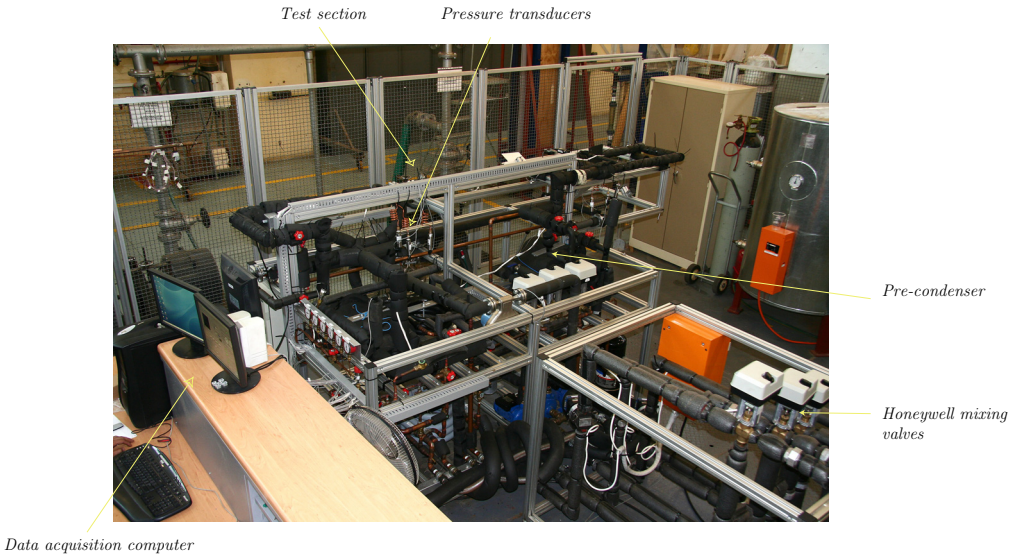

Figure 3.3: Rear view of the refrigerant bench

The refrigerant line splits into two after the compressor. The test line continues on to the pre-condenser. The bypass line contains only the bypass heat exchanger and an electronic expansion valve. The bypass line is used to divert flow from the test section for low mass flow tests, as was stated previously. The expansion valves on both these lines are discussed later.

The pre-condenser is used to control the properties at the inlet of the test section. The methods utilized are elaborated in more detail in Section 3.4. The properties at the inlet of the pre-condenser (exit of compressor) are assumed to be superheated. The refrigerant thermal properties are measured at the inlet

of the pre-condenser. The state of the refrigerant before the pre-condenser is used as the starting point for calculations of properties and energy balance; for testing to commence, the energy balance from the pre-condenser inlet up to the post-condenser outlet has to be below 1%. The measurement devices used are discussed later, in Section 3.4.

The test section splits into two after the pre-condenser and rejoins before the post-condenser. These lines can be used independently by opening and closing manual valves at the inlets and outlets of the test sections. This allows a new test section to be inserted without disturbing tests. The test section can be constructed to the required length that will allow for flow to fully develop and such that it has a long enough diabatic section for sufficient heat exchange (for tests to be accurate relative to the thermocouple accuracy). Both sections can be shut off with valves and are equipped with vacuum points and stainless steel flanges with Teflon seals. The test line will be instrumented with the necessary temperature and pressure measurement devices. Sight glasses are used directly before and after the diabatic section as insulators against axial conduction through the copper tube and for visual recordings to be made using a high-speed camera and uniform backlight. Fluid axial conduction can be neglected, as stated in Liebenberg (2002). The effect of axial conduction and the purpose of the sight glasses with respect to this phenomenon are discussed later. As mentioned previously, the energy balance is maintained until the exit of the post-condenser. The test line is the only part of the system where measurements are taken and on which calculations are performed. As such, it is not necessary to have an energy balance over the entire system.

After the test-section, the flow enters the post-condenser to remove any additional heat, depending on the setting of the pre-condenser and test-section, such that the outlet of the post-condenser reaches saturation. The post-condenser is followed by a sub-cooler to ensure that sub-cooled liquid enters the Coriolis flow meter to measure the flow of refrigerant in the test line.

Both the test line and bypass line have electronic expansion valves (EEVs). The test line valve is used to set the mass flow through the test section and the bypass expansion valve can then correct the system pressure in the test line. To cater for large flow ranges, two expansion valves are connected in parallel in both

the test line and bypass line. These expansion valves are connected one at a time while the other is shut off and closed. In the test line a large Carel E^{2}V EEV014 is used with a smaller Carel E^{2}V EEV009 to be used for accurate control at low mass fluxes. The bypass line expansion valve is then selected according to the selected test line expansion valve, either a Carel E^{2}V EEV024 or Carel E^{2}V EEV014. The expansion valves are bi-directional, although this function will not be used.

The refrigerant lines join after the expansion valves and enter the evaporator. The evaporator is designed with capacity for the maximum demand and will operate as the condenser when evaporation tests are done. The flow moves on after the evaporator into the suction accumulator and then into the compressor inlet.

Small sightglasses are positioned along the refrigerant line where necessary. There are sightglasses at the inlet to the coriolis flow meter, inlet and exit of the evaporator and after the bypass line expansion valve.

The system is currently usable with most common refrigerants and condensation tests are planned using R-22, R-134a and R-407C (over this study, and subsequent studies). The whole system, excluding only the compressor, is designed to withstand the high saturation pressures of R-410A. Provisions have been made for a high-pressure compressor to be installed in the system by leaving blanked-off pipes and space in the bench for such a compressor. The refrigerant lines, in and out of the compressors can be closed off with manual valves such that the operator can use the system with the correct compressor.

The system is reversible and as such this makes the required heat exchanger units named earlier dual-function. Thus the condensers would be evaporators and vice versa when evaporation tests are done. The pipe network is designed in such a way that the flow through the test sections is in the same direction for condensation and evaporation testing. This is done by controlling 29 valves throughout the system that would facilitate the reversal of function without reverse flow.

3.2.2 Water cycle

The water cycle consists of a hot and cold side. The majority of the water cycle systems are on a separate apparatus than the refrigerant cycle. The water is used to exchange heat with the refrigerant side at the condensers (cold water) and the evaporator (hot water). The supply is controlled by Honeywell-actuated valves and the required pressure head is supplied by Ebarra centrifugal pumps.

The water system is based on two insulated 5000 liter tanks. The two tanks share a 70 kW heating/50kW cooling heat pump and are thermostat-controlled between 13-17^{o}C and 23-27^{o}C respectively. The heat pump works in two modes; the first, the most efficient, is water to water, in which a vapor-compression cycle running R-22 is used to both heat up and cool down the two water flows. Further, if any of the two water tanks are on temperature, an alternate conditioning system is automatically switched to, in which the refrigerant flow of the on-temperature water heat exchanger is rather passed through a large radiator and over which air is forced by using fans. The size of the tanks, and the size of the heat pump allow the experimental setup to run indefinitely, due to the fact that it can maintain a relatively constant system inlet temperature, regardless of how much heat is being put in and out of the tanks.

The control bench is used as the connecting unit between the reservoirs and the test sections. The control units are each made up of a pump, flow meter and actuated valve. Figure 3.4 shows the flow meters, their transmitters and the servo-controlled valves on the control bench. Every heat exchanger on the refrigerant bench has a control unit. The control units are located on the control bench and on the refrigerant bench. The control bench is used to control the supply to the evaporator, sub-cooler and bypass heat exchanger (Figure 3.5) and it directs flow to the control units on the test bench. The control units on the test bench are for the pre-, test-section and post-condensers (Figure 3.6). Names used for the heat exchangers are for condensation experiments.

The basic control unit receives water from the reservoir and this gets pumped by a centrifugal pump through the heat exchangers. On the return, the water flow rate through the heat exchanger passes through a flow meter, either a coriolis flow meter or a Bürkert flow meter. The flow then enters the return line through a

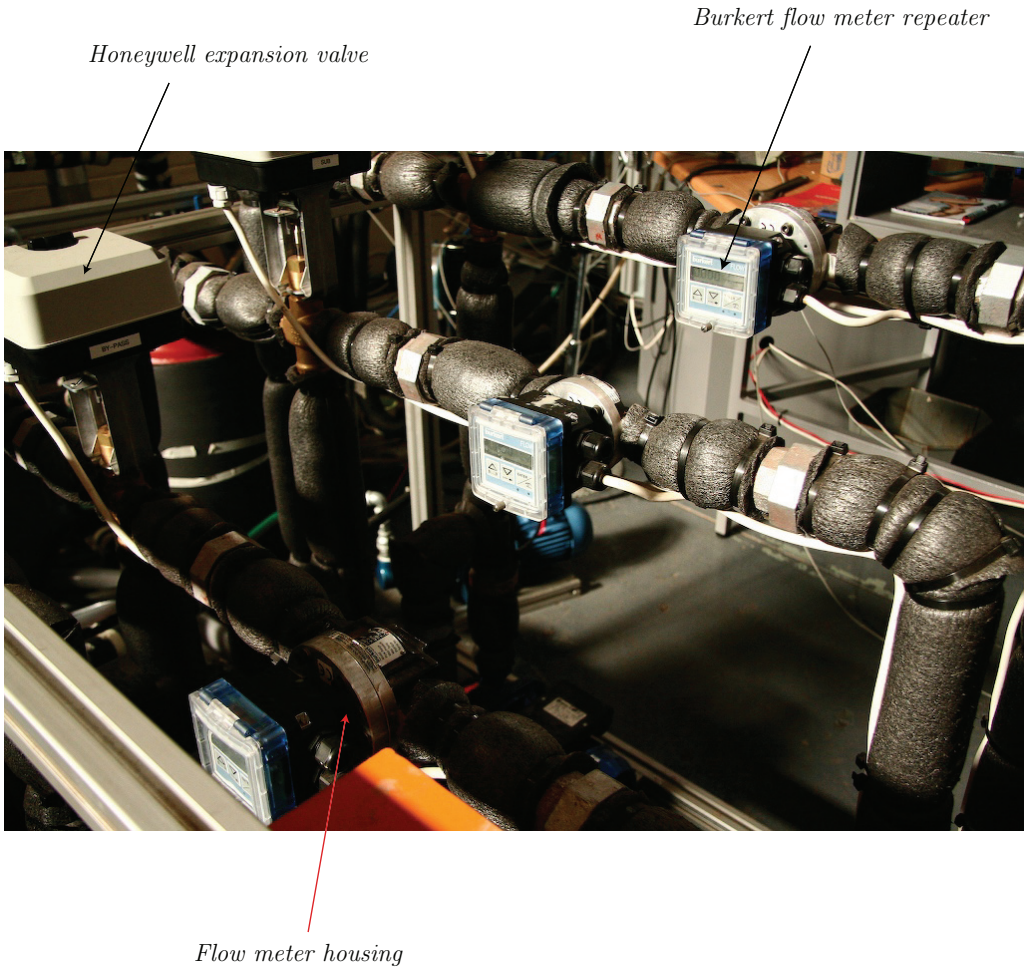

Figure 3.4: Control equipment on the water control bench

valve. The valves used are servo-actuated and control the flow through the heat exchangers while the remaining flow bypass the heat exchanger and immediately enters the return line back to the reservoirs. Each control loop is designed for the correct flow range expected through the heat exchanger. The pre-condenser is made up of two parallel heat exchangers; the large one, is specified for 10 kW heating capacity, and would be used when testing at high mass fluxes. The smaller pre-condenser is specified for 2.5 kW heating capacity and is used for low mass flux tests. The flow meters used by the control loops depend on the accuracy that

will be needed. Therefore the pre-condenser, test sections and post-condenser are fitted with coriolis flow meters and the rest use a less accurate and cheaper Bürkert flow meter. The flow meters are sized according to flow requirements and heat exchanger size.

3.2.3 Instrumentation and data acquisition

The experimental setup, as described above, is completely monitored and controlled using a computer. Signals from the thermocouples, pressure transducers, mass flow meters, mixing valves, and expansion valves are collected by a computerized data acquisition system. Furthermore, this system is controlled using the monitored data mentioned previously, in conjunction with signals sent to both the expansion (current input) and the water-mixing (volt input) valves. The entire acquisition system is comprised of:

1. IBM compatible PC, running Windows XP Professional.
2. LabView© 8.0, a graphical data acquisition programming language (National Instruments, 2005). A LabView program was written to perform manual/automatic system control, as well as automatic data acquisition (Section 3.3).
3. One NI SCXI-1001 12-slot chassis (Signal Conditioning eXtensions for Instrumentation).
4. One NI SCXI-1600, USB Data Acquisition and Control module for the SCXI-1001. It allows for 200 kS/s on a single channel, and can multiplex 1 kS/s on multiple channels.
5. Four (4) NI SCXI-1102 32-channel thermocouple amplifiers. These are the signal conditioning modules for thermocouples and low-bandwidth millivolt, volt and current inputs.
6. Three (3) NI SCXI-1303 32-channel Isothermal terminal blocks. These connect thermocouples and signals to two of the SCXI-1102 modules. Eighty four (84) of the available ninety-six (96) channels are utilized for measuring

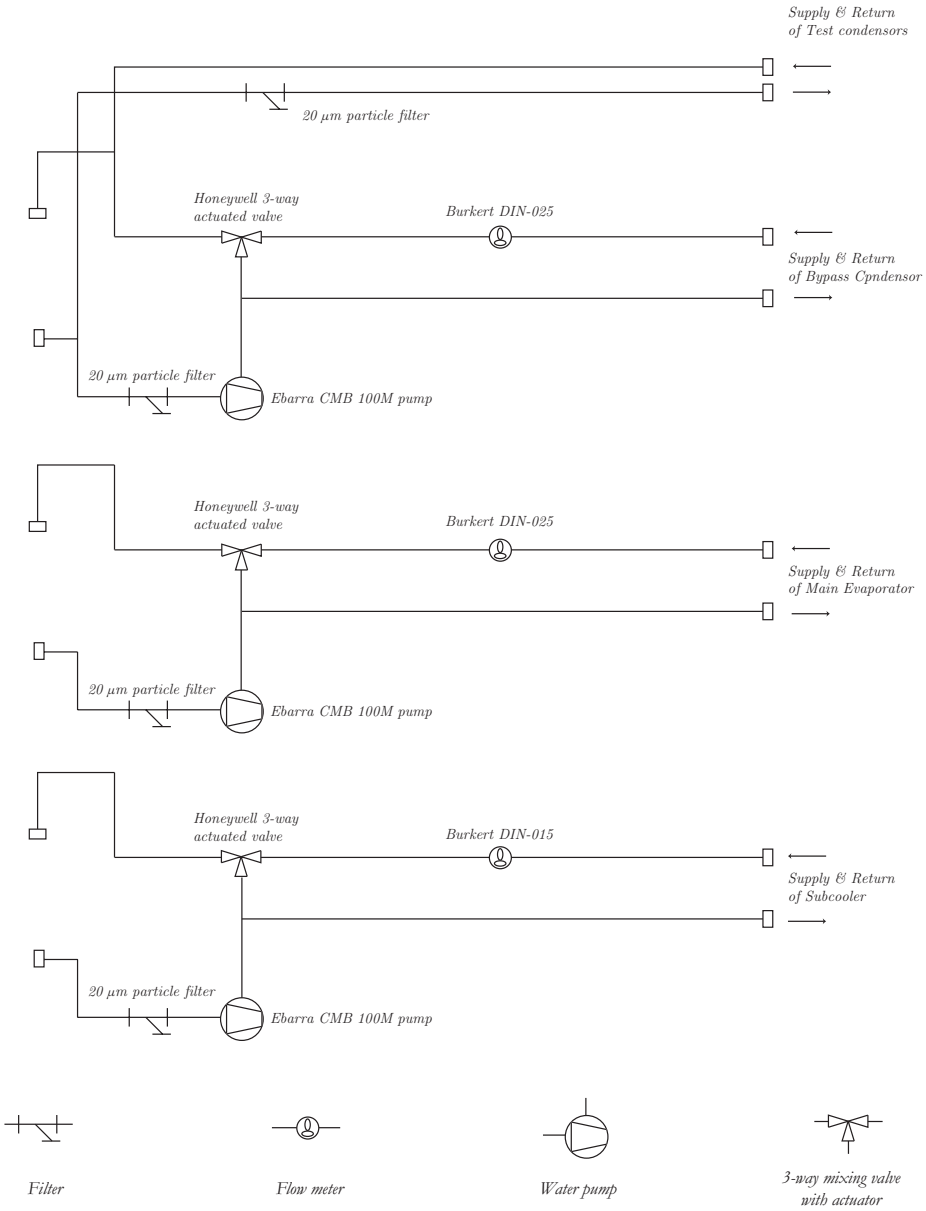

Figure 3.5: Control bench water pipe layout

thermocouple readings. The remaining twelve (12) channels may be utilized at a later stage.

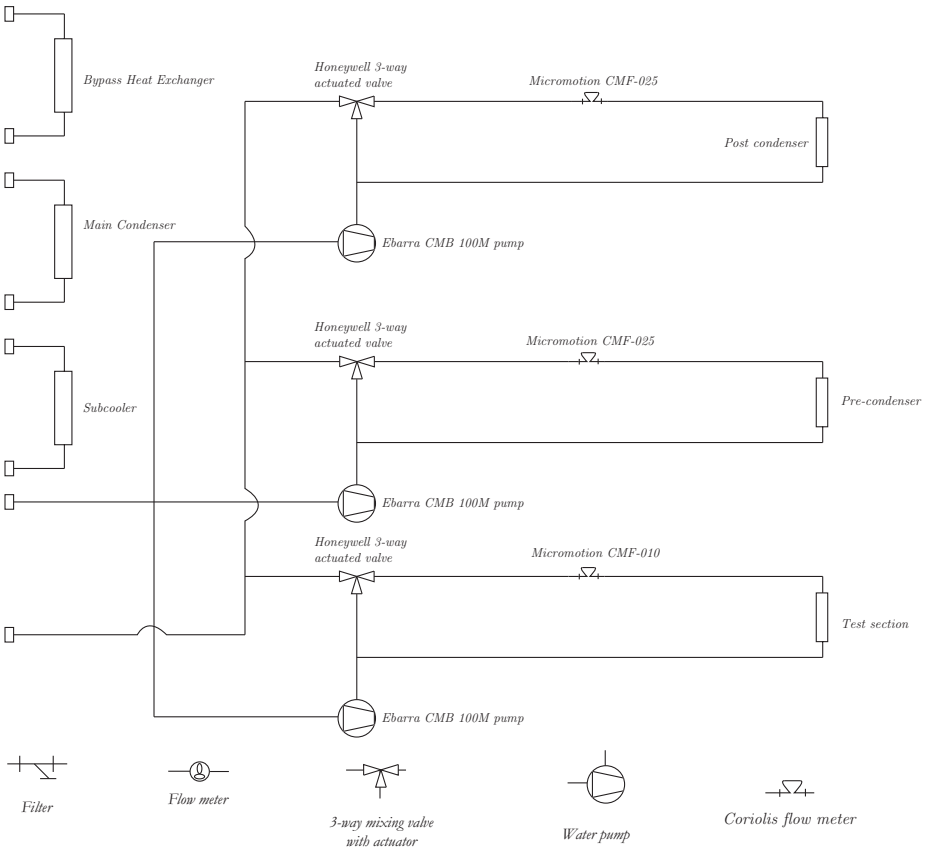

Figure 3.6: Water cycle layout on the refrigerant test bench

7. One (1) NI SCXI-1308 32-channel current input terminal block. It connects 0-20 mA and 4-20 mA signals to one of the SCXI-1102 modules. Fourteen (14) of the available channels are utilized for the pressure transducer and mass flow meter signals.

8. Two (2) NI SCXI-1124 6-channel isolated analog output modules. These are capable of supplying 0-10 V and 0-20 mA control signals. They are utilized to control the Honeywell mixing valves, and the Carel expansion valves.

9. Two (2) NI SCXI-1325 terminal blocks. These are used with the SCXI-1124 modules, and are utilized to send the generated current/volt signal. One

(1) of the two terminal blocks is fully utilized to control the six (6) water Honeywell mixing valves, using a 2-10 V signal, while in the other terminal block, only two 4-20 mA current signals are generated, to control the test-line and bypass-line expansion valves. There are four slots remaining, which may be used in the case of any expansion of the system.

10. One (1) NI SCXI-1322 terminal block. It measures ± 40V input signals, and connects to the SCXI-1122 module. Two (2) of the inputs are utilized; one measures voltages coming from the void fraction sensor, and the second input measures the DC voltage being produced from the AC/DC inverter, for use in the Sensotec pressure sensor ratiometric measurement system (more on this in Section 3.6).

11. One (1) NI SCXI-1122 6-channel voltage input module. It is used in conjunction with the SCXI-1322 terminal block.

12. One (1) NI PCI-8252 high-speed 1394a camera card; it couples with NI's Vision Development Module (Software) for both image processing and analysis, directly in LabView.

13. The high-speed camera in use is an 8-bit Basler A620f IEEE 1394a firewire camera capable of up to 300 frames per second, on a reduced Region of Interest[1] (ROI). It should be noted that there is a difference between the maximum video framerate and the shutter speed. The maximum shutter speed (which is only a function of available light) is 10 000^{th} of a second. The camera is used in conjunction with the National Instruments Vision Development module image software that allows saving and post-processing of the video images. The software is also used to trigger the start of a capture. The backlight used is a 98.7% uniform, 50 by 50 mm red LED light made by Phlox in France. It emits low heat and does not influence

[1]The region of interest is defined as the picture size (in pixels) that is presented to the user. The smaller this is, the greater the videography speed can be. At full size (640 x 480 pixels), the camera can sustain 100 frames per second videography. At a reduced ROI of 100 x 100 pixels, the camera can save video at 300 frames per second.

the refrigerant flow like an incandescent light would. The lens utilized is a μ-Tron FV2520. Details are shown in Table 3.1.

3.3 The LabView program

The experimental setup is comprised of the components and systems as set out in Section 3.2.1. The software backbone of the experimental setup, developed in National Instruments' *LabView*, utilizes both inputs received from sensors, and outputs sent to controllable operating systems to achieve data acquisition and manual/automatic control.

Table 3.1: Equipment utilized by the LabView software backbone in the two-phase experimental setup

Quantity	**Equipment**	**Range**
Temperature	Type T thermocouple wire *Omega*, UK, 30-gauge	-30 – 300^{o}C
Pressure Sensors		
Low	*Gems Sensor*, UK,	0 – 2000 kPa
High	*Gems Sensor*, UK	0 – 4000 kPa
Test	FP2000, *Sensotec*, USA	0 – 3400 kPa
Mass flow rate		
Water	Coriolis flow meter:	CMF 010 (0.4 kg/s)
	Micro Motion Inc., USA	CMF 025 (0.6 kg/s)
Refrigerant	Coriolis flow meter: *Micro Motion Inc.*, USA	CMF 010 (0.4 kg/s)
Water	Flow meter: DIN025,015	DIN025 (1.8 kg/s)
	Bürkert, Germany	DIN015 (0.6 kg/s)
Expansion valves		
Test line	*Carel* E^{2}V-014	4-20 mA input
	Carel E^{2}V-009	4-20 mA input
Bypass line	*Carel* E^{2}V-024	4-20 mA input
	Carel E^{2}V-014	4-20 mA input
	Italy	

Continued on next page

Table 3.1 – continued from previous page

Quantity	Equipment	Range
Data acquisition	*National Instruments*, USA	
Temperature	SCXI-1102 32-Channel multiplexer	±10 V, 4-20 mA inputs 250 kS/s single channel sampling rate
Pressure and Mass flow	SCXI-1102 32-Channel multiplexer	±10 V, 4-20 mA inputs 250 kS/s single channel sampling rate
Control	SCXI-1124 6-Channel low-bandwidth output module	±10 V, 0-20 mA outputs
Void Fraction	SXCI-1327 8-Channel analog voltage input	±40 V inputs
Flow visualization		
Camera	*Basler* A602f high-speed camera	Up to $\frac{1}{10\,000}^{th}$s aperture time dependent on ROI
Lens	*µTron* FV2520	25 mm, f/2 lens
Backlight	*Phlox* 50 mm x 50mm red LED backlight	98.7% even lighting

The main LabView VI (Virtual Instrument) performs both the control and data acquisition operations required. As shown in Figure 3.7, the program is divided into several 'tabs'; each one of these is utilized to show the salient information contained within each 'subsection'. What is more, there are several data which are not placed inside tabs; due to the fact that they are, in general, in continuous use, they have been placed off to the left of the tabbed section. These include the refrigerant in use, the water and refrigerant mass flow rates (the refrigerant mass flow rate includes the mass flux - 'G', its most common notations), salient temperatures in both the refrigerant and the water lines, and the pressures at several points in the system. The tabbed section comprises of 7 tabs; In no particular order, these are:

Control This tab is the manual control tab; both the expansion valves and the water mixing valves are controlled from here. As was stated in Section 3.2.1, although there are two expansion valves per line, only one is used at a

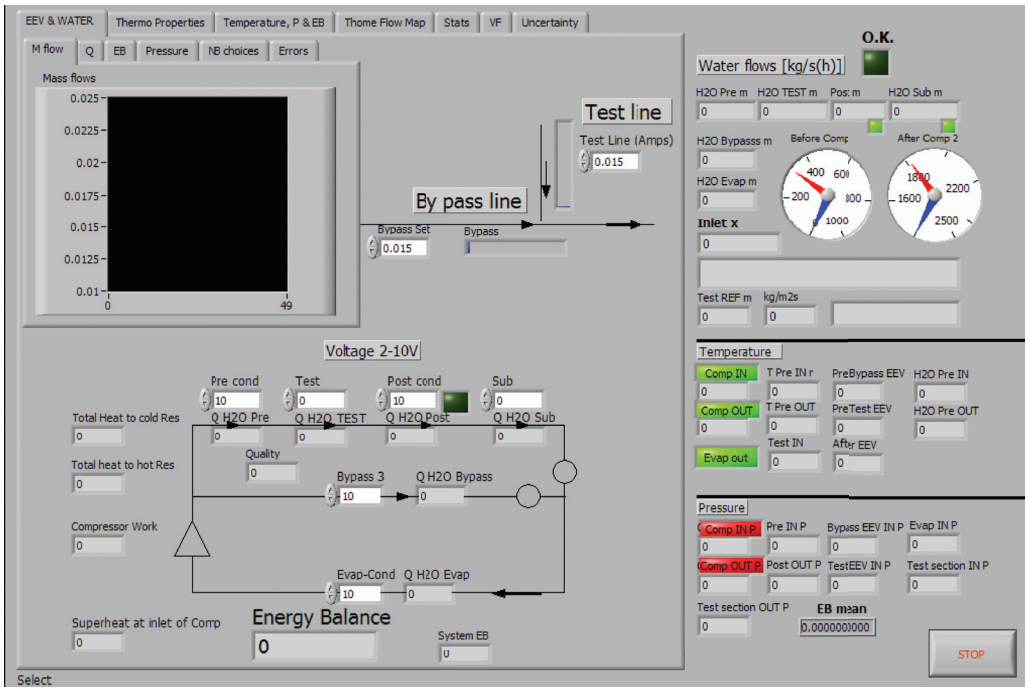

Figure 3.7: Front panel of the LabView program

time, depending on what the required test conditions are. As such, there is physically only one control signal going to each line, and the required EEV is selected by manually installing the connector to the correct EEV, and opening the necessary valves. In the control tab, two inputs are available, which will directly accept inputs from 4-20 mA, and actuate the expansion valves. It is also possible to change that 4-20 mA required input to an input varying from 0-1, indicating 'fraction opening' (where 1 is fully open). The conversion to required input happens automatically in the background. The theory behind the control aspect of the EEV movements is detailed later, in section 3.5. On the bottom half of the 'Control' tab is the section controlling the actuation and fraction-opening of all the Honeywell water mixing valves. Section 3.2.1 gives a brief explanation of the workings of the mixing valves. These valves are controlled using a 2-10 V signal; it is stated that these valves have fully continuous actuation, meaning that they, in theory, do not move on step input signals. However, it has been

seen that the lowest repeatable input signal change that will register, and make the valves operate, is 0.2 V. It should be noted that the 4 mA and 2 V signals correspond to the valves being fully closed, while 20 mA and 10 V represent the valves fully open. An indicator at the bottom of the tab shows the amount of superheat available at the inlet of the compressor, which is calculated using a Matlab script. This is utilized in the control of the system, as set out in section 3.5. Furthermore, indicators showing the compressor work, test energy balance and system energy balance are also shown. What is more, a sub-menu is available in this tab; a running history of the mass flows, heat transfer (hot and cold sides) and energy balance are available, along with a tab that lets the user make important choices, such as the inner diameter of the tube, heat exchanger length and conductivity of the copper. A final tab controls the error indicators, which are aural in nature and notify the user if any system parameters falls over or runs over the specified safety limits. The 'Save' tab is used to manually specify the file name convention, and the directory used for saving, as well as the number of samples to capture per saved data point.

Void Fraction The void fraction tab essentially runs the Void Fraction sub-VI, and shows the two most important graphs generated by the sensor. The sensor utilized is a capacitive void fraction sensor, which uses three electrodes to pick up the difference in vapor/liquid dielectric constant and generates a voltage signal (De Paepe *et al.*, 2006). A toggle switch is utilized to activate the Void Fraction sub-VI, while two outputs of the sub-VI, the power spectral density (PSD) graph of the voltage signal and the Void fraction statistical graph are output to the main control program for monitoring purposes. The statistical value of the void fraction sensor's signal is compared to the logarithmic-mean void fraction prediction and the percentage deviation is calculated.

Thermodynamic Properties This tab utilizes pressure and temperature data, coupled to the Matlab script to generate two graphs, the first, a T-s diagram, and the second, a P-h diagram. While these are not of direct influence, or importance, to two-phase testing and experimentation, it is useful from

a system-control point of view, as it is possible, in one quick glance, to summarize the complete operating window, instead of having to check each point separately. The method utilized to generate these graphs is detailed in section 3.4.

Temperature, Pressure and Energy Balance This tab includes all of the temperature and pressure measurements that are found in the system, both on the refrigerant and the water sides. Also, several energy balances are calculated in this tab. Furthermore, several key control aspects are also shown here, as are the amount of superheat available at the inlet of the compressor (also shown in the "Water & EEV" tab), the condensation temperature at the test pressure, and the refrigerant states at the temperatures. Furthermore, in terms of pressure, the experimental system has an operating range from 300 kPa up to 2500 kPa (at the moment; once R410a is used, the HP trip pressure will have to be increased up to at least 3800 kPa (Goto *et al.*, 2001)). Warning systems, which include sonic and visual alarms, notify the user when the low-pressure (*i.e.* in front of the compressor), the high-pressure (right after the condenser) or any of the temperatures (i.e. compressor inlet temperature $< 0^{o}$C, or compressor outlet $> 100^{o}$C) in the system fall out of their adequate range. While it has not been previously stated, the control program is heavily dependent on a Matlab script to calculate refrigerant and water properties, refrigerant quality and heat transferred ($\dot{Q}$). This will be detailed in section 3.4. Using experimentally calculated values for the heat transferred to and from the pre–, test– and post-condensers (in Condensation mode), both on the refrigerant side and water side, an overall test energy balance is calculated. For the purposes of any studies performed at UP's thermoflow research group, the energy balance must be less than 1%. It should be noticed that the total refrigerant mass flow is not measured (i.e. through the compressor), nor is the bypass line mass flow, as they are, for purposes of testing, irrelevant. Nonetheless, using several well-based assumptions (shown in section 3.4), it is possible to estimate the mass flow through the compressor. Using this approximated mass flow, the work input to the compressor, and the total energy input

into the main evaporator can be approximated. These are also shown in this tab. The system energy balance is calculated by checking the amount of energy in and out of the refrigerant system; that is, a control volume over the entire system allows us to equate energy out of the system (in the condensers) to the sum of the work input in the compressor and the thermal energy input in the main evaporator.

Thome flow map The method used to construct this flow map is as found in El Hajal *et al.* (2003). It is generated using a Matlab script, and is used to theoretically confirm the flow regime found in the sightglass during experimentation. The Rouhani-Axelsson void fraction and the LMTD void fraction are both calculated, and indicators are included in the Void Fraction tab as comparison values. The flow-regime based heat transfer coefficient and pressure drop prediction are automatically updated and presented in this section.

Stats Stemming from the fact that there are several key data that need to stabilize for useful testing to commence, the behavior of these is studied on a time basis, in the sense that the standard deviation about the point's mean value is calculated over 30 iterations of the main program's `while` loop. The mean is also updated at each iteration, such that the deviation comparison occurs in real-time. Information in this section includes temperatures, pressures, mass flows and void fraction signals.

Uncertainties The uncertainties in the system, as derived in Appendix B were included into a separate Matlab script that runs continously in the program. It takes the measurements made in the system and continously calculates the uncertainties in the system. This information is also saved when saving data. This tab can be utilized to decide in real-time whether the uncertainties are within tolerances to begin testing, or whether changes are required. These could be from an instrumentation point of view, or from a testing point point of view.

3.4 Matlab script

3.4.1 Thermodynamic properties

As has been stated previously, the Matlab script running the Control VI is critical to the control, data acquisition and monitoring aspects of the experimental system. At present, Matlab R16 (Matlab R16, 2006) is used. The major component of the Matlab script involves finding the properties of both the water and refrigerant at the required measuring points. This is done using XPROPS, a suite of Microsoft Excel, LabView and Matlab functions, developed by Thermal Analysis Partners (Thermal Analysis Partner XPROPS, 2006), which make reference to NIST's REFPROP 7 (National Institute of Standards and Technology, 2002) fluid property database. Thermal Analysis Partners is fully endorsed by NIST in its endeavors. XPROPS Matlab property functions are called using the required inputs to generate the desired fluid properties.

Due to the fact that the temperature and pressure stay constant during condensation and evaporation, additional information is required to calculate the temperature and pressure before and after the test section. This is done by assuming that the entirety of the energy transferred into the water goes out of the refrigerant (which is an acceptable assumption once the test line energy balance drops below 1%), and knowing what the properties of the refrigerant are at the inlet of the pre-condenser. However, one cannot always assume that the outlet of the precondenser is in the mixed regime, thus for generality purposes, a case structure must be utilized, using `if` statements in the Matlab script. With the known properties of the refrigerant at the inlet of the precondenser, two extra energy quantities are calculated:

1. $\mathbf{Q}_{satvap}$ This is the amount of energy required to make the outlet of the pre-condenser go to the saturated vapor point at the pressure and temperature measured at the inlet of the test section.

2. $\mathbf{Q}_{satliq}$ This is the amount of energy required to make the outlet of the pre-condenser go to the saturated liquid point at the pressure and temperature measured at the inlet of the test section.

As such we can easily surmise that there will be three possible cases; first, the inlet of the test section is fully liquid, second, in the mixed regime, and third, still superheated. This is shown in Figure 3.8.

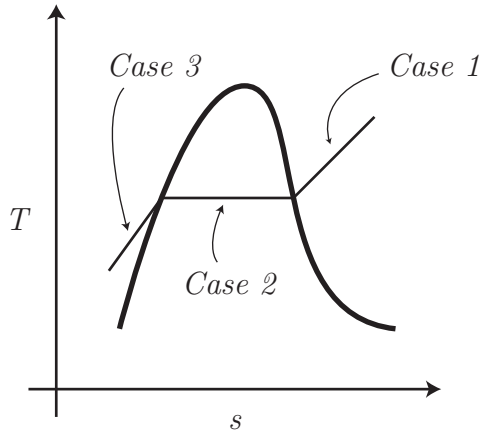

Figure 3.8: Refrigerant pre-condenser outlet possibilities

The first and third cases are not of large concern, as the properties of the refrigerant can be simply garnered from the pressure and temperature at the point. However, for the mixed regime, it is necessary to know what the quality is, such that the relevant properties may be found. In this case, though, it is necessary to first calculate the enthalpy of the outlet of the outlet of the precondenser, using:

$$h_{ref,pcout} = h_{ref,pc\,in} - |\frac{\dot{Q}_{H_2O,pre}}{\dot{m}_{ref}}| \tag{3.1}$$

where $h_{ref,i}$ is the specific enthalpy of the refrigerant at the inlet and outlet of the precondenser. Once the precondenser outlet enthalpy is known, this is equal to the enthalpy at the inlet of the test section. Then, knowing what the enthalpy at the inlet of the test section is, the saturation liquid and vapor enthalpies at the condensing temperature and pressure of the inlet of the test section are called up, to calculate the quality at the inlet:

$$x_{test,in} = \frac{h_{ref,testin}}{h_{ref,satvap} - h_{ref,satliq}} \tag{3.2}$$

To calculate the test outlet properties, a three-tiered approach is also used; depending on what the test inlet looks like, additional steps are performed. When the inlet of the test section is fully liquid, it stands to reason that the exit can only be liquid as well, thus the temperature and pressure are utilized to calculate the properties of the refrigerant at the exit. When the inlet regime is mixed, the amount of energy required to drop to fully saturated liquid at the exit temperature and pressure conditions is calculated. Then a two-level condition structure is utilized to calculate the properties at the outlet. When the inlet remains superheated, the same conditional structure used in the pre-condenser must be utilized.

The rest of the system refrigerant points can be directly calculated using XProps, and the refrigerant temperature and pressure, except for one point. After the expansion valves, the point at the lower temperature is almost certainly mixed, but without any other information other than pressure and temperature, one cannot know exactly where it is. Nonetheless, since this is not a critical point, and is only calculated for the sake of completeness, and to complete the cycle in the "Thermodynamic" tab, there are several assumptions one can make. First, it may be assumed that there is no heat loss over the expansion valve, nor is there any work done on, or by, the fluid. Furthermore, the mass flow stays constant over each expansion valve. As such, over each expansion valve,

$$h_{ref,EEV\ in} = h_{ref,EEV\ out} \tag{3.3}$$

And, when the bypass and test lines meet,

$$\dot{m}_{ref,test} h_{ref,test} + \dot{m}_{ref,bypass} h_{ref,bypass} = \dot{m}_{ref,tot} h_{ref,tot} \tag{3.4}$$

However, both $\dot{m}_{ref,bypass}$ and $\dot{m}_{ref,tot}$ are unknown. The mass flow of refrigerant through the bypass line may however be approximated by assuming that the pressure at the inlet of the bypass-condenser (which is not measured), is equal to

the pressure at the inlet of the pre-condenser. It is also assumed that the bypass heat exchanger's inlet is superheated. Thus, by using the measured temperature and the assumed pressure, a specific enthalpy for the refrigerant at the inlet of the bypass-condenser can be approximated. Then, using the known quantity of heat transferred into the water side of the bypass-condenser (assuming very good energy balances), and the known outlet state, an approximate refrigerant bypass mass flow can be found,

$$\dot{m}_{ref,bypass} = |\frac{\dot{Q}_{H_2O,bypass}}{h_{ref,bin} - h_{ref,bout}}| \tag{3.5}$$

With this approximated bypass refrigerant mass flow, the total mass flow can be shown to be:

$$\dot{m}_{ref,tot} = \dot{m}_{ref,bypass} + \dot{m}_{ref,test} \tag{3.6}$$

And, finally knowing the above, the specific enthalpy at the exit of the mixing chamber, located after the EEVs is

$$h_{ref,tot} = \frac{(\dot{m}_{ref,test}h_{ref,test}) + (\dot{m}_{ref,bypass}h_{ref,bypass})}{\dot{m}_{ref,tot}} \tag{3.7}$$

With this final point, it is possible to calculate the quality using the pressure at the point and the specific enthalpy. Finally, the entire cycle may be graphed, as in the 'Thermodynamic Properties' tab.

To estimate the real mass flow through the main and bypass lines, it is assumed that the main evaporator has a good enough energy balance such that the energy transferred into the refrigerant can be assumed to come only from the water. As such, if we calculate the energy transferred, we can work back to a refrigerant mass flow, since we have assumed that the inlet enthalpy into the evaporator is reasonably accurate as calculated above. Thus,

$$\dot{m}_{ref,tot} = |\frac{\dot{Q}_{H_2O,evap}}{h_{ref,evapout} - h_{ref,evapin}}| \tag{3.8}$$

3.4.2 Energy balance

The test-line energy balance must be calculated to make sure that, first of all, the assumptions made in the previous section are valid (*viz* the quality calculation), and second, to make sure there is no stray energy lost in the system. The system energy balance consists of comparing the total test-line energy transferred between the refrigerant and test sections, inside the pre-, test- and post-condensers. The equation for the system energy balance is:

$$EB_{sys}(\%) = |\frac{\dot{Q}_{ref} - \dot{Q}_{H_2O}}{\dot{Q}_{avg}}| \cdot 100 \tag{3.9}$$

where Q_{avg} is the mean of the absolute values of the experimentally found values for the heat transferred to and from the refrigerant test line, on both the refrigerant and water side.

3.4.3 Thome flow map

The Thome flow map, as stated beforehand is automatically calculated utilizing the most up-to-date inputs from the rest of the system, including the prevalent mass flux inside the test section, and the temperature at the test point. Utilizing these, and using a `for` loop, the entire flow map can be generated in realtime, with changing conditions reflected automatically. As stated in Section 3.2.1, two sight glasses, one each in front and back of the test-condenser, are installed. Due to the potential difference in quality between the inlet and outlet, these two points are plotted; a third point, using a linear average of the two condition qualities is also plotted. This vapor quality is the average quality used in the flowmap and heat transfer. Again, this flow map is utilized to corroborate the experimental findings, and to troubleshoot the system.

3.5 Control methodology

As has been shown previously, there are a multitude of factors and settings which can be changed in the system which will affect the working pressure P, mass flux

ϕ and test inlet quality x. Coincidentally, these are the three main areas which must be controlled in this setup to successfully carry out valid and meaningful experiments. However, changing one factor does not necessarily mean only one of these three main parameters change; in most cases, altering any one factor will have an effect on more than one of the three critical parameter.

As was previously stated, it is necessary to be able to control the working pressure, mass flux and test inlet/outlet vapor qualities. The methodology for this is stated in the following sections.

Due to the complex relation between the multiple parameters that affect the three main test criteria, automating the system is a non-trivial procedure. While this was begun during this study, as a part of both the author's work and Van Rooyen's work, it was not finalized. As such, any control performed in this system is still manual.

3.5.1 Mass flux control

To control the test line mass flux, the amount of refrigerant bypassed or let into the test line needs to be changed. In this case, as shown in Figure 3.9, this can be done using the test line expansion valve. By opening and closing the expansion valve, the general backpressure on the line changes, which means that more, or less flow will be diverted to the bypass line, depending on the action taken.

With the Carel expansion valves that are currently installed on the test-line, it is possible to test from 25 up to 1000 $\frac{kg}{m^2 s}$. Under 150 $\frac{kg}{m^2 s}$, the E^{2}V-009 should utilized as it affords accuracy of up ± 1 $\frac{kg}{m^2 s}$, with relatively small changes between valve settings. The E^{2}V-014 should be utilized when in higher mass flux situations; once the system has stabilized, it has been shown that the variations over and below the required mass flux can be kept at ± 1 $\frac{kg}{m^2 s}$. The methodology for control of mass flux would involve, firstly, setting the required mass flux and adjusting the test-line EEV to achieve said flux. Since the actuation of the test-line EEV will have an effect on the system pressure, the pressure will need to be controlled. In all cases, any changes made to the system parameters require adequate settling time.

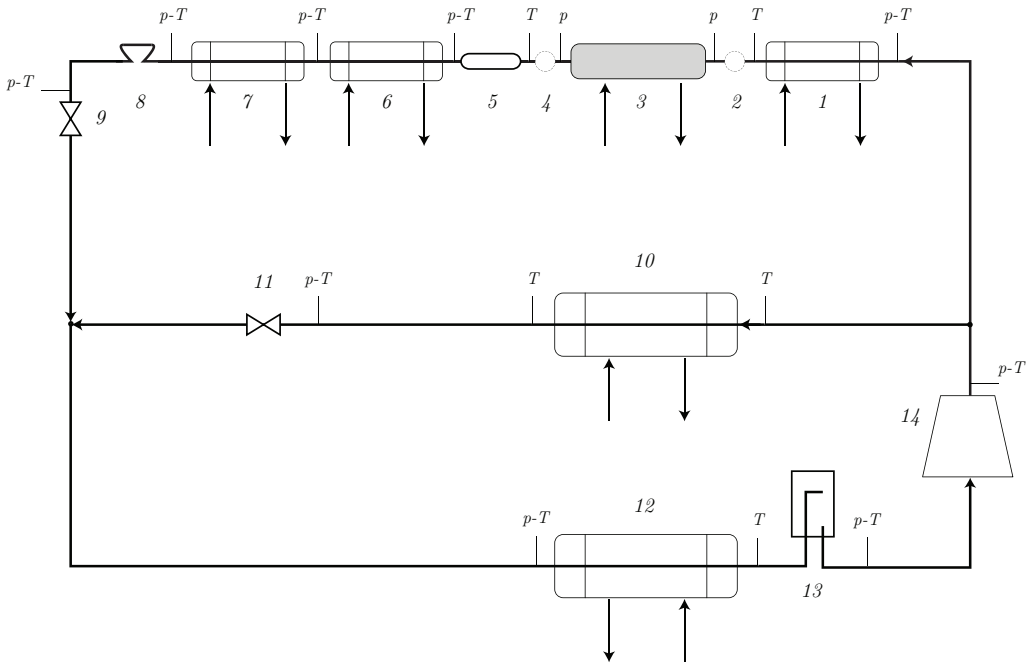

1. *Pre-condenser (water cooled)*
2. *Sight glass: high-speed videography*
3. *Test section (water cooled)*
4. *Sight glass*
5. *Capacitive void fraction sensor*
6. *Post-condenser (water cooled)*
7. *Sub-cooler (water cooled)*
8. *Coriolis mass flow meter*
9. *Test line expansion valve*
10. *Bypass condenser (water cooled)*
11. *Bypass line expansion valve*
12. *Evaporator (water cooled)*
13. *Suction Accumulator*
14. *Compressor*

Figure 3.9: Schematic of the system cycle

3.5.2 Test line pressure control

Due to the fact that the test-line expansion valve settings change to accommodate the mass flux requirement, the backpressure increases and decreases which cause the change in mass flux to also have an influence on the system pressure. To

control the pressure, there are several methods that can be utilized; namely the modification of the bypass line expansion valve setting. Further, to achieve the correct condensation pressure in the system, the bypass expansion valve is also opened and closed as is necessary. Thus, when the condensing pressure needs to be increased, the bypass EEV should be closed. To achieve the same effect, the bypass condenser water can also be used. That is, to increase the testing saturation pressure, the water flow through the condenser should be slightly dropped. The converse is also true. From experimentation, the system is more sensitive to small water flow changes than to medium changes in the EEV setting. A such, the water flow should be used for approximate settings, with the EEV used for precision control. Larger changes will affect the pressure in the system greatly, and should be avoided. As a last resort, if the system is in danger of tripping the HP (high pressure) switch, the bypass condenser water supply should be opened a large amount. This immediately drops the pressure. If the system is in danger of tripping the LP (low pressure), the bypass EEV should be closed and so should the bypass condenser water flow. While the test-line mass flux is quite insensitive to changes performed in the bypass EEV, it is not entirely so, which entails further small corrections.

3.5.3 Test inlet and outlet vapor quality control

The vapor quality of the refrigerant before and after the test section must be finely controlled, as the overall test quality is defined as the average between the inlet and outlet of the test section. As such, depending on what is required, the amount of heat taken out of the system needs to be controllable. As was stated in section 3.4, this is done by controlling the water mass flow rate through the pre-condenser. The method utilized requires monitoring the properties of the refrigerant at the inlet of both the pre- and the test-condenser. If the desired test inlet quality is known, then the Matlab script can calculate how much energy to take out from the refrigerant. Then, not taking into account the water outlet temperature change, it is possible to calculate the water mass flow required. Finally, the water inlet mixing valve can be opened or closed, depending on the amount of water necessary. The same procedure should be followed in the test section. It should be noted

that the refrigerant must be in fully liquid state at the exit of the post-condenser. This can be manually ensured by using indicators and alarms showing the state at the exit of the post-condenser — it can also be automatically controlled — there is a pressure transducer at the exit of the post-condenser, from which it is possible, using Xprops and Matlab, to find the saturation temperature at that pressure. Then, since the temperature of the refrigerant is also monitored, the water mass flow rate should be controlled such that the temperature at the exit of the post-condenser is always less than the calculated saturation temperature.

3.6 Sensotec FP2000 ratiometric measurements

The output of a strain gauge based sensor is directly proportional to the physical pressure measurement the sensor is detecting and also the excitation voltage across the bridge network. The full scale output of the transducer varies directly with the excitation thus, a sensor with a calibration factor of 3 mV/V will exhibit 30 mV at full pressure if it is being supplied with 10 V, but only 15 mV at full pressure if it is being supplied with 5 V (FP2000 User's Manual, Columbus, OH). This means that output varies with supply voltage. If the effect of the change in supply voltage cannot be perceived, then it is not truly possible to know how much the real pressure has changed. This approach is known as a ratio metric measurement because it relies on the ratio of voltage output to the calibration factor (mV/V) to determine pressure. Sensotec pressure sensors require the user to monitor both transducer output and power supply excitation (rather than being voltage-independent). Using the mV/V calibration constant given in the pressure sensors' factory calibration certificates, it is possible to redefine the output of the system such that, independent of incoming supply voltage, the milli-ampere output varies between 4-20 mA between 0-3447 kPa, using an independent pressure calculation sub-VI in the control VI.

3.7 Experimental procedure

To start the experimental setup, and to make sure there are no leaks, the system needs to be pumped up with nitrogen to 1500 kPa; once at this pressure, it must be kept there for at least 24 hours. If no pressure drop occurs, the system can be said to be leak-tight.

To evacuate the system of the nitrogen, the system must be evacuated (without use of a vacuum pump) until the internal pressure is not much higher than ambient pressure. This is due to the fact that, at higher internal pressures, the vacuum pump oil can be driven out, potentially causing large amounts of damage to the pump. In Liebenberg (2002), a system charged with 4 kilograms of R-22 was evacuated for 6 hours; in the case of this system, 13 kilograms constitute a full system charge. Thus, from linear extrapolation, the system needs to be evacuated for a minimum of 18 hours.

Of course, this is done only when changing refrigerants. If only the test section is to be replaced, the test section area is evacuated using the vacuum pump, charged with nitrogen and pressure tested. Once the system can be considered leak proof, it is charged with the proper refrigerant and testing can continue.

Once the system is charged, a minimum compressor warm-up time of eight hours is required, such that the crank-case heater ensures the refrigerant entrance to the compressor is fully superheated. For this reason, the crank case heater should always be on. Then, once the system is ready to be started, it is necessary to check that the water supply temperatures are within tolerances. In the case of the cold water supply, the water temperature should be between 13-17^{o}C, while the hot water temperature should between 23-27^{o}C.

To start up the system, the hot and cold water supply lines need to be fully opened at the control-bench distributor. Then, the control pumps for all six heat exchangers can be turned on. The compressor has a safety feature, which does not let it start up if any of the pumps are not working correctly. Once the mixing valves and the expansion valves are set to their midway points, the compressor can be turned on.

After a 10-20 minute stabilization period, it is possible to make modifications to the system's controllable parameters such that the first testing point can be

reached. Once the system is allowed to stabilize (i.e. the test-line energy balance $< 1\%$ for more than 5 minutes), data collection can commence.

As has been pointed out previously, the sight glasses are utilized as buffers against axial conduction in the system. Furthermore, just before the sight glass at the entrance to the test section, and straight after the sight glass at the exit of the test section, thermocouples and pressures are measured as shown in figure 3.10.

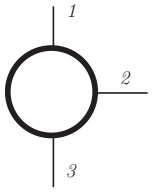

Figure 3.10: Pressure sensor and thermocouple placement at the inlet and outlet of the test section (1.: Top position, 2.: Side position, 3.: Bottom position)

The inside wall temperatures of the refrigerant line can be measured using direct measurements, or can be inferred using the Wilson-plot method.

Apart from thermocouple and pressure measurements, the calculated overall and semi-local heat transfer coefficients, as dynamically calculated in the Matlab program are saved. The general list of raw data saved is as follows:

1. Thermocouple readings (placement as shown in the figure) at the inlet and outlet of the test section. These readings are utilized by themselves and in averaged form.

2. Thermocouple readings along the outer diameter of the inner tube.

3. Pressure transducer readings (placement as shown in the figure) at the inlet and outlet of the test section. These are also used by themselves and in averaged form.

4. Calculated momentum pressure drop readings.

5. Raw void fraction voltage, as well as the PDF and statistically-separated bin void fraction measurement.

6. Overall and semi-local heat transfer coefficients.

7. Mass flux, and inlet and outlet qualities.

8. Heat transfer rates, on both water and refrigerant sides.

9. High-speed video images.

In terms of data reduction, the following is needed for the heat transfer and pressure drop correlation:

1. A time fraction map in the intermittent flow regime is generated using data processed from the high-speed camera videos.

2. When utilizing direct wall temperature measurements, the measured heat transferred on the annulus is divided into a unit heat flux and is propagated along the tube. Either way, this is utilized to calculate the inside heat transfer coefficients.

3. The time fraction data is used in conjunction with the shear stress-based and gravity-based correlations of Thome, to develop a more general prediction for the Intermittent flow regime.

4. The same type of regression analysis technique is also used for the pressure drop. In this case, the mass flux, inlet and outlet vapor qualities, and the fluid properties are required, among others.

The flow regime study involves using three methods of identifying flow regimes and comparing the results. The first method uses power spectral density analysis of pressure measurements to identify flow regime (Liebenberg, 2002). Secondly a capacitive void fraction measurement device will be used and by analyzing the frequency response of the signal a probability density of the current flow regime will be given. Thirdly by directly analyzing and manipulating the video feed from a high-speed camera in LabView and using IMAQ visual software a probability density of flow regime will again be constructed. The output of these three independent methods of flow regime identification will then be compared for conclusions to be made on the use of any of these methods. For modern heat transfer and pressure drop correlations the identification of flow regime plays an

important part and finding an effective and accurate method with rapid results will aid in future development and improvement towards a unified approach. The above flow regime study was performed by Van Rooyen (2007).

Tests will be done at all the necessary points by setting the system, correcting the imbalance, waiting for stability and running the test. This procedure is repeated until complete.

3.8 Test section design

The test section is comprised of a horizontal straight tube-in-tube counterflow heat exchanger. Furthermore, just before and after the heat exchanger, sight glasses are positioned on the refrigerant side. At the exit of the back sight glass (*i.e.* the sight glass at the (refrigerant) exit of the heat exchanger) the void fraction sensor (De Paepe *et al.*, 2006) is positioned. Refrigerant flows in the inner tube, while water flows in the annulus. The entire test system is installed into the apparatus using flanges, such that the experimental apparatus need not be stopped and deconstructed to fit a new type of tube. The test section is shown in Figure 3.11.

The test tubes utilized all have an outer diameter of 9.53 mm ($3/8^{th}$ in), which is a standard size in refrigeration systems. The reason why tubes of this size were chosen was precisely because they are widely used in industry. The annulus outer tube has an outer diameter of 15.88 mm ($5/8^{th}$ in). It has one inlet and outlet for water to circulate in and out from, at the refrigerant outlet and inlet sides respectively.

Between the inlet flange and the inlet sight glass, a minimum distance of 50 internal diameters is required, for settling and flow development (Cho and Tae, 2001). In this case, the maximum length this will ever be is 450 mm; as such, this distance is used for any changing inner diameters. At the inlet of the inlet sight glass, several circumferential thermocouple readings are taken; these are the test section refrigerant inlet thermocouple readings. As has been previously stated, the thermocouple readings are taken before and after the sightglasses, as they serve the important role of breaking up the axial conduction through the walls of the inner tube, which have a potentially large effect on the read temperature.

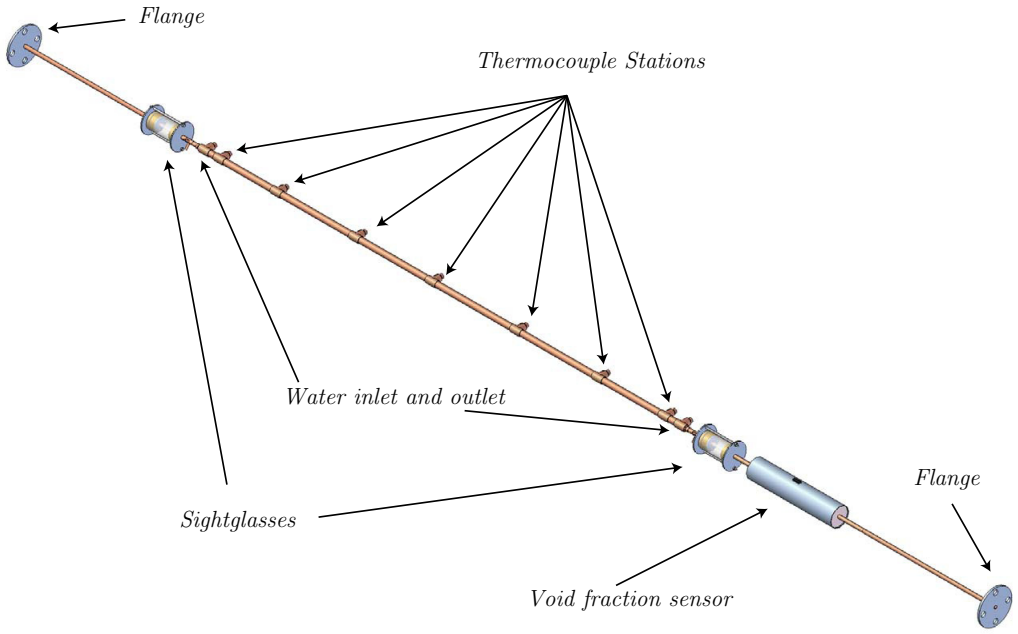

Figure 3.11: Test section model

The first sight glass is fitted with the Phlox backlight and the Basler camera for high-speed videography purposes.

The sight glass construction is shown in Figure 3.12. The main housing is made out of brass and consists of two identical parts that are machined. On the interior face, four holes are drilled and tapped, to keep the retaining plate secure. Also, a housing for the U-seal is machined out. The main reason that U-seals were utilized in this application is for their self-energizing capabilities; the higher the pressure in the refrigerant system, the more the seal will tend to expand and seal against the housing and the boron silicate inner tube. The material used in the seals is Teflon. These seals, however, are not compression seals; they need a thin layer of oil on which to press down. By soaking them in oil for 20 hours before installing the seals, the sightglasses could be proven leak-tight.

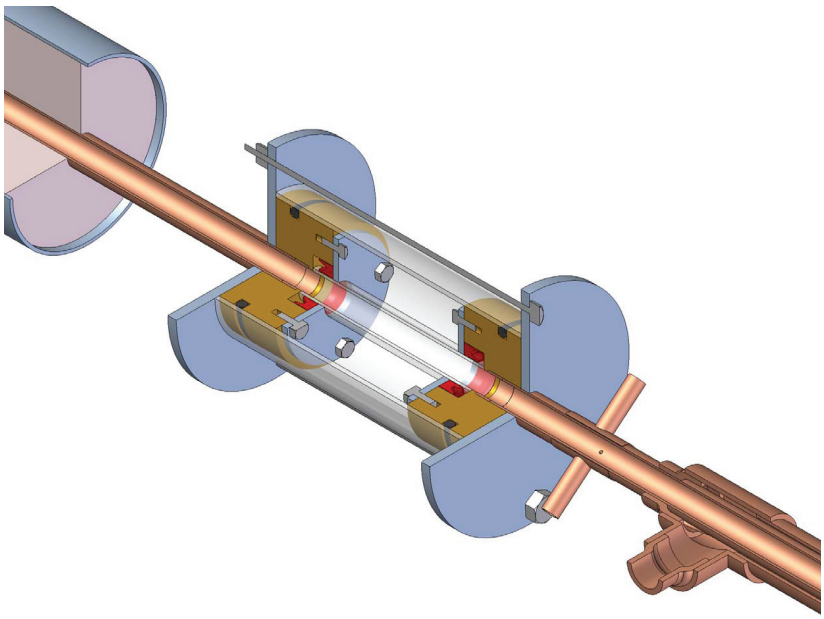

Figure 3.12: Cutaway view of the sight glass assembly

Both the inner refrigerant glass tube, as well as the safety tube around the housing are made out of boron-silicate, chosen for its good clarity and exceptional strength. The housings have grooves cut into the outside to fit the O-rings against the safety glass. Further, the housings have a hole machined out of

them, into which the tube coming and going from the rest of the system fit. The tube and housing are soldered together. Between the glass test tube and the incoming/outgoing tubes, there is a thin piece of housing to separate them, and to make sure that the two tubes do not press into each other, causing damage. The backing plates, connected by two bolts, hold the entire assembly together, under a slight amount of compression (such that there is no play among any of the components).

Between the sight glass and the test section, a distance of no more than 40 mm is left. Three circumferential pressure taps are made in this space. To ensure that the size of tap is not large, but to ease pressure transducer and capillary piping installation, a bush is installed over the outside of the tube and soldered at both ends. This bush has three fittings into which the capillary tubes slide. The tubes are also soldered into the fittings. The advantage of using this method is that, since you are applying heat and solder relatively far away from the small pressure tap hole, there is much reduced chance of plugging the hole. Also, it allows for the use of capillary tubes with much larger diameters, which help the responsiveness of the pressure signal, and can help make sure that the signal is not compromised by having liquid pockets in the line.

The heat exchanger itself, as previously stated, is a straight, horizontal tube-in-tube counterflow heat exchanger. The inner tube runs straight through, uninterrupted. A 2 mm copper wire is twisted onto the outside of the inner tube, at a pitch of about 300 mm. This acts both as a spacer between the inner and outer tubes of the annulus, and as a mixer, especially important to avoid temperature stratification when laminar flow is present in the annulus. The end connections between the annulus and inner tube are comprised of 15.88 mm ($5/8^{th}$ in) to 9.53 mm ($3/8^{th}$ in) reducers. At the ends, T-junctions are used to construct the inlet and outlet ports for the annulus. This construction is shown in Figure 3.13.

Rather than having an uninterrupted length of outer tube in the annulus, this length is split into several parts, in equidistant sections along the heat exchanger. At each junction, an extra T-junction is placed there. The main reason for these junctions is to allow for the thermocouple wire utilized in direct inner tube outer wall temperature measurements to be strung out into the DAQ. As such, seven extra 15.88 mm ($5/8^{th}$ in) to 9.53 mm ($3/8^{th}$ in) reducers are utilized, and the

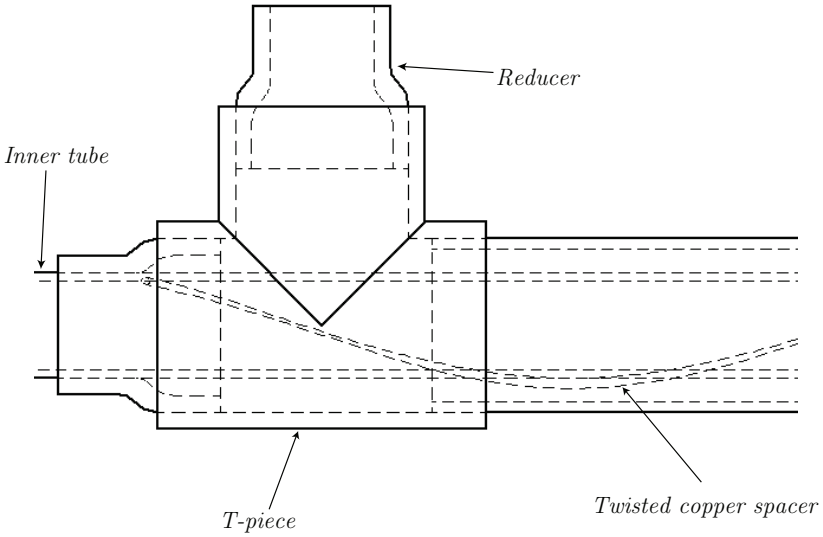

Figure 3.13: Inlet and outlet exchanger construction

remaining spaces between the exit and the wires are sealed using PTFE tape and put through a ferril connector, which is tightened until proven to be leak-tight.

The exit configuration of the heat exchanger is constructed in the same method as the inlet. Between the refrigerant exit and the sight glass, the same pressure tap bush construction as in the inlet is used. The sight glass exit then leads to the void fraction sensor. When doing void fraction testing, the pressure traces found at the exit of the test section heat exchanger are used. After the void fraction sensor, as was necessary at the inlet of the section, a minimum of 50 internal diameters are required, such that the effect of the ninety degree turn (after the flange) is not propagated into the void fraction sensor.

3.9 Conclusion

This chapter detailed the experimental setup; its design, layout, construction, the apparatus and instruments utilized and the software backbone of the control. It also covered, in broad strokes, the control methodology and instrumentation.

Furthermore, the experimental procedure is briefly discussed in this Chapter; this gives a brief overview of the methods that were utilized to fulfill the objectives

of this study. The in-depth discussion of the more pertinent procedural points (as set out in Section 1.3) is carried out in Chapter 5, and in Appendices A and B.

Chapter 4

Background Correlation Review

4.1 Introduction

From theory, mathematical models have been formulated for both the heat transfer and the pressure drop of refrigerants inside of horizontal tubes. However, since there is no available analytical solution, it is necessary to experiment, and find correlations that are of practical use in industry. In the following sections, heat transfer and pressure drop correlations for smooth tubes are shown.

4.2 Heat transfer correlations for smooth tubes

In this section, several correlations for condensation heat transfer in smooth tubes are discussed; namely those of Cavallini *et al.* (2006), Shah (1979) and Dobson and Chato (1998a).

4.2.1 Dobson and Chato (1998) correlation

The correlation of Dobson and Chato (1998a) is valid in the annular flow regime; the heat transfer coefficient is given as

$$h_{c,annular} = 0.023 \frac{k_l}{d_i} Re_l^{0.8} Pr_l^{0.4} \left\{1 + 2.22 X_{tt}^{-0.889}\right\} \tag{4.1}$$

where

$$Fr_{so} = \left\{ \begin{array}{l} 0.025 Re_l^{1.59} Ga^{-0.5} X_{tt}^{-1.5} (1 + 1.09 X_{tt}^{0.039})^{1.5} \; for: \; Re_l < 1250 \\ 1.26 Re_l^{1.04} Ga^{-0.5} X_{tt}^{-1.5} (1 + 1.09 X_{tt}^{0.039})^{1.5} \; for: \; Re_l > 1250 \end{array} \right\} \tag{4.2}$$

Ga, the Galileo number, is defined as

$$Ga = \frac{\rho_l (\rho_l - \rho_v) g D^3}{\mu_l^2} \tag{4.3}$$

and the Lockhart-Martinelli parameter, for turbulent-turbulent flow, is

$$X_{tt} = \left[\frac{1-x}{x} \right]^{0.9} \left(\frac{\rho_v}{\rho_l} \right)^{0.5} \left(\frac{\mu_l}{\mu_v} \right)^{0.1} \tag{4.4}$$

This equation is applicable when $Fr_{so} < 20$ and $G \geq 500 \, kg/m^2 s$, or when $Fr_{so} > 20$ and $G < 500 \, kg/m^2 s$. This correlation was tested with R-22, R-134a, and R-410a.

4.2.2 Shah (1979) correlation

The Shah (1979) correlation is also applicable in annular flow. It was tested using R-11, R-12, R-22, R-113, methanol, and ethanol. The heat transfer correlation is

$$h_c = \left[0.023 Re_l^{0.8} Pr_l^{\frac{1}{3}} \frac{k_l}{D_i} \right] \left[(1-x)^{0.8} + \frac{3.8 x^{0.76} (1-x)^{0.04}}{p_r^{0.38}} \right] \tag{4.5}$$

This correlation is valid in the following range only

$$0.001 \leq p_r \leq 0.44 \tag{4.6}$$
$$350 \leq Re_l \leq 10000 \tag{4.7}$$
$$10.8 < G < 16000\, kg/m^2 s \tag{4.8}$$
$$3 \leq \frac{G}{\rho_g} \leq 300\, m/s \tag{4.9}$$
$$Re_g > 35000 \tag{4.10}$$
$$Pr_l > 0.5 \tag{4.11}$$
$$7 \leq D_i \leq 40\, mm \tag{4.12}$$

4.2.3 Cavallini *et al.* (2006) correlation

The Cavallini *et al.* (2006) correlation is a flow-pattern-based method based on the dimensionless gas velocity J_v, much like that of Cavallini *et al.* (2002). In this correlation, rather than using a flow-pattern-based method, they defined the condensing flow as either ΔT dependent, or independent.

The dimensionless gas velocity J_v is

$$J_v = \frac{xG}{[gD\rho_v]} \tag{4.13}$$

The transition between the ΔT dependent and independent regimes occurs when the dimensionless gas velocity is

$$J_v^T = \left\{ \left[\frac{7.5}{4.3X_{tt}^{1.111} + 1} \right]^{-3} + C_T^{-3} \right\}^{-\frac{1}{3}} \tag{4.14}$$

where

$$C_T = 1.6 \text{ for hydrocarbons} \tag{4.15}$$
$$C_T = 2.6 \text{ for other refrigerants} \tag{4.16}$$

For ΔT independent flows ($J_v > J_v^T$),

$$h_A = h_{lo}\left[1 + 1.128x^{0.8170}\left(\frac{\rho_l}{\rho_v}\right)^{0.3685}\left(\frac{\mu_l}{\mu_v}\right)^{0.2363}\left(1-\frac{\mu_v}{\mu_l}\right)^{2.144} Pr^{-0.1}\right] \quad (4.17)$$

and for ΔT dependent flows ($J_v < J_v^T$),

$$h_D = \left[h_A\left(\frac{J_v^T}{J_V}\right)^{0.8} - h_{strat}\right]\left(\frac{J_v^T}{J_V}\right) + h_{strat} \quad (4.18)$$

where h_{lo} and h_{strat} are

$$h_{lo} = 0.023 Re_{lo}^{0.8} Pr_{lo}^{0.4}\left(\frac{k_l}{D}\right) \quad (4.19)$$

and

$$h_{strat} = \frac{0.725}{1 + 0.741\left[\frac{1-x}{x}\right]^{0.3321}}\left\{\frac{k_l^3\rho_l(\rho_l-\rho_v)gh_{lg}}{\mu_l D\Delta T}\right\}^{0.25} + (1-x^{0.087})h_{lo} \quad (4.20)$$

where h_{lg} is the isobaric latent heat of condensation.

This correlation was developed using a very wide database of refrigerants (from R-22 through R-718). It is valid for tubes with diameters between 3.1 mm and 17 mm, saturation temperatures of 23.1 up to 102^{o}C and a mass flow from 24 up to 2240 kg/m^{2}s.

4.3 Thome Flow map, flow-pattern-based heat transfer correlations

The objective of the development of the Thome *et al.* (2003) flow map, and heat transfer prediction method is to obtain a method with a minimum of empirical constants and exponents that not only gives a good statistical representation of the data, but also correctly captures the trends in the data.

4.3.1 Thome *et al.* (2003) correlation

The Thome *et al.* (2003) correlation utilizes the geometric model and flow map developed in El Hajal *et al.* (2003) to predict the heat transfer in the different physical flow regimes. The different equations for the transition lines, as well as the geometric parameters have been defined in Section 2.4.1. As a refresher, the El Hajal *et al.* (2003) utilizes the geometric models shown in Figure 4.1. The heat transfer coefficient is

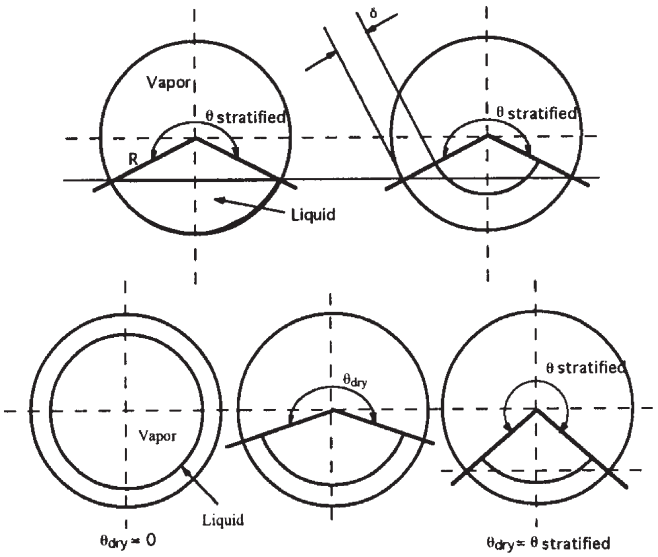

Figure 4.1: El Hajal *et al.* (2003) model for annular and stratified/stratified-wavy flow

$$h = \frac{h_f r\theta + (2\pi - \theta) r h_c}{2\pi r} \tag{4.21}$$

where r is the internal radius of the tube, and θ is the falling film angle around the top perimeter of the tube. For annular flow, it can be seen that $\theta = 0$, which

reduces the heat transfer coefficient to the heat transfer coefficient value calculated in the annular flow correlation.

The falling film angle is

$$\theta = \theta_{strat}\left[\frac{(G_{wavy} - G)}{G_{wavy} - G_{strat}}\right]^{0.5} \tag{4.22}$$

where G_{wavy} and G_{strat} are calculated with the equations in Section 2.4.1.

The film thickness for an annular film is calculated with

$$\delta = \frac{d(1-\epsilon)}{4} \tag{4.23}$$

For a stratified, or stratified-wavy flow, the film is a function of the film thickness. The equation then becomes,

$$\delta = \frac{d}{2} - \frac{1}{2}\left[d^2 - \left(\frac{8A_l}{2\pi - \theta}\right)\right]^{\frac{1}{2}} \tag{4.24}$$

The turbulent film heat transfer coefficient is found using

$$h_c = 0.003 Re_l^{0.74} Pr_l^{0.5} \frac{k_l}{\delta} f_i \tag{4.25}$$

The liquid film Reynolds number is

$$Re_l = \frac{4G(1-x)\delta}{(1-\epsilon)\mu_l} \tag{4.26}$$

and

$$f_i = \left\{ \begin{array}{r} 1 + \left(\frac{u_v}{u_l}\right)^{\frac{1}{2}} \left(\frac{(\rho_l - \rho_v)g\delta^2}{\sigma}\right)^{\frac{1}{4}} \quad \textit{for stratified-wavy, annular and intermittent} \\ 1 + \left(\frac{u_v}{u_l}\right)^{\frac{1}{2}} \left(\frac{(\rho_l - \rho_v)g\delta^2}{\sigma}\right)^{\frac{1}{4}} \left(\frac{G}{G_{strat}}\right) \quad \textit{for fully stratified} \end{array} \right\} \tag{4.27}$$

The falling film heat transfer correlation is,

$$h_f = 0.728 \left[\frac{\rho_l(\rho_l - \rho_v) g h_{lv} k_l^3}{\mu_l d(T_{sat} - T_w)} \right]^{\frac{1}{4}} \tag{4.28}$$

The Thome *et al.* (2003) correlation has been compared to test data for 15 fluids (R-11, R-12, R-22, R-32, R-113, R-125, R-134a, R-236ea, a R-32/R-125 near-azeotrope, R-404A, R-410A, propane, n-butane, iso-butane and propylene). The new model has been tested over the following range of conditions: mass velocities from 24 to 1022 kg/m^{2}s, vapor qualities from 0.03 to 0.97, reduced pressures from 0.02 to 0.80 and tube internal diameters from 3.1 to 21.4 mm.

4.3.2 Del Col *et al.* (2005) correlation

The Del Col *et al.* (2005) correlation extends the range of the Thome *et al.* (2003) heat transfer correlation to zeotropic mixtures. The local heat transfer coefficient for the mixture is obtained from

$$h = \frac{h_{f,m} r\theta + (2\pi - \theta) r h_{c,m}}{2\pi r} \tag{4.29}$$

Using the Bell and Ghaly (Liebenberg, 2002) approach to compensate for the mass transfer resistance in the zeotrope's liquid and vapor phases, the convective condensation heat transfer coefficient is obtained from

$$h_{c,m} = \left(\frac{1}{h_c} + R_c \right)^{-1} \tag{4.30}$$

where the appropriate Bell and Ghaly resistance is calculated from

$$R_c = x c_{p,v} \frac{\Delta T_{glide}}{\Delta h_m} \frac{1}{h_v^o} \tag{4.31}$$

which is a function of the vapor phase heat transfer coefficient referred to the vapor-liquid interface. Due to the interface between liquid and vapor,

$$h_v^o = h_v f_i \tag{4.32}$$

where the interfacial roughness factor can be calculated from Equation 4.27. The heat transfer coefficient in Equation 4.32 can be calculated from the Dittus and Boelter (Del Col *et al.*, 2005) equation,

$$h_v = 0.023 Re_v^{0.8} Pr_v^{\frac{1}{3}} \frac{k_v}{d} \tag{4.33}$$

where the Reynolds number is calculated using the vapor phase velocity and the tube diameter.

The Bell and Ghaly method can also be applied on the film heat transfer coefficient,

$$h_{f,m} = F_m \left(\frac{1}{h_f} + R_f \right)^{-1} \tag{4.34}$$

and the film resistance, R_f, is

$$R_f = x c_{p,v} \frac{\Delta T_{glide}}{\Delta h_m} \frac{1}{h_v} \tag{4.35}$$

and the non-equilibrium mixture factor, F_m, is

$$F_m = e^{-0.25(1-x)\left(\frac{G_{wavy}}{G}\right)^{\frac{1}{2}}\left(\frac{\Delta T_{glide}}{T_{sat}-T_w}\right)} \tag{4.36}$$

The mass transfer resistance depends on the temperature glide, which is why F_m decreases with increasing ΔT_{glide}. The effect of the saturation-to-wall temperature difference is the opposite to the one in the Nusselt theory.

This correlation was tested using Thome *et al.* (2003) and Cavallini *et al.* (2006)'s zeotropes, with the same vapor quality and mass flux limits.

4.4 Pressure drop correlations for smooth tubes

The correlation obtained for smooth tubes are: the Chisholm (Ould-Didi *et al.*, 2002), Grönnerud (Ould-Didi *et al.*, 2002), Friedel (Olivier, 2003), Müller-Steinhagen & Heck (Ould-Didi *et al.*, 2002) and Dukler et al. (ASHRAE, 2001).

4.4.1 Momentum pressure drop

The momentum pressure drop accounts for about 10% of the total pressure drop (Liebenberg, 2002), and from Section 2.8.1, it is given as

$$\Delta p_{mom} = G^2 \left\{ \left[\frac{(1-x)^2}{\rho_l(1-\epsilon)} + \frac{x^2}{\rho_v \epsilon} \right]_{out} - \left[\frac{(1-x)^2}{\rho_l(1-\epsilon)} + \frac{x^2}{\rho_v \epsilon} \right]_{in} \right\} \tag{4.37}$$

The frictional pressure drop correlations that follow are based on the separated flow model.

4.4.2 Friedel (1979) correlation

The Friedel correlation (Olivier, 2003) is valid for vapor qualities from $0 < x < 1$ and utilizes the two-phase multiplier as

$$\Delta p_f = \Delta p_l \phi_{lo}^2 \tag{4.38}$$

where Δp_l is calculated for the liquid phase as was done using the separated model,

$$\Delta p_l = 2 f_l \frac{G^2 (1-x)^2 L}{D_i \rho_l} \tag{4.39}$$

The liquid friction factor is obtained from the Blasius equation, as mentioned in Chapter 2, with the liquid Reynolds number

$$Re_l = \frac{G D_h}{\mu_l} \tag{4.40}$$

The two-phase multiplier is correlated as

$$\phi_{lo}^2 = E + \frac{3.24FH}{Fr_h^{0.045}\, We_l^{0.035}} \tag{4.41}$$

where Fr_h is the Froude rate given by

$$Fr_h = \frac{G^2}{gD_i\rho_h^2} \tag{4.42}$$

and the homogeneous density, ρ_h is

$$\rho_h = \left(\frac{x}{\rho_v} + \frac{1-x}{\rho_l}\right)^{-1} \tag{4.43}$$

The liquid Weber number is defined as

$$We_l = \frac{G^2 D_i}{\sigma\rho_h} \tag{4.44}$$

The rest of the variables, as defined in Equation 4.41 are

$$E = (1-x)^2 + x^2\frac{\rho_l f_{vo}}{\rho_v f_{lo}} \tag{4.45}$$

$$F = x^{0.78}(1-x)^{0.224} \tag{4.46}$$

$$H = \left(\frac{\rho_l}{\rho_v}\right)^{0.91}\left(\frac{\mu_v}{\mu_l}\right)^{0.19}\left(1-\frac{\mu_v}{\mu_l}\right)^{0.7} \tag{4.47}$$

In the above, the friction factors above are for liquid-only and vapor-only flows. The use of Friedel's correlation has been, historically, recommended only for flows where the ratio of (μ_l/μ_g) is less than 1000. It has also been recently tested and compared against other leading correlations in Ould-Didi *et al.* (2002), with R-134a, R-123, R-402A, R-404A, R-502. The mass flux covered the range between 150 and 800 kg/m^{2}s and was tested with a vapor quality between 0.04 and 1.

4.4.3 Chisholm (1973) correlation

The correlation proposes a detailed empirical method for a wide range of operating conditions. It is applicable for vapor qualities from $0 < x < 1$. The two-phase frictional pressure gradient is given by (Ould-Didi *et al.*, 2002) as

$$\left(\frac{dp}{dz}\right)_f = \left(\frac{dp}{dz}\right)_{lo} \phi_{lo}^2 \tag{4.48}$$

The single-phase frictional pressure gradients are taken from the standard expressions for the liquid and vapor phases,

$$\left(\frac{dp}{dz}\right)_{lo} = f_l \frac{2G^2}{D_i \rho_l} \tag{4.49}$$

$$\left(\frac{dp}{dz}\right)_{vo} = f_v \frac{2G^2}{D_i \rho_v} \tag{4.50}$$

The parameter Y defines the ratio of the single-phase frictional pressure gradient,

$$Y^2 = \frac{\left(\frac{dp}{dz}\right)_{vo}}{\left(\frac{dp}{dz}\right)_{lo}} \tag{4.51}$$

Then, the two-phase multiplier can be found to be

$$\phi_{lo}^2 = 1 + (Y^2 - 1)\left[Bx^{\frac{2-n}{2}}(1-x)^{\frac{2-n}{2}} + x^{(2-n)}\right] \tag{4.52}$$

where n is the exponent from the Blasius friction factor expression, *i.e.* $n = 0.25$.

If $0 < Y < 9.5$

$$B = \frac{55}{G^{0.5}} \quad for\ G \geq 1900\ kg/m^2s \tag{4.53}$$

$$B = \frac{2400}{G} \quad for\ 500 < G < 1900\ kg/m^2s \tag{4.54}$$

$$B = 4.8 \quad for\ G < 500\ kg/m^2s \tag{4.55}$$

If $9.5 < Y < 28$

$$B = \frac{520}{YG^{0.5}} \quad for\ G < 601\ kg/m^2s \tag{4.56}$$

$$B = \frac{21}{Y} \quad for\ G > 600\ kg/m^2s \tag{4.57}$$

And, if $Y > 28$

$$B = \frac{15000}{Y^2 G^{0.5}} \tag{4.58}$$

This correlation was originally tested using tubes with diameters between 10.92 *mm* and 12 *mm* and Ould-Didi *et al.* (2002) recently reappraised its range of operation using the same refrigerants, vapor quality and mass flux ranges as in the preceding section.

4.4.4 Müller-Steinhagen and Heck (1986) correlation

The two-phase frictional pressure gradient correlation is (Ould-Didi *et al.*, 2002)

$$\left(\frac{dp}{dz}\right)_f = G(1-x)^{\frac{1}{3}} + bx^3 \tag{4.59}$$

In the above equation, G is not the mass flux; rather, it is a factor, $G = a + 2(b-a)x$. a and b are the frictional pressure gradients for the liquid and vapor only pressure gradients, *i.e.* Equations 4.49.

This model is essentially an empirical two-phase extrapolation between liquid-only and vapor-only flow, and is applicable for $0 < x < 1$.

Ould-Didi *et al.* (2002) showed, using two horizontal test sections and five different refrigerants that the best available method for annular flow was that of Müller-Steinhagen and Heck. Ould-Didi *et al.* (2002) also showed that, for their experimental data, the correlation of Müller-Steinhagen and Heck had an average deviation of about 38%.

4.4.5 Grönnerud (1972) correlation

This method was developed specifically for refrigerants, and is as follows (Ould-Didi *et al.*, 2002)

$$\Delta p_f = \phi_{gd} \Delta p_l \tag{4.60}$$

The vapor phase multiplier is

$$\phi_{gd=} = 1 + \left(\frac{dp}{dz}\right)_{Fr} \left[\frac{\left(\frac{\rho_l}{\rho_v}\right)}{\left(\frac{\mu_l}{\mu_v}\right)^{\frac{1}{4}}} - 1 \right] \tag{4.61}$$

where

$$\Delta p_l = 4 f_L \frac{LG^2(1-x)^2}{2 d_i \rho_l} \tag{4.62}$$

which is the equation derived in the separated flow model of Chapter 2. His two-phase multiplier is a function of

$$\left(\frac{dp}{dz}\right)_{Fr} = f_{Fr}[x + 4(x^{1.8} - x^{10} f_{Fr}^{0.5})] \tag{4.63}$$

If the liquid Froude number, Fr_l is greater than, or equal to 1, then the friction factor f_{Fr} is set to 1; otherwise, if it less than 1,

$$f_{Fr} = Fr_L^{0.3} + 0.0055 \left(\ln \frac{1}{Fr_l}\right)^2 \tag{4.64}$$

The correlation of Grönnerud is applicable to flow qualities from $0 < x < 1$. It was shown to be the best performing correlation for stratified and stratified-wavy flow. The Grönnerud correlation was tested in the same range of operations as the Müller-Steinhagen and Heck correlation (Ould-Didi *et al.*, 2002).

4.4.6 Dukler (1964) correlation

The Dukler correlation (ASHRAE, 2001) defines the frictional pressure gradient as

$$\left(\frac{dp}{dz}\right)_f = \frac{2G^2 f_o G\alpha(\lambda)\beta}{D_i \rho_{NS}} \tag{4.65}$$

where f_o is the single-phase friction coefficient evaluated at the two-phase Reynolds number, and is

$$f_o = 0.0014 + 0.125\left(\frac{GD_i\beta}{\mu_{NS}}\right)^{-0.32} \tag{4.66}$$

and the factors are

$$\lambda = \left(1 + \frac{x}{1-x}\frac{\rho_v}{\rho_l}\right)^{-1} \tag{4.67}$$

$$\mu_{NS} = \mu_l\lambda + \mu_v(1-\lambda) \tag{4.68}$$

$$\rho_{NS} = \rho_l\lambda + \rho_v(1-\lambda) \tag{4.69}$$

$$\beta = \left(\frac{\rho_l}{\rho_{NS}}\right)\frac{\lambda^2}{1-\epsilon} + \frac{\rho_v}{\rho_{NS}}\frac{(1-\epsilon)^2}{\epsilon} \tag{4.70}$$

$$\alpha(\lambda) = 1 - \frac{\ln\lambda}{1.281 + 0.478\ln\lambda + 0.444(\ln\lambda)^2 + 0.094(\ln\lambda)^3 + 0.00843(\ln\lambda)^4} \tag{4.71}$$

4.5 Conclusion

Although a large amount of correlations were shown in this Chapter, the above is a brief survey of the breadth of research in condensation heat transfer. It is interesting to note that, regardless of the amount of independent research and effort, no single set of correlations (*i.e.* one for heat transfer, another for the void fraction and one for pressure drop) can be shown to be the absolute best; where some are easy to use, but relatively inaccurate, or uncertain, others are quite accurate, but are too complex to implement, and require a certain amount of effort to compute. This should serve to underline the importance of finding a single unifying theory for both heat transfer and pressure drop.

Chapter 5

Experimental Results

5.1 Introduction

In this section, the gathered experimental data are discussed. Section 3.7 presented a broad overview of both data gathered/required as well as the main purposes of its recollection. This chapter treats, first of all, a summary of the Wilson plot results, detailed in Appendix A. Then, the intermittent flow regime heat transfer coefficient is calculated, with the aid of the time fraction map, which is also generated in this section. A new correlation is developed and is compared to other leading correlations. The most important uncertainty analysis results are presented, including the effect of including the momentum pressure drop's uncertainty into the frictional pressure drop's uncertainty analysis. The uncertainty in void fraction (*viz.* the logarithmic-mean void fraction model) is calculated. These results are developed from the discussion of Appendix B.

5.2 Salient Wilson plot results

The inner tube of the test section heat exchanger has refrigerant flowing through it, and water flowing through the annulus. However, while it is certain that the minimum Reynolds number in the inner tube does not drop out of the turbulent regime (in the case of mass fluxes greater than 25 kg/m^{2}s), the same cannot be said about the annulus. In fact, the maximum amount of flow deliverable in the

annulus gives a maximum Reynolds number of roughly 1800. As such, it remains strictly in the laminar flow regime. For the above reason, a modified Wilson plot technique that utilizes a turbulent correlation for the inner tube and a laminar correlation was derived in Appendix A. While the majority of the results are shown in said Appendix, the final form of the correlation for the annulus heat transfer coefficient, and the tube-side heat transfer coefficient, along with the final values of the different coefficients of determination (which are used for the uncertainty) are presented in this section.

5.2.1 Laminar-turbulent analysis results

While both laminar-turbulent and turbulent-turbulent analyses were carried out, in which the annulus-side form of the heat transfer correlation was changed, only the laminar-turbulent data are presented in this section. The detailed analysis is presented in Appendix A. Utilizing data captured in 179 runs, the inner-tube heat transfer coefficient's leading constant multiplier was regressed utilizing the Wilson plot technique, and was calculated as $C_t = 0.204$. The coefficient of determination, a measure of adequacy in the curve fit was calculated as $R^2 = 0.967$. The inner-tube Wilson plot is shown in Figure 5.1.

Then, the laminar-turbulent annulus-side experimental curve fit is shown in Figure 5.2. The coefficient of determination was calculated as $R^2 = 0.88419$. In this case, it can be seen that the data are not as well described as in the tube.

The final form of the annulus-side heat transfer correlation is

$$h_{c,s} = 5.7036(x^\star)^{-0.4258}\left(\frac{\mu_w}{\mu}\right)^{-0.14} \tag{5.1}$$

There are several reasons that can explain the phenomena present in the data. It is most easily explained using the different heat transfer resistances encountered during condensation in a tube-in-tube heat exchanger, namely the inner heat transfer coefficient resistance, the wall conduction resistance and the annulus heat transfer coefficient resistance. Due to the material selection (copper), the wall conduction resistance is, out of the three resistances, negligible. Further, fouling was disregarded as negligible on either side of the tube. In a well designed Wilson plot experiment, the resistance of the auxiliary side (whether it is the tube-side or

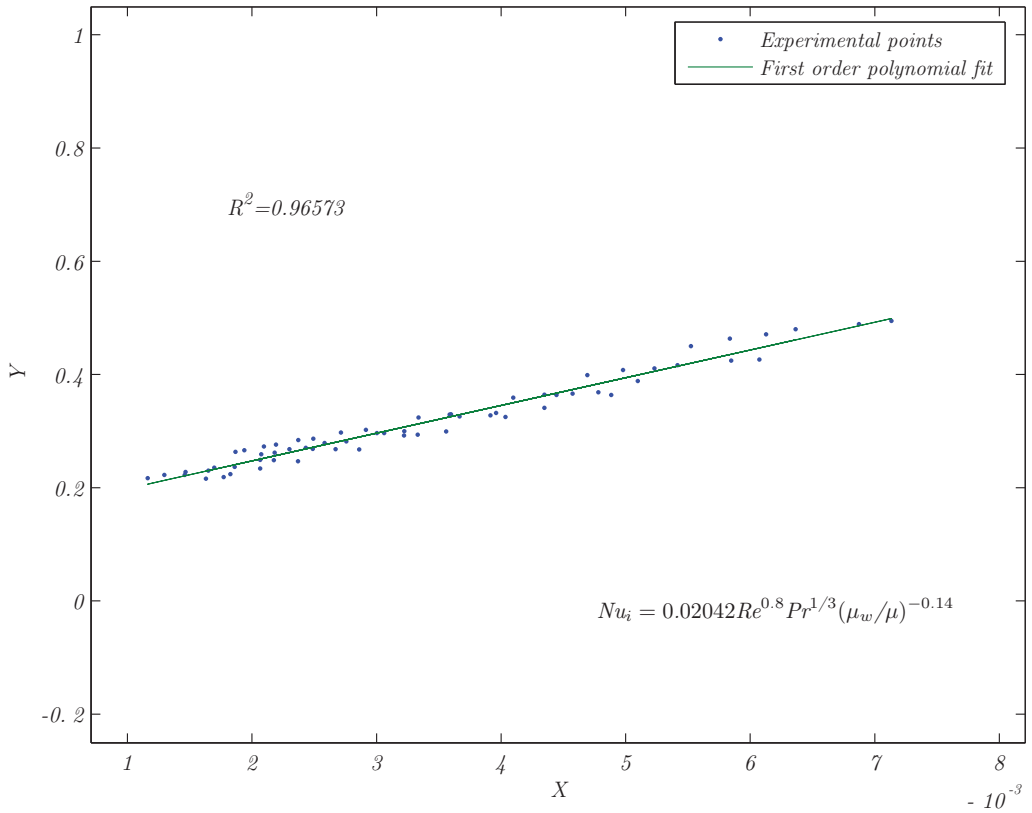

Figure 5.1: Laminar-turbulent tube-side Wilson plot

annulus depends on the goal of the experiment) should ideally be less than 10% of the main resistance. In the case of a tube-in-tube heat exchanger, if the inner tube resistance is the main resistance, the Reynolds number of the annulus side should be considerably larger than the inner tube. In this experiment however, not only was this not the case, but the annulus Reynolds number was generally the lower one, and in cases, an order of magnitude smaller. Although undesirable, it was unavoidable, due to the refrigerant testing conditions which were being emulated.

Second, the problem was exascerbated at several test points in which there were large differences in Reynolds numbers (inner tube - 10 000, annulus - 500). Due to the fact that the lower mass fluxes were on the limit of accuracy of the flow meter, there was significant variation in the steady-state value saved. This affected

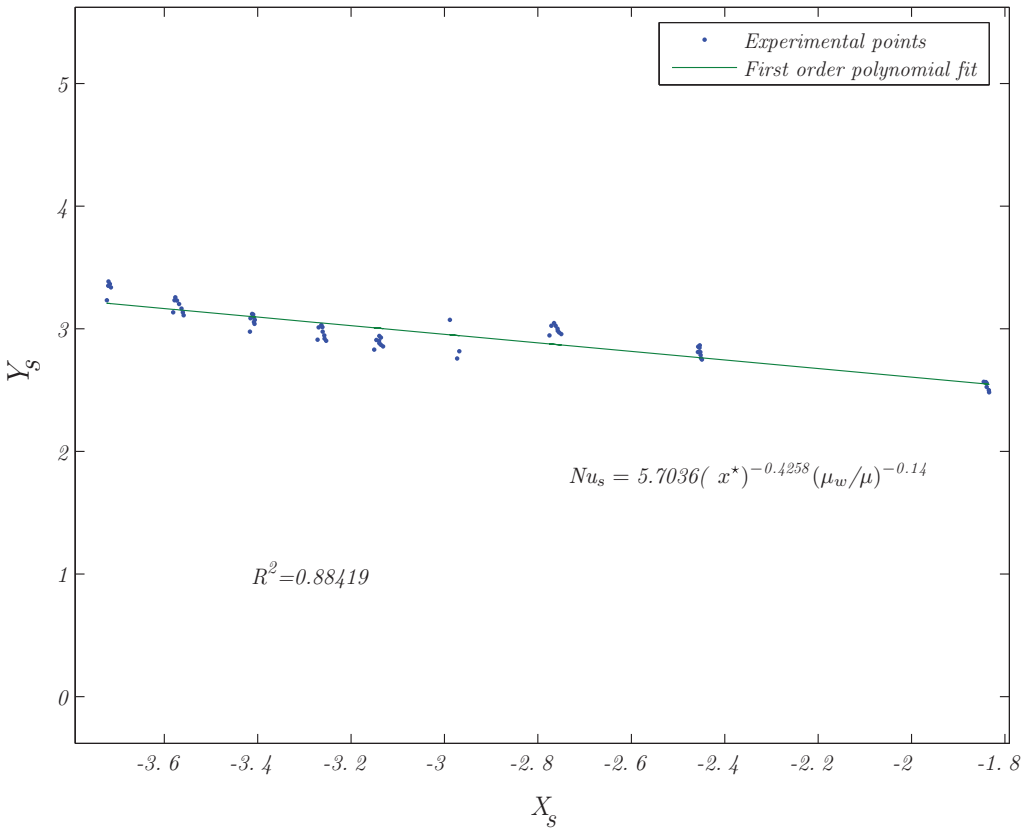

Figure 5.2: Laminar-turbulent annulus-side Wilson plot

the heat transfer quantity calculated for the annulus. Further, the large difference in mass flow led to temperature differences to be very small in the inner-tube, which led to a high fluctuation (and uncertainty) of the temperature drop in the inner-tube, and also resulted in heat transfer variations. The combination and comparison of these two quantities in the energy balance calculation resulted in EBs of up to 5%.

The effect of the fluctuating energy balances can be seen in the comparison of the experimentally measured inner-tube Nusselt number with that of the correlation developed with the Wilson Plot method. This is represented in Figure 5.3.

While it is evident that the majority of the data points lie within acceptable

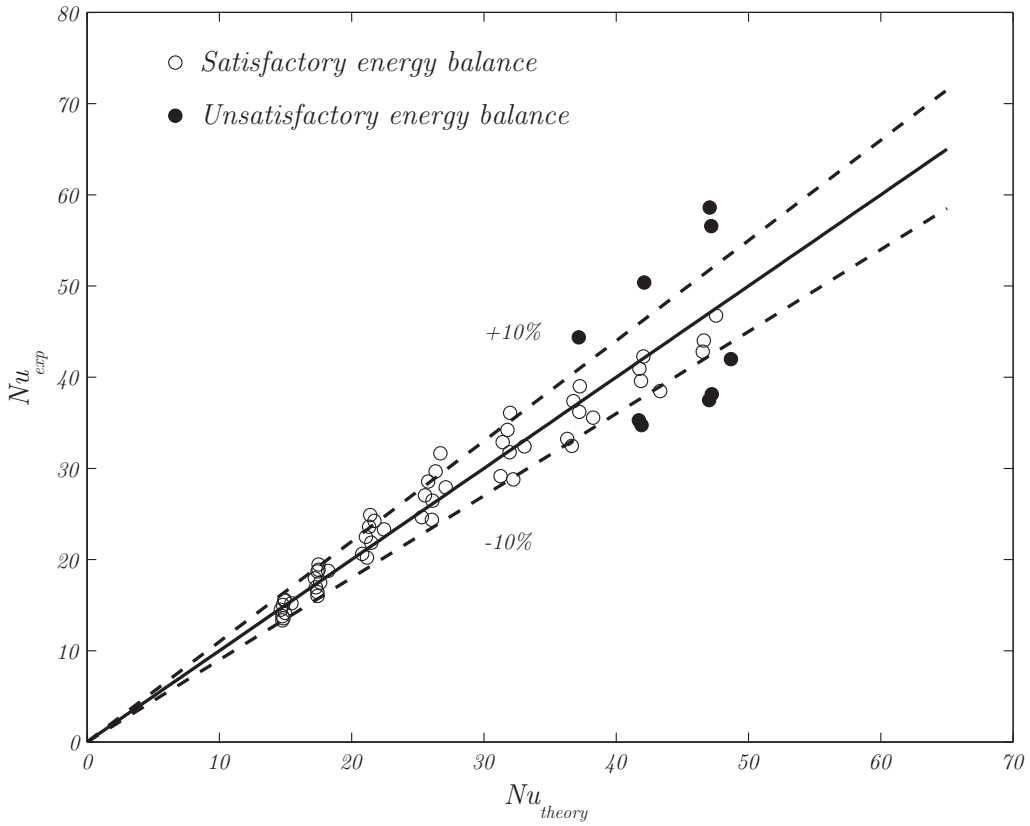

Figure 5.3: Comparison of the laminar-turbulent inner-tube heat transfer coefficient and experimental data

bounds (*i.e.* ±%10), there are several data points, shown in the figure as shaded points, which do not. These represent data which did not achieve satisfactory energy balances. Apart from these points, the close relation between the predicted heat transfer coefficients and the experimental data show that the Wilson Plot method can generate adequate results. This is, of course, dependent on utilizing the test section in an adequate range.

While it was shown that the inner-tube heat transfer coefficient could be approximated with a reasonable degree of accuracy, several data points were captured in areas where the energy balance was over 1%, due to the sensitivity over the mass fluxes and temperature drops.

Finally, the major problem in this specific Wilson plot experiment is that

outstanding accuracy will never be possible, due to the very specific range of Reynolds numbers required, which in turn lead to non-negligible heat transfer resistances in the annulus. As there is no way to circumvent this issue, the best recommendation that can be made is to forgo any further Wilson Plot experimentation (for this test apparatus) and to rather focus all time and effort into direct wall temperature measurements.

A more detailed discussion of these results, including different analysis methods, and a brief history of this particular Wilson Plot method are detailed in Appendix A.

5.3 Refrigerant experimental test matrix

Utilizing the smooth test-section as described in Chapter 3, and R-22 as the test refrigerant, tests were performed as described, also in Chapter 3. A total of 101 data points were captured, ranging in mass flux from 250 kg/m^{2}s up to 650 kg/m^{2}s, and with a vapor quality varying between 0.05% and 0.65%. Figure 5.3 shows all of the test points overlaid on the Thome flow map (El Hajal *et al.*, 2003). When developing the test matrix, it was required that some data points fall into what Thome defines as the Stratified-wavy regime and the Annular flow regime, such that the time-fractional analysis could be performed including flow regime transitions.

Each data point is actually the mean of 1000 samples taken over a continuous period of time, which usually took between 10 to 11 minutes, depending on the speed of the program and its update speed. Furthermore, to ensure that the refrigerant had the same properties at each point, each data point was only saved when the criteria in Table 5.1 were met.

Table 5.1: Experimental testing criteria

Measurand	
T_{sat}	40^{o}C
EB	<1%
$\dot{m}_{ref}$	±5 kg/m^{2}s max

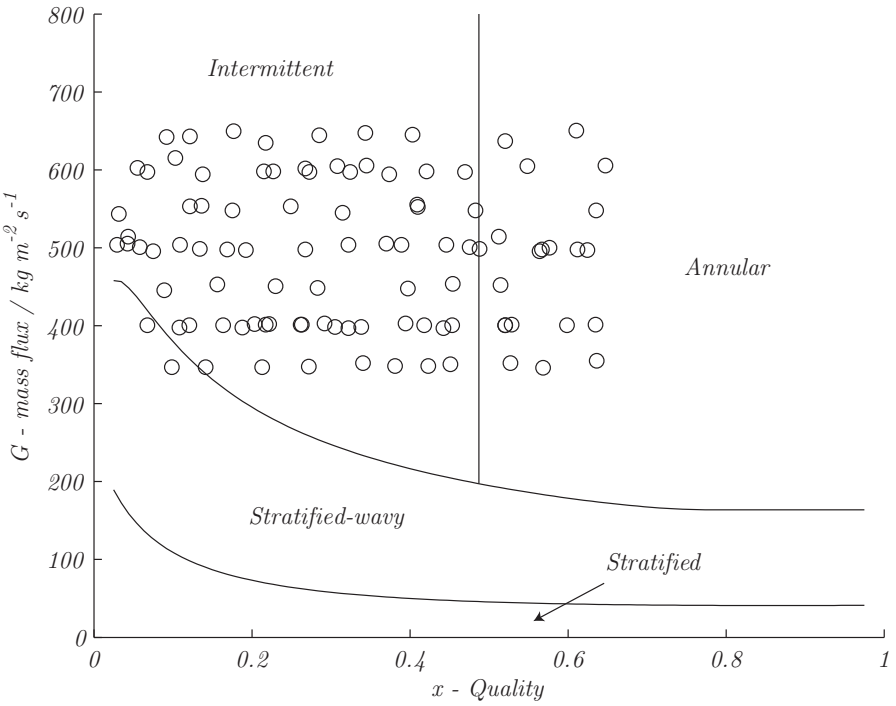

Figure 5.4: Experimental test matrix overlaid on the Thome flow map (El Hajal *et al.*, 2003) for R-22 condensing in an 8.38 mm ID smooth tube, at a nominal saturation temperature of 40^{o}C

From the analysis of the information of each data point pertaining to the saturation temperature, the mean energy balance and the mass flow, the overall average of these data are shown in Table 5.2.

Table 5.2: Mean testing point information

Measurand	Mean	Standard deviation
T_{sat}	39.7^{o}C	$\pm$1.9^{o}C
P_{sat}	1449 kPa	$\pm$65 kPa
EB	0.65%	$\pm$0.26%
$\dot{m}_{ref}$	Test dependent	max: 2 kg/m^{2}s

It is evident that the test equipment is very reliable, from a repeatability point of view, in the sense that it is easy to control the refrigerant conditions such that the required test criteria be met. Particularly effective were the Carel electronic expansion valves, in terms of their precise mass flow control. It was possible to very accurately set the mass flow through the test section, and to test at the desired mass flow, rather than, *'as close as possible'*. Table 5.3 lists the required mass fluxes, the mean testing mass fluxes and their standard deviations.

Table 5.3: Mean testing point information

Required G (kg/m^{2}s)	Mean obtained G (kg/m^{2}s)	Standard deviation (kg/m^{2}s)
250	250.83	±1.36
300	299.98	±0.99
350	349.28	±1.97
400	400.23	±1.86
450	450.05	±1.51
500	499.53	±1.68
550	550.23	±1.71
600	600.43	±1.98
650	648.10	±1.18

5.4 Time fraction map

Continuing the discussion begun in Chapter 2, we can clearly distinguish that in a single flow regime, the two separate heat transfer modes, that is, shear-stress and gravity-dominated heat transfer modes, will have an effect. So the main question now is: if analysis is carried out to find out what the probability is that at a certain vapor quality and mass flux one or the other heat transfer mode will dominate, can a more accurate method of predicting heat transfer be developed?

However we define the dominating heat transfer mode, the flow regime and its characteristics do not change; that is, although we are classifying sections of Intermittent flow as either shear-stress or gravity dominated, this does not

change the fact that slugs and plugs do, in fact, occur; the analysis is only an instantaneous evaluation of the flow regime.

The main methodology proposed is to separate the flow into two main heat transfer modes, *i.e.* gravity and shear-stress based modes. Thus, with the time fraction (probability) analysis, if we find that 40% of the images analyzed show that the heat transfer is dominated by the gravity-dominated model at a certain vapor quality and mass flux, then the rest of the images show that at that specified vapor quality and mass flux the dominant heat transfer mode is shear-stress dominated. We can then construct a probability map showing the probability that a specific heat transfer mode will occur (ranging from 0 to 1, that is, 0 to 100%) at discrete points of vapor quality and mass flux.

The methodology used to distinguish between the heat transfer modes objectively is separated into the time-frequency response analysis of the void fraction, pressure sensor data, and the light intensity through the tube. Further detail of the analysis is discussed in Section 5.4.1.

5.4.1 Development of a time fraction map for the Intermittent flow regime

The time fraction map for the intermittent flow regime varies as a function of mass flux and quality between two absolute values, 0 and 1, which describe fully gravity-dominated and shear stress-dominated flows respectively. In this work, the time fraction number, tf, has been defined for this purpose.

The objective method of data analysis required for this data was developed in parallel by Van Rooyen (2007), in which the high-speed videography data captured during testing was used in conjunction with measured dynamic void fraction (from the capacitive sensor) and pressure transducer data were used to obtain discrete measurements of this time fraction over a range of mass flux and vapor quality. The time fraction data, as developed by Van Rooyen (2007), is presented in Table 5.4.

The above presents the time fraction tf as was analyzed and calculated in Van Rooyen's work. As it is a large amount of information, and is quite difficult

Table 5.4: tf data, as found by Van Rooyen (2007)

G	x	tf	G	x	tf	G	x	tf
247.43	0.38	0.78	645.45	0.42	0.85	504.13	0.14	0.35
249.46	0.42	0.80	647.48	0.36	0.72	505.21	0.41	0.85
250.72	0.31	0.42	649.58	0.20	0.62	514.58	0.54	1.00
650.04	0.63	1.00	396.91	0.50	1.00	543.42	0.05	0.54
250.95	0.49	0.87	397.48	0.16	0.32	250.80	0.11	0.56
252.37	0.10	0.42	250.42	0.20	0.36	544.65	0.33	0.73
251.16	0.25	0.44	398.51	0.39	0.70	548.20	0.65	1.00
252.89	0.08	0.48	400.54	0.65	1.00	549.61	0.42	0.90
253.02	0.35	0.45	401.23	0.32	0.65	548.31	0.50	1.00
298.69	0.69	1.00	400.56	0.57	1.00	548.16	0.19	0.65
299.66	0.51	1.00	400.91	0.69	1.00	552.15	0.42	0.92
299.57	0.56	1.00	401.89	0.25	0.56	553.32	0.14	0.61
300.43	0.29	0.41	403.11	0.45	0.86	553.32	0.14	0.61
249.56	0.56	0.97	403.84	0.25	0.56	552.97	0.27	0.64
300.81	0.34	0.46	400.84	0.11	0.46	555.86	0.42	0.91
300.11	0.64	1.00	445.45	0.11	0.34	251.71	0.12	0.20
298.14	0.70	1.00	250.42	0.39	0.78	594.19	0.39	0.79
301.38	0.45	0.83	447.64	0.42	0.81	598.06	0.23	0.65
303.00	0.20	0.40	449.10	0.17	0.39	596.99	0.48	1.00
305.25	0.41	0.75	448.54	0.31	0.65	597.16	0.09	0.46
316.71	0.37	0.71	453.02	0.18	0.30	598.46	0.44	0.94
346.39	0.25	0.39	450.80	0.25	0.50	597.36	0.34	0.68
345.76	0.61	1.00	453.87	0.47	0.93	616.15	0.66	1.00
346.85	0.13	0.29	452.03	0.53	1.00	601.71	0.28	0.68
250.69	0.15	0.30	495.67	0.59	1.00	602.42	0.08	0.46
346.66	0.17	0.29	497.38	0.23	0.52	605.18	0.56	1.00
347.86	0.31	0.61	497.88	0.31	0.60	251.16	0.27	0.44
348.42	0.42	0.81	250.54	0.64	1.00	605.45	0.66	1.00
348.52	0.46	0.89	498.62	0.17	0.46	615.59	0.12	0.49
350.30	0.49	0.92	497.87	0.20	0.52	634.61	0.24	0.64
351.64	0.56	1.00	500.83	0.51	1.00	636.94	0.53	1.00
351.97	0.38	0.74	504.14	0.02	0.35	642.60	0.11	0.48
355.28	0.68	1.00	504.13	0.36	0.64	642.75	0.14	0.56

to visualize in its current state, Figure 5.5 and Figure 5.6 show the time fraction map overlaid on the Thome Flow regime map.

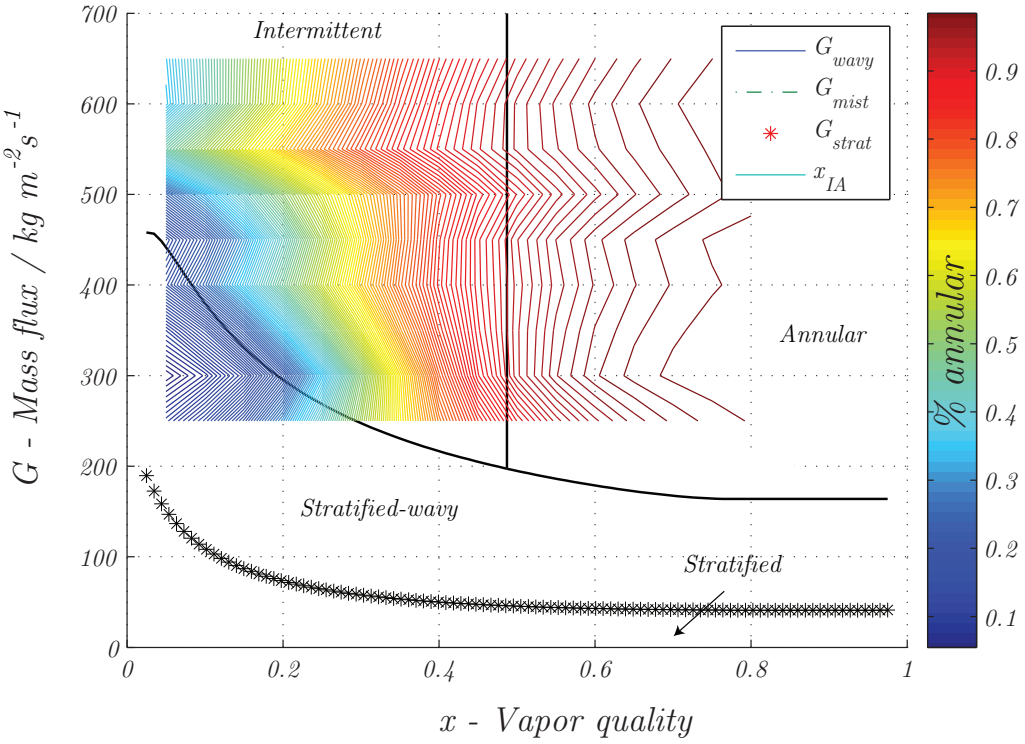

Figure 5.5: Time fraction map overlaid on the Thome Flow Map (Thome *et al.*, 2003) for R-22 condensing in an 8.38 mm ID smooth tube, at a nominal saturation temperature of 40°C

The data presented in Table 5.4 was fitted to a curve using the Generalized Linear Model's binomial fitting parameter; this is explained in detail in Van Rooyen (2007).

The above results, evidently, are only valid if one is using the tested refrigerant (in this case, R-22). These results are of limited use if independent time-fraction maps are generated for each refrigerant in use. As such, it is of considerable importance to find a way of relating the discrete time fraction measurements to the physical properties of the fluid in question. This is both done to minimize the arbitrariness of the time fraction map, and to present one single unifying method for all refrigerants in all flow regimes. Due to time limitations, it was

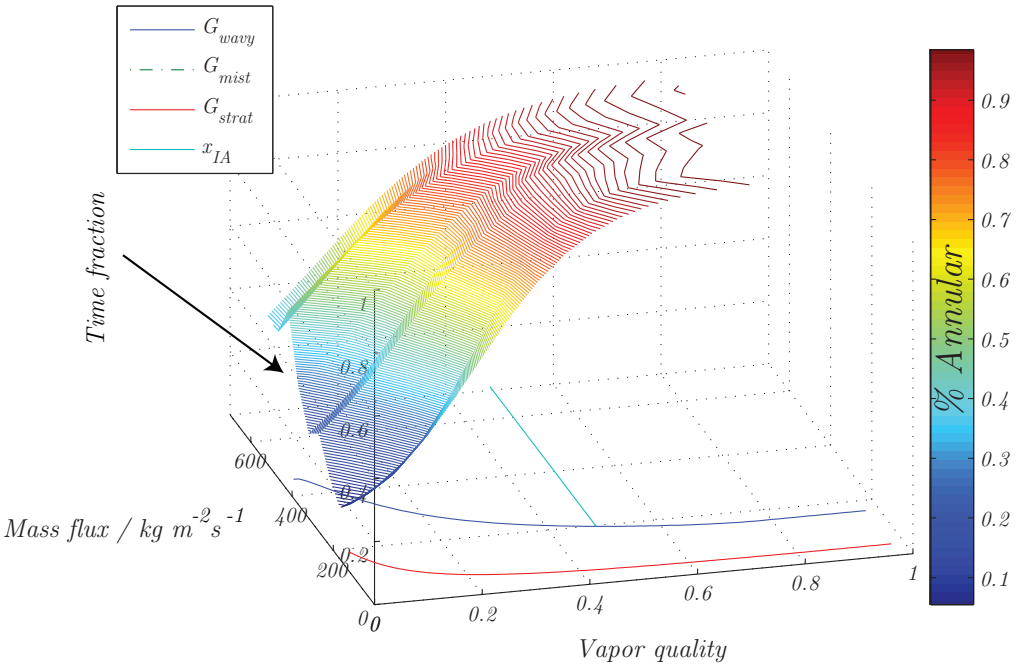

Figure 5.6: 3D Time fraction map overlaid on the Thome Flow Map (Thome *et al.*, 2003) for R-22 condensing in an 8.38 mm ID smooth tube, at a nominal saturation temperature of 40^{o}C

only possible to perform tests with one refrigerant; the above is the next clear step in the progression of this work.

5.5 Heat transfer coefficient calculation

Section 3.7 described the basic overview of the methodology that is followed to create a new intermittent flow heat transfer correlation. In this section, this is much expanded, results are presented and comparison against other heat transfer correlations is made.

5.5.1 Experimental heat transfer calculation methods

Due to the results obtained in the previous section, it was decided that the only viable alternative to obtaining accurate heat transfer coefficient measurements

would be to take direct wall temperature measurements, and combine it with the heat transfer measured in the test-section to gather experimental heat transfer coefficient data.

As was detailed in Chapter 3, it is not possible to measure the heat transfer through the test section on the refrigerant side, as both inlet and outlet have vapor qualities. As such, it is not possible to measure the enthalpy of the refrigerant at that state using just the pressure and temperature; however, it is possible to measure the refrigerant heat transfer through the pre-,test- and post-condensers, and through the individual heat exchanger water sides. As such, if the energy balance is less than 1%, and coupled to the fact that in water-to-water tests, the energy balance was also under 1% in the test section, it is possible to assume that the heat transfer through the water side of the test section (*i.e.* the annulus), is equal to that in the refrigerant.

Thus, we can combine the water-side heat transfer information, together with the refrigerant mass flow, inlet and outlet temperatures, as well as the annulus-outer wall temperatures to calculate the inner heat transfer coefficient.

Let us consider Newton's Law of Cooling, that is,

$$\dot{Q}_c = \bar{h_c} A_l \left(\bar{T_w} - \bar{T_b} \right) \tag{5.2}$$

The convective heat transfer coefficient can be calculated by re-arranging this equation. To begin, it is necessesary to approximate the inner wall temperatures at each measuring station, such that the proper temperature difference may be calculated. This can be done by

$$T^j_{w,i} = T^j_{w,o} + \left| \dot{Q}_{h_2O} \cdot R_w \right| \tag{5.3}$$

where $\dot{Q}_{h_2O}$ is the water-side heat transfer, R_w is the wall transfer resistance, and $T^j_{w,o}$ is the measured outer temperature of the inner wall, at each j^{th} measuring station.

It should be noted that semi-local heat transfer coefficients are measured, rather than truly local measurements. This is to say that a single average heat transfer is calculated over the heat exchanger, rather than seven, the number of

wall temperature stations (where each station is an average of four thermocouples). Although this decreases the accuracy somewhat, by maintaining the amount of heat transferred out of the exchanger low, and thus ensuring a small difference in vapor quality between inlet and outlet, the error introduced is minimized. The wall temperature average is found by using the physical distance between station and the Trapezium numerical integration method, ensuring that any non-linearity in temperature distribution over the length of the tube wall can be reflected in a more representative average. This is

$$\bar{T_{w,o}} = \frac{1}{L}\sum_{j=1}^{6}\left[\left(T_{w,o}^{j} + T_{w,o}^{j+1}\right)\left(x_{j+1} - x_j\right)\right] \tag{5.4}$$

Utilizing this averaging method when the temperature drop is linear results in the same average as a normal mean of all the temperature readings.

Due to the fact that the refrigerant flow is condensing, it is expected that the temperature should not drop. However, a very slight temperature drop is experienced over the test section's inlet and outlet thermocouple readings, due to the pressure drop (which then affects the saturation pressure, and thus, temperature). However, this change in temperature is very slight, usually less than 0.1^{o}C, which allows us to assume that the temperature drop is linear, and take the linear mean between the inlet and outlet values. Finally, the heat transfer on the water side, calculated for energy balance issues, is utilized, along with the inside heat transfer area. Then, the semi-local experimental heat transfer coefficient is

$$h_{c,exp} = \left|\frac{\dot{Q}_{H_2O}}{A_L(\bar{T}_{w,i} - \bar{T}_{b,m})}\right| \tag{5.5}$$

5.5.2 Experimental heat transfer results

At each point in the experimental test matrix, a heat transfer coefficient was measured. To present the data in a succint manner, Figure 5.7 shows the heat transfer coefficients measured at each test point in the test matrix.

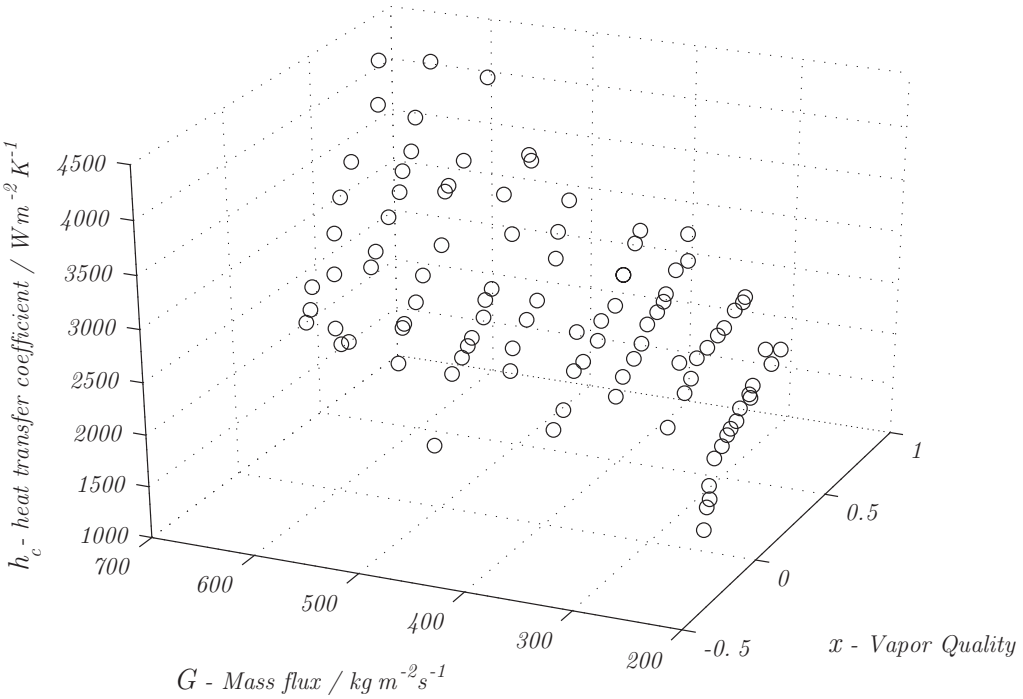

Figure 5.7: Measured heat transfer coefficients overlaid on the test matrix

However, the experimental data says nothing regarding the correctness of the heat transfer coefficient prediction; for this, it is necessary to compare the experimental heat transfer coefficient against a leading correlation. In Chapter 4, the Thome heat transfer correlation for smooth tubes was described. Due to the fact that it is flow-pattern-based, and that it is reasonably accurate ($\pm$25% for all tested refrigerants (Thome *et al.*, 2003)), this correlation was chosen as the comparator. Figure 5.8 presents the experimental heat transfer coefficient against the Thome heat transfer coefficient. The values for the Thome heat transfer coefficient were calculated utilizing the required heat transfer coefficient form, depending on the Flow regime in which the data point was situated.

The mean percentage deviation of the experimental heat transfer coefficient with respect to the Thome heat transfer coefficient is, on average, 13%, which shows that the heat transfer coefficients are being determined correctly, and gives

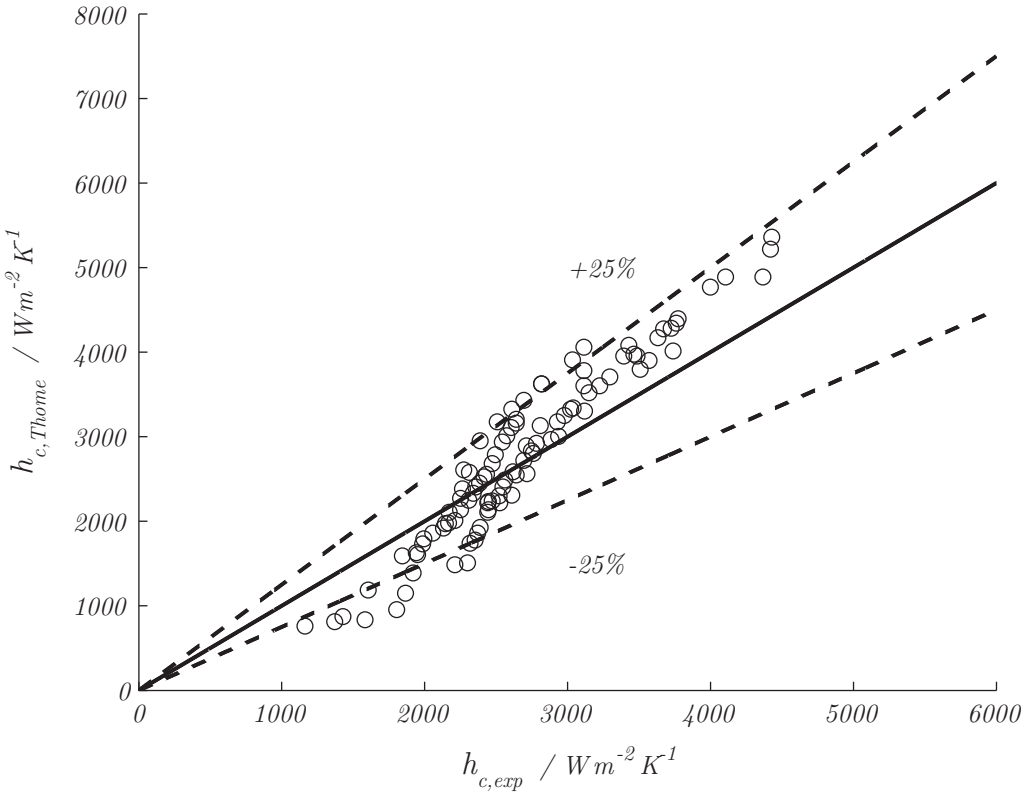

Figure 5.8: Experimental heat transfer results comparison to theoretical results

us confidence in the results found.

Most of the experimental points are within ±25%, however, there are a few that are overpredicted, and underpredicted. The points that are overpredicted are discussed in Section 5.8. On further analysis of the data, the points that are underpredicted correspond to the lowest mass flux and vapor qualities measured, that is, $G = 250$ kg/m^{2}s and $5\% < x < 15\%$. Upon further verification, these points can be seen to be in the stratified-wavy regime, near the transition line with intermittent flow. Furthermore, it is known that transition does not occur suddenly, over a well-defined and clear line, as shown in the flow map [(Thome, 2005);(Kattan *et al.*, 1998a)]; rather it occurs over a region, which could be over 50 kg/m^{2}s wide in some cases. As such, the points in this specific region measured might be in such a case where there is more than one dominating heat transfer

mode (since they are close to a transition line), and a more rigorous analysis might be in order. This leads directly to the following section.

5.5.3 Combination of the time fraction data with the experimental heat transfer coefficients

The ability to determine the probability that, at a certain mass flow and vapor quality, a certain heat transfer mode will prevail can directly aid us in increasing the accuracy of existing heat transfer correlations, not by changing the leading coefficients and exponents for ones that better fit our experimental data, but by directly modeling the physics of the flow. The time fraction map, primarily developed by Van Rooyen (2007), is based on one single, fundamental assumption. This assumption is that, at every single point in the time fraction map (*i.e.* at distinct combinations of mass flux and vapor quality), the heat transfer dominance is shifted from gravity-based to shear stress-based in a linear fashion. This is to say that if tf fraction of the time is spent in shear stress-dominated heat transfer mode, then $(1-tf)$ will be spent in the gravity-dominated heat transfer mode. From the above, we can begin by postulating that the time fraction corrected heat transfer coefficient in the Intermittent flow regime would be a linear combination of the shear stress- and gravity-based heat transfer coefficients, in the form

$$h_{c,tf} = tf \cdot h_{c,shear} + (1-tf) \cdot h_{c,grav} \tag{5.6}$$

Where $h_{c,shear}$ is (Thome *et al.*, 2003)

$$h_{c,shear} = 0.003 Re_l^{0.74} Pr_l^{0.5} \frac{k_l}{\delta} f_i \tag{5.7}$$

and $h_{c,grav}$ (Thome *et al.*, 2003)

$$h_{c,grav} = \frac{h_f r\theta + (2\pi - \theta) r h_{c,shear}}{2\pi r} \tag{5.8}$$

and h_f is (Thome *et al.*, 2003)

$$h_f = 0.728 \left[\frac{\rho_l(\rho_l - \rho_v) g h_{lv} k_l^3}{\mu_l d(T_{sat} - T_w)} \right]^{\frac{1}{4}} \tag{5.9}$$

In this case, the shear stress-based and gravity-based heat transfer coefficients are directly calculated from the equations developed in Section 4.3. The shear stress-based heat transfer coefficient correlation is not changed, while the only change that was performed to the gravity-based heat transfer coefficient correlation comes in with the term

$$\theta = \theta_{strat} \left[\frac{(G_{wavy} - G)}{G_{wavy} - G_{strat}} \right]^{0.5} \tag{5.10}$$

The term in square brackets is a multiplier that can vary between 0 and 1, in the limiting cases of the mass flux being equal to the transition values between Stratified and Stratified-Wavy (G_{strat}) and the transition value between Stratified-Wavy and Intermittent (G_{wavy}). The purpose of the multiplier is to change the value of the stratification angle smoothly from its highest value, θ_{strat}, at the interface between Stratified and Stratified-Wavy down to 0, at the interface with Intermittent. However, we are interested in finding the stratification angle for times in which the mass flux is larger than the Wavy transition. Attempting this with the multiplier gives a complex number, due to the fact that it is square-rooted (and the top substraction will always generate a negative number). The proposed change that is performed to this term is to make the multiplier a constant value of 1. This is to say that the falling film angle θ is made equal to the stratification angle θ_{strat}.

In the analysis of the Intermittent flow regime visual data, it was found that the periods classified as gravity-dominated (Stratified) actually had very small to no waves present, thus allowing us to assume that the stratification angle was that of the completely Stratified flow regime.

Carrying on with the analysis, the time fraction corrected heat transfer coefficient was calculated, and is shown in Figure 5.9 compared to the experimental heat transfer coefficient results. Figure 5.10 shows the experimental heat transfer coefficient plotted against both the time fraction-corrected and (classical) Thome heat transfer coefficient correlation.

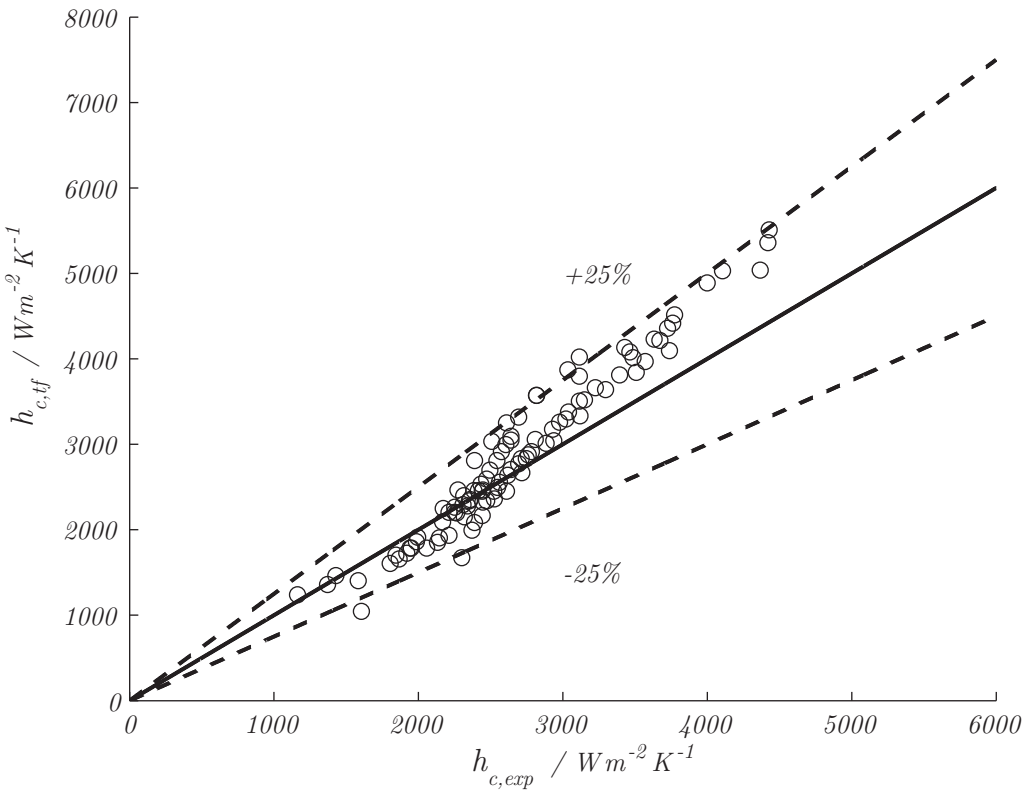

Figure 5.9: Comparison of experimental heat transfer coefficient against the time fraction-corrected heat transfer prediction

The experimental results' mean percentage deviation when compared against the time fraction-corrected heat transfer correlation is, on average, 10%. When looking at Figure 5.9, the points that were at the lower range of both mass flux (250 kg/m^{2}s) and vapor quality, which were both underpredicted by the (classical) Thome correlation are now within ±25% of the predicted value.

Figure 5.10 shows a very good comparison between all of the data points and their corresponding Thome and time fraction-corrected correlation; however, due to the large amount of data points, the detail is lost. The following figures (Figures 5.11-5.20) have the heat transfer coefficients decomposed by mass flux, such that a maximum of 12 points are plotted at any one time.

Figure 5.11 shows the experimental heat transfer coefficients compared to both the time fraction-corrected heat transfer and the (classical) Thome correlation for

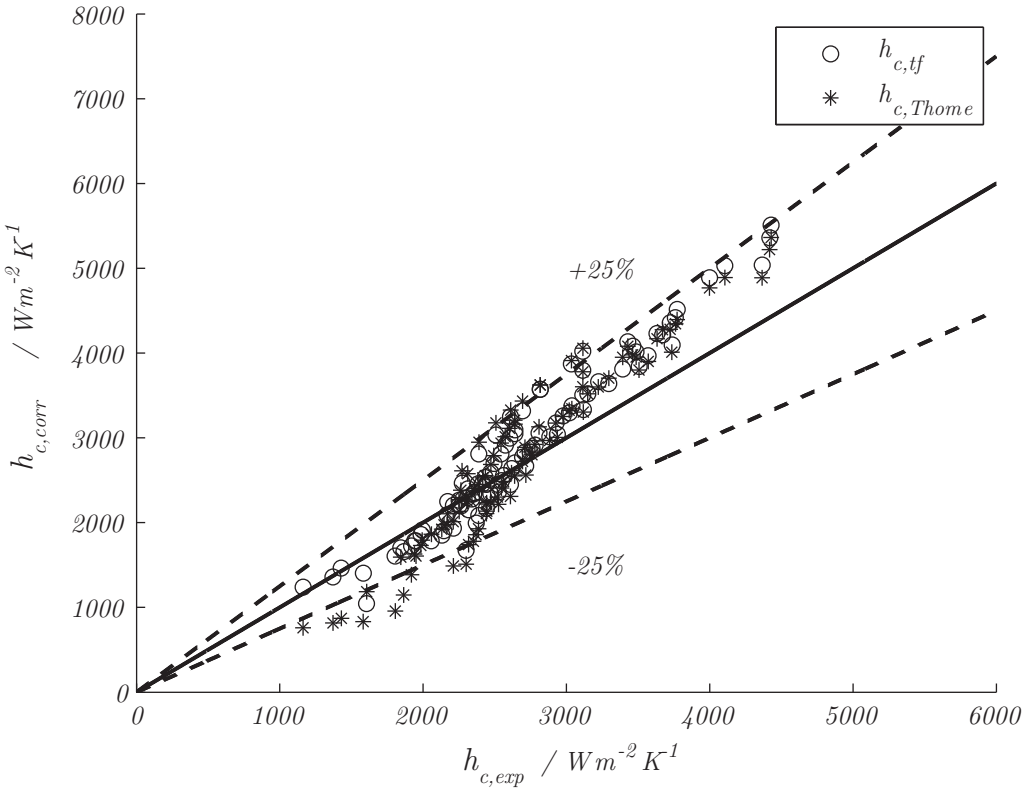

Figure 5.10: Comparison of experimental heat transfer coefficient against the time fraction-corrected heat transfer prediction

a constant mass flux of 250 kg/m^{2}s. The mean percentage deviation between the time fraction corrected heat transfer coefficients and the experimental results is 9%. In contrast, for the same mass flux, the experimental results' mean deviation from the Thome heat transfer coefficient predictions is 28%.

On a point-by-point direct comparison between the prediction of the time fraction-corrected model and the Thome prediction, it can be seen that the points at lower vapor qualities benefited the most from the application of the time fraction data. As the vapor quality increases, and the heat transfer coefficient increases (since the flow regime tends towards the Annular flow regime), the influence of the time fraction is lessened; this is mainly for two reasons, the first being that the tf is large, which makes the influence of the shear stress-based heat transfer coefficient more apparent, and secondly, at higher vapor qualities (and

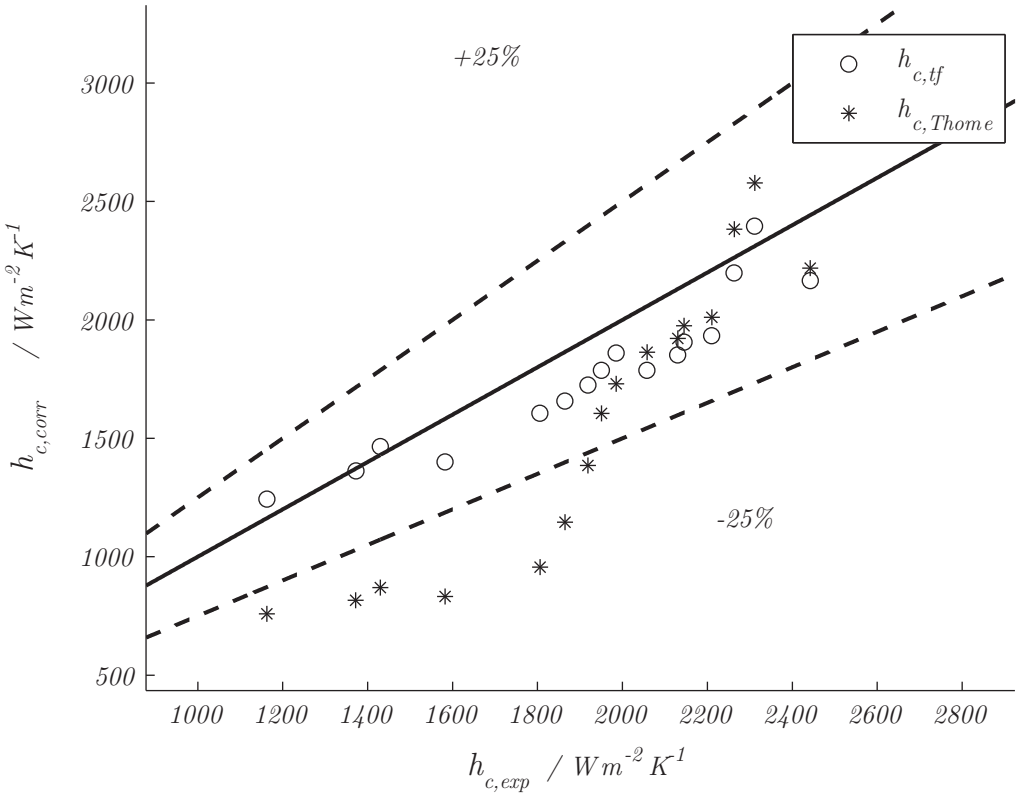

Figure 5.11: Comparison of the experimental heat transfer coefficients against predicted data at G = 250 kg/m^{2}s

mass fluxes), the shear stress-based heat transfer coefficient becomes dominant, as shown in Figure 5.12.

Due to their proximity to the stratified-wavy/intermittent Thome transition curve, the data points at the lowest vapor qualities (at G = 250 kg/m^{2}s) experience a large variation in heat transfer mode dominance, which is not captured well by the existing active Thome correlation. As the vapor quality increases, the heat transfer prediction tends towards the shear stress-based heat transfer coefficient prediction, which is expected from the form of the time fraction-corrected heat transfer correlation.

Figure 5.13 presents the comparison between methods at a mass flux of 300 kg/m^{2}s. The percentage deviation of the experimental points compared to the

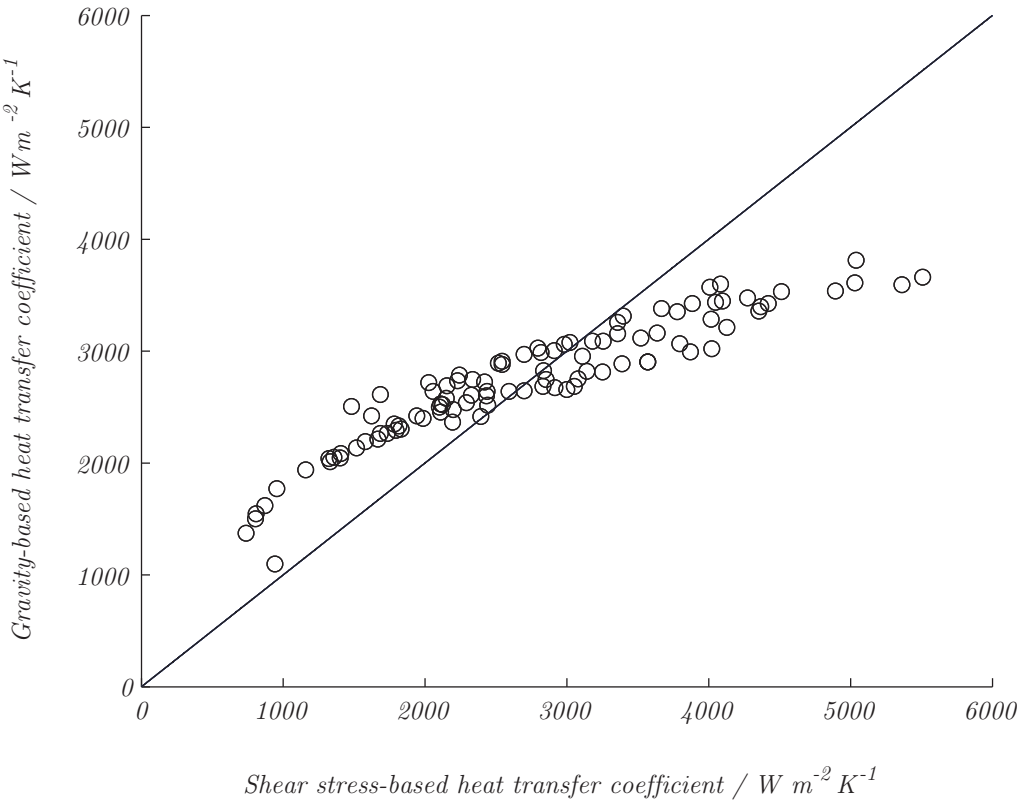

Figure 5.12: Comparison of shear stress-based and gravity-based coefficient dominance

time fraction points is 6.3%, while against the classical Thome correlation data points it is 9.8%. Although the results are already accurate, the same trend as that shown in the G=250 kg/m^{2}s results is present, namely that the time fraction-corrected points generate closer predictions to the experimental data. At this mass flux, the shear stress and gravity heat transfer coefficients values, as depicted in Figure 5.12, are very close to each other, which is why the time fraction corrected points do not vary very much from their Thome counterparts.

The comparison at a mass flux of 350 kg/m^{2}s is presented in Figure 5.14. At the lowest mass fluxes it can be seen that there was quite a large improvement, due to the fact that the experimental data were being underpredicted by the Thome heat transfer coeffficient. The mean percentage deviation of the experimental data from the time fraction-corrected data was 3.8%, while the original deviation from

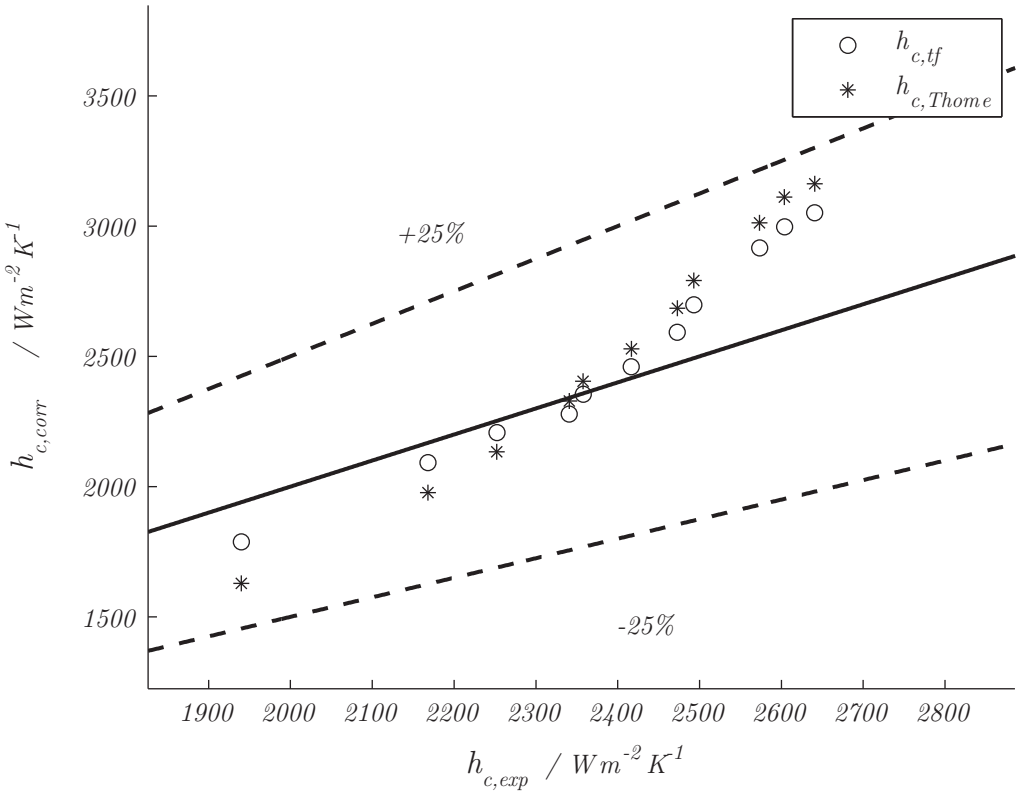

Figure 5.13: Comparison of the experimental heat transfer coefficients against predicted data at G = 300 kg/m^{2}s

the Thome prediction was 13%. As the tf goes to unity (*i.e.* purely shear-stress dominated flow), it can be seen that the predictions collapse exactly onto each other, indicating correct calculations.

Figure 5.15 shows the heat transfer coefficient data collected at a mass flux of 400 kg/m^{2}s. The mean percentage deviation against the time fraction-corrected data is 14.5% while it is 17.5% against the Thome classical correlation predictions. The heat transfer coefficients at the lower qualities show the best improvement, as has been the trend up to now. Once the vapor qualities increase, the correction is seen to be less effective, until the data is overpredicted by both the time fraction corrected correlation and the Thome correlation. The point that is very clear in this Figure is that, with increasing vapor quality, there is a monotonic increase in

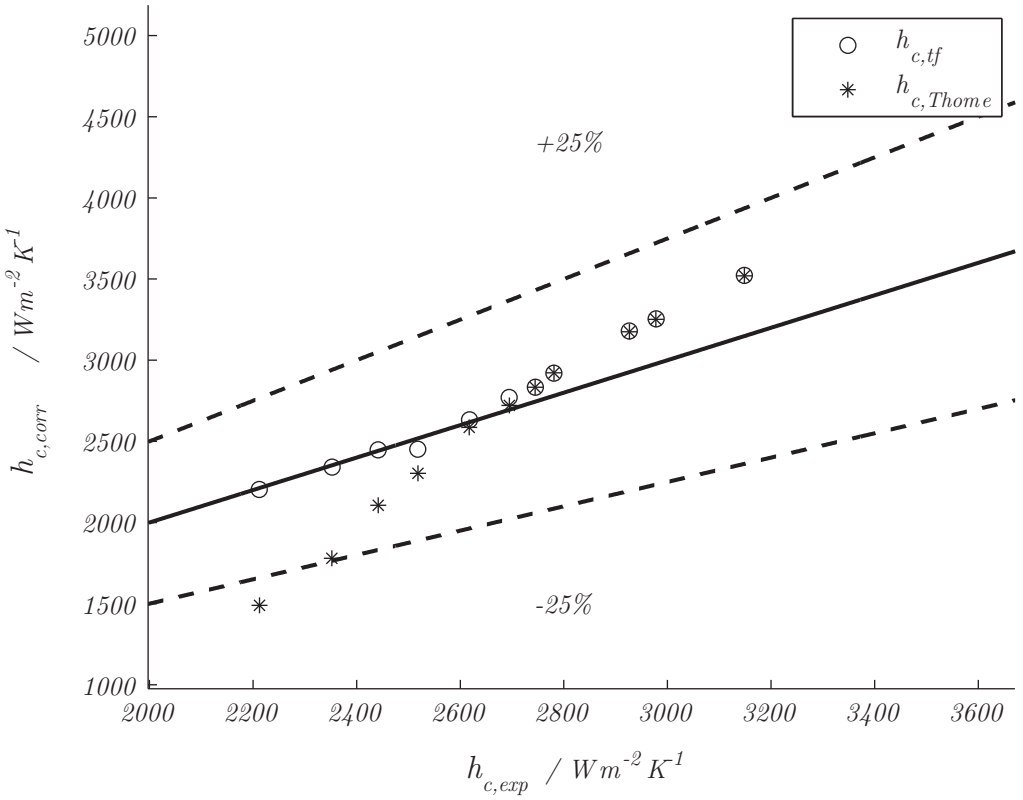

Figure 5.14: Comparison of the experimental heat transfer coefficients against predicted data at G = 350 kg/m^{2}s

heat transfer coefficient. We are able to state this as we are keeping the mass flux constant, and only vary the vapor quality. By increasing the vapor quality, the flow regime tends towards the Annular flow regime, and thus higher heat transfer coefficients in general.

Figure 5.16 presents the heat transfer coefficient data at a mass flux of 450 kg/m^{2}s. The percentage deviation of the experimental points compared to the time fraction points is 6.7%, while against the classical Thome correlation data points it is 12.4%. As the mass flux increases, the time fraction goes to high levels faster than at lower mass fluxes, which means that the number of data points that are heavily affected by the time fraction correction decrease. Case in point, at G=450 kg/m^{2}s, half of the data points are very near their Thome counterparts, all

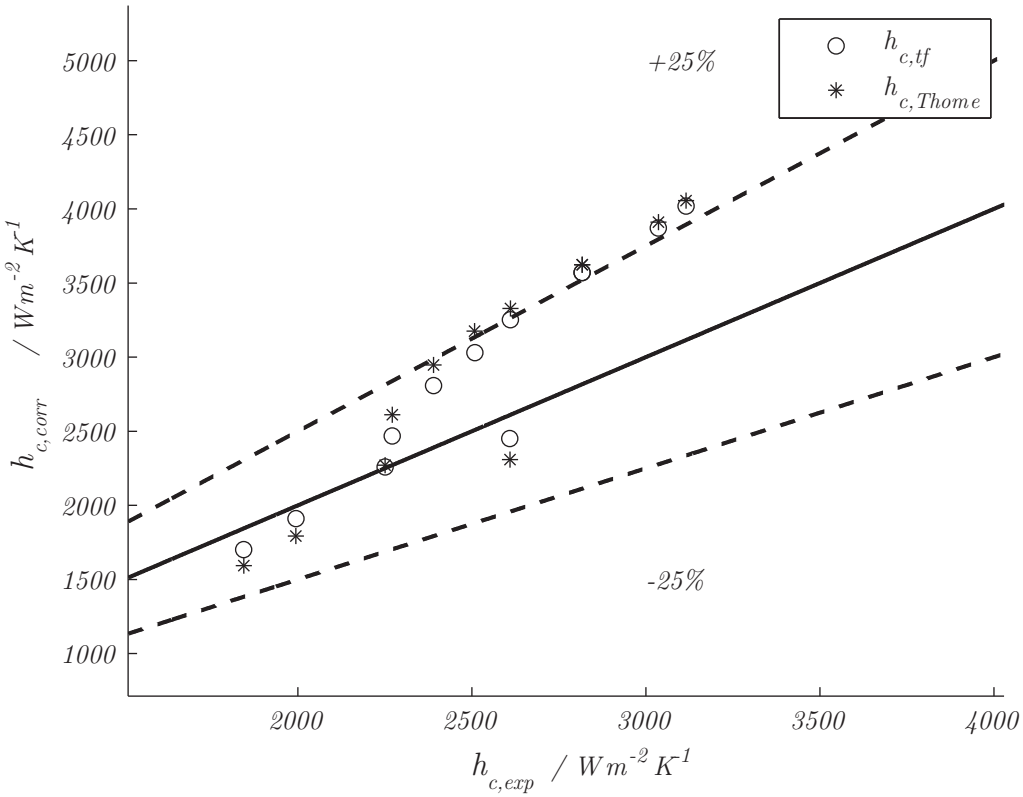

Figure 5.15: Comparison of the experimental heat transfer coefficients against predicted data at G = 400 kg/m^{2}s

of these at the higher vapor qualities, while the meaningful prediction corrections are still effected at lower vapor qualities.

The comparison at a mass flux of 500 kg/m^{2}s is presented in Figure 5.17. The percentage deviation of the experimental points compared to the time fraction points at this mass flux is 14%, marginally worse than the Thome predictions' mean deviation of 13.8%. There is one point predicted in this mass flux which does not agree with the rest of the data, namely that showing the lowest heat transfer coefficient. However, upon further analysis, it can be seen that the inlet vapor quality of this point was only 5%, and over the majority of the heat exchanger the refrigerant was fully condensed, giving a lower than anticipated heat transfer coefficient. The rest of the points, however, show a monotonic increase with vapor

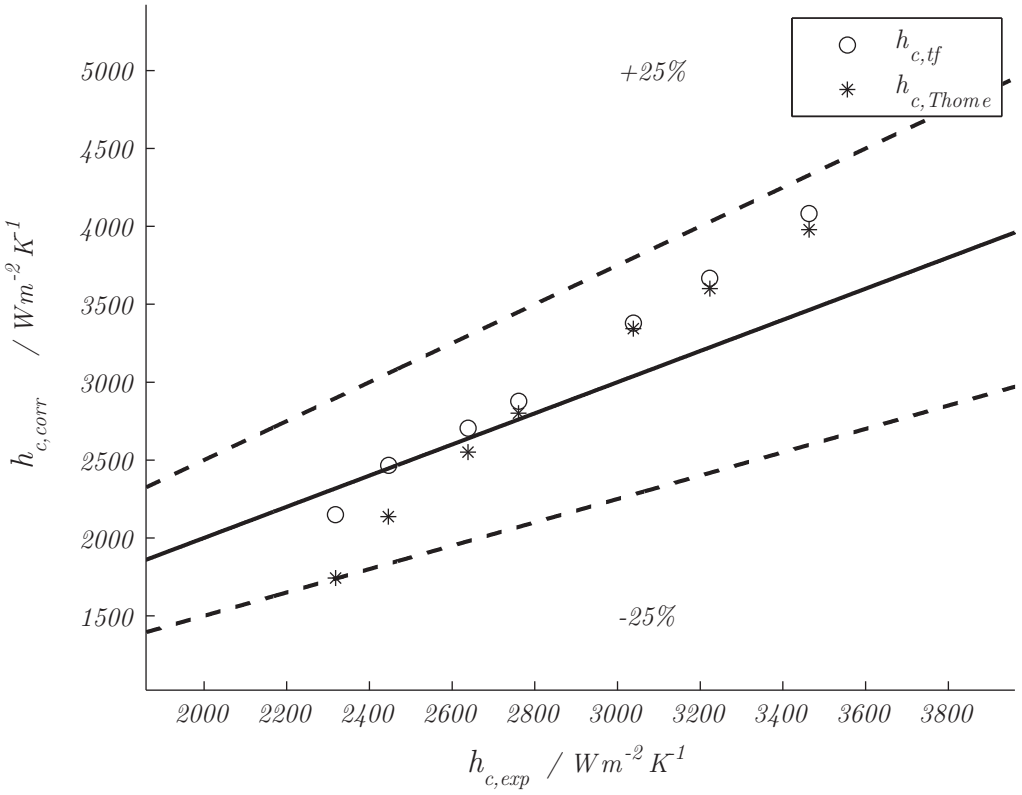

Figure 5.16: Comparison of the experimental heat transfer coefficients against predicted data at G = 450 kg/m^{2}s

quality, as expected. Furthermore, at heat transfer coefficients of 3 000 to 4 000 W/m^{2}K, the gravity- and shear-based predictions give quite similar results, which lead the time fraction-corrected heat transfer coefficients to be quite similar to the Thome predictions, regardless of the physical value of the tf.

At a mass flux of 550 kg/m^{2}s, as shown in Figure 5.18, the mean percentage deviation between the experimental data and the time fraction-corrected heat transfer coefficients is 11%, while the deviation against the Thome prediction is 12%. At the lower vapor qualities, and time fractions, the time fraction correction still generates more accurate results; however, at these high mass fluxes the time fraction increases rapidly, and at vapor qualities still in the Intermittent flow but not close to the Intermittent/Annular transition curve, the influence of the gravity

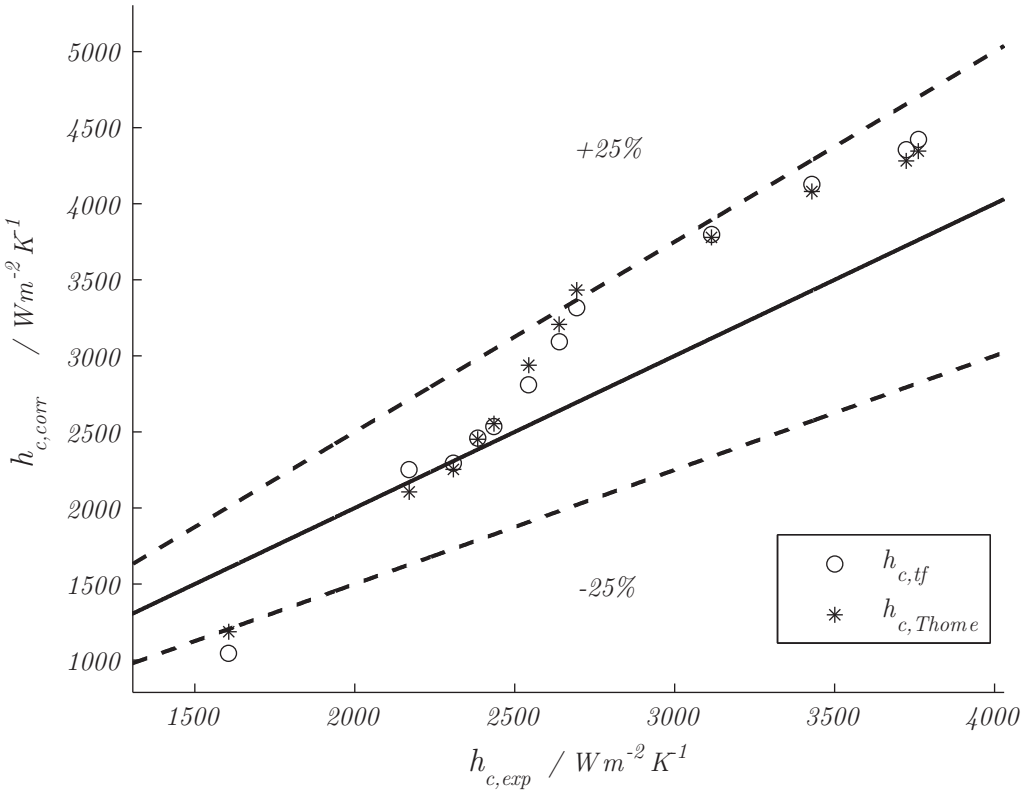

Figure 5.17: Comparison of the experimental heat transfer coefficients against predicted data at G = 500 kg/m^{2}s

term is attenuated, generating results similar to those found with the Thome correlation. As the time fraction increases, and reaches unity, the two predictions collapse onto each other.

The comparison at a mass flux of 600 kg/m^{2}s is presented in Figure 5.19. The mean percentage deviation of the experimental data compared to the time fraction-corrected results is 10.8%; the deviation as compared to the Thome heat transfer correlation is slightly higher, at 10.9%. As was stated in the analysis of the previous (G=550 kg/m^{2}s) results, the time fraction increases more rapidly at the higher mass fluxes, which again diminished the effect of the gravity-based term. Furthermore, on closer inspection of Figure 5.12, at the range of heat transfer coefficients encountered at these higher mass flow rates (in relation to

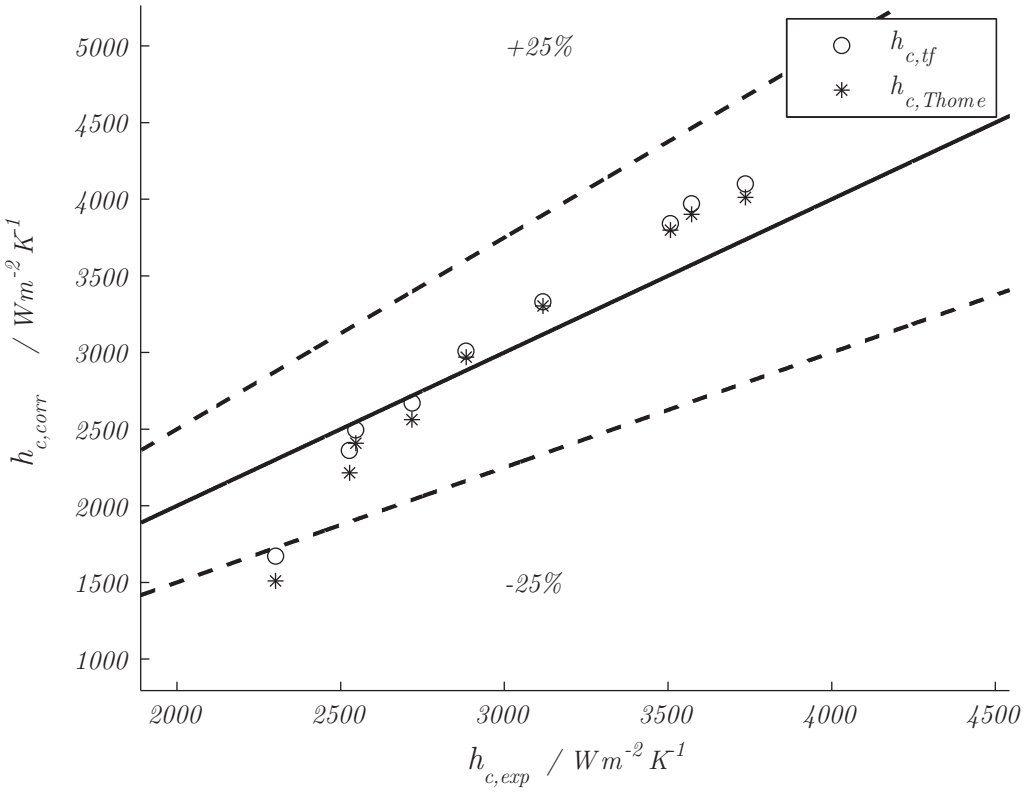

Figure 5.18: Comparison of the experimental heat transfer coefficients against predicted data at G = 550 kg/m^{2}s

the rest of the test matrix), it can be seen that the shear stress-based prediction is quite higher than the gravity-based coefficient. This, coupled with the reduced influence of the time fraction (since it is large for a majority of vapor qualities in the Intermittent regime) ends up with a heat transfer coefficient prediction similar to the Thome correlation.

The last mass flow tested was G = 650 kg/m^{2}s, at which the mean experimental deviation from the time fraction-corrected prediction was 12.2%. The deviation from the Thome heat transfer coefficient was slightly lower, at 12.1%. This is shown in Figure 5.20. At the high vapor qualities, the time fraction-corrected predictions collapsed into the Thome values, due to the fact that testing was indeed performed in the Annular regime. The rest of the values saw small variations

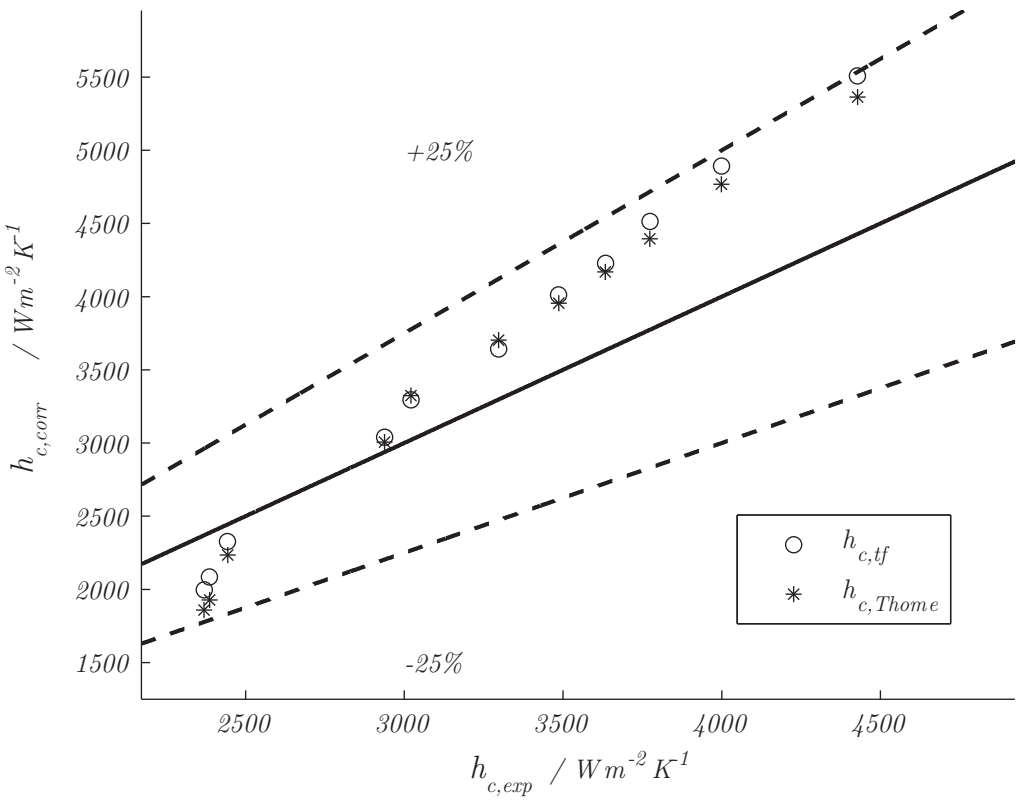

Figure 5.19: Comparison of the experimental heat transfer coefficients against predicted data at G = 600 kg/m^{2}s

from the Thome coefficients, due to the rapid increase in time fraction with vapor quality, as described for the mass fluxes of 550 kg/m^{2}s and 600 kg/m^{2}s. Although the effect is not quite large, the prediction for all but one point was improved.

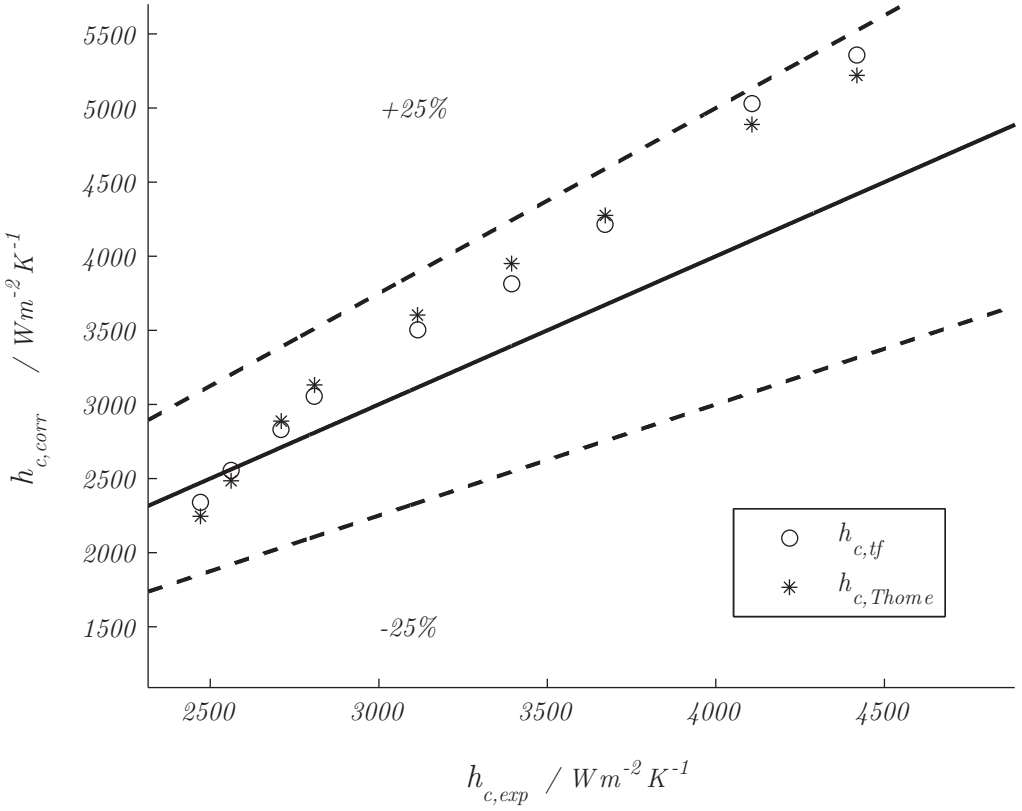

Figure 5.20: Comparison of the experimental heat transfer coefficients against predicted data at G = 650 kg/m^{2}s

5.6 Pressure drop results

At the same time as the heat transfer was being collected, pressure drop information was also gathered. Before the frictional pressure drop may be measured, the momentum pressure drop must be calculated. In the following sections the momentum pressure drop and the frictional pressure drop results will be discussed.

5.6.1 Momentum pressure drop

The momentum pressure drop term was presented in the Chapter 2, the result of an extensive derivation. This term is indepedent of the tube type, size or shape, and is only a function of the refrigerant states at the inlet and outlet of the test section, and the refrigerant mass flux. The momentum pressure drop (or rather, pressure rise), as calculated for each data point in the test matrix described in Section 5.3, ranged between 134 Pa and 316 Pa. The momentum pressure drop varied between 1% and 15% of the total pressure drop measured over the test section. Quantifying the size of the momentum term with respect to the total pressure drop term is important in terms of the uncertainty of the frictional pressure drop. This is detailed in Appendix B.

5.6.2 Frictional pressure drop

In this section, the frictional pressure drop results are presented and analyzed. Pressure drop information was saved at each of the data points described in Section 5.3. The data presented in this section are compared to the leading correlations suggested in Ould-Didi *et al.* (2002). Improvements regarding the accuracy of the measurements are also suggested.

5.6.2.1 Experimental results and theoretical predictions

In the same manner that the entirety of the heat transfer coefficient results were presented in a three-dimensional version, the frictional pressure drop results are shown in Figure 5.21.

Due to the fact that some of the points were in the Stratified-wavy regime, and some of the points were in the Annular flow regime, two pressure drop correlations

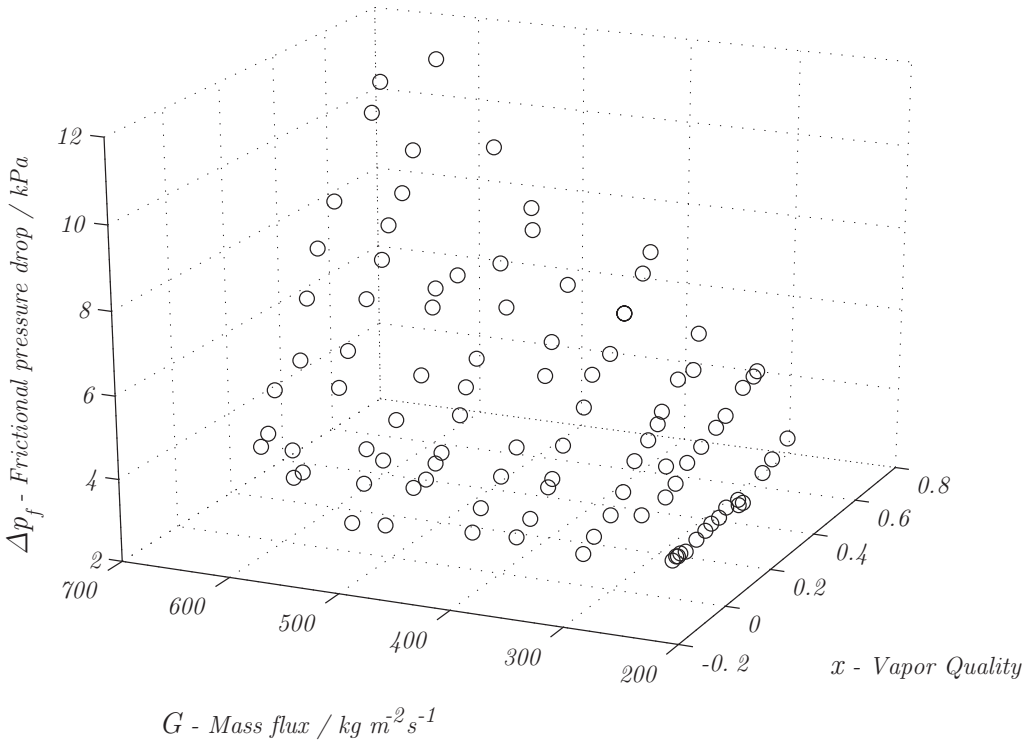

Figure 5.21: Measured frictional pressure drops overlaid on the test matrix

were utilized as theoretical predictors of the experimental data, namely the Müller-Steinhagen and Heck (Ould-Didi *et al.*, 2002) correlation for annular flow, and that of Grönnerud for stratified flow (Ould-Didi *et al.*, 2002). The results obtained are shown in Figure 5.22.

The most evident point shown in Figure 5.22 is that the theoretical preditions vastly underpredict the experimental data. The most important reason that this occurs has nothing to do with the adequacy of the correlations; rather, it is directly influenced by the choice of pressure transducer.

Due to the fact that it is necessary to measure the gauge pressure both at the refrigerant inlet and outlet of the test section, it is not possible to simply instrument it using one (or more) differential pressure transducers. However, due to the large full-scale range of the transducers utilized, and to the short test section length, the uncertainty in the measurements were extremely large;

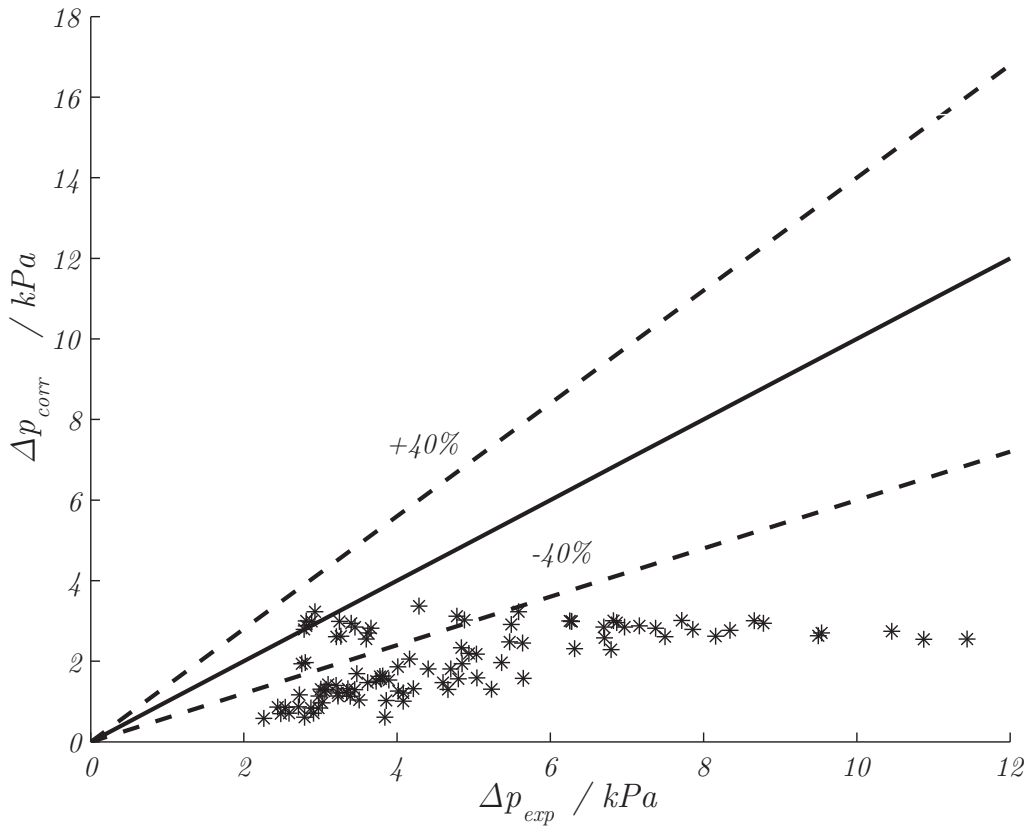

Figure 5.22: Experimental pressure drop results comparison to theoretical results

furthermore, some of the pressure drop measurements taken were below 0.1% of the full-scale value of the transducers, further worsening the prediction. As such, any future pressure drop measurement must be taken with a well specified differential pressure transducers. Reduced accuracy notwithstanding, further analysis can take place with the data saved from the experimental setup. Plotting the pressure drop against vapor quality, as in Figure 5.21 shows no sharp discontinuity on a constant mass flux line; however, this is not the case when using the two required prediction methods. The following section develops a flow-pattern-based time fraction correlation that alleviates this issue.

5.6.2.2 Time fraction-corrected frictional pressure drop data

As was stated beforehand, at some mass fluxes, the predictions between the two required pressure drop correlations (for annular and stratified flow) are not continuous; that is, there is a sharp discontinuity between two contiguous measurements.

Although the time fraction map was originally developed to distinguish between gravity-dominated and shear stress-dominated heat transfer modes, the very fact that the heat transfer is dominated by these methods indicates that there might be an application of the time fraction in the pressure drop domain. Thus, in this case, as was previously done for the heat transfer coefficient correlation, we can correct the prediction by utilizing a linear combination (in time fraction) of the two predictors, resulting in

$$\Delta p_{tf} = tf \cdot \Delta p_{shear} + (1 - tf) \cdot \Delta p_{grav} \tag{5.11}$$

And the Δp_{shear} (Ould-Didi *et al.*, 2002) is

$$\left(\frac{dp}{dz}\right)_f = G(1-x)^{\frac{1}{3}} + bx^3 \tag{5.12}$$

with G not the mass flux but $G = a + 2(b-a)x$, and a and b are

$$a = 0.079 Re_l^{-0.25} \tag{5.13}$$
$$b = 0.079 Re_v^{-0.25} \tag{5.14}$$

and Δp_{strat} (Ould-Didi *et al.*, 2002) is

$$\Delta p_f = \phi_{gd} \Delta p_l \tag{5.15}$$

The vapor phase multiplier is

$$\phi_{gd=} = 1 + \left(\frac{dp}{dz}\right)_{Fr} \left[\frac{\left(\frac{\rho_l}{\rho_v}\right)}{\left(\frac{\mu_l}{\mu_v}\right)^{\frac{1}{4}}} - 1 \right] \tag{5.16}$$

Applying this time fraction correction to the two theoretical pressure drop models results in the prediction shown in Figure 5.23. We may also compare these predictions against the original two correlations; this is shown in Figure 5.24.

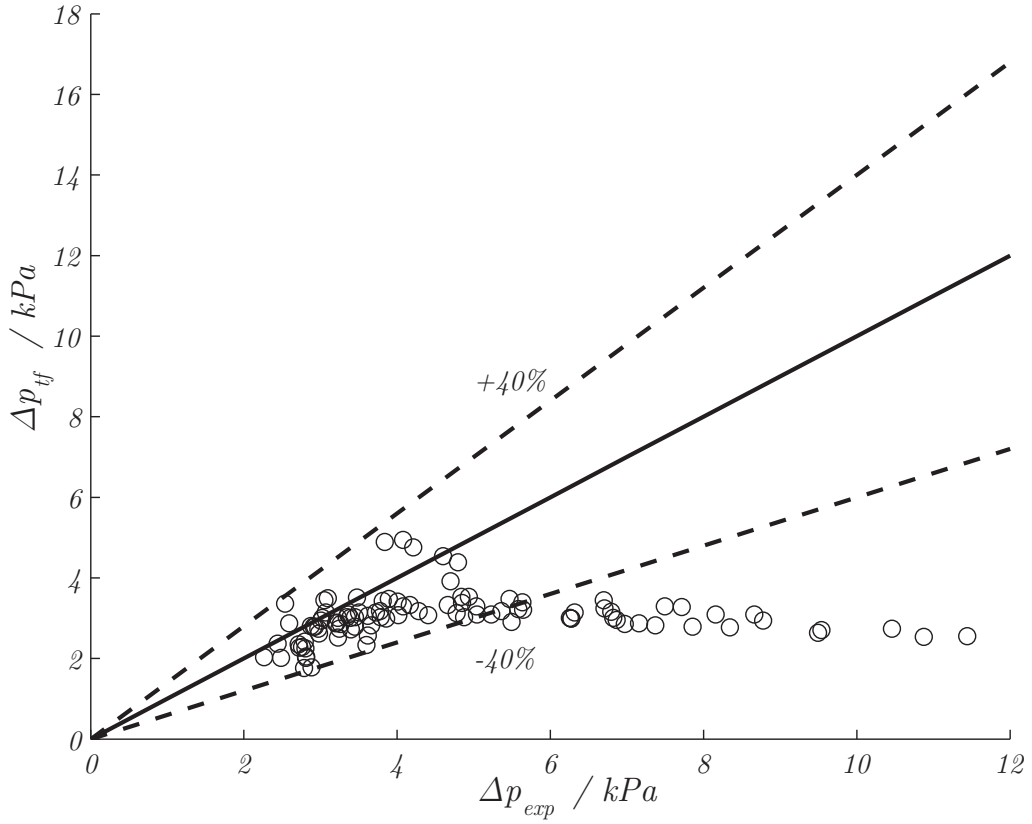

Figure 5.23: Comparison of the experimental frictional pressure drop against time fraction-corrected data

First, it is evident that there is a general increase in accuracy, due to the fact that the mean percentage deviation of the experimental data from the time fraction-corrected data is 62% and from the original correlation 156%. However, even the more accurate values are still too imprecise to be of value to a designer.

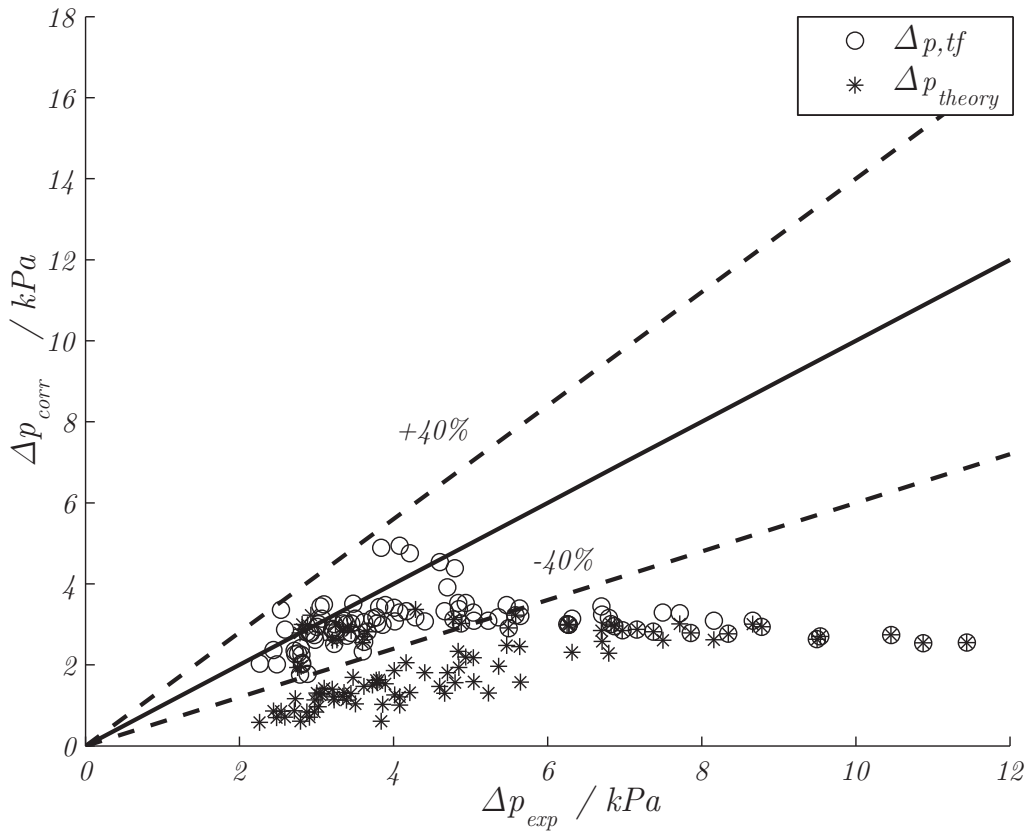

Figure 5.24: Comparison of the experimental frictional pressure drop against predictors

However, due to the amount of points plotted on a single figure, several interesting phenomena are not visible, which is why, much like with the heat transfer coefficient results, we decompose the figure into several figures showing constant mass flux predictions.

Figure 5.25 shows the comparison between the experimental results and the time fraction-corrected pressure drop results, as well as the original results. At this mass flux, the mean deviation from the time fraction-corrected results is 22%, while the mean deviation from the classical results is 81%. Although there is a large vapor quality change in the points tested, the difference between the predictions is not very large; this can be attributed to the low accuracy of the transducers for such small pressure drops, but also to the fact that both the

Müller-Steinhagen and Heck, as well as the Grönnerud correlations predict these points relatively well (with no disparity or discontinuities between contiguous points).

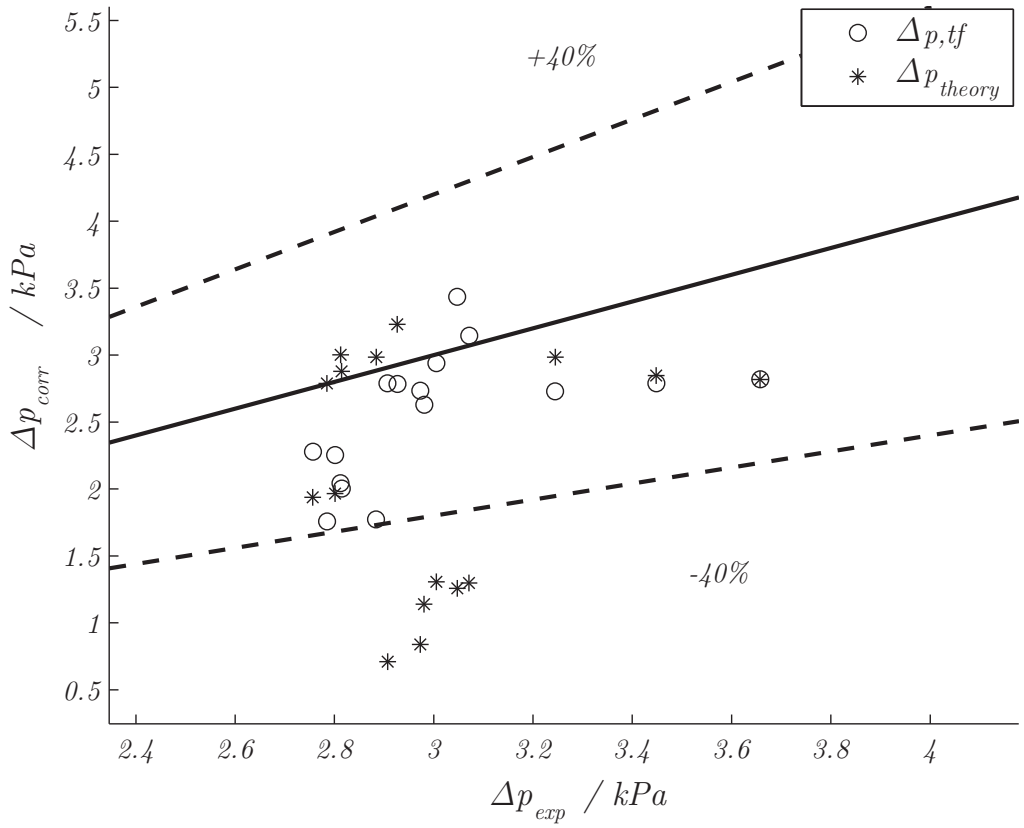

Figure 5.25: Comparison of the experimental frictional pressure drop against predicted data at G = 250 kg/m^{2}s

At a mass flux of G = 300 kg/m^{2}s, the mean deviation from the time fraction data is 20%, while it is 154% against the two correlations, as shown in Figure 5.26. The points that were best corrected by the time fraction were the higher vapor quality points, in which the annular (Müller-Steinhagen and Heck) correlation was more dominant than the stratified correlation.

The lower vapor quality points were not affected by a large amount, due to the fact that the Grönnerud predictions are very much lower than the Müller-Steinhagen and Heck, as shown in Figure 5.27.

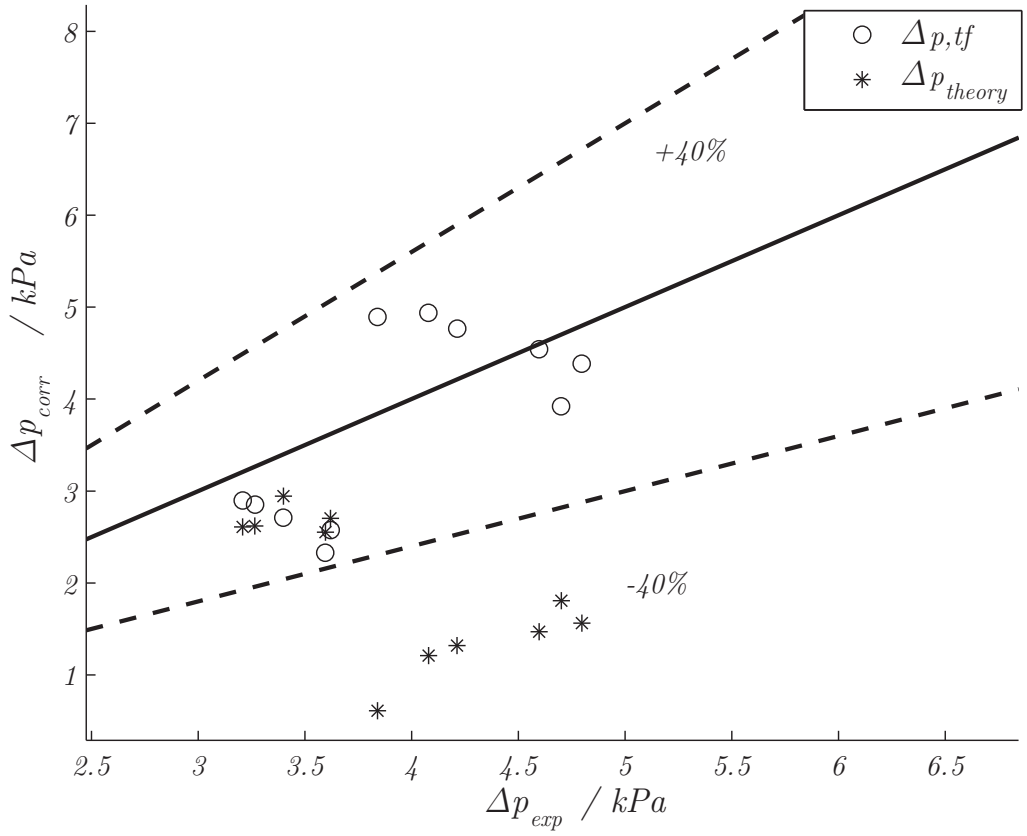

Figure 5.26: Comparison of the experimental frictional pressure drop against predicted data at G = 300 kg/m^{2}s

Figure 5.28 shows the results of the experimental pressured drop comparison against theoretical results. The experimental deviation from the time fraction corrected results is 32%, and it is 183% from the two correlations. The major point of discussion in this figure however is not the large deviation; rather, it is the different models' predictions of the pressure drop on a constant vapor quality. From Figure 5.21, it is known that the pressure drop increases as the vapor quality increases (at a constant mass flux). In Figure 5.28, the Grönnerud pressure drop correlation is used as the vapor quality increases and approaches the transition to Annular flow from Intermittent; however, as that boundary is crossed, the pressure drop correlation used is changed to the Müller-Steinhagen

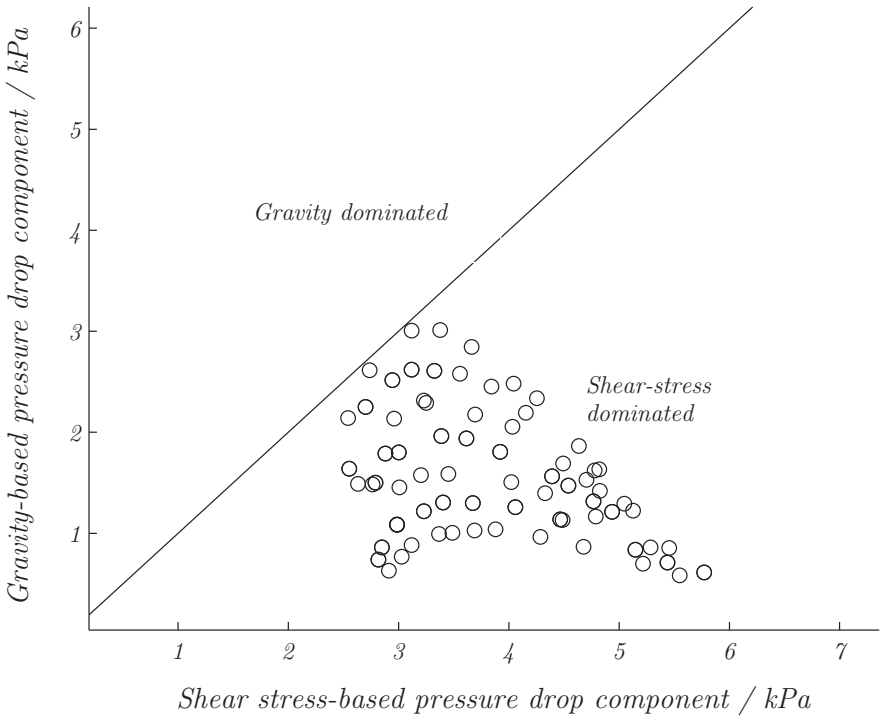

Figure 5.27: Comparison of shear stress-based and gravity-based prediction dominance

and Heck. From experimental results, it is know that the pressure drop increases in a continuous fashion. However, there is a large discontinuity in the prediction from the two correlations, which has always been a problem, not only for pressure drop correlations, but for heat transfer coefficient correlations as well. By utilizing the time fraction correction for the pressure drop, not only is the prediction closer to the experimental results, but the pressure drop increases continuously, without a large discontinuity.

At a mass flux of 400 kg/m^{2}s, the deviation from the time fraction data is 70%, while it is 188% from the classical predictions. The same comments as made when discussing the G = 350 kg/m^{2}s results are valid, namely that the time fraction correction allows for a smooth transition between prediction methods without a discontinuous jump. It is also important to note that while the experimental pressure drop increases, the predicted results do not. This would mean that in

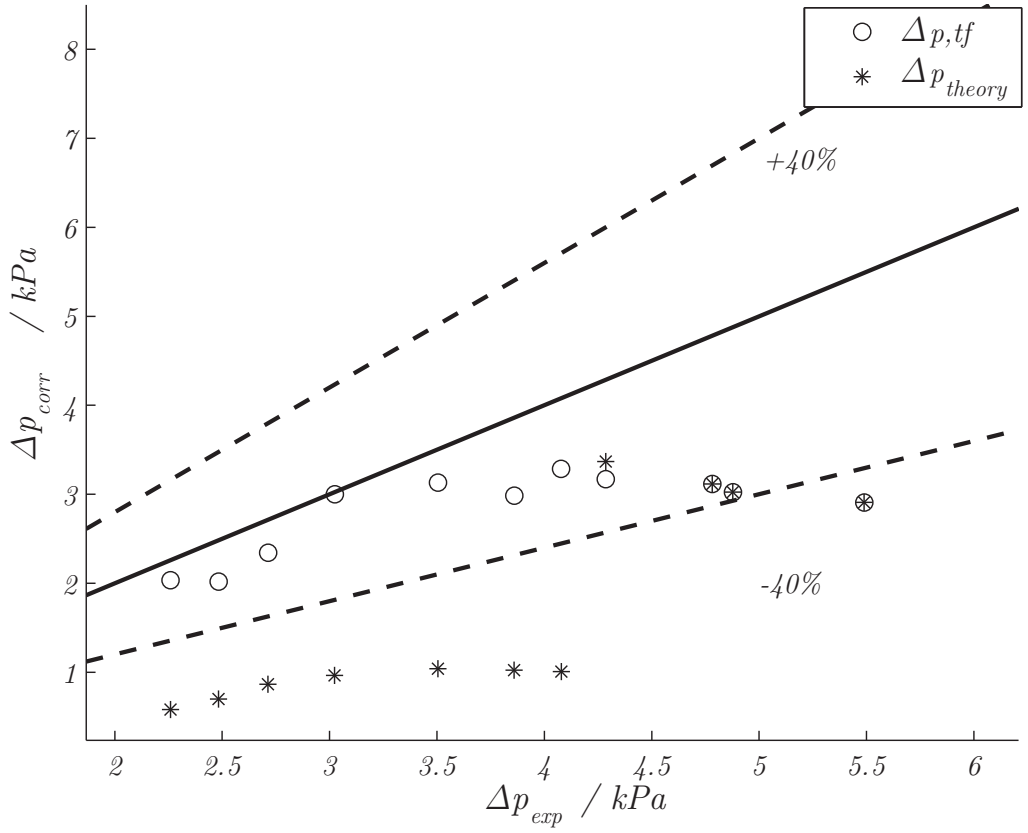

Figure 5.28: Comparison of the experimental frictional pressure drop against predicted data at G = 350 kg/m^{2}s

addition to having experimental accuracy problems, the prediction is also faulty, and severely underpredicts the data. While it would be the norm to change the correlation to better match the experimental results, the experimental uncertainty in these results dictate that it would be more prudent to gather more accurate data before proceeding. Furthermore, the time fraction correction would still work, due to the fact that it linearly combines two predictions. At the limit vapor qualities and mass flows, it would still collapse to the original correlations, due to the correction's functional form.

The comparison of the experimental and theoretical data is shown in Figure 5.30. The mean percentage deviation between the experimental data and

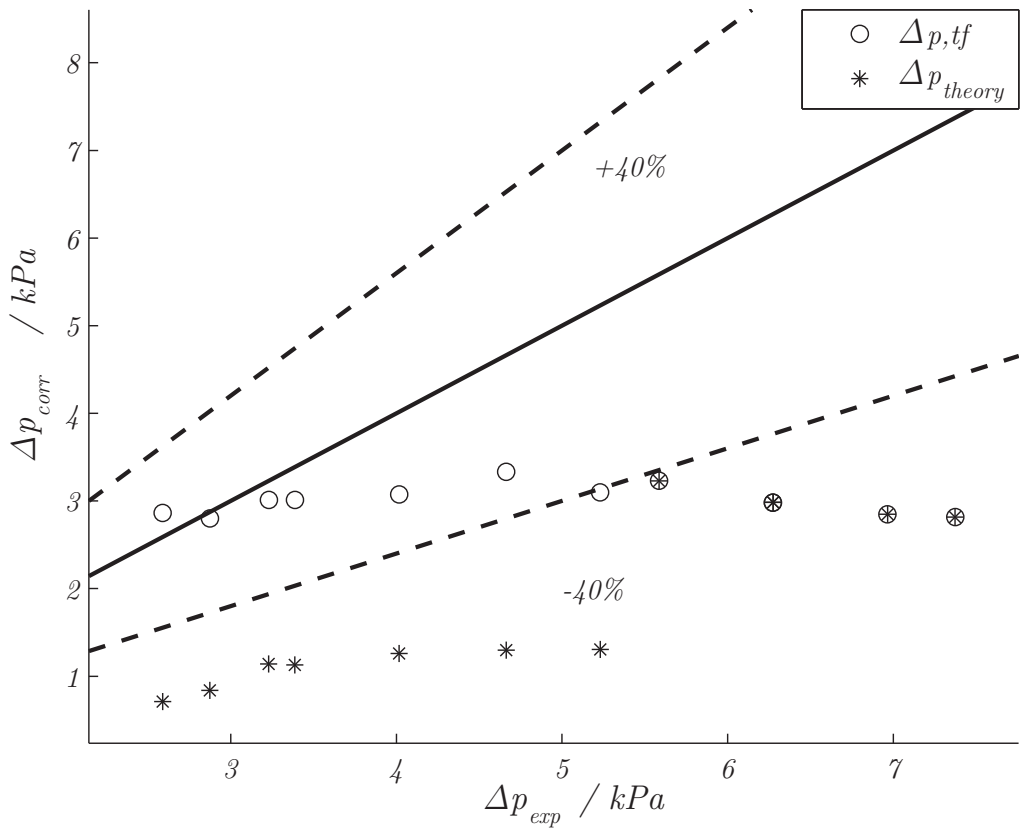

Figure 5.29: Comparison of the experimental frictional pressure drop against predicted data at G = 400 kg/m^{2}s

the time fraction-corrected data is 42%. The deviation from the two original correlations is 166%. Again, all of the data were under predicted by the original correlations. However, the time fraction correction generates a large difference in accuracy, even at small time fractions, due to the fact that the annular correlation predictions are very much larger than the stratified predictions, as was shown in Figure 5.27. Furthermore, the correction still delivers a continuous prediction, while a discontinuity is present in the original prediction.

The same comments can be made about the phenomena that occur for the pressure drop predictions at mass fluxes of G = 500, 550 and 600 kg/m^{2}s (respectively shown in Figures 5.31, 5.32 and 5.33). The mean percentage deviations against the time fraction data for these three mass fluxes are 62%, 82% and 122%

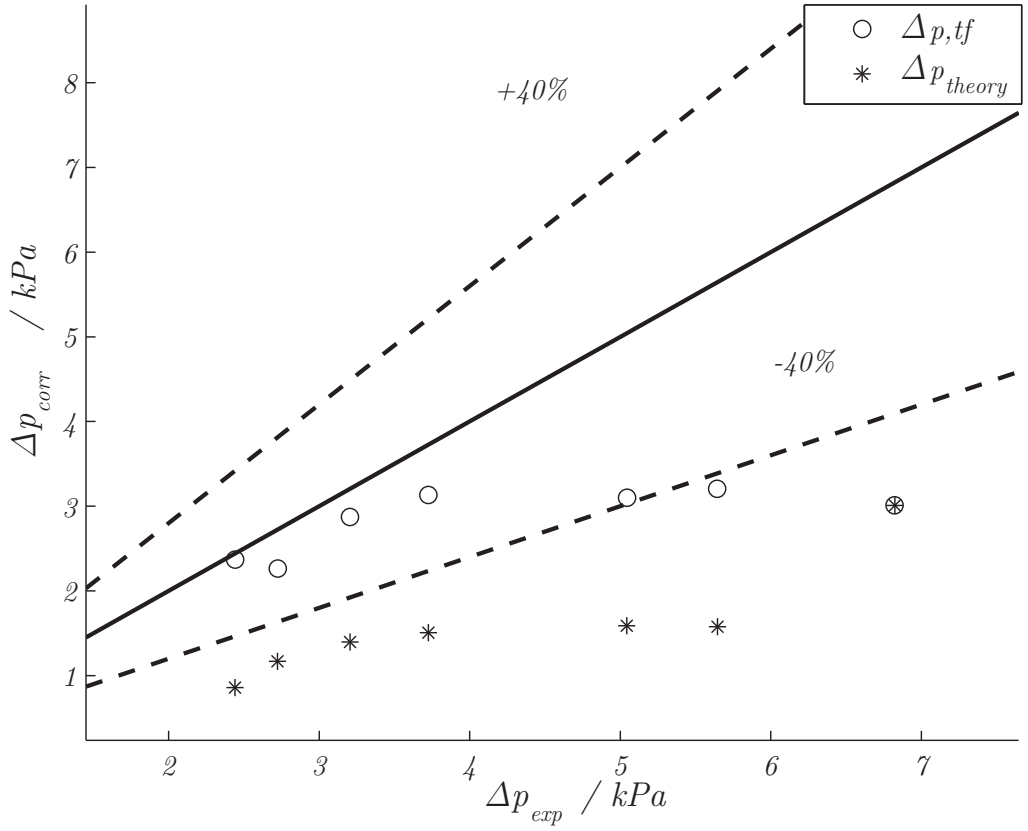

Figure 5.30: Comparison of the experimental frictional pressure drop against predicted data at G = 450 kg/m^{2}s

respectively, while the deviations from the classical correlations were 170%, 160% and 189%. At these higher mass fluxes, and especially noticeable at G = 600 kg/m^{2}s, the time fraction increases rapidly, which decreases the effect of the time fraction correction. This is also evidenced in the increasing mean deviation. This is also readily apparent when a comparison is made with the average correction at low vapor qualities, at lower mass fluxes, such as G = 250 and 300 kg/m^{2}s. The increased influence of the annular pressure drop correlation, coupled to the experimental uncertainty in the measurements, as well as the prediction problems addressed earlier contribute to these increasing mean deviations.

Finally, at a mass flux of 650 kg/m^{2}s, the mean percentage deviation of the experimental data against the time fraction data increased to 127%, while the

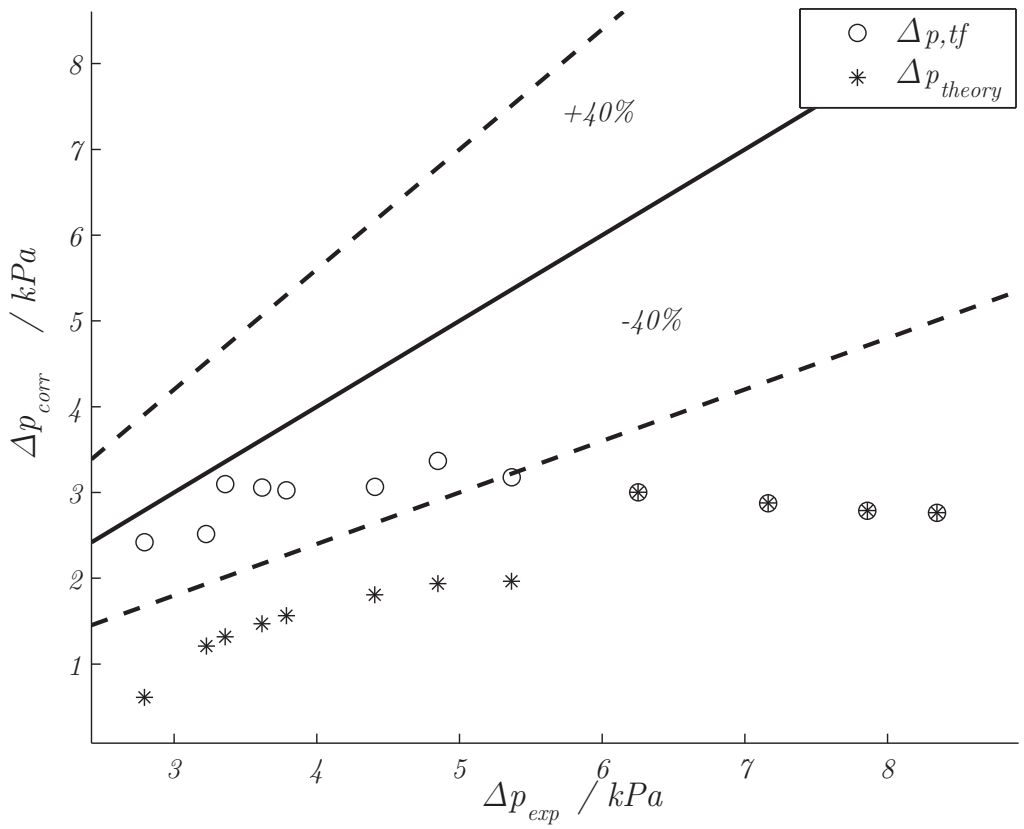

Figure 5.31: Comparison of the experimental frictional pressure drop against predicted data at G = 500 kg/m^{2}s

deviation against the original correlations was 174%. The influence of the stratified correlation decreased a large amount, due to the rapid increase in the time fraction with vapor quality. As such, while there was a general increase in accuracy, the mentioned problems with the annular pressure drop prediction, as well as the experimental results limited said increase.

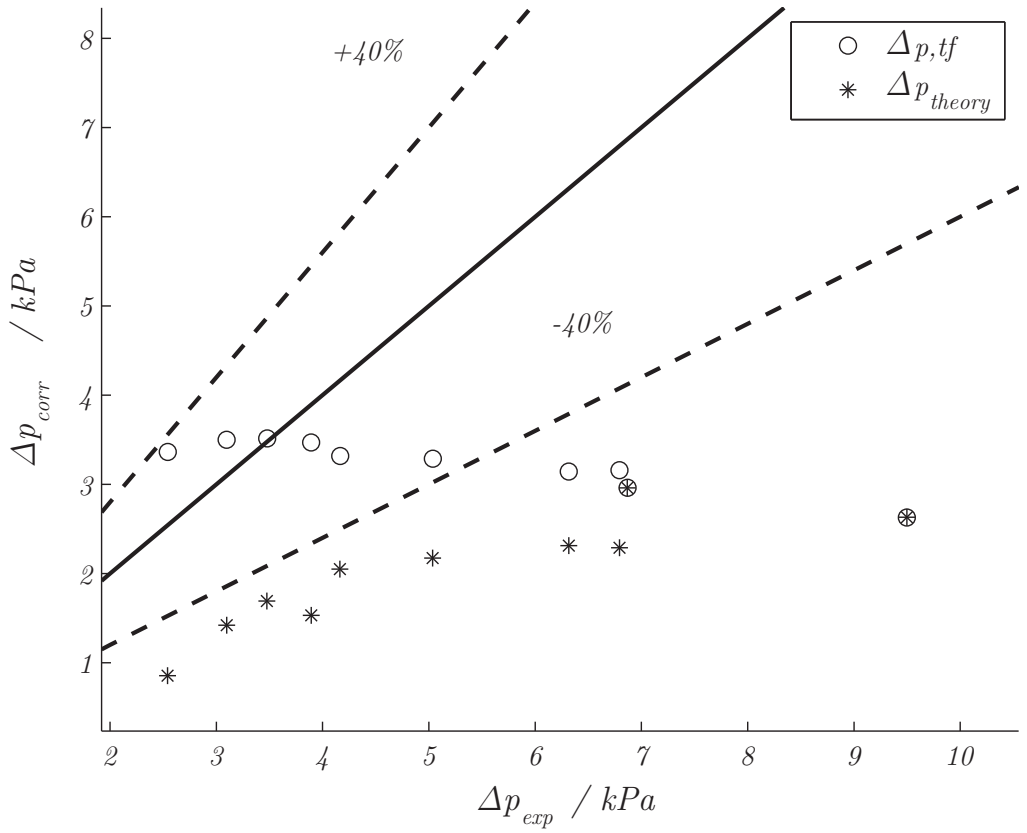

Figure 5.32: Comparison of the experimental frictional pressure drop against predicted data at G = 550 kg/m^{2}s

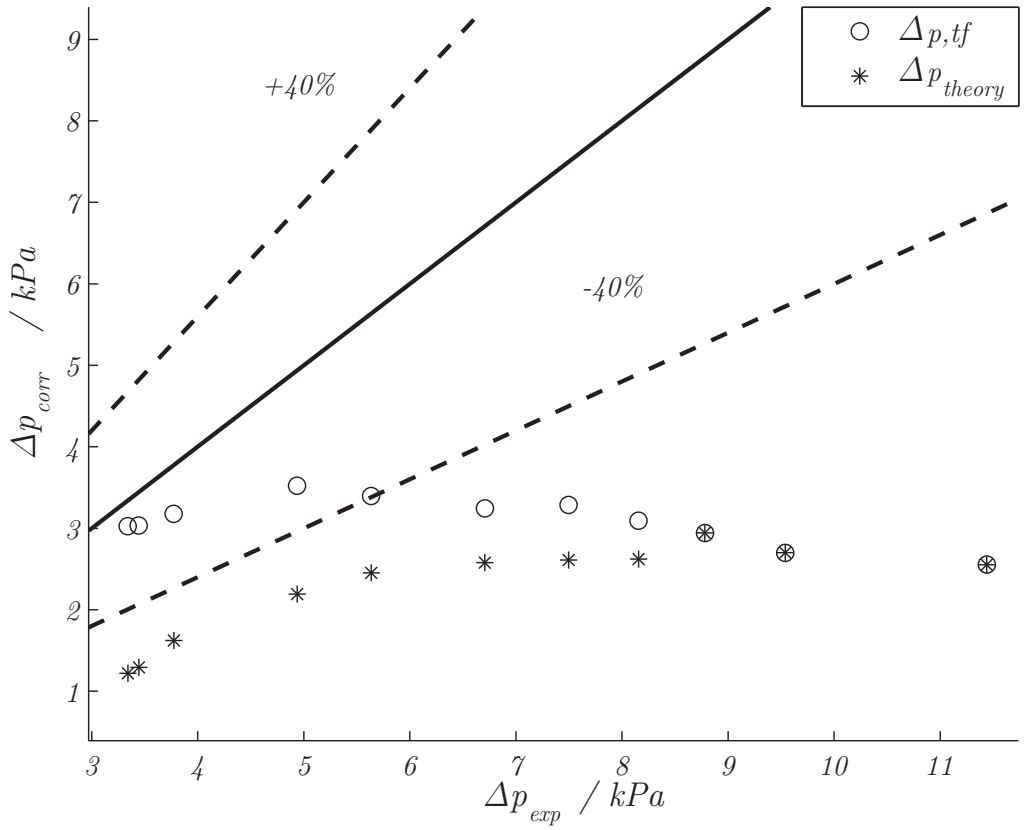

Figure 5.33: Comparison of the experimental frictional pressure drop against predicted data at G = 600 kg/m^{2}s

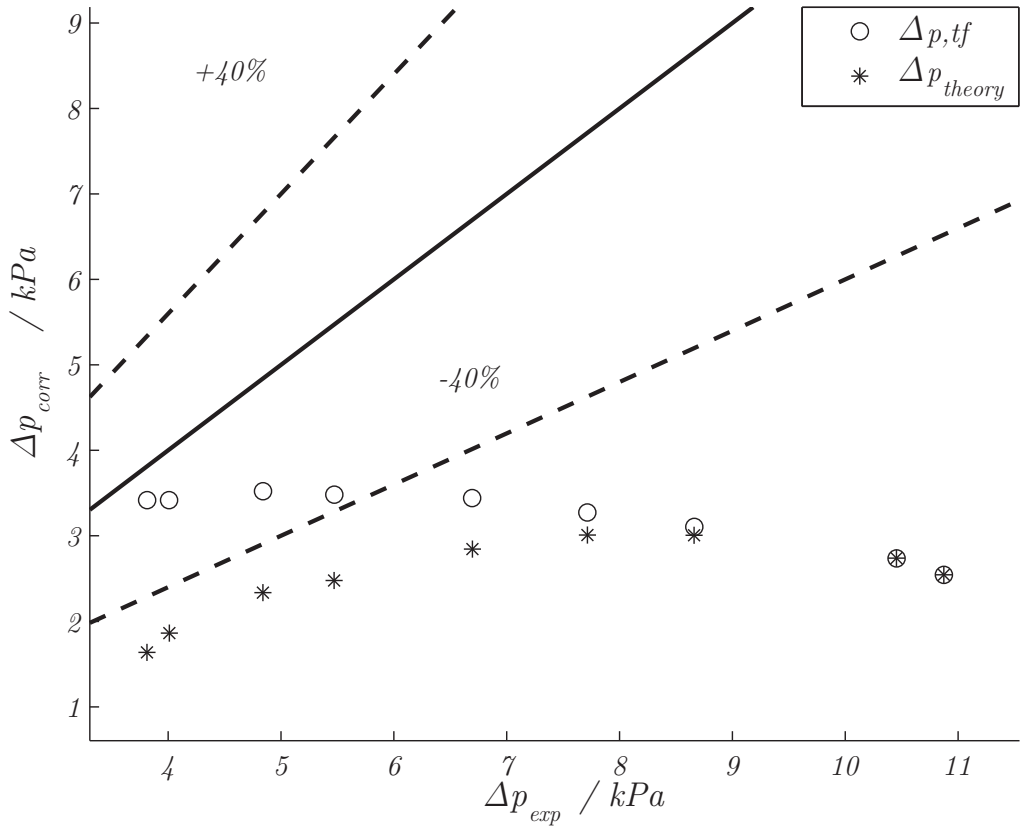

Figure 5.34: Comparison of the experimental frictional pressure drop against predicted data at G = 650 kg/m^{2}s

5.7 Sensitivity of the correlations to changes in the accuracy of the prediction components

Both the heat transfer and pressure drop coefficients are built up using three components, namely the time fraction, and the shear stress- and gravity-based correlations. It was found that, in general, the accuracy of the predictions increased using the time fraction correction. However, since the predictions are not only based on the time fraction data, it would be ideal to discuss the most important factors affecting the correlations. A sensitivity analysis with respect to the time fraction data, and the two local flow-pattern-based correlations would allow future research to be focused on the relevant and required areas.

The sensitivity analysis was performed by perturbing the general form of both the time fraction-corrected heat transfer and pressure drop correlations, in terms of the time fraction, as well as the gravity-based and shear stress-based pressure drop and heat transfer correlations. Each term was uniquely perturbed with $\pm 10\%$, and the mean percentage deviation against the experimental data was found. The main objective here was to gauge the response of the overall prediction to relatively small changes in the composition of its integrants.

5.7.1 Heat transfer

The first component perturbed was the time fraction tf, with $\pm 10\%$. When the time fraction is increased by 10%, the mean percentage deviation is 9.9%. From the previous sections, it is known that the mean deviation of the time fraction-corrected predictions versus the experimental data was 10.4%. However, decreasing the time fraction by 10% increases the deviation to 17%. If we take an average, and find the standard deviation, perturbing the time fraction by $\pm 10\%$ generates a deviation of 13.5%, with a standard deviation of $\pm 5\%$. This mean deviation is 30% higher than the original mean percentage deviation.

Then, only perturbing the gravity-based heat transfer component by 10% generates a mean deviation of 12%, while decreasing the gravity component by 10% increases the deviation sightly to 11%. The mean perturbed percentage

deviation from experimental data is 11.3% with a standard deviation of 0.56%. The perturbed deviation is 9% higher than the original deviation.

Finally, increasing the shear stress-based heat transfer component by 10% generates a mean deviation of 7.6%, while decreasing the prediction by 10% results in a deviation of 16% from experimental results. Thus, perturbing the shear-stress component generates a mean deviation of 11.6%, with a standard deviation of ±6%. The mean deviation is 11% higher.

From the above we may conclude that to increase the accuracy of the heat transfer correlation, not only must the time fraction be as precise as possible (due to the fact that changing the component by ±10% can generate a total deviation of ±5%), but the shear stress-based heat transfer component's accuracy is an extremely important factor, since a ±10% change in this component generated a ±6% change in the total deviation. The only perturbed constituent that had a very small effect on the total prediction was the gravity-based correlation, mainly due to the smaller range of affected data points.

5.7.2 Pressure drop

The same method is applied in the pressure drop as in the heat transfer analysis. Perturbing the time fraction tf by ±10% results in a new mean percentage deviation of 71% compared to the time fraction corrected deviation of 62%. Decreasing the time fraction by 10% increases the deviation to 98%. Thus a ±10% change in the time fraction tf results in a mean deviation of 85%, with a standard deviation of 19%.

Increasing the shear-stress component by 10% results in a mean deviation of 67%, compared to a deviation of 106% when decreasing the component by 10%. The mean deviation when disturbing the shear-stress component by ±10% is 86.3% with a standard deviation of 28%. The mean deviation is 39% higher than the mean time fraction-corrected pressure drop deviation.

Finally, increasing the gravity-based component by 10% generates a mean deviation of 88%, while decreasing the prediction by 10% increases the deviation up to 78%. The mean deviation for a ±10% change is 83%, with a standard

deviation of 8%. The mean deviation is also 34% higher than the mean time fraction-corrected pressure drop deviation.

In the case of the pressure drop, it can be seen that the final result in much more sensitive to perturbances in any of the components than in the heat transfer. However, to increase the accuracy of the prediction, it must be stated that the most sensitive constituent is, by far, the shear stress-based pressure drop correlation, due to the fact that a ±10% change in the prediction alters the deviation by 28%. The second most important aspect which will alter the accuracy of the general prediction is the time fration tf, followed by a non-negligible third, the gravity-based correlation.

In general terms, it can be seen that both the heat transfer and pressure drop predictions' accuracies are highly dependent on the shear stress-based heat transfer correlation component, and the time fraction, while the gravity-based component is less important. This could be due to the fact that the mean time fraction in the Intermittent flow regime is 0.71, indicating that most of the time is spent in shear stress-dominated heat transfer and pressure drop modes.

5.8 Oil concentration in the testing refrigerant

The oil concentration in the refrigerant was tested using ASHRAE standard 41.4 (ASHRAE, 2006) which describes the correct procedure to analyze the oil content of the refrigerant circulating in the system. The oil concentration in the refrigerant was sampled at the inlet of the test section, at mass fluxes of 250, 450 and 600 kg/m^{2}s, with the refrigerant subcooled and superheated. Furthermore, the system was allowed to settle at these points for 15 minutes before sampling was begun. After following the procedure setout in the ASHRAE standard, the oil concentration was found to be a maximum of 2.3% at the higher mass fluxes and qualities tested. At lower vapor qualities and mass fluxes, the oil entrainment was 0.6%. The influence on the results show that the heat transfer was degraded at the higher mass fluxes. This is most easily identifiable by the trend that the correlations all tend to overpredict the heat transfer data (at higher mass fluxes, from 450 kg/m^{2}s and higher), and underpredict the pressure drop data at the same mass fluxes.

The effect of oil entrainment was analyzed by Shao and Granryd (1995), and an oil concentration of 2% was shown to affect the measured heat transfer coefficient by a maximum of 10% (degradation), and to increase the measured pressure by a maximum of 5%.

On the heat transfer experimental side, at high mass fluxes, where the oil entrainment is non-negligible, taking into account the effects of the oil entrainment by increasing the measured experimental heat transfer coefficients by 8% (this average comes from Shao and Granryd (1995)) at the higher mass fluxes (that is, $G > 500$ kg/m^{2}s) results in the modified comparison presented in Figure 5.35.

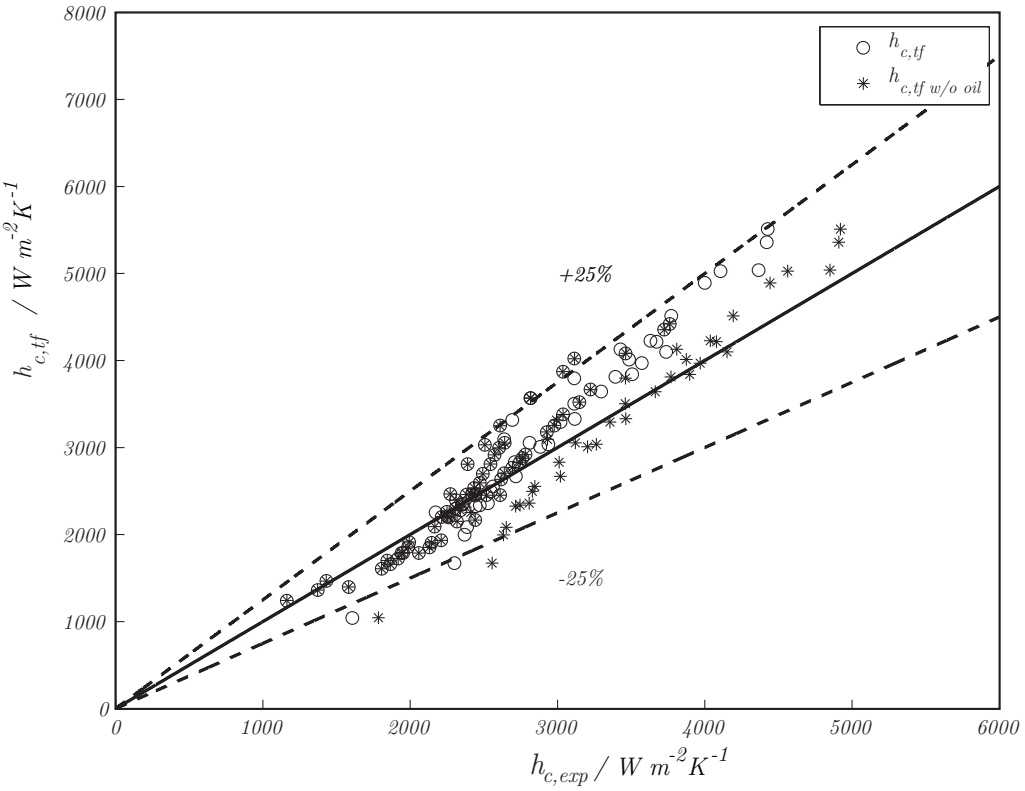

Figure 5.35: Oil entrainment effect on the heat transfer at high mass fluxes

On the pressure drop side, the theoretical increase in pressure drop does not readily increase the accuracy of the pressure drop results, mainly due to the fact that the physical measurements are still uncertain.

5.9 General uncertainty analysis

In this section, the general results obtained in the detail discussion of Appendix B are briefly discussed. Only the pertinent results are shown here. The entire discussion, including the derivation and the rest of the important results are discussed in the mentioned appendix.

5.9.1 Mean uncertainty analysis

In this section, the mean value of each measurand's uncertainty, with the associated standard deviation is presented. The full results encapsulating the entire test matrix are presented in Appendix B. Table 5.5 presents the average uncertainty in vapor quality at the inlet of the test section, the vapor quality difference between inlet and outlet of test section, the mean void fraction measurement, the momentum pressure drop, while Table 5.6 shows a more detailed presentation of the uncertainty in the frictional pressure drop and the heat transfer coefficient.

Table 5.5: Experimental uncertainties for condensation heat transfer and pressure drop

Measurand	Uncertainty (%)	
	Average uncertainty	**Standard Deviation**
δx_{in}	4.2%	±3%
δx_m	6%	±4.5%
$\delta \epsilon_m$	0.5%	±0.4%
$\delta \Delta p_{mom}$	7.5%	±4%

The inlet and outlet test vapor qualities, being functions of several heat exchangers' assorted uncertainties have widely varying uncertainties. Furthermore, they were also a function of the refrigerant's properties uncertainties, a large factor that is often neglected. On a constant vapor quality point of view, it was found that the best uncertainties in quality could be found at lower mass flux, while on a constant mass flux point of view, the best uncertainties were found at the higher vapor qualities.

The refrigerant properties did not play a major role in any of the uncertainties calculated in this study due to the fact that they were much smaller than the most uncertain factor in their equations. However, were experimental Nusselt numbers to be calculated, the uncertainty in thermal conductivity would be a very large factor, due to the fact that refrigerant thermal conductivity uncertainties vary between 2% and 6% (depending on the refrigerant), as stated in National Institute of Standards and Technology (2002).

The void fraction model is a strong function of the vapor quality, evidenced by the fact that the void fraction uncertainty was at its worse when the vapor quality also had a large uncertainty. Apart from the vapor quality, the logarithmic-mean void fraction model is a function of the vapor mass flux and the refrigerant properties; however, the density uncertainty of the refrigerant, as well as the mass flux uncertainty are quite low, which allow us to infer that vapor quality uncertainty has the largest influence in the uncertainty of the void fraction logarithmic-mean model.

As can be seen in Table 5.5, the uncertainty in momentum pressure drop is actually quite a large percentage of the physical momentum pressure drop value. However, the influence of this value is not readily noticeable in the frictional pressure drop, as the relative size of the term has a large influence. When the pressure drop measured over two pressure transducers is on the same order as the momentum pressure drop, the uncertainty in the momentum term will have a non-negligible effect on the frictional pressure drop. Furthermore, if a differential transducer is used, with a very high accuracy, the uncertainty in either term is on the same magnitude (assuming a differential transducer whose full-scale reading is 18 kPa and is 0.1% accurate); this means that both the uncertainties in the total pressure drop and the momentum pressure drop will have significant roles to play.

Table 5.6: Experimental uncertainties for the pressure drop and heat transfer coefficients

Measurand	***G*-250**	***G*-250**	***G*-650**	***G*-650**
Uncertainty	***x*-65%**	***x*-11%**	***x*-56%**	***x*-12%**
$\delta\Delta p_{f,L}$	60%	72%	38.5%	82%
$\delta h_{c,exp}$	0.21%	3.3%	0.6%	4%

In the specific case of the frictional pressure drop uncertainty reported in Table 5.6, the high uncertainty value is due to the fact that instead of utilizing a high accuracy differential pressure transducer over the test section, the difference in reading between two averaged gauge pressure sensor values was taken. The main problem with this, however, is that the pressure drop measured is very small compared to the full-scale reading of the pressure sensor, which eventually leads to a high uncertainty in the pressure sensor reading. It can also be seen that the uncertainty is greater at lower vapor qualities and at higher mass fluxes.

The heat transfer coefficient uncertainty described in Table 5.6 varies a large amount with vapor quality and less so with mass flux. The largest uncertainties are found at lower vapor qualities, when the temperature increase over the water side of the test heat exchanger drops, and the uncertainty in the temperature difference (reflected in the uncertainty in the water enthalpies measured) increases.

5.10 Conclusion

In this chapter, the experimental data collected in the smooth tube in water-to-water tests were discussed in the formulation of a new laminar to turbulent Wilson Plot method. It was found that the annulus-side thermal resistance was non-negligible and negatively affected the performance of the Wilson Plot method.

Furthermore, the experimental data gathered using the new system designed and built for this, and the related study of Van Rooyen (2007), were analyzed using refrigerant R-22. Through use of several objective flow pattern discriminators, the time fraction map of the Intermittent flow regime was developed (Van Rooyen, 2007).

Heat transfer coefficient measurements were made in the smooth tube test section, and compared against theoretical (Thome *et al.*, 2003) results. The mean percentage deviation of the entire data set was found to be $\pm 13\%$. Furthermore, the time fraction map was utilized to combine the shear stress-based and gravity-based Thome heat transfer predictors, and resulted in an increase of accuracy, especially at low vapor qualities (in the Intermittent flow regime). The mean percentage deviation of the entire data set decreased to $\pm 10\%$.

The pressure drop data was also combined using the time fraction data. Although the predictions were still very imprecise (mean deviation of ±60%), the most important result achieved was to generate a pressure drop correlation capable of predicting a continuous pressure drop increase as the vapor quality increased at a constant mass flux; this was seen as a very important deficiency in previous correlations, in the sense that the most correlations were not able to predict the pressure drop over flow regime transitions without discontinuities in their predictions.

Lastly, an in-depth uncertainty study of the experiment was undertaken, with the major goal of calculating uncertainties in vapor qualities, void fraction models utilized, momentum and frictional pressure drops, and heat transfer coefficients.

Chapter 6

Conclusions and Recommendations

6.1 Introduction

This chapter concludes the work performed on the Wilson plot method, new time fraction-corrected heat transfer and pressure drop correlations and the experimental uncertainties in refrigerant condensation in smooth tubes. Validation of the work done will be discussed in terms of the latest findings pertaining to these areas, and the objectives that have been met. Aspects meriting further investigation, as well as recommendations in terms of the experimental system will be detailed.

6.2 Consolidation of the work performed

Throughout the study many findings were made pertaining to tube-in-tube condensation experiments in the newly designed system, in regards mainly to the heat transfer and pressure drop. First, a study regarding the feasibility of utilizing the Wilson plot method in this setup was undertaken. Second, the time fraction map generated by Van Rooyen (2007) was utilized together with the heat transfer and pressure drop data, to generate two new flow-pattern-based heat transfer and pressure drop correlations for refrigerant condensation in smooth tubes. Finally,

an uncertainty study of the experimental system was carried out.

6.2.1 Consolidation of work pertaining to the Wilson plot method

Due to the increased difficulty and cost in the manufacture of test sections with direct wall temperature measurements, a feasibility study was carried out to examine the possibility of using the Wilson plot method to accurately predict the inner-tube heat transfer coefficients. Due to the unique test section flow rate requirements, the annulus water Reynolds number would never be in the turbulent regime, requiring a laminar correlation for the shell-side heat heat transfer coefficient. The following results were observed:

- The laminar-turbulent tube-side Wilson plot regression analysis resulted in a moderate curve, with little scatter (The coefficient of determination was $R^2 = 0.967$).
- The laminar-turbulent annulus Wilson plot regression analysis resulted in a curve fit with a large amount of scatter (with a coefficient of determination value of $R^2 = 0.884$).
- The turbulent-turbulent analysis of the experimental data resulted in an annulus side Wilson plot with a very large degree of data scatter, while the tube side correlation prediction was essentially identical to that found in the laminar-turbulent Wilson plot.

Apart from the major issue of data scatter on the annulus-side of both analysis methods, it was found that the experimental heat transfer coefficients' mean percentage deviation from the developed inner tube correlation was relatively large (7.3%), due mainly to two reasons; the first is that there were several points where achieving adequate energy balances ($< 1\%$) proved to be impossible, not because of physical heat loss issues, but rather due to inaccuracies in measurements. Second, the poor performance of the Wilson plot method in the annulus-side negatively affects the prediction of the inner tube heat transfer coefficients.

Upon further analysis, it was found that the underlying problem with the above experimentation stemmed from the fact that to generate accurate Wilson plots, the thermal resistance of the annulus must be small compared to the inner-tube thermal resistance, meaning that the heat transfer coefficient must be very high (which in turn means the flow must be as high as possible). However, in this case, the inner tube was fully turbulent, while the annulus was in the laminar flow regime, meaning that the controlling thermal resistance was actually in the annulus. Due to the refrigeration testing requirements, it was not possible to circumvent these problems.

The above problems, coupled with the in-house development of quick, leak-tight and hassle-free direct wall thermocouple installation procedures completely negated the advantages of the Wilson plot method. As such, the main conclusion that can be made regarding the application of the Wilson plot method to this experimental setup is that, due to the inaccuracies originating from the refrigeration testing requirements, this method be completely forgone, and only direct wall temperature measurements be considered for the measurement of inner-tube heat transfer coefficients.

A conjecture that arises from this study is that there is no reason why a laminar-turbulent Wilson plot analysis, where the inner tube is in the laminar flow regime and the annulus is fully-turbulent, should not give adequate and accurate results. This statement cannot be proved from the results gathered in this section, however.

6.2.2 Validation of the experimental test section in terms of the heat transfer prediction

In this study, the well-known and accurate correlation of Thome *et al.* (2003) was utilized to benchmark the system, in the sense that it was used to compare the heat transfer experimental data. The experimental heat transfer coefficient was measured using the water mass flow rate, the measured heat transfer out of the refrigerant, the mean condensing refrigerant temperature, and the mean of the wall temperature measurements. A total of 101 data points were captured using

refrigerant R-22 in a smooth 8.38 mm (3/8 *in*) outer diameter tube, ranging from a mass flux of 250 kg/m^{2}s to 650 kg/m^{2}s and a vapor quality range of 5% up to 65%. The selection of these parameters was taken to maximize the time spent in the Intermittent flow regime (the flow regime of most interest to this study), but to not neglect transitions into the outlying flow regimes; that is, the Annular and Stratified-wavy flow regimes.

The flow regime-based heat transfer correlation of Thome *et al.* (2003) predicted the experimental data with a mean percentage deviation of 13%, as shown in Figure 6.1.

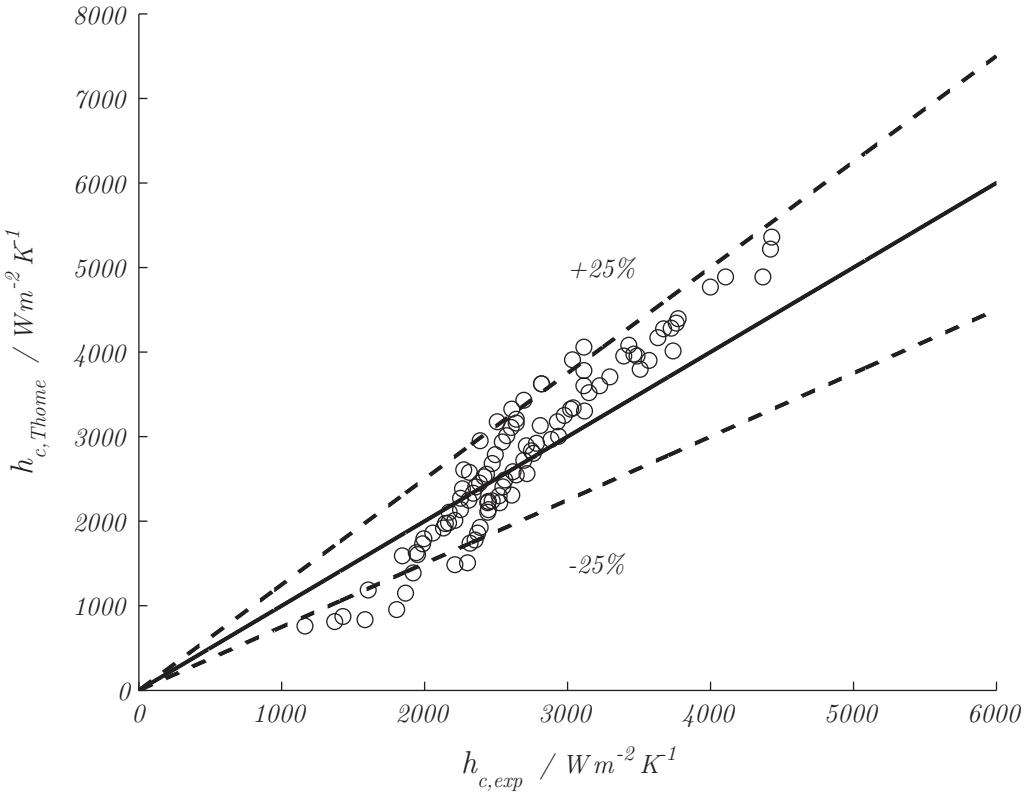

Figure 6.1: Comparison of the experimental heat transfer coefficients and the Thome correlation predictions

At the lowest mass flux and vapor qualities (the lowest heat transfer coefficients, ranging from 1 000 to 2 000 W/m^{2}K), the Thome correlation underpredicted the

heat transfer coefficient by as much as 30%. These points were shown to be close to the transition line between the Stratified-Wavy and Intermittent flow regimes, and could be in a transition band, where the flow alternates between these two flow regimes (Thome, 2005). Since this is not modeled by the Thome flow map nor his correlation, this underprediction is expected. The majority of the rest of the data lie well inside the published accuracy band of the correlation (the few that do not have been discussed in the discussion).

The relatively close agreement between the experimental data and the Thome correlation support the conclusion that the instrumentation, data analysis and test section construction are all correct.

6.2.3 Development of a flow-pattern-based time fraction-corrected heat transfer coefficient correlation

The time fraction map of Van Rooyen (2007) was used in conjunction with the Thome flow map (El Hajal *et al.*, 2003) and the Thome flow-pattern-based heat transfer correlation for smooth tubes to generate a new flow-pattern-based time fraction-corrected heat transfer correlation.

The major objective in this section was to generate a heat transfer correlation that depended not on 'fudge-factors' or 'modifiers' but rather on the physics of the flow. Thus, instead of modifying Thome's correlation (which was developed using data from several independent laboratories worldwide and a very large amount of experimental data), complementary information was required to what was already available.

The time fraction map was developed by Van Rooyen (2007) and essentially accounts for the probability that, at any moment, the flow in the Intermittent flow regime will either have a shear stress-dominated heat transfer mode, a gravity-dominated heat transfer mode or a combination of both. Thus a time fraction of $tf = 0.6$ essentially states that 60% of the time, at that mass flux and vapor quality, the dominating heat transfer mode will be shear stress-based.

The method utilized to generate this heat transfer coefficient correlation was to perform a linear combination of the shear stress-based and gravity-based heat

transfer coefficient correlations as used by Thome. The final form of the flow regime-based time fraction-corrected heat transfer correlation is

$$h_{c,tf} = tf \cdot h_{c,shear} + (1 - tf) \cdot h_{c,grav} \tag{6.1}$$

This new correlation predicts the R-22 experimental data to a mean deviation of 10%. The points that were best improved were those at low vapor qualities, where the time fraction was also low, which increased the influence of the gravity-based heat transfer prediction. The new correlation's predictions compared to the experimental data and the Thome correlation predictions are shown in Figure 6.2.

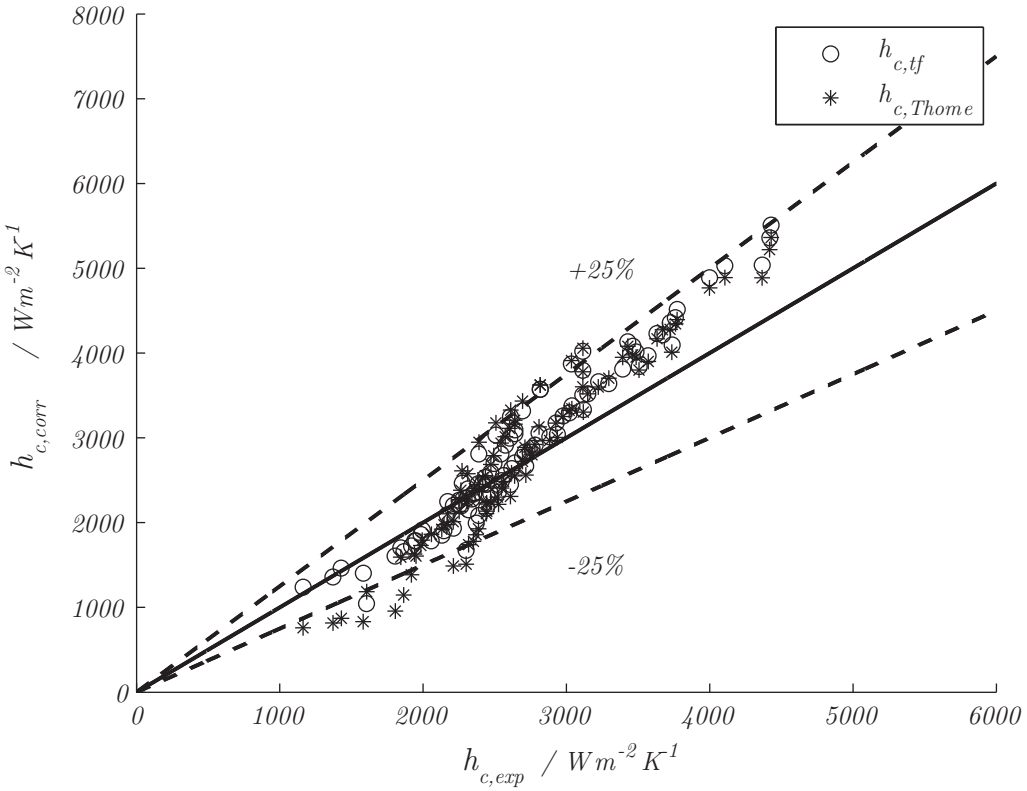

Figure 6.2: Comparison of the experimental data with theoretical predictions

The main objective of adding new data to Thome's correlation, to improve the accuracy in the Intermittent flow regime, without changing the functional form of

his gravity- and shear stress-based correlations was successfully completed.

6.2.4 Validation of the experimental test section in terms of the pressure drop prediction

In this study, two well-known correlations, that of Müller-Steinhagen and Heck, and that of Grönnerud (Ould-Didi *et al.*, 2002)were utilized to benchmark the system, in the sense that they were used to compare the pressure drop experimental data. The experimental matrix was the same as described in Section 6.2.2. These two correlations were chosen due to the fact that they were found to be the most accurate in the Annular flow regime (Müller-Steinhagen and Heck) and the Stratified flow regime (Grönnerud) by Ould-Didi *et al.* (2002) in a study performed with data gathered in several sizes of tubes and with many refrigerants.

The two correlations predicted the experimental data with a mean percentage deviation of 156%, as shown in Figure 6.3.

It was concluded that there were two major problems. First, the pressure drop was measured using the difference of the measurement of two gauge pressure readings (themselves the average of three pressure sensors). However, due to the large full-scale range of the transducers utilized, and to the short test section length, the uncertainty in the measurements were extremely large; furthermore, some of the pressure drop measurements taken were below 0.1% of the full-scale value of the transducers (the accuracy of these sensors), further worsening the prediction. Second, it can be seen that the predicted pressure drop flattens out at about 3 kPa (differential); this shows that the prediction is flawed; however, due to the large uncertainty, it was thought best to not forcefit the experimental data by changing the leading coefficients or exponents of the pressure drop correlations based on these experimental data. The target correlation of any change would be the Annular (*i.e.* Müller-Steinhagen and Heck) correlation.

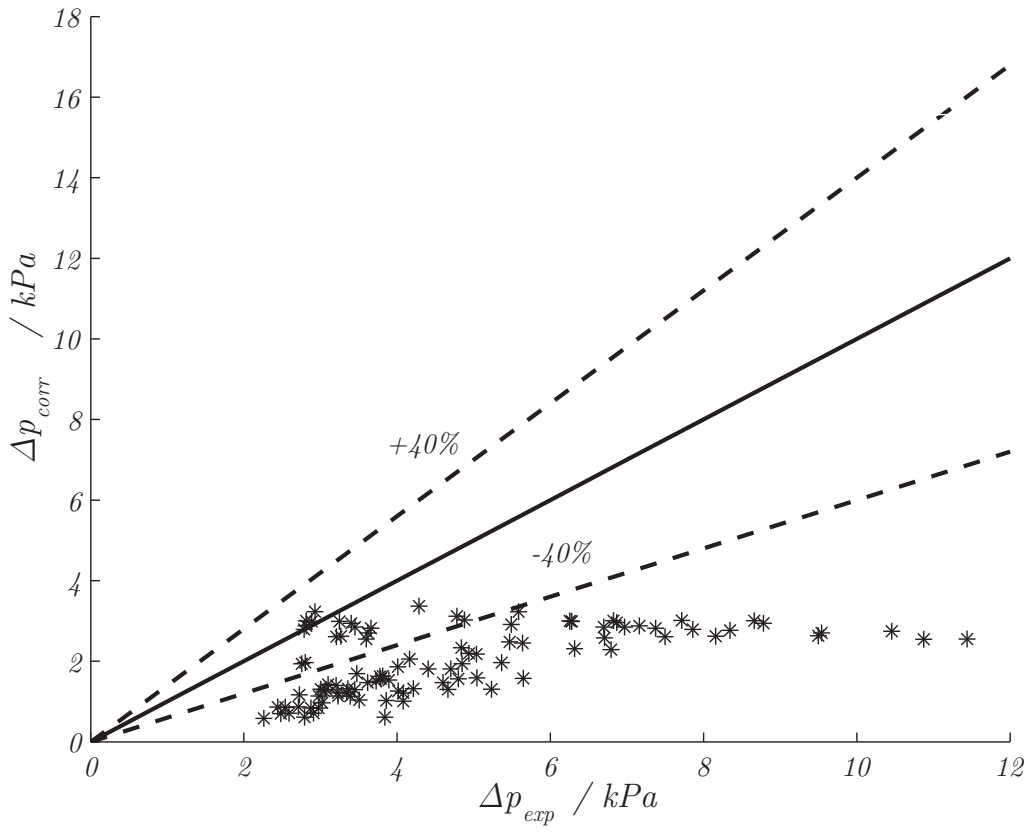

Figure 6.3: Comparison of the experimental pressure drop results and the theoretical predictions

6.2.5 Development of a flow-pattern-based time fraction-corrected frictional pressure drop correlation

Due to the success in increasing the accuracy of the Thome heat transfer prediction, it was hypothesized that the pressure drop correlations might also benefit from correction using the physically relevant time fraction, even if the experimental data were inaccurate, and that the time fraction was developed to distinguish between dominant heat transfer modes. Thus, the time fraction map of Van Rooyen (2007) was used in conjunction with the correlations utilized in the two defining flow regime (*i.e.* the Annular and Stratified-wavy regimes) to generate a

new flow-pattern-based time fraction-corrected heat transfer correlation.

The method utilized to generate the pressure drop correlation was the same as with the heat transfer coefficient correlation, namely to perform a linear combination of the shear stress-based and gravity-based heat transfer coefficient correlations as used by Thome. The final form of the flow regime-based time fraction-corrected pressure drop correlation is

$$\Delta p_{f,tf} = tf \cdot \Delta p_{f,shear} + (1 - tf) \cdot \Delta p_{f,grav} \tag{6.2}$$

This new correlation predicts the R-22 experimental data to a mean deviation of 62%. The points that were best improved were those at low vapor qualities, in which previously the annular pressure drop correlation had absolutely no influence. As the time fraction increases, the time fraction-corrected correlation's predictions tend towards the annular (Müller-Steinhagen and Heck) correlation predicitons, which have been shown to be innacurate, due to the fact that they remain constant regardless of mass flux, or vapor quality. The new correlation's predictions compared to the experimental data and the theoretical correlation predictions are shown in Figure 6.4.

The major benefit arising from the adoption of the time fraction into the pressure drop stems from the continuous pressure drop predictions that occur over flow regime transition regions, unlike previous correlations which, over transitions, would predict a discontinuous step in pressure drop, which does not happen in real systems. This is illustrated in Figure 6.5, a comparison of predicted pressure drops at a mass flux of 350 kg/m^{2}s.

6.2.6 Consolidation of work pertaining to the experimental uncertainty analysis

An in-depth uncertainty study of the experiment was undertaken, with the major goal of calculating uncertainties in vapor qualities, void fraction models utilized, momentum and frictional pressure drops, and heat transfer coefficients.

It was found that the vapor quality uncertainty has a large influence on the void fraction model's uncertainty, and these two have a large influence on the

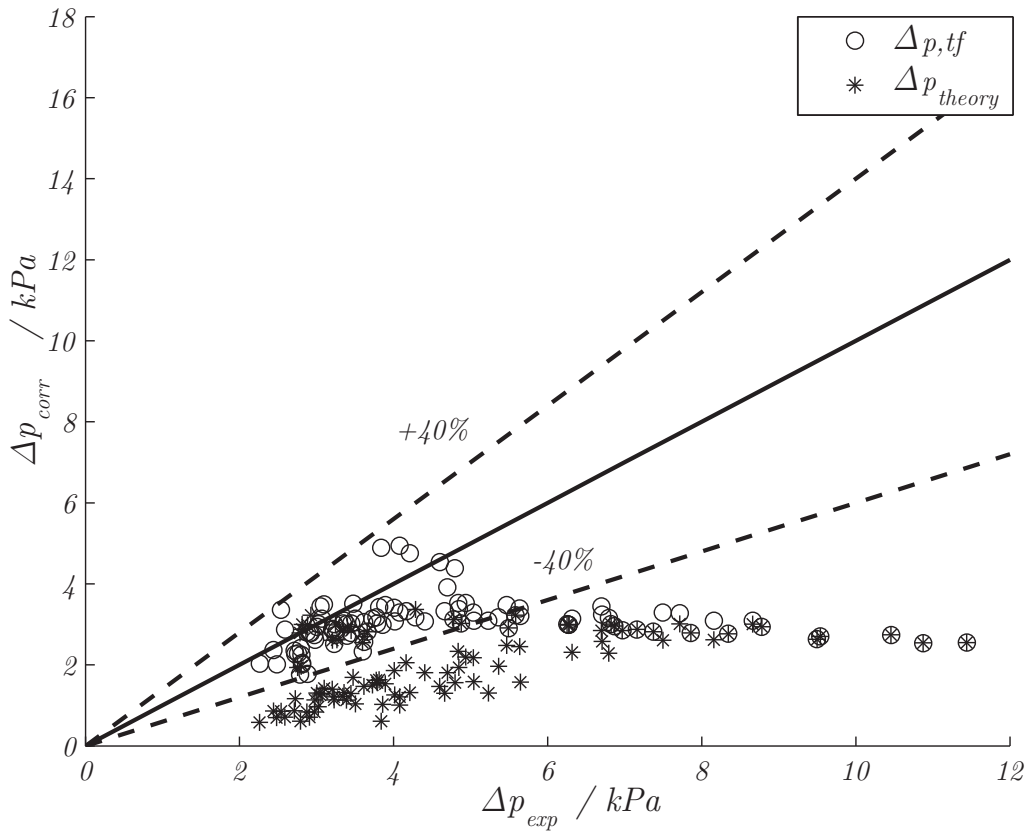

Figure 6.4: Comparison of the pressure drop experimental data and theoretical predictions

momentum pressure drop uncertainty. The momentum pressure drop uncertainty, on the other hand, only has a large influence on the frictional pressure drop when the uncertainty in the total pressure drop measurement is relatively low (*e.g.* when using a high accuracy differential pressure transducer).

The very high uncertainty in the frictional pressure drop ($30\% < \delta\Delta p_f < 80\%$) illustrates that the measurements being taken at the moment are not sufficient for high-quality research purposes.

At low vapor qualities, the heat transfer coefficient uncertainty is a strong function of the test heat exchanger water-side temperature difference, as the uncertainty increases to its maximum of 4%, and that temperature differential is

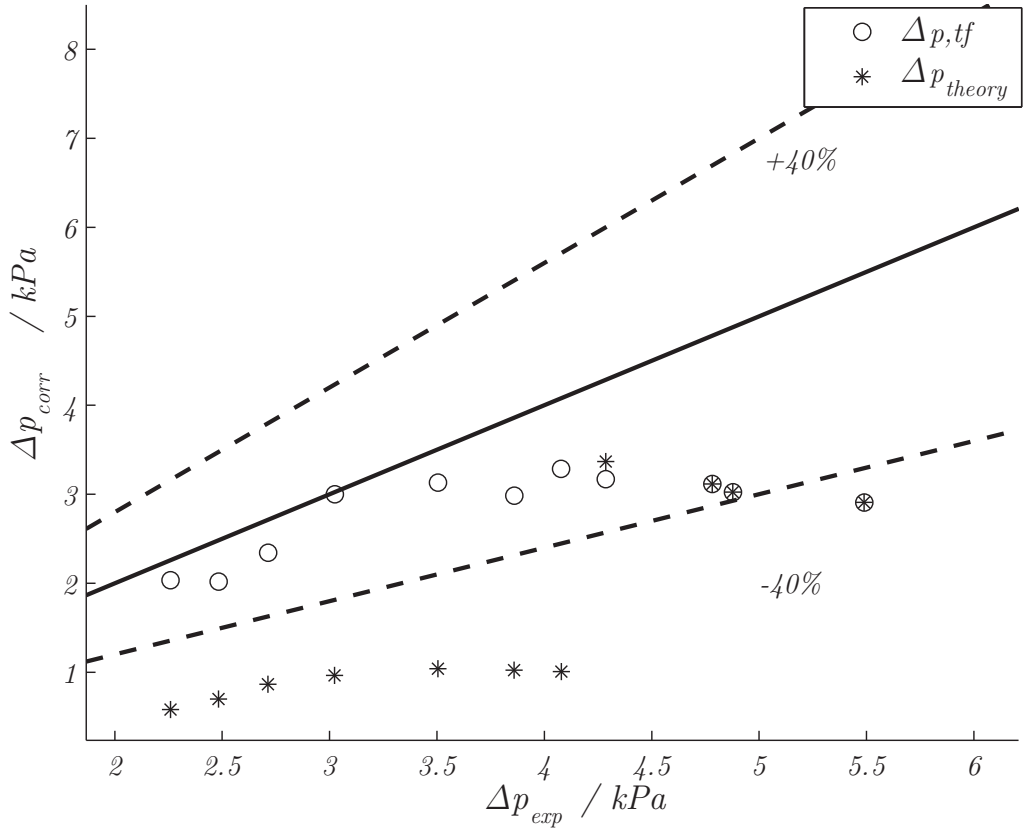

Figure 6.5: Comparison of experimental and theoretical pressure drop at G = 350 kg/m^{2}s

low.

Although it was shown that for the quantities calculated the refrigerant properties were not the over-riding factor, it should be noted that dimensionless numbers such as the Nusselt number and the Reynolds numbers, functions of the thermal conductivity and dynamic viscosity of the fluid respectively will have quite large uncertainties, due to the high innate uncertainties of those specific refrigerant properties.

6.3 Validation in terms of the objectives

The objectives that were presented in Section 1.3 were satisfied by the presented work.

First, the sound design, manufacture and operation of the experimental system were established and confirmed by the comparison of the results gathered from the setup, in which the majority of the results positively reflect published data.

Second, a study into the suitability of the use of the Wilson plot method in the test rig was undertaken, and it was shown that heat transfer coefficient measurements using direct wall temperature measurements were more reliable and accurate.

Third, the time fraction data obtained by Van Rooyen (2007) was utilized to develop a flow regime-based time fraction-corrected heat transfer correlation, which increased the accuracy of the heat transfer prediction in the Intermittent flow regime. This was successfully achieved by adding more information about the physical occurrences in the flow, rather than through use of non-natural multipliers.

Fourth, the time fraction data was utilized to show that a flow regime-based time fraction-corrected pressure drop correlation is achievable using more accurate total pressure data, which apart from increasing the accuracy of the prediction, can also predict continuous pressure drop readings over transition curves, unlike existing correlations.

Both the heat transfer and the pressure drop results have been summarized and will be presented to the international community in Christians-Lupi *et al.* (2007b) and Christians-Lupi *et al.* (2007a).

Finally, an in-depth uncertainty of the experimental setup was carried out, in which the effect of seldom accounted for variables, such as the refrigerant properties, the void fraction model prediction and the momentum pressure drop were taken into account. It was shown that none of these are always negligible, and their inclusion must be studied on a case by case basis.

6.4 Aspects meriting further investigation

As some of the aspects of this work are new, and complex, further research definitely needs to be carried out. Specific areas that should be given priority should be the expansion of the time fraction mapping into other refrigerants. It should be noted that the time fraction was not given as a function of mass flux and vapor quality, due to the fact that testing was only carried out with R-22, and only in smooth tubes.

Therefore, the only type of curve fit that would have been possible would not have been physically representative. That is to say that the time fraction map behavior should be studied in several refrigerants, and in differently-sized tubes, such that the time fraction map may be formulated specifically in terms of the refrigerant properties.

Once work is concluded using the smooth tube and several refrigerants (such as R-134a, R-407C and R-410a), the time fraction-correction method should be applied to enhanced tubes. In enhanced tubes, since transition to Intermittent flow is retarded to lower vapor qualities ($25\% < x_{IA} < 30\%$), it should be expected that the time-fraction map could only be applied to a smaller test matrix. This, by itself, presents a unique challenge, due to the fact that very fine control is required over the inlet vapor quality, such that enough data can be gathered for correct conclusions to be made.

Of interest would be to analyze different laboratories' data using the time fraction-corrected correlation, to prove it is a general method.

In terms of the pressure drop work, once a differential pressure transducer is setup over the test section, the R-22 data points should be redone, and data should be gathered using more refrigerants. The same course of action as for the heat transfer coefficient correlation should be taken, seeing as the method shows promise, due to the fact that it has actual physical meaning (rather than being an arbitrary multiplier), and that it can predict pressure drops over flow regime transitions correctly.

In terms of the experimental setup, although the system has very few faults, they are there and could be addressed.

First, to speed up testing and to allow for complete modularity, one more SCXI-1303 – SCXI-1102 combo should be purchased, such that a second test section may be instrumented with wall thermocouples while the first is undergoing testing. At the moment, there is only one card available for wall temperatures (which is fully used), and to make sure that the calibration constants do not change, the thermocouples should not be taken out until work is completely finished.

Second, while the Honeywell mixing valves work very well, it is sometimes necessary to make extremely fine adjustements, and they are not sensitive enough for those. It might be advantageous to replace the test line water mixing valves (*i.e.* the pre-, test- and post-condensers' valves) with either more sensitive mixing valves, or to replace the pumps with inverter-controlled counterparts, similar to those in use by the research group's single phase flow setup.

Also, the current refrigerant mass flow meter allows the user to test at a maximum of 0.04 kg/s (roughly 720 kg/m^{2}s in an 8.38 mm inside diameter tube). The installation of a parallel larger flow meter, such as a Coriolis CMF-025, would expand the test matrix up to a mass flux of 3 000 kg/m^{2}s.

Finally, if a brighter Phlox backlight is available, it might be advantageous to purchase it, such that the shutter speed of the high speed camera may be increased to its maximum of 1/10 000th of a second, and truly sharp images (especially in the Annular Flow regime) may be saved.

6.5 Conclusion

The research that was performed in this study was neither exhaustive nor definitve, and as such, should not be seen as a final conclusion. And, although the objectives of the study have been fulfilled, further research is required to fully explore the possibilities that time fraction mapping may have for the accuracy of both heat transfer and pressure drop predictions during refrigerant condensation.

References

S. Abu-Eishah. Correlations for the thermal conductivity of metals as a function of temperature. *International Journal of Thermophysics*, 22:1855–1868, 2001. 200

ASHRAE. *ASHRAE Handbook, Fundamentals*. American Society of Heating, Refrigeration and Air-Conditioning Engineers, 1^{st} edition, 2001. 90, 94

ASHRAE. Ashrae standard 41.4: Method for measurement of proportion of lubricant in liquid refrigerant. Technical report, ASHRAE, 2006. 144

J. Bear. *Dynamics of Fluids in Porous Media*. Dover Publications Inc., New York, NY, 2^{nd} edition, 1988. 23

D. Briggs and E. Young. Modified Wilson plot techniques for obtaining heat transfer correlation for shell and tube heat exchangers. *Journal of Heat Transfer*, 5:51–56, 1969. 171, 173

A. Cavallini, G. Censi, D. D. Col, L. Doretti, G. Longo, and L. Rosetto. Condensation of halogenated refrigerants inside smooth tubes. *International Journal of HVAC&R Research*, 8:429–451, 2002. 84

A. Cavallini, D. D. Col, L. Doretti, M. Matkovic, L. Rosetto, and C. Zilio. Condensation in horizontal smooth tubes: A new heat transfer model for heat exchanger design. *Heat Transfer Engineering*, 27:31–38, 2006. 3, 82, 84, 89

K. Cho and S. Tae. Condensation heat transfer for R-22 and R-407C refrigerant-oil mixtures in a microfin tube with a U-bend. *International Journal of Heat and Mass Transfer*, 44:2043–2051, 2001. 76

M. Christians-Lupi, E. van Rooyen, L. Liebenberg, and J. Meyer. Flow pattern-based heat transfer correlations for condensing refrigerants in smooth tubes. *International Journal of Heat and Mass Transfer*, Submitted, To be published, 2007a. 161

M. Christians-Lupi, E. van Rooyen, L. Liebenberg, and J. Meyer. Flow pattern-based heat transfer correlations for refrigerant R-22 in smooth tubes. In *HEFAT - July 1-4, Sun City, South Africa*, 2007b. 161

S. Coetzee. The development of an experimental set-up to investigate heat transfer enhancement in tube-in-tube heat exchangers. Master's thesis, Rand Afrikaans University, Department of Mechanical Engineering, 2000. 193

J. Collier and J. Thome. *Convective Boiling and Condensation*. Clarendon Press, Oxford, 3^{rd} edition, 1994. x, 26, 30, 31, 32, 35, 38, 39, 40, 41, 42

M. De Paepe, H. Caniére, C. T'Joen, H.-J. Steeman, A. Willockx, M. Christians-Lupi, E. van Rooyen, L. Liebenberg, and J. Meyer. Refrigerant flow regime detection with a capacitance void fraction sensor. *9^{th} AIAA/ASME Joint Thermophysics and Heat Transfer Conference, 3-8 June, San Francisco, California*, 1:12, 2006. 25, 61, 76

P. De Vos. Experimental determination of the forced convective boiling heat transfer coefficients of R-407C in fluted-tubes. Master's thesis, University of the North-West, 2006. 171

D. Del Col, A. Cavallini, and J. Thome. Condensation of Zeotropic Mixtures in Horizontal Tubes: New Simplified Heat Transfer Model Based on Flow Regimes. *Journal of Heat Transfer*, 127:221–230, 2005. doi: NA. 88, 89

M. Dobson. *Heat Transfer and Flow Regimes during Condensation in Horizontal tubes*. PhD thesis, University of Illinois at Urbana–Champaign, 1994. 2

M. Dobson and J. Chato. Condensation in smooth horizontal tubes. *Journal of Heat Transfer*, 120:192–213, 1998a. 10, 82

M. Dobson and J. Chato. Condensation in smooth horizontal tubes. *Journal of Heat Transfer*, 120:193–213, 1998b. 27

J. El Hajal, J. Thome, and A. Cavallini. Condensation in horizontal tubes, part 1: two-phase flow pattern map. *International Journal of Heat and Mass Transfer*, 46:3349–3363, 2003. x, xi, xvi, 11, 12, 13, 14, 15, 16, 24, 63, 86, 101, 102, 154, 201

FP2000 User's Manual. *http://www.sensotec.com*. Sensotec, Columbus, OH. 72, 197

M. Goto, N. Inoue, and N. Ishiwatari. Condensation and evaporation of r410a in internally grooved enhanced tubes. *International Journal of Refrigeration*, 24: 628–638, 2001. 62

E. Jassim. *Probabilistic flow regime map modelling of two-phase flow*. PhD thesis, University of Illinois at Urbana-Champaign, 2007. 29, 30

N. Kattan, J. Thome, and D. Favrat. Flow Boiling in Horizontal Tubes. Part 1: Development of a Diabatic Two-Phase Flow Pattern Map. *Heat Transfer*, 120: 140–147, 1998a. doi: NA. 11, 111

N. Kattan, J. Thome, and D. Favrat. Flow Boiling in Horizontal Tubes. Part 3: Development of a New Heat Transfer Model Based on Flow Patterns. *Heat Transfer*, 120(1):156–165, 1998b. doi: NA. 11

H. Khartabil, R. Christensen, and D. Richards. A modified Wilson-plot technique for determining heat transfer correlations. *Proceedings of the Second UK National Conference on Heat Transfer*, 11:1331–1357, 1988. xiii, 178, 179

S. Kline and F. McClintock. Describing uncertainties in single-sample experiments. *Mechanical Engineering*, 75:3–8, 1953. 193

E. Lemmon. Refprop 7 enthalpy uncertainty. Private e-mail conversation 08-Nov-06, November 2006. 198

L. Liebenberg. *A Unified Prediction Method for Smooth and Microfin Tube Condensation Performance*. PhD thesis, Rand Afrikaans University, Department of Mechanical Engineering, 2002. 1, 10, 18, 26, 50, 73, 75, 88, 90, 171, 194

J. Lienhard and J. Lienhard. *A Heat Transfer Textbook*. Phlogiston Press, 3^{rd} edition, 2005. 9, 10, 170

Matlab R16. *http://www.mathworks.com*. Reading, MA, 2006. 64

A. Mills. *Heat Transfer*. Prentice Hall, Inc., 2^{nd} edition, 1999. 9

National Institute of Standards and Technology. *NIST Thermodynamic PProperties of Refrigerants and Refrigerant Mixtures Database*. ver 7.0, Gaithersburg, MD, 2002. xiv, 8, 64, 147, 197

National Instruments. *LabView 8 Academic Edition*. Austin, Texas, 2005. 54

V. Niño, P. Hrnjak, and T. Newell. Characterization of two-phase flow in microchannels. *Air conditioning and refrigeration center*, Project 107:1–97, 2002. 29

J. Olivier. Pressure Drop during Condensation inside Smooth, Helical Microfin, and Herringbone Microfin tubes. Master's thesis, Rand Afrikaans University, Department of Mechanical Engineering, 2003. 8, 10, 17, 90

J. Olivier, L. Liebenberg, M. Kedzierski, and J. Meyer. Pressure drop during refrigerant condensation inside horizontal smooth, helical microfin, and herringbone microfin tubes. *Journal of Heat Transfer*, 126:687–696, 2004. 17

M. Ould-Didi, N. Kattan, and J. Thome. Prediction of two-phase pressure gradients of refrigerants in horizontal tubes. *International Journal of Refrigeration*, 25: 935–947, 2002. 90, 91, 92, 93, 94, 126, 127, 129, 156

Z. Rouhani. Internal report, AE-RTV 841. *AB Atomenergi*, 1969. 21, 23

Z. Rouhani and E. Axelsson. Calculation of volume void fraction in the subcooled and quality region. *International Journal of Heat and Mass Transfer*, 13: 383–393, 1970. 15, 24

F. Rowland and M. Molina. Stratospheric sink for chlorofluoromethanes: Chlorine atom catalyzed catalyzed destruction of ozone. *Nature*, 249:810–812, 1974. 1

M. Shah. A general correlation for heat transfer during film condensation inside pipes. *International Journal of Heat and Mass Transfer*, 22:547–556, 1979. 27, 82, 83

R. Shah. Assessment of modified Wilson plot techniques for obtaining heat exchanger design data. *Journal of Heat Transfer*, 5:51–56, 1990. 171, 177

R. Shah and A. London. *Laminar Flow: Forced Convection in Ducts*. Academic Press, New York, NY, 1^{st} edition, 1978. 180

D. Shao and E. Granryd. Heat transfer and pressure drop of R-134a-oil mixtures in a horizontal condensing tube. *International Journal of Refrigeration*, 18: 524–533, 1995. 145

E. Sieder and G. Tate. Heat transfer and pressure drop of liquids in tubes. *Industrial and Engineering Chemistry*, 28(12):1429–1435, 1936. 171, 172

D. Steiner. Heat transfer to boiling saturated liquids. *VDI-Wärmeatlas (VDI Heat Atlas)*, Verein Deutscher Ingenieure, VDI-Gessel schaft Verfahrenstechnik und Chemieingenieurswesen (GCV), D usseldorf, 1993. 15, 24

Thermal Analysis Partner XPROPS. *http://www.thermalanalysispartners.com*. University of Maryland, MD, 2006. 64

J. Thome. Update on Advances in Flow Pattern Based Two-Phase Heat Transfer Models. *Experimental Thermal and Fluid Science*, 29(3):341–349, 2005. doi: 10.1016/j.expthermflusci.2004.05.015. 11, 12, 111, 154

J. Thome. On recent advances in modeling of two-phase flow and heat transfer. *Keynote address: 1st International Conference on Heat Transfer, Fluid Mechanics, and Thermodynamics*, 8 - 10 April:13 pages, 2002. 10

J. Thome, J. El Hajal, and A. Cavallini. Condensation in horizontal tubes, part 2: new heat transfer model based on flow regimes. *International Journal of Heat*

and Mass Transfer, 46:3365–3387, 2003. xi, 3, 10, 15, 16, 25, 26, 27, 28, 85, 86, 88, 89, 106, 107, 110, 112, 148, 152, 153

T. Ursenbacher, L. Wojtan, and J. Thome. Interfacial Measurements in Stratified Types of Flow, Part I: New Optical Measurement Technique and Dry Angle Measurements. *Journal of Multiphase Flow*, 30(2):107–124, 2004. doi: NA. 25

E. Van Rooyen. Time-fractional analysis of flow patterns during refrigerant condensation. Master's thesis, University of Pretoria, Department of Mechanical Engineering, 2007. xiv, 4, 76, 104, 105, 106, 112, 148, 150, 154, 157, 161

K. Watanabe. Uncertainties in enthalpy for the iapws formulation 1995 for the thermodynamic properties of ordinary water substance for general and scientific use (iapws-95) and the iapws industrial formulation 1997 for the thermodynamic properties of water and steam (iapws-if97). Technical Report 1, The International Association for the Properties of Water and Steam, 2003. 198

E. Wilson. A basis for rational design of heat transfer apparatus. *ASME transactions*, 37:546–668, 1915. 171, 172

L. Wojtan, T. Ursenbacher, and J. Thome. Measurement of Dynamic Void Fractions in Stratified Types of Flow. *Journal of Experimental Thermal and Fluid Science*, 29(3):383–392, 2005. doi: 10.1016/j.expthermflusci.2004.05.017. 25, 26

Wolverine Tube Inc. *Wolverine Product Brochure*. Wolverine, Hunstville, AL, 1999. 199

S. Zivi. Estimation of steady-state steam void-fraction by means of the principle of minimum entropy generation. *Journal of Heat Transfer*, 37:247–252, 1964. 18, 19, 20

N. Zuber and J. Findlay. Average volumeric concentration in two-phase flow systems. *Journal of Heat Transfer*, 87:453, 1965. 21

O. Zürcher, J. Thome, and D. Favrat. Evaporation of Ammonia in a Smooth Horizontal Tube: Heat Transfer Measurements and Predictions. *Journal of Heat Transfer*, 121:89–101, 1999. doi: NA. 17

Appendix A

Wilson Plot Method

A.1 Background

The analysis of a heat exchanger is usually hampered by the fact that neither the tube-side or the annulus-side heat transfer coefficients are known. As has been previously stated, condensing refrigerant flows in the inner tube, while cold water is circulated in a counterflow direction in the annulus. In the case of this study, the condensation tube-side heat transfer coefficient is required; it can be found from (Lienhard and Lienhard, 2005)

$$\frac{1}{UA} = \frac{1}{h_i A_i} + R_w + \frac{1}{h_o A_o} \tag{A.1}$$

where UA is the overall heat transfer coefficient, h_i and A_i are, respectively, the inside tube heat transfer coefficent and area, while R_w is the wall conduction resistance, and h_o and A_o are the annulus heat transfer coefficient and area. The above can be rearranged as shown in equation A.2 to find, using the experimental heat transfer data gathered, the inner tube heat transfer coefficient, which will then lead to Nusselt number calculations. It can be seen that fouling resistance is disregarded; in the case of condensation (or evaporation) heat transfer, this is not an issue.

$$h_i = \left(\frac{1}{UA} - R_w - \frac{1}{h_o A_o} \right)^{-1} \tag{A.2}$$

According to Shah (1990), accurate design data can be gathered from equation A.1 if the thermal resistance is significantly higher than the sum of the rest of the resistances (i.e. conductivity through the tube walls, and fouling resistance). In an experimental setup, it is not possible to estimate correctly these other resistances, which then gives us at least two additional unknowns in equation A.2, namely R_w and h_o. In these types of cases, the Wilson plot method can be utilized, as discussed in Wilson (1915), Briggs and Young (1969) and implemented in Liebenberg (2002) and De Vos (2006).

The original Wilson plot method determined the individual resistances from the overall resistances in turbulent flow, by establishing a relation between the tube annulus Nusselt number and the Reynolds and Prandtl numbers. Once this relationship has been set out, the heat transfer between tubes can be calculated using the inlet and outlet mean temperatures, and the two mass fluxes. The original Wilson Plot method has been modified, notably by Briggs and Young (1969), who included a viscosity correction term and gave the Nusselt numbers the same formulation as that proposed by Sieder and Tate (1936). Further modifications have been made to the Briggs and Young method by Shah (1990), who included effects on unknown wall resistances, among others.

A.2 Wilson Plot technique

As was stated in section A.1, the procedure utilized in this study requires the knowledge of the annulus-side heat transfer characteristics. The overall heat transfer coefficient can be found if one knows the quantity of heat transfer between the tube and the annulus - this is done using the average inlet and outlet temperatures of the two streams, and the two fluid mass flows. Checking the energy balance, and making sure it is less than 1%, allows us to neglect axial heat loss. Furthermore, this allows us to write:

$$UA = \frac{\dot{Q}_w}{\Delta T_{LMTD}} = \left(\frac{1}{h_i A_i} + R_w + \frac{1}{h_o A_o} \right)^{-1} \tag{A.3}$$

where UA is the overall heat transfer coefficient, $\dot{Q}_w$ is the heat input into the annulus-side ($\dot{m} c_p \Delta T$) and ΔT_{LMTD} is the log mean temperature difference, defined as:

$$\Delta T_{LMTD} = \frac{(T_{shell,in} - T_{shell,out}) - (T_{tube,in} - T_{tube,out})}{ln|\frac{(T_{shell,in} - T_{shell,out})}{(T_{tube,in} - T_{tube,out})}|}$$

while the conductive resistance of a smooth-walled tube is:

$$R_w = \frac{ln|\frac{D_o}{D_i}|}{2\pi k_{Cu} L}$$

where D_o is the outside diameter of the inner tube, D_i is the inside diameter of the inner tube, k_{Cu} is the thermal conductivity of the copper tube, and L is the length of the heat exchanger.

The annulus-side coefficient is assumed to be in the form proposed by Sieder and Tate (1936), for turbulent heat transfer inside a pipe:

$$Nu = \frac{hD}{k} = C_{ST} Re_w^a Pr_w^{0.4} \left(\frac{\mu}{\mu_w} \right)^{0.14} \tag{A.4}$$

where C_{ST} is the Seider-Tate coefficient. In their study, Seider and Tate found that $C_{ST} = 0.027$. However, in his original work, Wilson (1915) neglected the difference between the bulk and wall temperatures, leading to his eventual neglect of the viscosity term. Through experimental trial and error, he found $a = 0.82$. By substituting his values into the definition as shown in equation A.4 (Wilson, 1915):

$$h_i A_i = A_i \left(C_o k^{0.6} \rho^{0.82} c_p^0.4 \mu^{-0.42} D_h^{-0.18} \right)_i v^{0.82} \tag{A.5}$$

Due to the fact that, per point generated, $A_i \left(C_o k^{0.6} \rho^{0.82} c_p^0 .4\mu^{-0.42} D_h^{-0.18}\right)_i$ is constant, we can let it equal to C_1, an arbitrary constant.

Then, equation A.5 is converted to:

$$h_i A_i = C_1 v^{0.82} \tag{A.6}$$

Substituting equation A.6 into equation A.1, while also designating its last two right-hand terms as C_2:

$$\frac{1}{UA} = \frac{1}{C_1 v^{0.82}} + C_2 \tag{A.7}$$

Equation A.7 has a linear form of $Y = mx + b$, where $Y = (UA)^{-1}$, $b = C_2$, $x = v^{-0.82}$ and $m = C_1^{-1}$. This means that Wilson plotted $Y = (UA)^{-1}$ against $v^{-0.82}$ on a linear scale. Since both of these are known from the experimental data acquired during testing, both the intercept $m = C_1^{-1}$ and $b = C_2$ can be found. Furthermore, once C_1 is known, all of the heat transfer coefficients can be determined. However, the Wilson plot method does have several restrictions. Firstly, it requires that the flow rate and the fluid temperature be maintained constant (i.e. maintain C_2 constant). Additionally, the difference between the bulk and wall temperatures is not taken into account either. Furthermore, the major requirement of this method (which is carried over to both the Briggs and Young, as well as the modified Shah methods) is that both fluid streams must be in the turbulent regime.

A.3 Briggs and Young modifications to the original Wilson Plot technique

Briggs and Young (1969) proposed several modifications to the original Wilson Plot technique to address the shortcomings detailed in the previous section. In

their method, the heat transfer coefficients for both the inside tube and the annulus are assumed to be of the following form:

$$h_i = C_i \frac{k_i}{D_i} Re_i^a Pr_i^{0.4} \left(\frac{\mu}{\mu_w}\right)_i^{0.14} \tag{A.8}$$

$$h_o = C_o \frac{k_o}{D_o} Re_o^p Pr_o^{\frac{1}{3}} \left(\frac{\mu}{\mu_w}\right)_o^{0.14} \tag{A.9}$$

One of the first modifications to the Wilson Plot introduced by Briggs and Young was the assumption that the exponent a, of the inner tube's correlation Reynolds number is equal to 0.8. Further, it is shown that the Prandtl number exponent should be 0.4 for cooling, and 1/3 for heating. Equations A.9 and A.9, once introduced into equation A.1 result in:

$$\frac{1}{UA} = \frac{1}{C_i \frac{k_i}{D_i} A_i Re_i^{0.8} Pr_i^{0.4} \left(\frac{\mu}{\mu_w}\right)_i^{0.14}} + R_w + \frac{1}{C_o \frac{k_o}{D_o} A_o Re_o^p Pr_o^{\frac{1}{3}} \left(\frac{\mu}{\mu_w}\right)_o^{0.14}} \tag{A.10}$$

In the above equation, there are three unknowns remaining, namely the two heat transfer coefficient constants C_i, C_o and the exponent p. Furthermore, equation A.10 can be rewritten as:

$$\left[\frac{1}{UA} - R_w\right] \left(\frac{k_o}{D_o} A_o Re_o^p Pr_o^{\frac{1}{3}} \left(\frac{\mu}{\mu_w}\right)_o^{0.14}\right) = \frac{1}{C_i} \left[\frac{\frac{k_o}{D_o} A_o Re_o^p Pr_o^{\frac{1}{3}} \left(\frac{\mu}{\mu_w}\right)_o^{0.14}}{\frac{k_i}{D_i} A_i Re_i^{0.8} Pr_i^{0.4} \left(\frac{\mu}{\mu_w}\right)_i^{0.14}}\right] + \frac{1}{C_o} \tag{A.11}$$

Now, if we group everything on the left-hand side of the equal sign into a single term (since all of the terms within are known), and separate the right hand side into $mx + b$, as below:

$$Y = \left[\frac{1}{UA} - R_w\right]\left(C_o \frac{k_o}{D_o} A_o Re_o^p Pr_o^{0.4}\left(\frac{\mu}{\mu_w}\right)_o^{0.14}\right) \tag{A.12}$$

$$m = \frac{1}{C_i} \tag{A.13}$$

$$X = \left[\frac{\frac{k_o}{D_o} A_o Re_o^p Pr_o^{\frac{1}{3}}\left(\frac{\mu}{\mu_w}\right)_o^{0.14}}{\frac{k_i}{D_i} A_i Re_i^{0.8} Pr_i^{0.4}\left(\frac{\mu}{\mu_w}\right)_i^{0.14}}\right] \tag{A.14}$$

$$b = \frac{1}{C_o} \tag{A.15}$$

Due to the fact that it is possible to group the above in a linear form ($Y = mx + b$), a linear regression of Y on X, giving the least-squares values for m and b, will allow the approximation of the heat transfer coefficient correlation constants, C_i and C_o. However, this linear regression cannot be run only once, due to the fact that the wall temperatures are not known, which means that the viscosity correction terms will not be initially correct. The wall temperatures can be calculated as follows:

$$T_{w,i} = T_{b,i} - \frac{\dot{Q}}{h_i A_i} \tag{A.16}$$

Having approximated the inner-tube wall temperature, the shell-side inner-tube wall temperature can be calculated using the experimentally measured heat transferred (as long as the condition of the energy balance <1% holds):

$$T_{w,o} = T_{w,i} - \frac{\dot{Q} ln\left(\frac{D_o}{D_i}\right)}{2\pi k_{Cu} L} \tag{A.17}$$

Once this has been done, it is now possible to calculate the newest values for the shell(annulus)-side (C_o) empirical constant, and for p, the Reynolds number exponent for the annulus side. Equation A.10 can be rearranged as:

$$\left[\frac{1}{UA} - R_w - \frac{1}{C_i \left(\frac{k}{d}\right)_i Re_i^{0.8} Pr_i^{0.4} A_i \left(\frac{\mu}{\mu_w}\right)_i^{0.14}}\right] \left\{\left(\frac{k}{d}\right)_o Pr_o^{\frac{1}{3}} A_o \left(\frac{\mu}{\mu_w}\right)_o^{0.14}\right\} = \frac{1}{C_o Re_o^p} \tag{A.18}$$

If we let y_s equal the left hand side, then

$$\frac{1}{y_s} = C_o Re_o^p \tag{A.19}$$

by taking the natural logarithm of both sides,

$$\ln \frac{1}{y_s} = p \ln Re_o + \ln C_o \tag{A.20}$$

which can be rewritten as

$$Y = mX + b \tag{A.21}$$

where, evidently,

$$\begin{aligned} Y &= \ln \frac{1}{y_s} && \text{(A.22)} \\ m &= p && \text{(A.23)} \\ X &= \ln Re_o && \text{(A.24)} \\ b &= \ln C_o && \text{(A.25)} \end{aligned}$$

Hence, the annulus-side empirical constant and exponent can be calculated. The temperature iterative scheme is not calculated this step, as it already known, having been calculated in the previous step.

Consider the following hypothetical experimental matrix, where the annulus-side Reynolds number is plotted against the tube-side Reynolds number. This

shows that, for a certain test-side Reynolds number, the annulus-side Reynolds number is varied.

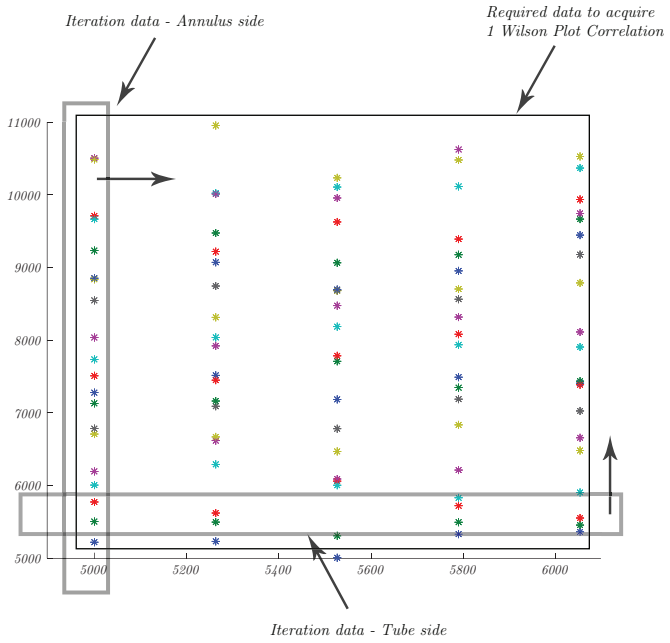

Figure A.1: Wilson Plot experimental matrix

To complete the Wilson Plot method, Equation A.15 must be iterated by varying the annulus-side linear interpolation, while keeping the tube-side Reynolds number constant. Then, Equation A.20 needs to be iterated by varying the tube-side mass flow and maintaining the same mass flow through the annulus.

A.4 Modified method of Shah

In Shah (1990) a modified Wilson plot technique, with five or four unknowns, to be used when testing augmented tube geometries is detailed. The main problem when testing in augmented geometries is that the heat transfer coefficients, as well as the thermal resistance of the wall R_w can be unknown. These are C_i, C_o, the empirical constants for the heat transfer correlations, a and p, the Reynolds

number exponents for the tube and shell side, and finally, the thermal resistance of the tube, R_w.

For the analysis, in addition to Equations A.11 and A.18, two additional equations are required; a tube-side modified Wilson-plot by manipulating Equation A.10 as

$$\ln \frac{1}{y_t} = a \ln Re_t + \ln C_i \tag{A.26}$$

where y_t is

$$y_t = \left[\frac{1}{UA} - R_w - \frac{1}{C_o} \left(\frac{k}{d} \right)_o Re_o^p Pr_i^{\frac{1}{3}} A_o \left(\frac{\mu}{\mu_w} \right)_o^{0.14} \right] \left\{ \left(\frac{k}{d} \right)_i Pr_i^{0.4} A_i \left(\frac{\mu}{\mu_w} \right)_i^{0.14} \right\} \tag{A.27}$$

and a wall resistance Wilson plot using,

$$\frac{1}{UA} = \left[\frac{1}{h_i A_i} + \frac{1}{h_o A_o} \right] + R_w \tag{A.28}$$

This equation also has the form of $Y = mX + b$ where $m = 1$, X is the bracketed term on the left and $b = R_w$. The iterative scheme of Khartabil *et al.* (1988), shown in Figure A.2, can be used to calculate all of the unknowns.

The three data sets referred to in the figure make allusion to:

Set 1 Dominant annulus-side data with complete range of annulus-side flow rates;

Set 2 Dominant tube-side data with complete range of tube side flow rates;

Set 3 Dominant wall resistance data with full range of both annulus- and tube-side flow rates

The main limitation of the Wilson Plot holds, namely the fact that all test data on one fluid side must be in one flow regime only.

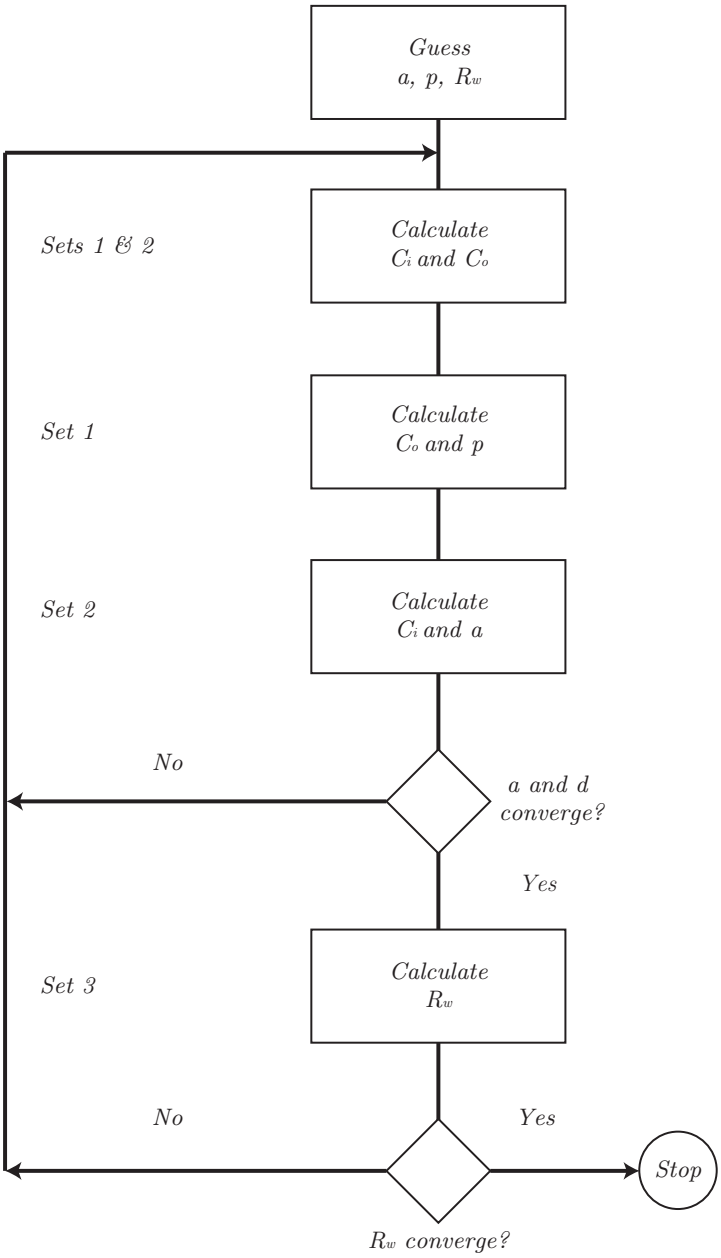

Figure A.2: Khartabil *et al.* (1988) iterative scheme

A.5 Turbulent-laminar modified Wilson plot method

While there are many instances in which turbulent-turbulent flow is encountered in shell and tube heat exchangers, there are, ocasionally, times when turbulent-turbulent flow is not found; rather, one of the two sides of the heat exchanger could be in the laminar flow regime. This is, in fact, the case in the experimental setup under investigation. In the tube (that is, the refrigerant side), turbulent flow is maintained throughout the test range; however, on the annulus side, the maximum Reynolds number that can be found is 1800. This limitation is encountered due to the small amount of heat transfer that is required such that small vapor quality changes occur over the test heat exchanger.

The equation for the overall heat transfer coefficient has been shown in Equation A.1, while the heat transfer coefficient for the tube side is also shown in Equation A.9. However, according to Shah and London (1978), the heat transfer coefficient correlation for the annulus side is

$$h_o = c_3 (x^*)^e \left(\frac{\mu}{\mu_w}\right)^{0.14} \left(\frac{k}{D_h}\right) \tag{A.29}$$

where

$$x^* = \frac{x}{D_h RePr} \tag{A.30}$$

where x is the length of the annulus (this is to account for the entrance effects), and the D_h is the hydraulic diameter, calculated as

$$D_h = \frac{4A_c}{P} = \frac{D_{o,i}^2 - D_{i,o}^2}{D_{o,i} + D_{i,o}} = D_{o,i} - D_{i,o} \tag{A.31}$$

$D_{o,i}$ is the inner diameter of the outer tube, while $D_{i,o}$ is the outer diameter of the inner tube.
Thus, substituting,

$$\frac{1}{UA} = \frac{1}{C_i \left(\frac{k}{D}\right)_i Re_i^{0.8} Pr_i^{0.4} \left(\frac{\mu}{\mu_w}\right)_i^{0.14} A_i} + R_w + \frac{1}{C_3 (x^*)^e \left(\frac{\mu}{\mu_w}\right)_o^{0.14} \left(\frac{k}{D}\right)_o A_o} \quad \text{(A.32)}$$

Rearranging, as previously,

$$\left(\frac{1}{UA} - R_w\right) \left[(x^*)^e \left(\frac{\mu}{\mu_w}\right)_o^{0.14} \left(\frac{k}{D}\right)_o A_o\right] = \left(\frac{1}{C_i}\right) \frac{(x^*)^e \left(\frac{\mu}{\mu_w}\right)_o^{0.14} \left(\frac{k}{D}\right)_o A_o}{\left(\frac{k}{D}\right)_i Re_i^{0.8} Pr_i^{0.4} \left(\frac{\mu}{\mu_w}\right)_i^{0.14} A_i} + \frac{1}{C_3} \quad \text{(A.33)}$$

The above is in the form of $Y = mX + b$, and is used to iterate for C_3 and C_i. For the tube-side Wilson Plot, we find, after performing the same operations in Section A.3

$$\left(\frac{1}{UA} - R_w - \frac{1}{C_i \left(\frac{k}{D}\right)_i Re_i^{0.8} Pr_i^{0.4} \left(\frac{\mu}{\mu_w}\right)_i^{0.14} A_i}\right) \left[\left(\left(\frac{\mu}{\mu_w}\right)_o^{0.14} \left(\frac{k}{D}\right)_o A_o\right)\right] = \frac{1}{C_3 (x^\star)^e} \quad \text{(A.34)}$$

Which, as was also shown in Section A.3, ends up in a formula of the form $Y = mX + b$ where

$$Y = \ln \frac{1}{Y_s} \quad \text{(A.35)}$$

$$m = e \quad \text{(A.36)}$$

$$X = \ln x^\star \quad \text{(A.37)}$$

$$b = \ln \frac{1}{C_3} \quad \text{(A.38)}$$

A.6 Wilson Plot Results for the experimental setup

The method developed in the preceding sections was developed for use with the experimental test section as described in Chapter 3. The procedure followed during experimentation was initially described in the section describing Briggs and Young's modification to the original Wilson Plot method. However, the method described there was stated in general terms, and was not specifically developed for the experiment range found in the two-phase experimental test section. Thus, a brief description of the experimental matrix is required.

A.6.1 Experimental Matrix

First of all, the test section was instrumented exactly as described in Chapter 3. The mass flow in the inner tube was varied over the entire valid range of the flow meter that it is coupled to, that is, a CMF-010 Coriolis mass flow meter (0.004 to 0.04 kg/s); this allowed us to experiment with a Reynolds number range that varied from 12 000 down to 500. On the annulus side, although it is know that the maximum mass flow is on the range of 0.03 kg/s (from previous experiments using the apparatus available for this experiment), the mass flow was varied over the entire valid range of the CMF-010 flow meter used. This allowed us to experiment with a Reynolds number range that varied between 2 500 and 300.

It should be evident that both sides of the heat exchanger transition from laminar to turbulent flow over the range of mass flows. For the Wilson Plot to successfully predict heat transfer coefficients, it is required that the flow strictly remain in a single regime. As such, before analysis of the data may be carried out, an initial filter must be applied on the data regarding the Reynolds number ranges. In the tube, data that was captured and that had a Reynolds number less than 2 500 was set aside, while in the annulus, data that had a Reynolds number greater than 2 000 was also set aside. This ensured, on both sides of the heat exchanger, that there was no flow regime transition.

For purposes of the Wilson Plot, a total of 200 data points were saved, of which 21 points were pre-filtered out due to the flow regime transition criteria set out above. Thus, a total of 179 data points were taken into account for the Wilson Plot analysis. Each data point consists of 400 samples taken over a 10 minute period. The average energy balance over the entire test matrix was 1.34%, with specific cases with an energy balance as low as 0.04% and as large as 4.75%. This large variance, its probable reason and its effects will be discussed in further detail in the following sections.

The general objective of the Wilson plot method is to find the leading coefficients and exponent of the tube-side and annulus-side correlations. We described the method in which we may calculate these using first order least-squares curve fits to the data. Then, the turbulent-turbulent and laminar-turbulent analysis methods were presented. For comparison's sake, the data captured were analyzed using both methods presented above.

A.6.2 Laminar-turbulent analysis results

The exponents and leading coefficients that were under consideration in this experiment were the following:

$$Nu_t = C_s Re^{0.8} Pr^{0.4} \left(\frac{\mu_w}{\mu}\right)^{-0.14} \tag{A.39}$$

and, on the annulus-side,

$$Nu_s = C_t (x^\star)^e \left(\frac{\mu_w}{\mu}\right)^{-0.14} \tag{A.40}$$

where the above have been explained in their respective sections. A custom Matlab code was written to analyze the data. To complete the Wilson Plot method, the recursive procedures involved were iterated until the relative errors were less than $1 \cdot 10^{-5}$, where the relative errors are calculated using the following formula,

$$error = |i_{j,old} - i_{j,new}| \tag{A.41}$$

where i can be any of the parameters being iterated, such as the shell-side and annulus-side leading coefficients, and the annulus-side exponent.

Due to the fact that the Wilson Plot method requires least-squares fits to be calculated, an indication of the adequacy of the fit is necessary. This can be achieved utilizing a statistical parameter called the coefficient of determination, or R^2, as it is usually shown. This coefficient varies between 0 and 1, where 0 indicates that the trends in the data are absolutely not described by the curve fit, while 1 indicates a perfect correlation between the experimental data and the correlation.

The laminar-turbulent tube-side experimental curve fit is shown in Figure A.3. The coefficient of determination can be calculated as 0.967, showing that the trends in the data are well represented by the curve fit.

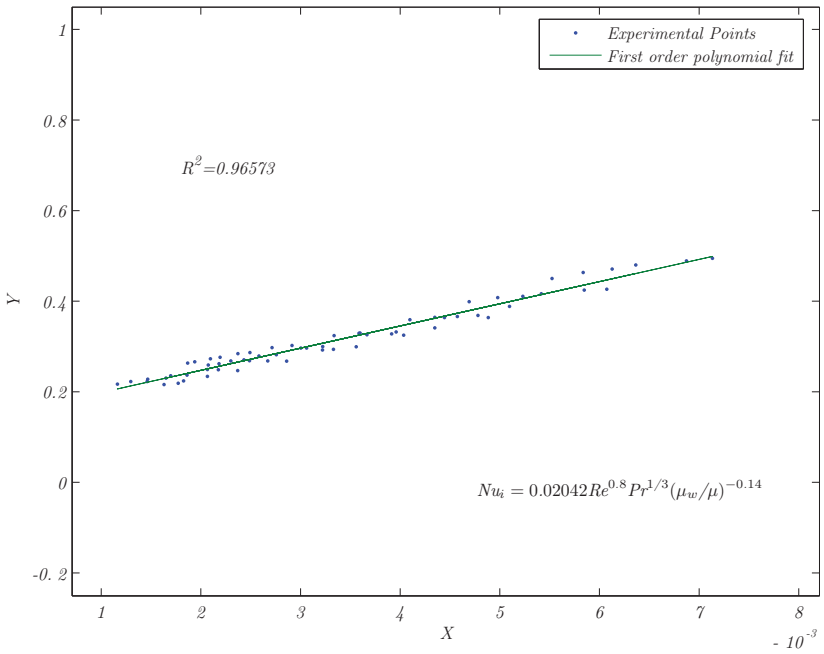

Figure A.3: Laminar-turbulent tube-side Wilson plot

The tube-side leading coefficient was iterated to a final value of $C_t = 0.0204$. Thus, in the case of the tube-side heat transfer correlation, with the leading

coefficient now calculated, the final form of the correlation becomes:

$$h_{c,t} = 0.0204 Re^{0.8} Pr^{0.4} \left(\frac{\mu_w}{\mu}\right)^{-0.14} \tag{A.42}$$

Then, the laminar-turbulent annulus-side experimental curve fit is shown in Figure A.4. The coefficient of determination was calculated as $R^2 = 0.88419$. In this case, it can be seen that the data are not as well described as in the tube.

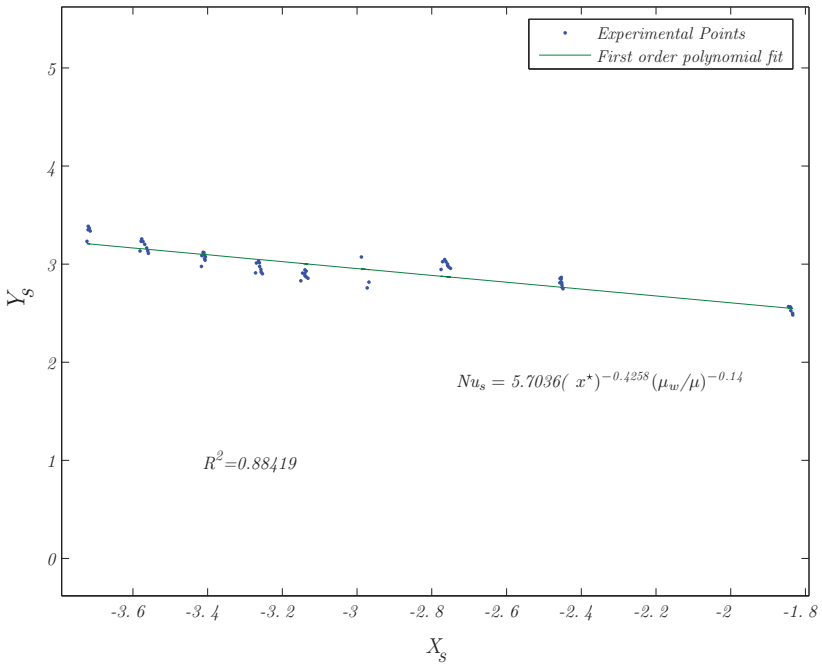

Figure A.4: Laminar-turbulent annulus-side Wilson plot

The final form of the annulus-side heat transfer correlation is

$$h_{c,s} = 5.7036(x^\star)^{-0.4258} \left(\frac{\mu_w}{\mu}\right)^{-0.14} \tag{A.43}$$

There are several reasons that can explain the phenomena present in the data. The first can more easily be explained with aid from Figure A.5. It shows a section

of a general tube-in-tube setup, with the three main heat transfer resistances singled out.

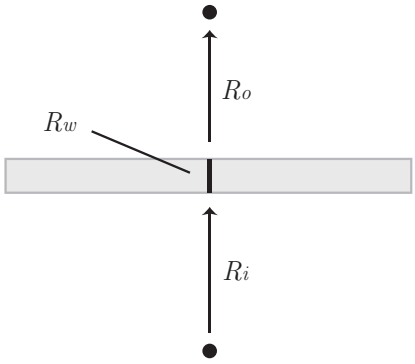

Figure A.5: Wall resistance schematic in a tube-in-tube heat exchanger

Due to the material selection (copper), the wall conduction resistance is, out of the three resistances, negligible. Further, fouling was disregarded as negligible on either side of the tube. In a well-designed Wilson plot experiment, the resistance of the auxiliary side (whether it is the tube-side or annulus depends on the goal of the experiment) should ideally be less than 10% of the main resistance. In the case of a tube-in-tube heat exchanger, if the inner tube resistance is the main resistance, the Reynolds number of the annulus side should be considerably larger than the inner tube. In this experiment however, not only was this not the case, but the annulus Reynolds number was generally the lower one, and in cases, an order of magnitude smaller. Although undesirable, it was unavoidable, due to the refrigerant testing conditions which were being emulated.

Second, the problem was exascerbated at several test points, in which there were large differences in Reynolds numbers (inner tube - 10 000, annulus - 500). Due to the fact that the lower mass fluxes were on the limit of accuracy of the flow meter, there was significant variation in the steady-state value saved. This affected the heat transfer quantity calculated for the annulus. Further, the large difference in mass flow led to temperature differences to be very small in the inner-tube, which led to a high fluctuation (and uncertainty) of the temperature drop in the inner-tube, and also resulted in heat transfer variations. The combination and

comparison of these two quantities in the energy balance calculation resulted in energy balances of up to 5%.

The effect of the fluctuating energy balances can be seen in the comparison of the experimentally measured inner-tube Nusselt number with that of the correlation developed with the Wilson Plot method. This is represented in Figure A.6.

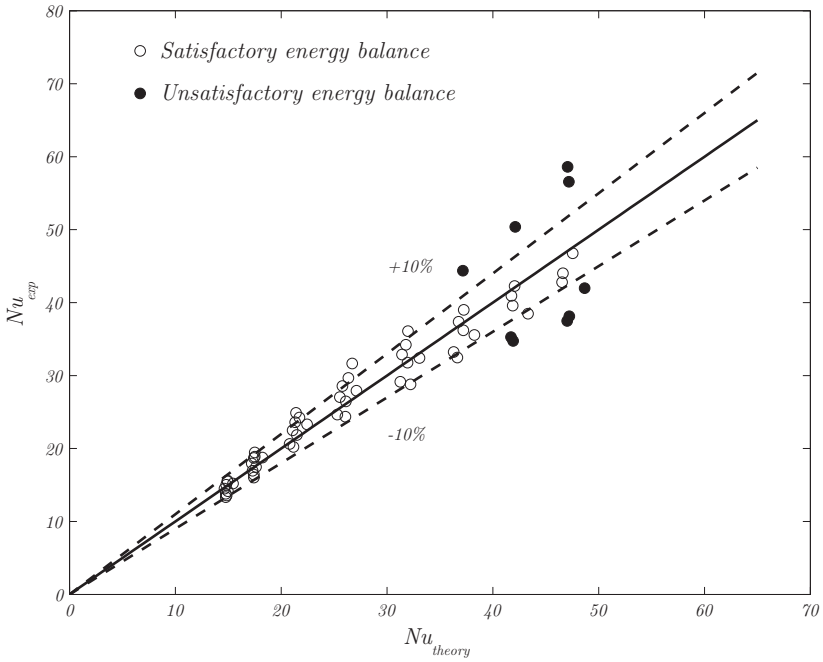

Figure A.6: Comparison of the laminar-turbulent inner-tube heat transfer coefficient and experimental data

While it is evident that the majority of the data points lie within acceptable bounds (*i.e.* $\pm\%10$), there are several data points, shown in the figure as shaded points, which do not. These represent data which did not achieve satisfactory energy balances. Apart from these points, the close relation between the predicted heat transfer coefficients and the experimental data show that the Wilson Plot method can generate adequate results. This is, of course, dependent on utilizing the test section in an adequate range.

A.6.3 Turbulent-turbulent analysis results

The data collected to be analyzed using a laminar-turbulent was also analyzed using the classical approach utilized for turbulent-turbulent flow, as describeb previously. This was done since the annulus-side correlation's major change was a change in exponent for the Prandtl and Reynolds number. The laminar correlation utilized was for forced laminar convection, in which mixed convection with natural convection was not taken into account. Due to the less than ideal result from the laminar-turbulent result, the turbulent-turbulent analysis was carried out, to check whether there might be a slight chance of an increase in accuracy, from a equation-form point of view.

The turbulent-turbulent tube-side Wilson plot least squares curve fit is shown in Figure A.7. The coefficient of determination was $R^2 = 0.96618$, showing that the inner tube data was well described by the form of the correlation chosen.

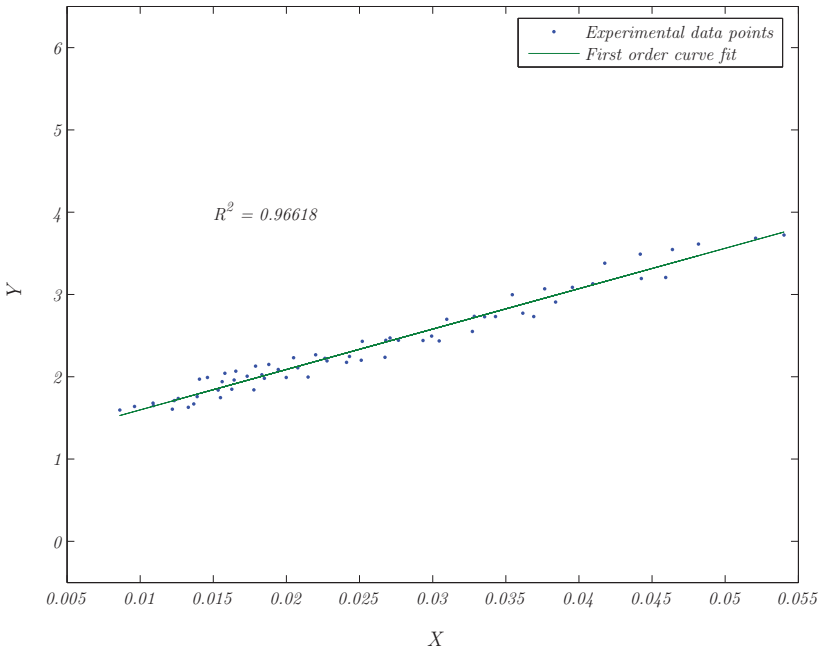

Figure A.7: Turbulent-turbulent tube-side Wilson plot

The leading coefficient iterated to a final value of $C_t = 0.0204$, exactly the

same as in the previous analysis. Further, the two coefficient of determination values were very close to each other, which led to significant confidence in the iterated value. The inner-tube correlation for the heat transfer then was

$$h_{c,t} = 0.0204 Re^{0.8} Pr^{0.4} \left(\frac{\mu_w}{\mu}\right)^{-0.14} \tag{A.44}$$

On the annulus-side, applying a turbulent form for the correlating equation yielded considerably worse results than the laminar-turbulent correlation equation. The annulus-side Wilson plot curve fit is shown in Figure A.8. Its coefficient of determination was $R^2 = 0.78788$, which shows that the form of the correlating equation does not actually capture the trends shown in the experimental data. Further, the calculated leading coefficient, and the Reynolds number exponent are, respectively, $C_s = 0.90796$ and $m = 0.3556$, considerably far away from the traditional values found in the turbulent flow.

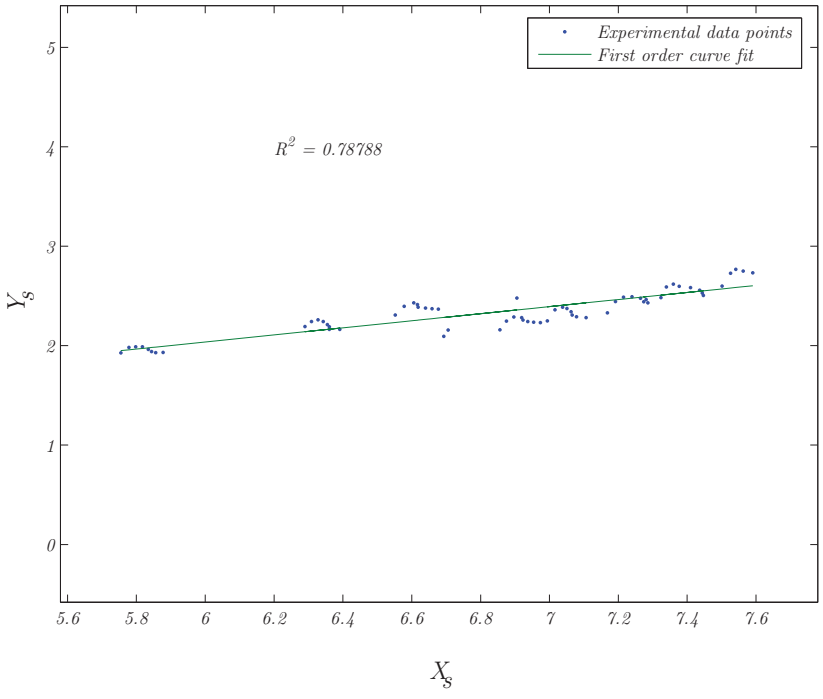

Figure A.8: Turbulent-turbulent annulus-side Wilson plot

The annulus-side equation is

$$h_{c,s} = 0.90796 Re^{0.3556} Pr^{\frac{1}{3}} \left(\frac{\mu_w}{\mu}\right)^{-0.14} \tag{A.45}$$

The effects of the inadequate fit can also be seen in the comparison between the measured Nusselt number and the calculated Nusselt number. Figure A.9 shows that, apart from the energy balance problems discussed in the previous section, there is also a fair amount of scatter arising from the suboptimal annulus-side heat transfer coefficient correlation.

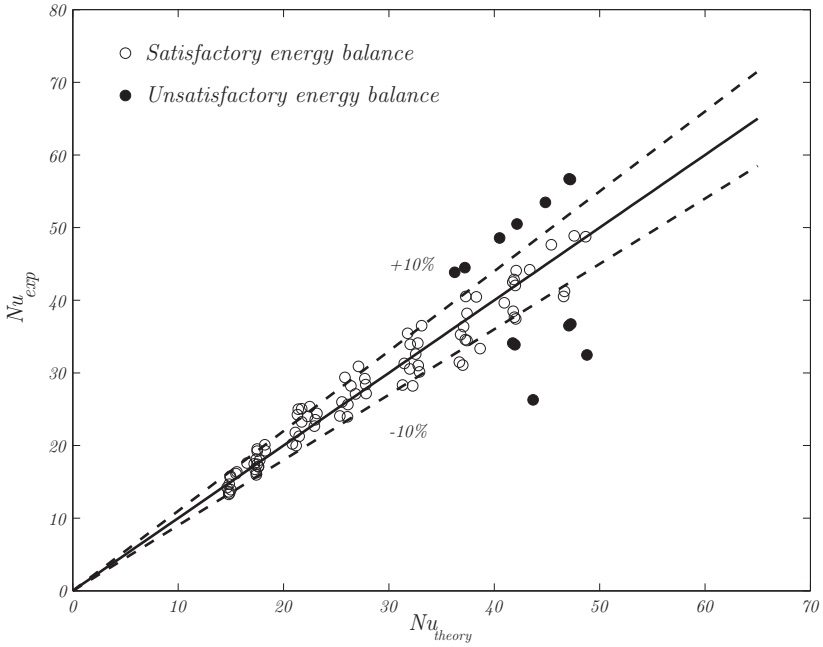

Figure A.9: Turbulent-turbulent comparison of the predicted Nusselt number against experimental data

Again, the data that were affected by the low temperature difference and mass flow sensitivity, and by the correlating equation for the annulus-side are shown in shaded form.

A.7 Conclusion

The Wilson Plot method, when properly utilized, and calculated, can generate extraordinarily good results; these, in turn, can simplify the development and construction of an experimental test section, especially considering that a vastly reduced number of thermocouples are needed. However, it is necessary to consider the implementation and setup of the experiment, to make sure that the Wilson Plot method returns usable results.

In this chapter, a laminar-turbulent implementation of the modified Wilson Plot method was attempted for the experimental test-section, as described in Chapter 3. While it was shown that the inner-tube heat transfer coefficient could be approximated with a reasonable degree of accuracy, several data points were captured in areas where the energy balance was over 1%, due to the sensitivity over the mass fluxes and temperature drops.

Second, it was attempted to analyze the data using a turbulent form for the annulus-side heat transfer correlation, which also did not give accurate results. While the general form is the same, the value of the exponents of the terms, particularly the Prandtl number, are very different, and lead to large errors. This suboptimal prediction of the annulus-side heat transfer coefficient is reflected in the subpar distribution of the predicted Nusselt numbers, when compared against sampled data from the system.

Finally, the major problem in this specific Wilson plot experiment is that outstanding accuracy will never be possible, due to the very specific range of Reynolds numbers required, which in turn lead to non-negligible heat transfer resistances in the annulus. As there is no way to circumvent this issue, the best recommendation that can be made is to forgo any further Wilson Plot experimentation (for this test apparatus) and to rather focus all time and effort into direct wall temperature measurements. The method for construction described in Chapter 3 works quite well in this regard.

Appendix B

Experimental Uncertainty Analysis

B.1 Introduction

In an experimental setup, any amount of measuring equipment may be utilized, and will return information; however, depending on the sensitivity and accuracy of the equipment, said information may have some slight bias, or drift, or may even be completely wrong. This problem is exacerbated when, not only are we interested in the values that are read, but calculations need to be performed using these values. If there is any error in an original reading, this error is carried forward into the equation, which, in turn, introduces error into an otherwise exact equation.

Uncertainty analysis is the general term for the method utilized to ascertain how accurately one can predict what one is measuring (and subsequently, calculating). The method utilized is described in Section B.2. The experiment-specific uncertainties are derived and calculated in the rest of this appendix.

The uncertainties derived in this section are all for single-sample data, seeing as test point data have been determined using averaged measurands, and evaluated using the same data-sampling rates. The work can be classified as single-sample

due to the large number of repeated tests which would need to be carried out to obtain acceptable multi-sample uncertainties.

B.2 Generalized uncertainty analysis methods

The term *uncertainty* refers to: 'a possible value than an error may have' (Kline and McClintock, 1953). The terms *uncertainty* and *uncertainty interval* both refer to the interval around a measured value, in which the true value is expected to lie.

The uncertainty of a measurement is typically given in terms of percentages, and is shown as δ(measurand). If we consider a variable X_1, its uncertainty would be represented as δX_1. Uncertainties are also shown, usually, with a confidence level; this value, in terms of percentage, refers to a confidence that X_1 will not deviate by more than δX_1.

The uncertainty is made up of two components; the Bias, which is a fixed error (B_1), and the Precision (P_1), which can be a random error in the measurement. The uncertainty is calculated as the Euclidian norm of the two; *i.e.*

$$\delta X_1 = \left\{ (B_1)^2 + (P_1)^2 \right\}^{\frac{1}{2}} \tag{B.1}$$

While some researchers deal with Bias and Precision separately (as was done in Coetzee (2000)), others deal with the uncertainty directly. In this case, we will only deal with the uncertainty, except in the rare cases where assumptions are made which necessitate the use of both Bias and Precision.

Let us take a quantity R, function of n variables, X_0 through X_n, each with uncertainty δX_i. So,

$$R = f\left(X_0, X_1 ... X_n\right) \tag{B.2}$$

Then, the effect of the uncertainty of a single variable on quantity R is the partial derivative of R with respect to that single variable (*i.e.* X_i), times that variable's uncertainty (δX_i). That is,

$$\delta R_{X_i} = \frac{\partial}{\partial X_i}(R)\,\delta X_i \tag{B.3}$$

By summing the uncertainties of R in terms of its variables, the maximum uncertainty is found. However, it is very unlikely that such a value be obtained (from Liebenberg (2002)); rather, the Euclidian norm of the individual uncertainties is taken, as

$$\delta R = \left\{\sum_{i=1}^{n}\left(\frac{\partial}{\partial X_i}(R)\delta X_i\right)^2\right\}^{\frac{1}{2}} \tag{B.4}$$

This equation is valid only when:

- The errors and uncertainties of each variable are independent of one another
- The distribution of errors or uncertainties is Gaussian, for all X_i
- All the X_is are quoted at the same odds.

It is customary to normalize Equation B.4 with respect to the full value of R, with percentage units. However, this cannot be done with temperatures, due to the fact that different temperature scales will have different percentages, and special cases, such as when the temperature being measured is 0^oC.

B.3 Uncertainty in temperature measurements

Temperatures in this experimental system are measured using type-T thermocouples. Type-T thermocouples use constantin and copper as the two metals. The cold junction utilized is built-in into National Instruments' SCXI-1303 card. The thermocouples are calibrated in two temperature baths, one at 5^oC and the other at 60^oC, against a Pt-100 resistance temperature detector (RTD).

The temperatures were calibrated using a linear scale. As they were calibrated using a precise RTD, the thermocouples' Bias was taken to be that of the Pt-100 RTD used. Furthermore, the precision of each thermocouple measurement is

known to be the standard deviation from the steady-state value it measures. Then, the uncertainty in each thermocouple's reading is

$$\delta T_i = \sqrt{B^2 + P^2} \tag{B.5}$$

where the precision P is directly equal to the standard deviation of the reading, σ. There are several sections of the experimental set-up that utilizes the average of several thermocouples (up to four) to find the mean temperature. It follows that

$$T_m = \frac{T_1 + T_2 + ... + T_n}{n} \tag{B.6}$$

And, the partial derivative in this mean temperature per averaged temperature is

$$\frac{\partial T_{m,T_i}}{\partial T_i} = \frac{1}{n}\delta T_i \tag{B.7}$$

Taking the Euclidian norm, and assuming that the thermocouples have the same uncertainty,

$$\begin{aligned} \delta T_m &= \left\{\sum_{i=1}^{n} \left(\tfrac{1}{n}\delta T_i\right)^2\right\}^{\frac{1}{2}} = \left(\frac{n}{n^2}\delta T_i^2\right)^{\frac{1}{2}} \\ &= \left(\tfrac{1}{n}\right)^{\frac{1}{2}} \delta T_i \end{aligned} \tag{B.8}$$

B.4 Wall temperature uncertainty

The outer diameter of the inner tube is instrumented using seven stations of four thermocouples each. However, since we are only interested in finding the average wall temperature of the tube, we can take an average. Thus, the uncertainty becomes,

$$\delta Tw, o = \frac{1}{\sqrt{28}}\delta T_{w,i} \tag{B.9}$$

where the average uncertainty in the wall temperatures is used as the single uncertainty.

B.5 Refrigerant mass flow rate uncertainty

The coriolis flow meters have an accuracy of 0.1% of the nominal reading. Thus, the uncertainty in the Coriolis CMF-010 is

$$\delta\dot{m} = \frac{0.1}{100}\dot{m}_{reading} \tag{B.10}$$

B.5.1 Mass flux uncertainty

The mass flux is defined as

$$G = \frac{\dot{m}}{A_c} \tag{B.11}$$

From the uncertainty of cross-sectional area, and that of the flow rate,

$$\delta G = \left(\left(\frac{\partial}{\partial \dot{m}} G\delta\dot{m} \right)^2 + \left(\frac{\partial}{\partial A_c} G\delta A_c \right)^2 \right)^{\frac{1}{2}} \tag{B.12}$$

and the partial derivatives are

$$\frac{\partial G}{\partial \dot{m}} = \frac{1}{A_c} \tag{B.13}$$

$$\frac{\partial G}{\partial A_c} = -\frac{\dot{m}}{A_c^2} \tag{B.14}$$

B.6 Water mass flow rates uncertainty

The coriolis flow meters have an uncertainty of 0.1% of the actual reading, when in the nominal flow regime. Thus, the uncertainty in the Coriolis CMF-010 and the CMF-025 is

$$\delta\dot{m} = \frac{0.1}{100}\dot{m}_{reading} \tag{B.15}$$

The Bürkert flow meters, models $DIN-015$ and $DIN-025$, have an uncertainty of 0.2% of the full scale reading. Then, the uncertainty is

$$\delta\dot{m} = \frac{0.2}{100}\dot{m}_{reading} \tag{B.16}$$

B.7 Pressure measurement uncertainty

The pressure transducers, Sensotec FP-2000s (FP2000 User's Manual, Columbus, OH), with a full-scale value of ± 3447 kPa (500 psi) have an uncertainty of 0.1% of full-scale. This gives

$$\delta p_j = \pm\frac{0.1}{100}3447 \tag{B.17}$$

$$= reading \pm 3.447\ kPa \tag{B.18}$$

B.8 REFPROP uncertainty analysis

National Institute of Standards and Technology (2002)'s REFPROP uses user inputs of pressure and temperature to calculate the correct property. The main thermo-physical properties of the fluid in question (R-22), the average uncertainties in terms of percentages, are available in the `.fld` fluid files in the Refprop directory. However, for such properties as enthalpy and entropy, it is not possible to directly garner the uncertainty from the fluid files. This is due to the fact that these are calculated using the governing equation of state. However, the governing

equations are complicated, and it is time-consuming to properly calculate the required derivatives. Lemmon (2006) in a private e-mail communication with the author states that the accepted practice is to take the uncertainty of the enthalpy as half of that of the isobaric specific heat.

Thus, from the REFPROP fluid files, and the private conversation held with Dr. Lemmon, the following typical uncertainties are found.

$$\delta h = 0.5\% \tag{B.19}$$
$$\delta k_{l,v} = 3.7\% \tag{B.20}$$
$$\delta \mu_l = 1.09\% \tag{B.21}$$
$$\delta \mu_v = 1.09\% \tag{B.22}$$
$$\delta \rho_l = 0.1\% \tag{B.23}$$
$$\delta \rho_v = 0.1\% \tag{B.24}$$
$$\delta \sigma = 0.05\% \tag{B.25}$$
$$\delta c_p = 1\% \tag{B.26}$$

The water side uncertainties are found in the water fluid file from REFPROP and the IAPWS Advisory Note (Watanabe, 2003) regarding uncertainties of enthalpy, thermal conductivity and surface tension. The uncertainties are summarized as

$$\delta h = 0.05\% \tag{B.27}$$
$$\delta k_{l,v} = 1.8\% \tag{B.28}$$
$$\delta \mu_l = 1\% \tag{B.29}$$
$$\delta \mu_v = 0.5\% \tag{B.30}$$
$$\delta \rho_l = 0.001\% \tag{B.31}$$
$$\delta \rho_v = 0.001\% \tag{B.32}$$
$$\delta \sigma = 0.1\% \tag{B.33}$$
$$\delta c_p = 0.1\% \tag{B.34}$$

B.9 Temperature difference uncertainty

The temperature difference between inlet and outlet of any of the heat exchangers is a function, evidently, of the inlet and outlet temperatures. Each temperature has its own uncertainty (though, because of prior calibration, and method of manufacturing, which is the same, for correctly working thermocouples, the uncertainty should be of the same order, at the least), and taking a difference will only increase the uncertainty. Thus, for a generic temperature difference, the uncertainty is

$$\delta\Delta T = \left(\delta T_1^2 + \delta T_2^2\right)^{\frac{1}{2}} \tag{B.35}$$

B.10 Uncertainty in measurement of tube diameters

The inside tube diameters were measured by the manufacturers Wolverine Tube Inc. (1999) to a total uncertainty of $25 \cdot 10^{-6}$m, that is $\delta D_i = 25 \cdot 10^{-6} m$.

B.11 Uncertainty in measurement of heat exchanger length

The precision limit was taken as twice the smallest increment of the tape measure, *i.e.* 0.5 mm, and a bias limit of 1 mm was assumed. Thus, the uncertainty in the measurement of the exchanger length is

$$\delta L = \sqrt{1^2 + 0.5^2} = 1.11\ mm \tag{B.36}$$

This gives an uncertainty of $\delta L = 1.11\ mm$.

B.12 Uncertainty in measurement of surface area

The tube surface area is calculated from

$$A_i = \pi D_i L \ , \ A_o = \pi D_o L \tag{B.37}$$

Then, the uncertainty in A is

$$\delta A = \left[\left(\frac{\partial}{\partial L} A \delta L \right)^2 + \left(\frac{\partial}{\partial D_i} A \delta D_i \right)^2 \right]^{\frac{1}{2}} \tag{B.38}$$

The partial derivatives are

$$\frac{\partial A}{\partial L} = \pi D_i \tag{B.39}$$

$$\frac{\partial A}{\partial D_i} = \pi l \tag{B.40}$$

B.13 Uncertainty in the value of thermal conductivity of the copper tubing

Abu-Eishah (2001) performed a detailed analysis of the uncertainty of the copper tube thermal conductivity. He found the total uncertainty in the conductivity to be,

$$\frac{\delta k_{Cu}}{k_{Cu}} \cdot 100 = \frac{0.04}{400} \cdot 100 = 0.01\% \tag{B.41}$$

in the temperature region of this study (*i.e.* 0-100^{o}C).

B.14 Uncertainty in the wall thermal resistance

The wall thermal resistance is

$$R_w = \frac{ln\left(\frac{d_{io}}{d_{ii}}\right)}{2\pi k_{cu} L} \tag{B.42}$$

The partial derivatives are

$$\frac{\partial R}{\partial d_{io}} = \frac{1}{2\pi k_{cu} L d_{io}} \tag{B.43}$$

$$\frac{\partial R}{\partial d_{ii}} = -\frac{1}{2\pi k_{cu} L d_{ii}} \tag{B.44}$$

$$\frac{\partial R}{\partial k_{cu}} = -\frac{\ln \frac{d_{io}}{d_{ii}}}{2\pi L k_{cu}^2} \tag{B.45}$$

$$\frac{\partial R}{\partial L} = -\frac{\ln \frac{d_{io}}{d_{ii}}}{2\pi k_{cu} L^2} \tag{B.46}$$

Then, the uncertainty in wall thermal resistance is:

$$\delta R_w = \left(\left(\frac{\partial}{\partial d_{io}} \delta d_{io} \right)^2 + \left(\frac{\partial}{\partial d_{ii}} \delta d_{ii} \right)^2 + \left(\frac{\partial}{\partial k_{cu}} \delta k_{cu} \right)^2 + \left(\frac{\partial}{\partial L} \delta L \right)^2 \right)^{\frac{1}{2}} \tag{B.47}$$

B.15 Void fraction uncertainty

The void fraction is calculated using the logarithmic mean model of El Hajal *et al.* (2003). This model, however, represents a curve fit, which describes the majority of the measured void fraction data. However, while the coefficient of determination (R^2), which is a measure of the statistical adequacy of the fit, is not known, the void fraction is known to be a function of fluid properties; in this manner, the uncertainty of the void fraction can be calculated, since the void fraction is,

$$\epsilon = \frac{\epsilon_h - \epsilon_{ra}}{\ln \frac{\epsilon_h}{\epsilon_{ra}}} \tag{B.48}$$

The homogeneous void fraction is,

$$\epsilon_h = \left[1 + \left(\frac{1-x}{x}\left(\frac{\rho_v}{\rho_l}\right)\right)\right]^{-1} \tag{B.49}$$

and the Rouhani-Axelsson void fraction is,

$$\epsilon_{ra} = \frac{x}{\rho_v}\left([1 + 0.12(1-x)]\left[\frac{x}{\rho_v} + \frac{1-x}{\rho_l}\right] + \frac{1.18(1-x)[g\sigma(\rho_l - \rho_v)]^{0.25}}{G\rho_l^{0.5}}\right)^{-1} \tag{B.50}$$

The partial derivative of the void fraction with respect to vapor quality is:

$$\frac{\partial \epsilon}{\partial x} = \frac{\frac{\left(\frac{\rho_v}{\rho_l}\right)\left(\frac{1}{x}+\frac{1-x}{x^2}\right)}{\left[1+\left(\frac{1-x}{x}\right)\left(\frac{\rho_v}{\rho_l}\right)\right]^2} - \frac{1}{\rho_v C} + \frac{x}{\rho_v C^2}\left(\begin{array}{r} -0.12\left(\frac{x}{\rho_v}+\frac{1-x}{\rho_l}\right) \\ +(1.12-0.12x)\left(\frac{1}{\rho_v}-\frac{1}{\rho_l}\right) \\ -\frac{1.18[g\sigma(\rho_l-\rho_v)]^{0.25}}{G\rho_l^{0.5}} \end{array}\right)}{ln\left|\left(\frac{\rho_v}{x}\right)\frac{C}{1+\left(\frac{1-x}{x}\right)\left(\frac{\rho_v}{\rho_l}\right)}\right|} - \frac{\left[\left(\left(1+\left(\frac{1-x}{x}\right)\left(\frac{\rho_v}{\rho_l}\right)\right)^{-1} - \frac{x}{\rho_v C}\right)\times\left(x\left(1+\left(\frac{1-x}{x}\right)\left(\frac{\rho_v}{\rho_l}\right)\right)\right)\right]}{ln\left|\frac{\rho_v C}{x\left(1+\left(\frac{1-x}{x}\right)\left(\frac{\rho_v}{\rho_l}\right)\right)}\right|^2 \rho_v C}\left[\begin{array}{r} -\frac{\rho_v C}{x^2\left(1+\left(\frac{1-x}{x}\right)\left(\frac{\rho_v}{\rho_l}\right)\right)} \\ +\frac{\rho_v C\left(\frac{1}{x}+\frac{1-x}{x^2}\right)\left(\frac{\rho_v}{\rho_l}\right)}{x\left(1+\left(\frac{1-x}{x}\right)\left(\frac{\rho_v}{\rho_l}\right)\right)^2} \\ +\frac{\rho_v\left\{\begin{array}{r} -0.12\left(\frac{x}{\rho_v}+\frac{1-x}{\rho_l}\right) \\ +(1.12-0.12x)\left(\frac{1}{\rho_v}-\frac{1}{\rho_l}\right) \\ -\frac{1.18[g\sigma(\rho_l-\rho_v)]^{0.25}}{G\rho_l^{0.5}} \end{array}\right\}}{x\left(1+\left(\frac{1-x}{x}\right)\left(\frac{\rho_v}{\rho_l}\right)\right)} \end{array}\right] \tag{B.51}$$

where the constant C was introduced for brevity. It stands for

$$C = (1.12-0.12x)\left(\frac{x}{\rho_v}+\frac{1-x}{\rho_l}\right) + \frac{1.18(1-x)[g\sigma(\rho_l-\rho_v)]^{0.25}}{G\rho_l^{0.5}} \tag{B.52}$$

The partial derivative of the void fraction with respect to the mass flux is

$$\frac{\partial \epsilon}{\partial G} = \frac{\dfrac{1.18x(1-x)[g\sigma(\rho_l-\rho_v)]^{0.25}}{\rho_v C^2 G^2 \rho_l^{0.5} ln\left|\frac{\rho_v C}{x\left(1+\left(\frac{1-x}{x}\right)\left(\frac{\rho_v}{\rho_l}\right)\right)}\right|} + \dfrac{\left(\left(1+\left(\frac{1-x}{x}\right)\left(\frac{\rho_v}{\rho_l}\right)\right)^{-1} - \frac{x}{\rho_v C}\right) 1.18(1-x)[g\sigma(\rho_l-\rho_v)]^{0.25}}{ln\left|\frac{\rho_v C}{x\left(1+\left(\frac{1-x}{x}\right)\left(\frac{\rho_v}{\rho_l}\right)\right)}\right|^2 G^2\rho_l^2 C}}{} \tag{B.53}$$

C is defined as

$$C = (1.12-0.12x)\left(\frac{x}{\rho_v}+\frac{1-x}{\rho_l}\right) + \frac{1.18(1-x)[g\sigma(\rho_l-\rho_v)]^{0.25}}{G\rho_l^{0.5}} \tag{B.54}$$

The partial derivative with respect to the vapor density is

$$\frac{\partial \epsilon}{\partial \rho_v} = -\frac{\left[\left(\left(1+\left(\frac{1-x}{x}\right)\left(\frac{\rho_v}{\rho_l}\right)\right)^{-1} - \frac{x}{\rho_v C}\right) \times x\left(1+\left(\frac{1-x}{x}\right)\left(\frac{\rho_v}{\rho_l}\right)\right)\right]}{\left(ln\left|\frac{\rho_v C}{x\left(1+\left(\frac{1-x}{x}\right)\left(\frac{\rho_v}{\rho_l}\right)\right)}\right|^2 \rho_v C\right)} \left[\begin{array}{c} \dfrac{C}{x\left(1+\left(\frac{1-x}{x}\right)\left(\frac{\rho_v}{\rho_l}\right)\right)} \\ -\dfrac{\rho_v C(1-x)}{x^2\left(1+\left(\frac{1-x}{x}\right)\left(\frac{\rho_v}{\rho_l}\right)\right)^2 \rho_l} \\ -\dfrac{\frac{\rho_v}{x}\left\{\begin{array}{c}\frac{(1.12-0.12x)x}{\rho_v^2} \\ +\frac{1}{4}\frac{1.18(1-x)g\sigma}{[g\sigma(\rho_l-\rho_v)]^{0.75}G\rho_l^{0.5}}\end{array}\right\}}{1+\left(\frac{1-x}{x}\right)\left(\frac{\rho_v}{\rho_l}\right)} \end{array}\right] \tag{B.55}$$

where C, again, was introduced for brevity. It is defined as

$$C = (1.12 - 0.12x)\left(\frac{x}{\rho_v} + \frac{1-x}{\rho_l}\right) + \frac{1.18(1-x)[g\sigma(\rho_l - \rho_v)]^{0.25}}{G\rho_l^{0.5}} \tag{B.56}$$

The partial derivative with respect to the liquid density is

$$\frac{\partial \epsilon}{\partial \rho_l} = \left\{ \frac{\rho_v^2 C(1-x)}{x^2\left(1+\left(\frac{1-x}{x}\right)\left(\frac{\rho_v}{\rho_l}\right)\right)^2 \rho_l^2} + \rho_v \frac{\left[\begin{array}{r} -\dfrac{(1.12-0.12x)(1-x)}{\rho_l^2} \\ +\dfrac{1}{4}\dfrac{1.18(1-x)(g\sigma)}{[g\sigma(\rho_l-\rho_v)]^{0.75}G\rho_l^{0.5}} \\ -\left(\dfrac{1}{2}\right)\dfrac{1.18(1-x)[g\sigma(\rho_l-\rho_v)]^{0.25}}{G\rho_l^{1.5}} \end{array}\right]}{x\left(1+\left(\frac{1-x}{x}\right)\left(\frac{\rho_v}{\rho_l}\right)\right)} \right\} - \frac{\left[\begin{array}{r} \dfrac{(1-x)\rho_v}{\left(1+\left(\frac{1-x}{x}\right)\left(\frac{\rho_v}{\rho_l}\right)\right)^2 x\rho_l^2} + x\left(-\dfrac{1.18(1-x)^2}{\rho_l^2}\right) \\ +x\left(\dfrac{1}{4}\dfrac{1.18(1-x)g\sigma}{[g\sigma(\rho_l-\rho_v)]^{0.75}G\rho_l^{0.5}} - \left(\dfrac{1}{2}\right)\dfrac{1.18[g\sigma(\rho_l-\rho_v)]^{0.25}}{G\rho_l^{1.5}\rho_v C^2}\right) \end{array}\right]}{ln\left|\frac{\rho_v C}{x\left(1+\left(\frac{1-x}{x}\right)\left(\frac{\rho_v}{\rho_l}\right)\right)}\right|} - \frac{\left[\begin{array}{r} \left(\left(1+\left(\dfrac{1-x}{x}\right)\left(\dfrac{\rho_v}{\rho_l}\right)\right)^{-1} - \dfrac{x}{\rho_v C}\right) \\ \times x\left(1+\left(\dfrac{1-x}{x}\right)\left(\dfrac{\rho_v}{\rho_l}\right)\right) \end{array}\right]}{\left(ln\left|\frac{\rho_v C}{x\left(1+\left(\frac{1-x}{x}\right)\left(\frac{\rho_v}{\rho_l}\right)\right)}\right|^2 \rho_v C\right)} \times \tag{B.57}$$

And C, as before is

$$C = (1.12 - 0.12x)\left(\frac{x}{\rho_v} + \frac{1-x}{\rho_l}\right) + \frac{1.18(1-x)[g\sigma(\rho_l - \rho_v)]^{0.25}}{G\rho_l^{0.5}} \tag{B.58}$$

B.16 Heat balance, Refrigerant side

The heat transferred from the refrigerant is calculated by multiplying the refrigerant mass flux by the change in enthalpy (from inlet of precondenser to the outlet of the postcondenser). This is

$$\dot{Q}_{ref} = \dot{m}_{ref}\Delta h \tag{B.59}$$

And the uncertainty is

$$\delta\dot{Q}_{ref} = \left(\left[\frac{\partial}{\partial\dot{m}}(\dot{Q})\delta\dot{m}\right]^2 + \left[\frac{\partial}{\partial\Delta h}(\dot{Q})\delta\Delta h\right]^2\right)^{\frac{1}{2}} \tag{B.60}$$

where,

$$\delta\Delta h = \left(\left(\frac{\partial}{\partial h_{in}}\Delta h\delta h_{in}\right)^2 + \left(\frac{\partial}{\partial h_{out}}\Delta h\delta h_{out}\right)^2\right)^{\frac{1}{2}} \tag{B.61}$$

B.17 Heat balance uncertainty, water side

The water side heat transferred is,

$$\dot{Q}_{water} = \sum \dot{Q}_{i,H_2O} \tag{B.62}$$

Where the total heat transferred from the water is equal to the sum of the individual

heat exchangers' water side heat balance. This entails that the uncertainty in the water side of the heat balance is

$$\delta\dot{Q}_{H_2O} = \left(\sum_{i=1}^{3}\left(\frac{\partial}{\partial\dot{Q}_i}\dot{Q}_{H_2O}(\delta\dot{Q}_i)\right)^2\right)^{\frac{1}{2}} \tag{B.63}$$

The individual heat exchangers' water side heat balance uncertainty can be calculated using

$$\dot{Q}_i = \dot{m}_{H_2O,i}c_{p,i}\Delta T_i \tag{B.64}$$

Thus, the uncertainty in the water-side energy transfer, knowing what the uncertainties in the water mass flow rate, isobaric specific heat and temperature difference, are

$$\delta\dot{Q}_i = \left[\left(\frac{\partial}{\partial\dot{m}}\dot{Q}_i\delta\dot{m}\right)^2 + \left(\frac{\partial}{\partial c_{p,i}}\dot{Q}_i\delta c_{p,i}\right)^2 + \left(\frac{\partial}{\partial\Delta T_i}\dot{Q}_i\delta\Delta T_i\right)^2\right]^{\frac{1}{2}} \tag{B.65}$$

B.18 Average heat transfer uncertainty

The average heat transferred, $\dot{Q}_{avg}$ is

$$\dot{Q}_{avg} = \frac{\dot{Q}_{H_2O} + \dot{Q}_{ref}}{2} \tag{B.66}$$

Then, the uncertainty in the average heat transfer is

$$\delta\dot{Q}_{avg} = \left(\frac{1}{2}\right)^{\frac{1}{2}}\left[\delta\dot{Q}_{h_2O}^2 + \delta\dot{Q}_{ref}^2\right]^{\frac{1}{2}} \tag{B.67}$$

B.19 Inlet and outlet vapor quality uncertainty analysis

B.19.1 Inlet vapor quality uncertainty

The vapor quality at the inlet and outlet of the test section is calculated using measured data, including temperature, pressure and water-side heat transferred. This means, though that the inlet and outlet enthalpies are calculated. And,

$$h_{in,test} = h_{in,pre} - |\frac{\dot{Q}_{pre,H_2O}}{\dot{m}_{ref}}| \tag{B.68}$$

Thus, the uncertainty in test inlet enthalpy is

$$\delta h_{in,test} = \left[\left(\frac{\partial}{\partial h_{in,pre}} (h_{in,test}) \delta h_{in,pre} \right)^2 + \left(\frac{\partial}{\partial \dot{Q}_{pre,H_2O}} (h_{in,test}) \delta \dot{Q}_{pre,H_2O} \right)^2 + \left(\frac{\partial}{\partial \dot{m}_{ref}} (h_{in,test}) \delta \dot{m}_{ref} \right)^2 \right]^{\frac{1}{2}} \tag{B.69}$$

where the partial derivatives above are,

$$\frac{\partial h_{in,test}}{\partial h_{in,pre}} = 1 \tag{B.70}$$

$$\frac{\partial h_{in,test}}{\partial \dot{Q}_{pre,H_2O}} = -\frac{1}{\dot{m}_{ref}} \tag{B.71}$$

$$\frac{\partial h_{in,test}}{\partial \dot{m}_{ref}} = \frac{\dot{Q}_{H_2O}}{\dot{m}_{ref}^2} \tag{B.72}$$

Then, knowing what the enthalpy at the point is, the quality can be calculated as

$$x_{in} = \frac{h_{in,test} - h_f}{h_v - h_l} \tag{B.73}$$

And from the above, the uncertainty in x_{in}

$$\delta x_{in} = \left[\left(\frac{\partial}{\partial h_{in,test}}(x_{in})\delta h_{in,test} \right)^2 + \left(\frac{\partial}{\partial h_{f,test}}(x_{in})\delta h_{f,test} \right)^2 + \left(\frac{\partial}{\partial h_{v,test}}(x_{in})\delta h_{v,test} \right)^2 \right]^{\frac{1}{2}} \tag{B.74}$$

The partial derivatives are

$$\frac{\partial x_{in}}{\partial h_{in,test}} = \frac{1}{h_{v,test} - h_{l,test}} \tag{B.75}$$

$$\frac{\partial x_{in}}{\partial h_{v,test}} = \frac{h_f - h_{in,test}}{(h_v - h_f)^2} \tag{B.76}$$

$$\frac{\partial x_{in}}{\partial h_{f,test}} = -\frac{1}{h_{v,test} - h_{f,test}} - \frac{h_{in,test} - h_{f,test}}{(h_{v,test} - h_{f,test})^2} \tag{B.77}$$

Where h_l and h_v are evaluated at the saturation pressure and temperature measured at the inlet of the test section, and are functions of REFPROP.

B.19.2 Outlet vapor quality uncertainty

The outlet vapor quality, much like the inlet quality, is dependent on the amount of heat extracted out of the test section (rather than the precondenser, in the inlet's case), and is calculated from

$$h_{out,test} = h_{in,test} - |\frac{\dot{Q}_{test,H_2O}}{\dot{m}_{ref}}| \tag{B.78}$$

Like above, the uncertainty of this enthalpy is,

$$\delta h_{out,test} = \left[\left(\frac{\partial}{\partial \dot{Q}_{test,H_2O}} (h_{out,test}) \delta \dot{Q}_{test,H_2O} \right)^2 + \left(\frac{\partial}{\partial \dot{m}_{ref}} (h_{out,test}) \delta \dot{m}_{ref} \right)^2 + \left(\frac{\partial}{\partial h_{in,test}} (h_{out,test}) \delta h_{in,test} \right)^2 \right]^{\frac{1}{2}} \tag{B.79}$$

Where the partial derivatives are

$$\frac{\partial h_{out,test}}{\partial h_{in,pre}} = 1 \tag{B.80}$$

$$\frac{\partial h_{out,test}}{\partial \dot{Q}_{pre,H_2O}} = -\frac{1}{\dot{m}_{ref}} \tag{B.81}$$

$$\frac{\partial h_{in,test}}{\partial \dot{m}_{ref}} = \frac{\dot{Q}_{H_2O}}{\dot{m}_{ref}^2} \tag{B.82}$$

And the uncertainty in quality is

$$\delta x_{out} = \left[\left(\frac{\partial}{\partial h_{f,test,out}} (x_{out}) \delta h_{f,test,out} \right)^2 + \left(\frac{\partial}{\partial h_{v,test,out}} (x_{out}) \delta h_{v,test,out} \right)^2 + \left(\frac{\partial}{\partial h_{out,test}} (x_{out}) \delta h_{out,test} \right)^2 \right]^{\frac{1}{2}} \tag{B.83}$$

The partial derivatives are

$$\frac{\partial x_{out}}{\partial h_{out,test}} = \frac{1}{h_{v,test,out} - h_{l,test,out}} \tag{B.84}$$

$$\frac{\partial x_{out}}{\partial h_{v,test,out}} = \frac{h_f - h_{out,test}}{(h_{v,out} - h_{f,out})^2} \tag{B.85}$$

$$\frac{\partial x_{out}}{\partial h_{f,test,out}} = -\frac{1}{h_{v,test,out} - h_{f,test,out}} - \frac{h_{out,test} - h_{f,test,out}}{(h_{v,test,out} - h_{f,test,out})^2} \tag{B.86}$$

B.19.3 Average test vapor quality uncertainty

The average test vapor quality is

$$x_{avg} = \frac{x_{in} + x_{out}}{2} \tag{B.87}$$

And its uncertainty becomes

$$\delta x_{avg} = \left[\left(\frac{\partial}{\partial x_{in}} (x_{avg} \delta x_{in}) \right)^2 + \left(\frac{\partial}{\partial x_{out}} (x_{avg} \delta x_{out}) \right)^2 \right]^{\frac{1}{2}} \tag{B.88}$$

B.20 Uncertainty in the inner wall temperature

The mean inner wall temperature is

$$T_{w,i} = T_{w,o} + \left| \dot{Q}_{test} R_w \right| \tag{B.89}$$

The partial derivatives are

$$\frac{\partial T_{w,i}}{\partial T_{w,o}} = 1 \tag{B.90}$$

$$\frac{\partial T_{w,i}}{\partial \dot{Q}_{test}} = R_w \tag{B.91}$$

$$\frac{\partial T_{w,i}}{\partial R_w} = \dot{Q}_{test} \tag{B.92}$$

The uncertainty in the inner wall temperature is

$$\delta T_{w,i} = \left[(\delta T_{w,o})^2 + \left(R_w \partial \dot{Q}_{H_2O} \right)^2 + \left(\dot{Q}_{H_2O} \delta R_w \right)^2 \right]^{\frac{1}{2}} \tag{B.93}$$

B.21 Heat transfer coefficient uncertainty analysis

The overall heat transfer coefficient is given as

$$h_{c,exp} = \frac{\dot{Q}_{test}}{A_{li}\left(T_{w,i} - T_b\right)} \tag{B.94}$$

where T_b is the mean bulk temperature of the fluid, whose uncertainty is calculated as set in the previous sections, $T_{w,i}$ is the mean inner wall temperature of the heat exchanger, A_{li} is the heat transfer area and $\dot{Q}_{test}$ is the heat transferred in the heat exchanger. The uncertainty in the temperature difference is calculated as shown in the previous sections.

The partial derivatives required are

$$\frac{\partial h_{c,exp}}{\partial \dot{Q}_{H_2O}} = \frac{1}{A_{li}\left(T_{w,i} - T_b\right)} \tag{B.95}$$

$$\frac{\partial h_{c,exp}}{\partial A_{li}} = -\frac{\dot{Q}_{H_2O}}{A_{li}^2\left(T_{w,i} - T_b\right)} \tag{B.96}$$

$$\frac{\partial h_{c,exp}}{\partial A_{li}\Delta T} = -\frac{\dot{Q}_{test}}{A_{li}} \tag{B.97}$$

The uncertainty is

$$h_{c,exp} = \left[\left(\frac{1}{A_{li}\Delta T}\delta\dot{Q}_{test}\right)^2 + \left(-\frac{\dot{Q}_{test}}{A_{li}^2\Delta T}\delta A_{li}\right)^2 + \left(-\frac{\dot{Q}_{test}}{A_{li}\Delta T}\delta\Delta T\right)^2\right]^{\frac{1}{2}} \tag{B.98}$$

B.22 Pressure drop uncertainty analysis

The measured pressure drop over the entire test section is a function of the momentum pressure drop, and the friction pressure drop, as shown in Equation B.99. As such, the uncertainty in the pressure drop, in addition to being a function of the accuracy of the pressure transducers, is also a function of the vapor quality, void fraction and fluid properties.

$$\Delta p_{measured} = \Delta p_{mom} + \Delta p_{fric} \tag{B.99}$$

We rearrange the above equation to isolate Δp_{fric}

$$\Delta p_{fric} = p_{in} - p_{out} - \Delta p_{momentum} \tag{B.100}$$

B.22.1 Measured pressure drop uncertainty

The measured pressure drop's uncertainty is only a function of the accuracy and uncertainty of the pressure transducers. As can be recalled from Section 3.7, there are three pressure sensors at the inlet and outlet of the test section. As such, the measured pressures at the inlet and outlet are the mathematical average of three individual transducers, each with the same uncertainty δP. The pressure transducers are all calibrated over the same range, and the factory uncertainty can be used as indicated. Thus, we have, mathematically,

$$p_{in/out,measured} = \frac{1}{3}\sum_{1}^{3} p_{measured,j} \tag{B.101}$$

$$\delta p_{in/out,measured} = \left(\sum_{j=1}^{3}\left(\frac{\partial}{\partial p_j} p_{in/out,measured}\delta p_j\right)^2\right)^{\frac{1}{2}} \tag{B.102}$$

And, since we known that the pressure transducers' uncertainties are the same, we can say,

$$\delta p_{in/out,measured} = \left(\frac{1}{3}\right)^{\frac{1}{2}} \delta p_j \tag{B.103}$$

Which, knowing that the uncertainty of each reading is ±3.447 kPa, gives the total uncertainty at the inlet and outlet pressure of

$$\delta p_{in/out,measured} = reading \pm 1.9901\ kPa \tag{B.104}$$

B.22.2 Momentum pressure drop uncertainty

The momentum pressure drop was defined in Section 4.4.1 as

$$\Delta p_{mom} = G^2 \left\{ \left[\frac{(1-x)^2}{\rho_l(1-\epsilon)} + \frac{x^2}{\rho_v \epsilon} \right]_{out} - \left[\frac{(1-x)^2}{\rho_l(1-\epsilon)} + \frac{x^2}{\rho_v \epsilon} \right]_{in} \right\} \tag{B.105}$$

We can see that this equation is a function of mass flux, vapor and liquid densities, quality and void fraction, at the inlet and outlet. The derivatives of the momentum pressure drop in terms of its components are

$$\frac{\partial}{\partial G}(\Delta p_{mom}) = 2G \left\{ \begin{array}{l} \left[\frac{(1-x)^2}{\rho_l(1-\epsilon)} + \frac{x^2}{\rho_v \epsilon} \right]_{out} - \\ \left[\frac{(1-x)^2}{\rho_l(1-\epsilon)} + \frac{x^2}{\rho_v \epsilon} \right]_{in} \end{array} \right\} \tag{B.106}$$

$$\frac{\partial}{\partial x_{in}}(\Delta p_{mom}) = G^2 \left[\frac{2(1-x)}{\rho_l(1-\epsilon)} + \frac{2x}{\rho_v \epsilon} \right]_{in} \tag{B.107}$$

$$\frac{\partial}{\partial x_{out}}(\Delta p_{mom}) = G^2 \left[\frac{2(1-x)}{\rho_l(1-\epsilon)} + \frac{2x}{\rho_v \epsilon} \right]_{out} \tag{B.108}$$

$$\frac{\partial}{\partial \rho_{l,in}}(\Delta p_{mom}) = \frac{G^2(1-x_{in})^2}{\rho_{l,in}^2(1-\epsilon_{in})} \tag{B.109}$$

$$\frac{\partial}{\partial \rho_{l,out}}(\Delta p_{mom}) = -\frac{G^2(1-x_{out})^2}{\rho_{l,out}^2(1-\epsilon_{out})} \tag{B.110}$$

$$\frac{\partial}{\partial \rho_{v,in}}(\Delta p_{mom}) = \frac{G^2 x_{in}^2}{\rho_{v,in}^2 \epsilon_{in}} \tag{B.111}$$

$$\frac{\partial}{\partial \rho_{v,out}}(\Delta p_{mom}) = -\frac{G^2 x_{out}^2}{\rho_{v,out}^2 \epsilon_{out}} \tag{B.112}$$

$$\frac{\partial}{\partial \epsilon_{in}}(\Delta p_{mom}) = G^2 \left(-\frac{(1-x_{in})^2}{\rho_{l,in}(1-\epsilon_{in})^2} + \frac{x_{in}^2}{\rho_{v,in}\epsilon_{in}^2} \right) \tag{B.113}$$

$$\frac{\partial}{\partial \epsilon_{out}}(\Delta p_{mom}) = G^2 \left(\frac{(1-x_{out})^2}{\rho_{l,out}(1-\epsilon_{out})^2} - \frac{x_{out}^2}{\rho_{v,out}\epsilon_{out}^2} \right) \tag{B.114}$$

Now that the partial derivatives are available, the total uncertainty can be calculated,

$$\delta\Delta p_{mom} = \left(\begin{array}{c} \left(\frac{\partial}{\partial G}(\Delta p_{mom})\delta G\right)^2 + \left(\frac{\partial}{\partial x_{in}}(\Delta p_{mom})\delta x_{in}\right)^2 + \\ \left(\frac{\partial}{\partial x_{out}}(\Delta p_{mom})\delta x_{out}\right)^2 + \left(\frac{\partial}{\partial \rho_{l,in}}(\Delta p_{mom})\delta \rho_{l,in}\right)^2 \\ \left(\frac{\partial}{\partial \rho_{l,out}}(\Delta p_{mom})\delta \rho_{l,out}\right)^2 + \left(\frac{\partial}{\partial \rho_{v,in}}(\Delta p_{mom})\delta \rho_{v,in}\right)^2 \\ \left(\frac{\partial}{\partial \rho_{v,out}}(\Delta p_{mom})\delta \rho_{v,out}\right)^2 + \left(\frac{\partial}{\partial \epsilon_{in}}(\Delta p_{mom})\delta \epsilon_{in}\right)^2 \\ \left(\frac{\partial}{\partial \epsilon_{out}}(\Delta p_{mom})\delta \epsilon_{out}\right)^2 \end{array} \right)^{\frac{1}{2}} \tag{B.115}$$

B.22.3 Frictional pressure drop uncertainty

In the above two sections, the uncertainty in the measured pressure drop and in the momentum pressure drop were calculated. Using this, the frictional pressure drop's uncertainty is

$$\delta\Delta p_{fric} = \left(\begin{array}{c} \left(\frac{\partial}{\partial p_{in,measured}}(\Delta p_{fric})\delta p_{in,measured}\right)^2 + \\ \left(\frac{\partial}{\partial p_{out,measured}}(\Delta p_{fric})\delta p_{out,measured}\right)^2 + \\ \left(\frac{\partial}{\partial \Delta p_{mom}}(\Delta p_{fric})\delta \Delta p_{mom}\right)^2 \end{array} \right)^{\frac{1}{2}} \tag{B.116}$$

B.23 Uncertainty Results

The above equations were coded into a Matlab program that automatically calculated the uncertainties for all the data points, in real-time, during operation of the system. The uncertainties are summarized in Table B.1 and discussed thereafter.

Rather than present a single average value of the system uncertainties, or present the uncertainty analysis for each point in the test matrix, four values are presented, each representing one corner of the experimental test matrix (refer to

Table B.1: Experimental uncertainties for condensation heat transfer

Measurand	Uncertainty (%)			
	***G*-250 – *x*-65%**	***G*-250 – *x*-11%**	***G*-650 – *x*-56%**	***G*-650 – *x*-12%**
$\delta T_{ref,m}$	0.0178^{o}C	0.0208^{o}C	0.0727^{o}C	0.0117^{o}C
$\delta p_{test,m}$	0.1314%	0.1351%	0.1424%	0.1316%
$\delta \dot{m}_{ref}$	0.1%	0.1%	0.1%	0.1%
δx_{in}	1.524%	4.661%	2.378%	8.238%
δx_m	1.873%	8.322%	2.518%	11.12%
$\delta \epsilon_{in}$	0.061%	0.4386%	0.1191%	0.5710%
$\delta \epsilon_m$	0.0995%	0.7811%	0.1327%	0.9012%
$\delta \Delta p_{mom}$	3.727%	5.823%	13.25%	7.118%
$\delta \Delta p_{f,L}$	60.43%	72.02%	38.47%	81.78%
$\delta h_{c,exp}$	0.2087%	3.2672%	0.5484%	4.023%

Chapter 5). During the analysis of the data, it was found that the uncertainties varied, on both constant vapor quality and mass flux, between the boundary values presented in Table B.1.

Due to the fact that the inlets and outlets of the test section were instrumented using several thermocouples (three thermocouples were used to find the mean temperatures), the uncertainty in the saturation temperature was quite precise, nearing that of a high-precision Pt-100 RTD ($\pm 0.01^o$C).

The saturation pressure was also measured using the average of three gauge pressure transducers, which resulted in very certain saturation pressure readings. Although these transducers are normally rated as 0.1% accurate, this is relative to their full-scale value; averaging the readings of six of these transducers brought the uncertainty of the average saturation pressure back to a value near that of

a single transducer reading a full-scale measurement. The uncertainty remained essentially constant over the entire test matrix.

The refrigerant mass flow, since it was measured using a Micromotion CMF-010 flow meter (with MVD technology), had a constant uncertainty of 0.1% over the entire mass flow range that was tested in this setup. The mass flow's uncertainty is not a constant once the flow drops sufficiently low, to a mass flow of about 0.001 kg/s (these low flows were not reached in this experiment). Again, the uncertainty remained constant over the test matrix, as expected.

The inlet and outlet test vapor qualities, being functions of several heat exchangers' assorted uncertainties have widely varying uncertainties. Furthermore, they were also a function of the refrigerant's properties uncertainties, a large factor that is often neglected. On a constant vapor quality point of view, it was found that the best uncertainties in quality could be found at lower mass flux, while on a constant mass flux point of view, the best uncertainties were found at the higher vapor qualities. The major reason that the uncertainties at lower vapor qualities were higher than at higher vapor qualities is due to the fact that the temperature difference (on the water side) was lower, which increased the uncertainty in the temperature difference.

In terms of the void fraction model's uncertainty, Table B.1 shows that there was a variance between 0.06% and 1% of the measured void fraction signal. It should be noted that the void fraction is a strong function of the vapor quality, evidenced by the fact that the void fraction uncertainty was at its worse when the vapor quality also had a large uncertainty. Apart from the vapor quality, the logarithmic-mean void fraction model is a function of the vapor mass flux and the refrigerant properties; however, the density uncertainty of the refrigerant, as well as the mass flux uncertainty are quite low, which allow us to infer that vapor quality uncertainty has the largest influence in the uncertainty of the void fraction logarithmic-mean model.

The momentum pressure drop uncertainty is an area that is not simple to either dismiss or include in a thorough analysis. As can be seen in the Table above, the uncertainty in momentum pressure drop can vary from 3% to almost 15% of the physical momentum pressure drop value. However, the influence of this value is not readily noticeable in the frictional pressure drop, as the relative

size of the term has a large influence. When the pressure drop measured over two pressure transducers is on the same order as the momentum pressure drop, the uncertainty in the momentum term will have a non-negligible effect on the frictional pressure drop. If we investigate the form of the momentum pressure drop, as shown below,

$$\Delta p_{mom} = G^2 \left\{ \left[\frac{(1-x)^2}{\rho_l(1-\epsilon)} + \frac{x^2}{\rho_v \epsilon} \right]_{out} - \left[\frac{(1-x)^2}{\rho_l(1-\epsilon)} + \frac{x^2}{\rho_v \epsilon} \right]_{in} \right\} \tag{B.117}$$

it can be seen that it is a function of the inlet and outlet quasi-equilibrium refrigerant states, as well as the mass flux. Again, it can be seen that this term is a function of the vapor quality, refrigerant properties and the void fraction. If the vapor quality uncertainty is high (such as in regions of low vapor quality), the void fraction uncertainty will also be relatively high, leading the momentum pressure drop to have a large uncertainty.

Furthermore, inspecting the above equation, no difference is expected (in the momentum pressure drop) between a short heat exchanger and a long one, as long as the inlet and outlet states are the same. However, the frictional pressure drop will be affected. In the case of a long heat exchanger, or a microfin tube, in which the momentum pressure drop term is less than 10% of the total measured pressure drop, the effect of the uncertainty of the momentum term is negligible. However, in shorter tubes, with smaller total pressure drops, in which the momentum term is on the same order as the total pressure drop term, the uncertainty in momentum pressure drop will have a large effect. When using a high precision differential pressure transducer, measuring close to its full scale reading (such that the uncertainty is lowest, or closest to its theoretical value) in a low pressure drop environment (*i.e.* a short, smooth tube), the momentum term uncertainty would become the controlling factor in the frictional pressure drop uncertainty.

As a refresher, the pressure drop over the test section was measured using two sets of absolute gauge pressure transducers (average of three signals each). However, the total pressure drop over the entire test range, as described in Chapter 5, varied between 2 kPa at the lowest mass fluxes and vapor qualities and 12 kPa at the highest mass fluxes and vapor qualities. Immediately it can be

seen that the uncertainty in the total pressure drop is a large percentage of the calculated frictional pressure drop. This allows us to identify that, while gauge pressure transducers are necessary, both at the inlet and outlet of the test section, to calculate thermal properties, an additional differential pressure transducer must be utilized. In the experimental matrix, the momentum pressure drop uncertainty was only a significant factor at the lowest mass fluxes, where the total pressure drop was on the same order of magnitude as the momentum pressure drop. It is clear from these results that to obtain reasonable uncertainty in the pressure drop results in this system, at least one differential pressure transducer, instrumented between the inlet and outlet of the test section, is required.

The heat transfer coefficient uncertainty results are also tabulated in Table B.1. The maximum deviation that is found is on the order of 4%, with the best uncertainties on the order of about 0.2%. The highest uncertainties occur at lower vapor qualities, irrespective of mass flux; the fluctuations seen in Table B.1 are due to the fact that the qualities are not exactly the same. If a direct comparison could be made, it would be most probable that the uncertainties found at a constant quality, with varying mass flux (within limits of the flow meter and with a good enough temperature drop on the water side of the test heat exchanger) would compare well. This is evidenced in the case of the low vapor quality data, in which the vapor quality is almost the same.

B.24 Conclusion

In this chapter, a thorough analysis of the experimental uncertainties of the developed two-phase refrigerant system was undertaken. The general method was described, and the important uncertainty equations were derived. Particular attention was paid to the heat transfer coefficient uncertainty, the fluid properties, and the pressure drop. To accurately calculate these, the uncertainties in the vapor quality, the momentum pressure drop and the void fraction model had to be calculated.

A program was written to evaluate the uncertainties at each data point, while only four points were presented; namely, the four corners of the experimental

test matrix. It was found that the uncertainties varied between those four values, rendering the presentation of all values needless, while presenting a single value would have been a gross misrepresentation of the data.

It was found that the heat transfer coefficient uncertainty varies between 4% and 0.2%, while the frictional pressure drop uncertainty varied between 30% and 80%. This is mainly due to the use of gauge transducers rather than a differential pressure transducer.

Further, in terms of the logarithmic-mean void fraction model, it was found that its uncertainty was highly dependent on the uncertainty of the vapor quality, while the momentum pressure drop uncertainty was highly dependent on the uncertainty of the vapor qualities and the void fraction approximations. Further, it was shown that neither of these can be neglected when the order of the total pressure drop is the same as that of the momentum pressure drop. Furthermore, with a high-accuracy differential pressure transducer, the momentum pressure drop uncertainty will become the largest influence on the uncertainty of the frictional pressure drop.

Appendix C

Raw Data